Capturing and characterising pre-failure strain on failing slopes

MELANIE JANE FROUDE

Capturing and characterising pre-failure strain on failing slopes

Melanie J. Froude

Effective management of slope hazards requires an understanding of the likely triggers, geometry, failure dynamics, mechanism and timing; of these the last two remain most problematic. Reducing the epistemic uncertainty of these elements is crucial, particularly for landslides that are not easily mitigated. The 'inverse-velocity method' utilises the linearity in inverse-strain-rate change through time in brittle materials to forecast the timing of final slope collapse. A significant body of published deformation data is available, yet to date there has been no attempt to collate a catalogue of landslide deformations from a large number of sites to examine emergent behaviour; notably variations in and controls on movement prior to failure. This thesis collates thirty-one examples of tertiary creep and related attributes from a broad literature search of over 6,000 peer-reviewed journals. Results show that tertiary creep operates over durations ranging from ~37 minutes to 3,171 days. Patterns of acceleration corroborated with published parameterisations of brittle failure; namely Voight's (1989) model. Most examples (86%) were best-fit with hyperbolic curves, described by an α coefficient within the 1.7 and 2.2 range; indicative of deformation driven by crack growth. No significant relationships between slope and creep characteristics were found within the database of examples, however the lack of standard reporting of slope failures, particularly between industry documents and academic papers, limits the analysis. The database validates the 'inverse-velocity method' as a robust forecasting technique. Iterative *a priori* analysis of data has shown that slopes deforming in a brittle manner are more likely to predict slope collapse 'too soon' as a false positive prediction. Analysis has also shown that tertiary creep is typically delimited (87% of examples) within the first 25% of the total creep duration. Recommendations towards monitoring specifically highlight the need for instruments to deliver spatial accuracies to ~10mm, surface based capture and continuous measurement. Developing processing procedures for point cloud data derived from a permanent terrestrial laser scanning system is recommended as the best approach to small-scale deformation monitoring.

Capturing and characterising pre-failure strain on failing slopes

Melanie J. Froude

Thesis submitted for the degree of

Master of Science

Institute of Hazard, Risk and Resilience

Department of Geography

University of Durham

2011

Table of Contents

List of figures

List of tables

List of boxes

Declaration of Copyright

I confirm that no part of the material presented in this thesis has previously been submitted for a degree in this or any other university. In all cases the word of others, where relevant, has been fully acknowledged.

Melanie J. Froude

Institute of Hazard, Risk and Resilience
Department of Geography
University of Durham

February 2011

Acknowledgements

Many people have contributed to the production of this thesis by providing me with academic and personal support during the research and writing up process.

Firstly I would like to thank my supervisors Dr Nick Rosser and Dr Patrice Carbonneau. Nick: for your continued support, encouragement and patience throughout the ups and downs of my Masters year (and beyond). I have tremendous admiration for your innovative approaches to landslide research, and hope I will get the privilege of working with you again in the future. Patrice: thank you for introducing me to Matlab; I am converted and continue to learn clever ways of processing large unwieldy datasets. Your presentation practise sessions and attempts at "ambition management" over the last year were much appreciated; sorry if the latter wasn't entirely successful.

Field work on the North Yorkshire coast with the terrestrial laser scanner could not have been carried out without help from Emma Norman, Mike Lim, Sam Waugh and Chris Longley. Emma: thank you for letting me tie into your PhD work and empathising on all the learning curves. Mike: your fountain of knowledge (including rock pool ecology- crab attack!) was an invaluable resource. Sam: thank you for teaching me (and reminding me) how to use the differential GPS and total survey- essential skills for the modern Geographer. Chris: you provided exceptional chit-chat, were strong as an ox with that generator and drove the van (when I couldn't reach the pedals); all in return for a few pork pies- bargain!

Special recognition goes to several specific people and groups. Camila Caiado, you are an incredible mathematician and teacher, thank you for showing me lots of neat Matlab tricks. Prof. Chris Kilburn (UCL): for entertaining discussion on my pre-failure creep data following a chance meeting on the train. Peter Schurch: for suggestions during data processing. Thank you to all the technicians and admin staff; you guys are the backbone behind all research carried out in the Geography department. Specific thanks to Alison Clark, Merv Brown and Eddie Million who put up with me in the lab.

Not only did the department and IHRR provide a fantastic environment in which to conduct research, they also helped to fund it. I gratefully acknowledge the financial support received from the Geography department postgraduate studentship which covered my fees for the year and contributed to my accommodation costs. Without this I would not have been able to continue seamlessly between my Bachelor's and Master's degree.

"Writing a thesis is like having a baby it takes up all your time!" Emma you express this so well (and mine was only a Master's!). Behind every thesis lies a solid group of friends who remained onside despite the limited 'normal' conversation, moaning and long periods without contact that gradually crept in as the year progressed. John Barlow: I don't know how you put up with me, thank you for providing escape through climbing. Siobhan Whadcoat: I will never forget the exhilaration of our work break, cycling coast to coast. Harriet Tomlinson, Rob Parker and all the other fantastic PGRs- couldn't have asked for a better bunch to spend the year with! Kate Goddard: thank you for being there, particularly in November '09. To Fran D'Cruz, Georgie Bennett and friends new at UEA, Norwich, thank you for keeping life in perspective, particularly when a feat of balancing was required.

Finally, I would like to acknowledge the unwavering support of my parents. Thank you for being on the end of the phone, even into the small hours of the morning. I am incredibly lucky to have you; to you I dedicate this work.

Thank you all

"catastrophic failure might have been forecasted almost a month before it occurred." (Kilburn and Petley, 2003, p.27)

This photograph depicts the aftermath of the 1963 Vajont reservoir disaster; the most deadly landslide to have occurred in Europe in recorded history, claiming ~2,500 lives[1].

[1] http://daveslandslideblog.blogspot.com/2008/12/vaiont-vajont-landslide-of-1963.html

CHAPTER 1

Introduction

1.1. Context and thesis justification

Landslides are complex natural phenomenon (Malamud et al., 2004), dominating hillslope mass wasting (Hovius et al., 1997), playing a major role in landscape evolution (Malamud et al., 2004) and posing a significant geological hazard to local communities, particularly in mountainous regions of the developing world (Alexander, 2004; Clague and Evans, 1994; Petley et al., 2005). This widespread dynamic process (Noferini et al., 2007; Petley, 2009) claimed in excess of 75,000 lives between 2000 and 2009 (Petley, 2010), causes billions of dollars (US$) of damage annually and worryingly, considerable evidence suggests landslide impact is increasing with time (Alexander, 2004).

Effective management of slope hazards requires an understanding of the likely triggers, geometry, failure dynamics, mechanism and timing (Bell et al., 2006; Rosser et al., 2007); of these the last two remain most problematic (Rosser et al., 2007). Reducing the epistemic uncertainty of these elements is crucial, particularly for landslides that are not easily mitigated (Petley, 2009), for example the Anzola landslide, Ceno Valley, Italy (Mandrone et al., 2007). In these cases, identifying the extent of the hazard in space, predicting slope failure in time and disseminating this as an early warning is critical (Corominas et al., 2003; Petley, 2009). Widely considered the best predictive measure (Rose and Hungr, 2007) strain-rate underlies the 'Inverse-velocity method' which utilises the linearity in inverse-strain-rate change through time in brittle materials (Petley et al., 2008aa).

Predicting final failure using this technique has been successful for a number of retrospective (Rose and Hungr, 2007; Saito, 1969) and a priori failures (Hungr et al., 2005; Hungr and Kent, 1995a; Kilburn and Petley, 2003; Suwa, 1991; Zvelebil, 1984). The Vajont landslide, Italy (Kilburn and Petley, 2003) is one such example where retrospective analysis has indicated that catastrophic failure may have been forecast using the Inverse-velocity method up to 30 days in advance. Tragically, over 2,000 people drowned on 9th October 1963 when a 270 million m^3 rock avalanche generated a 245m high wave that overtopped Vajont dam.

Our understanding of the controls on pre-failure behaviour in brittle slopes is still very poor, potentially limiting the wider application of strain-rate based prediction.

One approach to this problem is to investigate the relationships between a large number of brittle failures and their attributes. A significant body of published data is available yet to date, there has been no attempt to collate a generic catalogue of landslide deformations from a large enough number of sites to facilitate the examination of emergent behaviour; notably variations in and controls upon movement prior to failure.

The collation of such data is a critical basis for failure prediction models and informs methods of quantifying pre-failure strain for slope hazard assessment (Crosta and Agliardi, 2003). In turn, this feeds directly into improvements in landslide early warning system.

1.2. Research aims and objectives

This thesis aims to: (1) build a database on the nature of pre-failure acceleration from published examples of monitored failing slopes; and (2) using observations from this database, to consider the methodological constraints on detecting movement in the context of applying the inverse-velocity method for failure prediction.

Objective 1: To build a database of pre-failure deformations for collapsed slopes, to assess variables contributing to and controlling the nature of pre-failure strain accumulation

Objective 2: To identify patterns of tertiary creep which may reflect physical deformation mechanisms

Objective 3: To assess the application of the inverse velocity method to brittle failing rock slopes for purposes of forecasting and early warning

Objective 4: To consider the constraints on ground-based remote sensing for monitoring pre-failure movements

1.3. Thesis structure

This thesis is structured to reflect the wider context of slope deformation and landslide forecasting within which the collated database is situated and analysed.

Chapter 2: reviews key concepts in landslide mechanics, broadly describing different stages of slope movement from stable through to reactivation. The focus of the chapter then moves to overview the physical mechanisms controlling pre-failure deformation.

Chapter 3: overviews different approaches to forecasting and prediction within the context of landslide risk management. The Inverse-velocity method is outlined here, followed by a review on displacement monitoring.

Chapter 4: describes the method of database collation. Results are then presented to consider variations in patterns of pre-failure creep and the practical application of the Inverse-velocity method for *a priori* forecasting.

Chapter 5: uses results from the database to critique the accuracy and precision of forecasts derived from the Inverse-velocity method and to inform instrument specifications for pre-failure deformation monitoring.

Chapter 6: provides a synthesis of research findings and conclusions.

CHAPTER 2

Hillslope stability and landslide behaviour

2.1. Landslide definition

Landslides are complex natural phenomenon, and part of a broader group of slope processes commonly referred to as mass movements (Glade and Crozier, 2005) . The term 'landslide' describes:

> "...the movement of a mass of rock, debris or earth down a slope." (Cruden, 1991, p.4 in ; Sassa, 2007)

This definition was established by the International Geotechnical Societies' UNESCO Working Party on World Landslide Inventory- in conjunction with the United Nations International Decade for Natural Disaster Reduction (IDNDR) - and is widely cited by geomorphologists.

2.2. Slope stability

Mountainous topography reflects the interplay between uplift and erosion (Schmidt and Montgomery, 1995). Hillslopes dominate these dynamic landscapes, adjusting to rapid bedrock incision through increased rates of landsliding (Korup, 2008). Hillslope morphology is controlled by slope stability that sets a threshold on slope angle (Montgomery, 2001). Slope stability is controlled by the balance between forces driving and resisting the downslope movement of material. This relationship is best illustrated by a simple force diagram of an object at rest on a plane inclined at angle (ϑ) to the horizontal (Figure 2.1). The forces in this problem are all generated by the weight of the object, which acts vertically. The driving force is the product of object weight and resultant. Resisting the weight of the object, the frictional force is the product of the coefficient of friction (roughness of surfaces in contact) and the normal force (equal and opposite too the normal reaction) acting perpendicular to the slope. Engineers commonly refer to the balance of these forces as a factor of safety (F_s) (see Figure 2.1 for equation). When the object is stable, $F_s > 1$. However when driving forces exceed resisting forces, $F_s < 1$ and the object is in a state to move downslope.

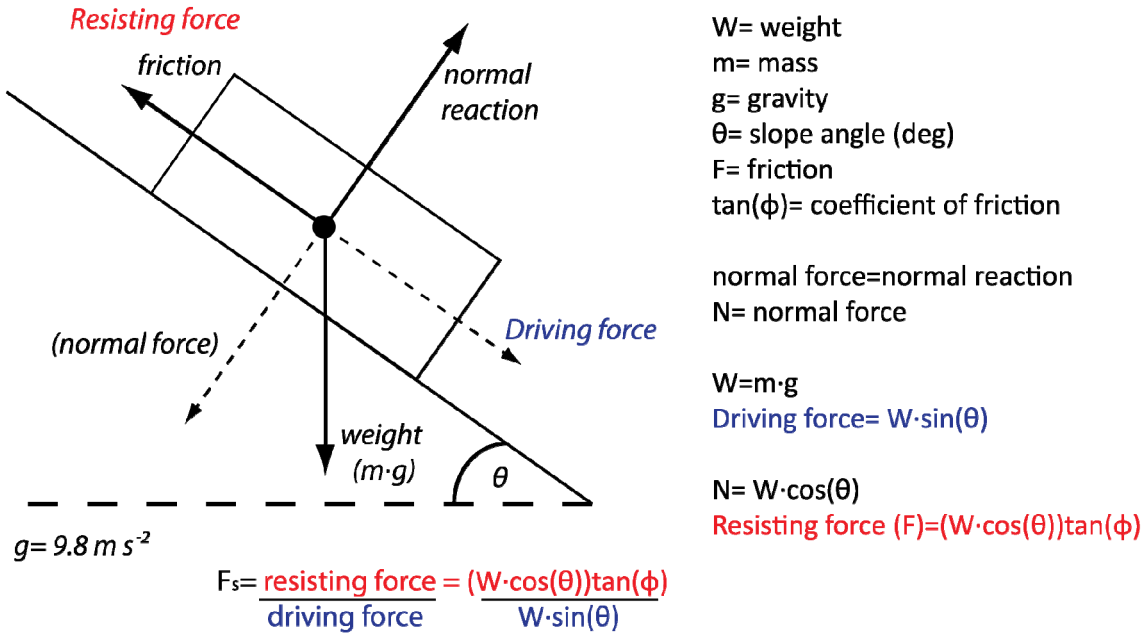

Figure 2.1: Force diagram for a simple object stable on a plane

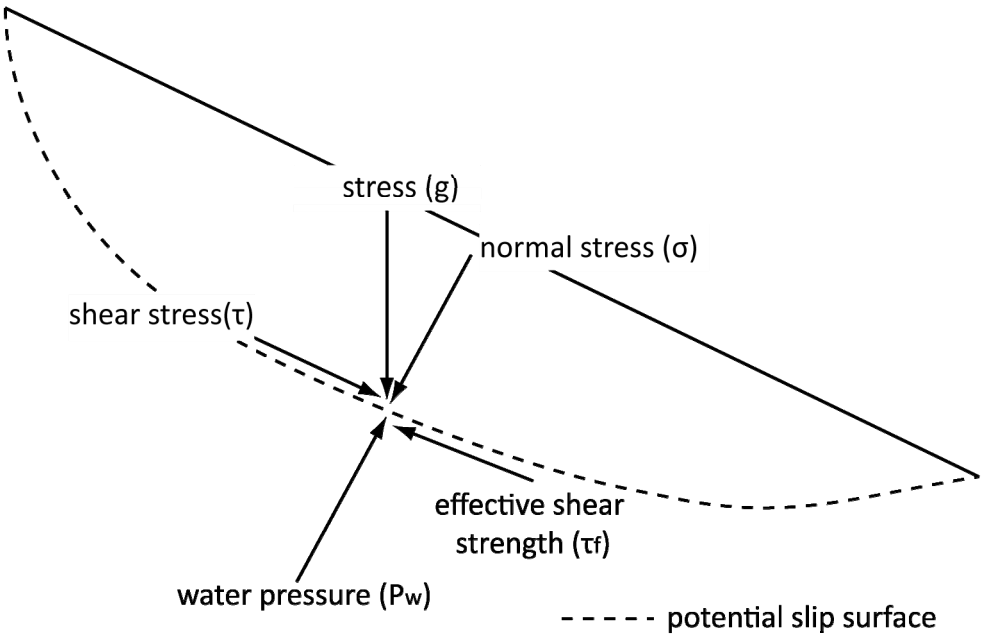

Figure 2.2: Theoretical slope model: forces acting at a point on a potential failure plane. (Adapted from Selby, 2005, figure 13.7, p.269)

Translating the mechanics of a simple force model into the stresses operating in a hillslope, Figure 2.2 depicts the *stress* attributes acting on a point on a potential shallow slide shear plane. Here *shear stress* promotes downslope movement, assisted by water pressure within the hillslope. The *shear strength* of the slope material will prevent movement, until maximum *shear stress* is reached, causing the material to rupture, or fail (Selby, 2005). It is more appropriate to model landslide mechanics in terms of *stress* rather than force. Hillslopes typically behave as a continuum at scale, composed of continuous mass or arbitrary blocks of soil and/or rock, rather than discrete blocks on a plane, such as the object in Figure 2.1. *Stress* is a measure of the average force per unit area; the force is distributed continuously through a deformable body across imaginary internal surfaces (i.e. *stress tensor)*. Using a method of analysis similar to (Skempton and Delory, 1957) infinite slope model, (Anderson and Anderson, 2010) illustrate slope stability in terms of *stress* using a 3D slope segment from a planar hillslope (Figure 2.3). The slab of regolith and/or rock in the model rests on a potential slip surface, defined as the interface between regolith and bedrock or alternatively a joint plane/ plane of weakness within bedrock.

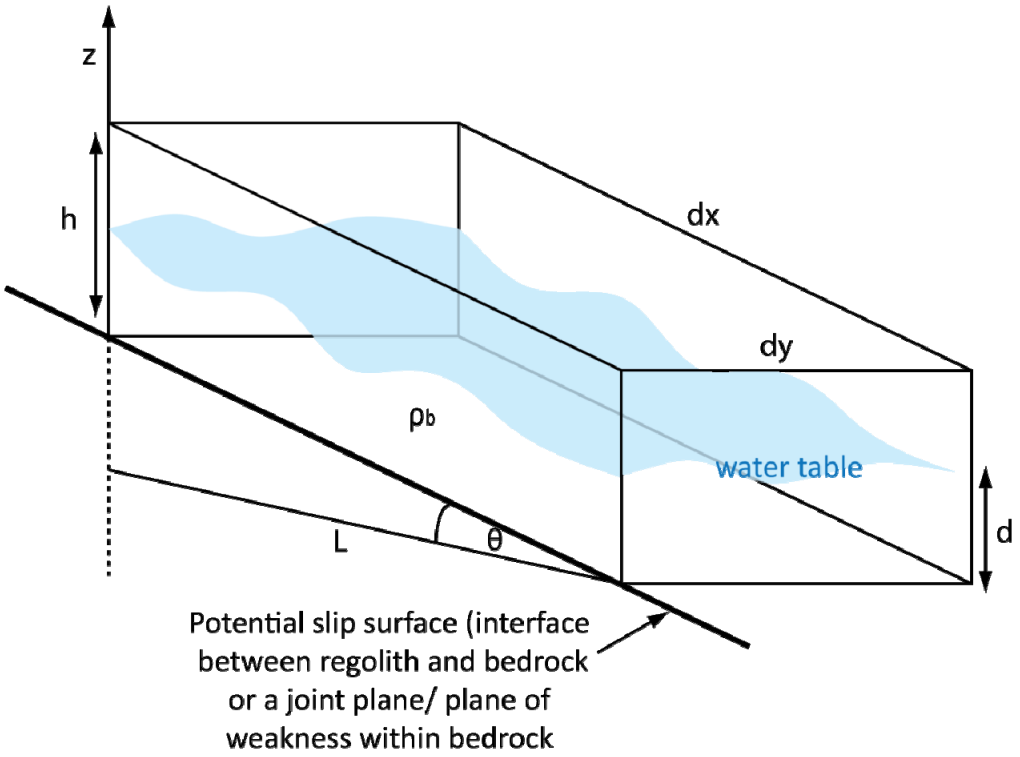

Figure 2.3: Segment of planar hillslope showing geometry of a slab of regolith.

(From Anderson and Anderson, 2010, figure 10.25, p.331)

Forces

area=dx·dy
m= ρ_b·h·dx·dy
cross-sectional area= L·h
L= dx·cos(θ)
Driving force= ρ_b(h·dx·dy·cos(θ))g·sin(θ)

R= W·cos(θ)
Φ= angle of internal friction
friction coefficient= tan(Φ)
Resisting force=
[ρ_b(h·dx·dy·cos(θ))g·cos(θ)]·tan(Φ)

Force → stress

...divide expressions for driving and resisting forces by area= (dx·dy)

Stresses

Driving stresses= resisting stresses
$\rho_b \cdot h \cdot g \cdot \cos(\theta) \cdot \sin(\theta) = \rho_b \cdot h \cdot g \cdot \cos^2(\theta) \cdot \tan(\Phi)$

Water
w= water
b= bulk
g= grains
η= porosity of the medium
d= water table height above failure plan

$\rho_b = \rho_g(1-\eta)+\rho_w\eta$
$\overline{\rho_b} = \frac{\rho \frac{d}{sat} + \rho_{dry}(h-d)}{h}$

σ= normal stress ($\overline{\rho_b}$·g·h)
P_w= water pressure (ρ_w·g·d)

σ'= effective normal stress
$\sigma' = \overline{\rho_b} \cdot g \cdot h - \rho_w \cdot g \cdot d$ *[Equation 1]*

Cohesion
(sum mineral root contributions at failure interface)

C= cohesion
C'= effective cohesion

τ= shear strength
τ_f= effective shear strength

Coulomb equation...
$\tau = \sigma \cdot \tan(\Phi) + C$ *[Equation 2]*
$\tau_f = (\sigma - P_w)\tan(\Phi) + C'$

Water and cohesion are accounted for...

Driving stress= $\overline{\rho_b}$·h·cos(θ)·g·sin(θ)
Resisting stress= $\overline{\rho_b}$·g·h·cos²(θ)-ρ_w·g·d]·tan(Φ)+C' *[Equation 3]*

Factor of safety master equation...

$$F_s = \frac{\overline{\rho_b} \cdot g \cdot h \cdot \cos^2(\theta) - \rho_w \cdot g \cdot d] \cdot \tan(\Phi) + C'}{\overline{\rho_b} \cdot h \cdot \cos(\theta) \cdot g \cdot \sin(\theta)}$$

Box 2.1: Equations related to the Factor of Safety calculation

As previously stated, *shear stress* drives downslope movement. Adding complexity (and reality) to the model, the resisting *stress (effective shear strength)* is defined not only by the *angle of internal friction* but also by *effective cohesion* and water pressure. *Shear strength* in a dry slab is expressed as a straight line on a *normal stress-v-shear stress* plot, in which *cohesion* is defined by the intercept on the *shear stress* axis, and the angle of internal friction is defined by the gradient of the line. This relationship is described by the Coulomb equation *(Equation 2, Box 2.1)* (Selby, 2005). *Effective shear strength* accounts for the presence of water within the slab which changes the material's bulk density and increases pore-pressure, undermining the *normal stress* with a buoyancy effect (Selby, 2005). *Effective normal stress (=normal stress- water pressure)* is calculated to account for water presence *(Equation 1, Box 2.1)*. *Cohesion* is redefined as *effective cohesion*, to acknowledge the loss of surface tension and resultant reduction in *cohesion*, with increasing pore pressures. The resisting *stress* is thus the product of the *effective normal stress* and the *coefficient of friction*, plus the *effective cohesion (Equation 3, Box 2.1)*. The definition of the factor of safety does not alter; as F_s decreases towards 1, the probability of instability increases- most landsliding occurs when F_s is between 1 and 1.3 (Selby, 2005).

2.3 Stages of slope movement

A hillslope is said to be in a *state of stress*, when external forces are applied, setting up internal forces within the slope material. *Strain,* the ratio of change in dimensions of the stressed body to its original dimensions or put simply, deformation- is produced by stresses operating on and within the slope (Selby, 2005). Crozier (1986) conceived slopes on a stability spectrum, essentially ranging from stable to actively unstable (undergoing continuous or intermittent movement) based on slope *stress state*. Once destabilised a slope progresses through four different movement stages outlined in figure 2.4. This model, adapted from Leroueil et al. (1996) illustrates the life-cycle of an unstable part of a hillslope. The duration of each stage depends on many factors such as slope material properties, slope geometry, local seismicity, local rainfall and anthropogenic interaction. This section outlines each stage of the model, particularly focusing on pre-failure movements and mechanisms.

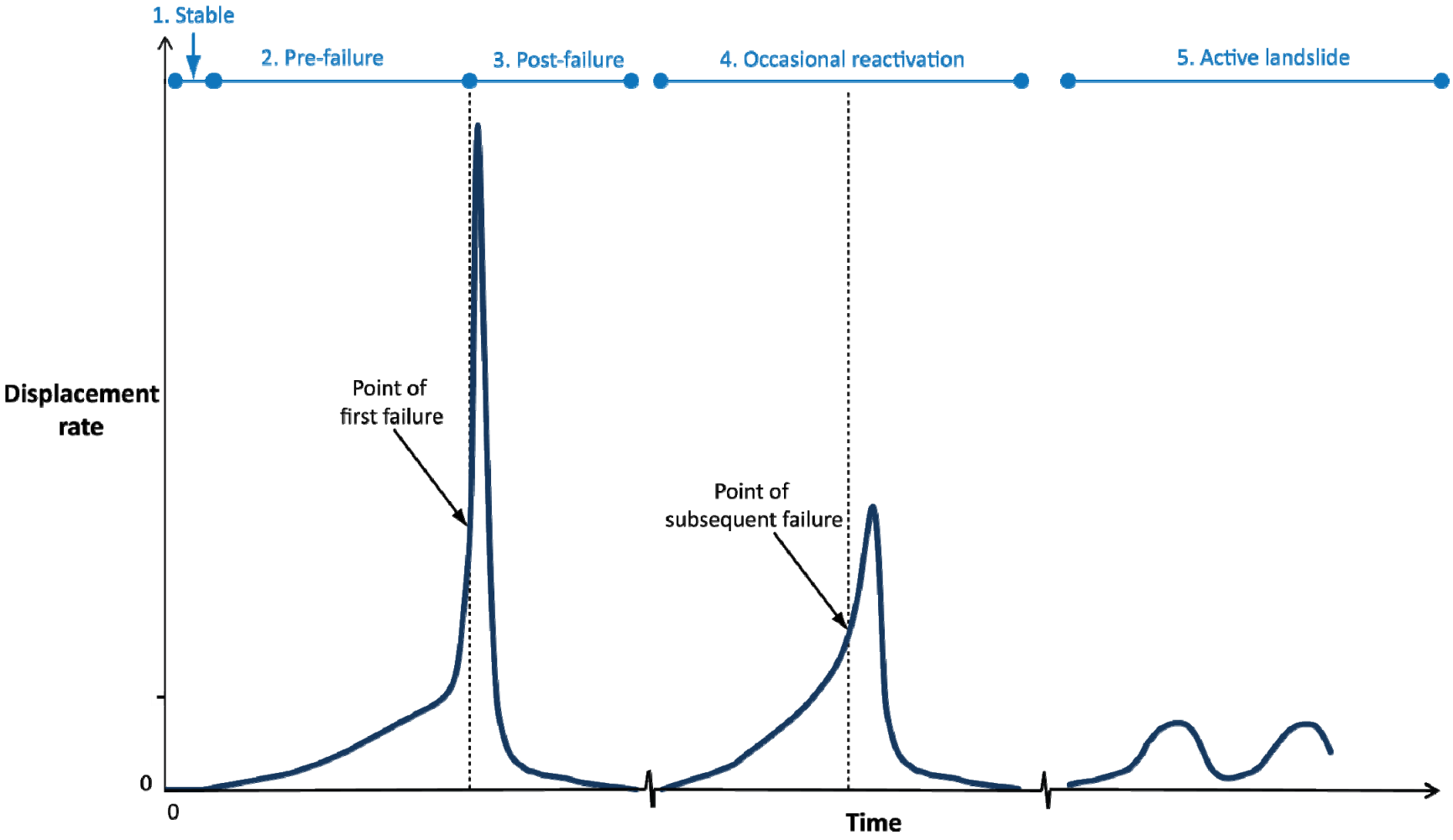

Figure 2.4 Different stages of slope movements (adapted from Leroueil et al., 1996, in Picarelli et al., 2005, fig.1, p.29)

2.3.1. Pre-conditions to slope instability

Hillslopes are stable when they are able to withstand the action of all natural dynamic destabilising forces likely to be imposed under the current environmental conditions and geomorphic regime. The composition of slope material is an important pre-condition to landsliding; potentially acting as a catalyst for other dynamic destabilising factors to operate more effectively (Glade et al., 2005).

2.3.1.1. Material intact strength

Lab-based measurement of material intact strength using stress testing (i.e. triaxial cell) provide values for cohesion and the angle of internal friction, equating to the y-intercept and slope angle respectively, of the Mohr- Coulomb failure line plotted on a normal stress- shear stress graph (Selby, 2005). Cohesion is the main differentiation between soil and rock; rocks possess significantly higher values of cohesion (e.g. granite = 35,000kPa) in comparison to soils (e.g. sand = 0kPa; cohesionless) (Selby, 2005). Cohesive strength is dictated by the nature of material bonds on a microscopic scale. Frictional strength is the frictional resistance between mineral particles, greatly influenced by particle density within a volume of material (Selby, 2005). Friction provides the main control on strength for most rocks and soils, but does not necessarily operate uniformly throughout a mass. In crystalline rocks and clays, strength is anisotropic if minerals have a consistent orientation within the lattice (Goodman, 1989). Here micro-scale damage (e.g. fissuring) is likely to occur preferentially in weaker orientations that are aligned to the mineral fabric. In comparison strength in undamaged soils is isotropic, in some cases purely controlled by friction if the mass is cohesionless. Understanding basic distinctions in the petrology of slope materials is important when discussing the wider context of hillslope lithology. The chemical composition of soil and rock determines its response to stresses imposed by temperature fluctuation or water immersion, for example. It also dictates the strain energy needed for deformation (Selby, 2005).

2.3.1.2. Hillslope structure

Hillslope form is determined by the response of rock and soil to destabilising processes. This response is governed by the physical properties of the material. Although intact material strength is important to understanding slope stability,

hillslopes are never composed entirely of intact rock or undamaged soil. An arbitrary distinction may be made here between the behaviour of hillslopes composed of hard rocks, soft rocks or soils. The persistence of asperities in a hard rock slope, tend to control its stability. Asperities concentrate stress, control water movement in the rock body and permit weathering to penetrate and weaken the mass. The shear strength of partings is significantly lower than intact rock and greatly varies between fractures within the same mass. Their effective shear strength is controlled by the material's frictional strength, the roughness of the walls of the parting and the thickness and strength of infill material within the parting (Selby 2005). Measurement of rock mass strength, taking into account the intact strength and nature of discontinuities, provides a better value estimate of overall material strength when considering slope stability. Soft rocks and some soils may also contain fissures; however the stability of these materials is generally controlled by the action of water within slope.

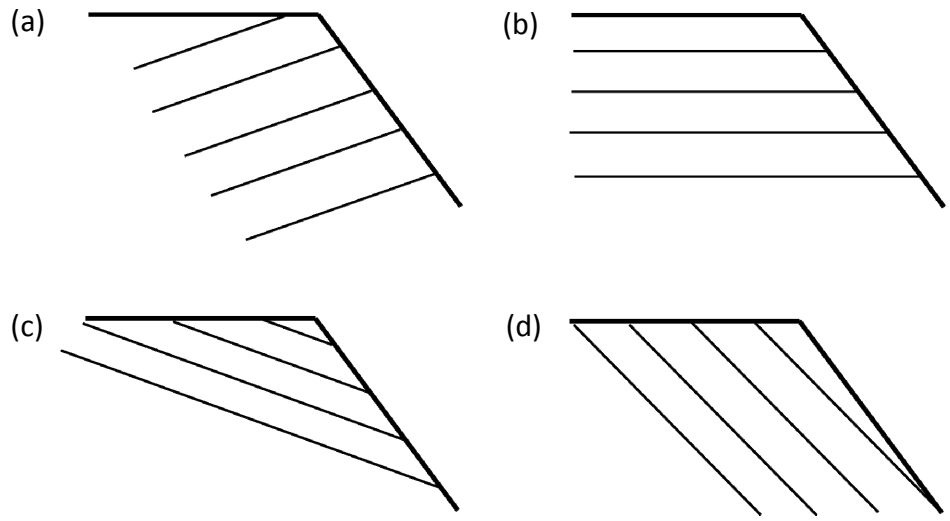

Figure 2.5: Orientation of rock discontinuities in relation to hillslope gradient: (a) joints are inclined against hillslope gradient and enhance rock strength, (b) joints are horizontal and have near neutral effect on rock strength, (c) joints dip gently out of the hillslope and moderately weaken rock strength, (d) joints dip steeply out of the hillslope and greatly weaken rock strength. (Parsons, 1988, p.76 fig. 5.6).

Hillslope lithology is often complex, containing different geological layers each with their own physical properties and internal structure. The orientation of macro-structures within the slope has important bearings on material stability and surface morphology. Parsons (1988) presents four structurally controlled hillslopes (figure 2.5). Where discontinuities are inclined perpendicular to the gradient of the slope surface

(figure 2.5(a)) the mass is strengthened, but where inclination is near parallel to the slope surface, instability is promoted (figure 2.5(d)). Internal structure, material properties and interactions between lithological boundaries are important factors pre-conditioning hillslopes to destabilise. These features dictate how slopes behave under *stress* and influence the magnitude of driving forces necessary to overcome effective shear strength.

2.3.3. Pre-failure movements and mechanisms

Pioneering work by Bishop (1967), Bjerrum (1967) and Skempton (1964), documented that slopes are able to undergo progressive failure, i.e. fail without mobilising peak strength. This process may be termed 'creep', although definitions of creep vary by discipline, but is defined within engineering and material science as "the deformation of slope materials under constant shear stress towards failure" (Ng, 2007; p.30). Work attempting to understand landslide precursory movement has demonstrated that behaviour appears to be dominated by the mode of shear zone deformation (brittle or ductile) (Petley et al., 2005; Picarelli et al., 2005a), rather than state- and rate- dependent friction proposed by Helmstetter et al., (2004), derived from the Dieterich-Ruina friction law (Dieterich, 1978; Ruina, 1983). It is important to understand both the time-dependant dimension and dynamic nature of pre-failure creep. This section initially outlines differences in material deformation behaviour, the development in understanding of the creep phenomenon and the three phase creep model for strain development. It then proceeds to look at preparatory factors causing strain to accumulate in hillslopes and triggering factors that initiate final failure.

2.3.3.1. Material deformation behaviour

Material behaviour under load is understood using intact samples in laboratory pressure tests (Mazanti and Sowers, 1966). Pore-pressure reinflation tests, which use pore-pressure inflation to reduce effective stress of a material under constant load, provide insight into different modes of deformation relevant hillslope materials (Petley et al., 2005a). Brittle deformation prevails in bonded or cemented materials at low effective stresses, while ductile mechanisms are commonly found in materials with little or no inter-particle bonding at higher effective stresses (Ng, 2007). Figure 2.6

illustrates the different *stress-paths* produced by materials deforming in a brittle and ductile manner under constant load.

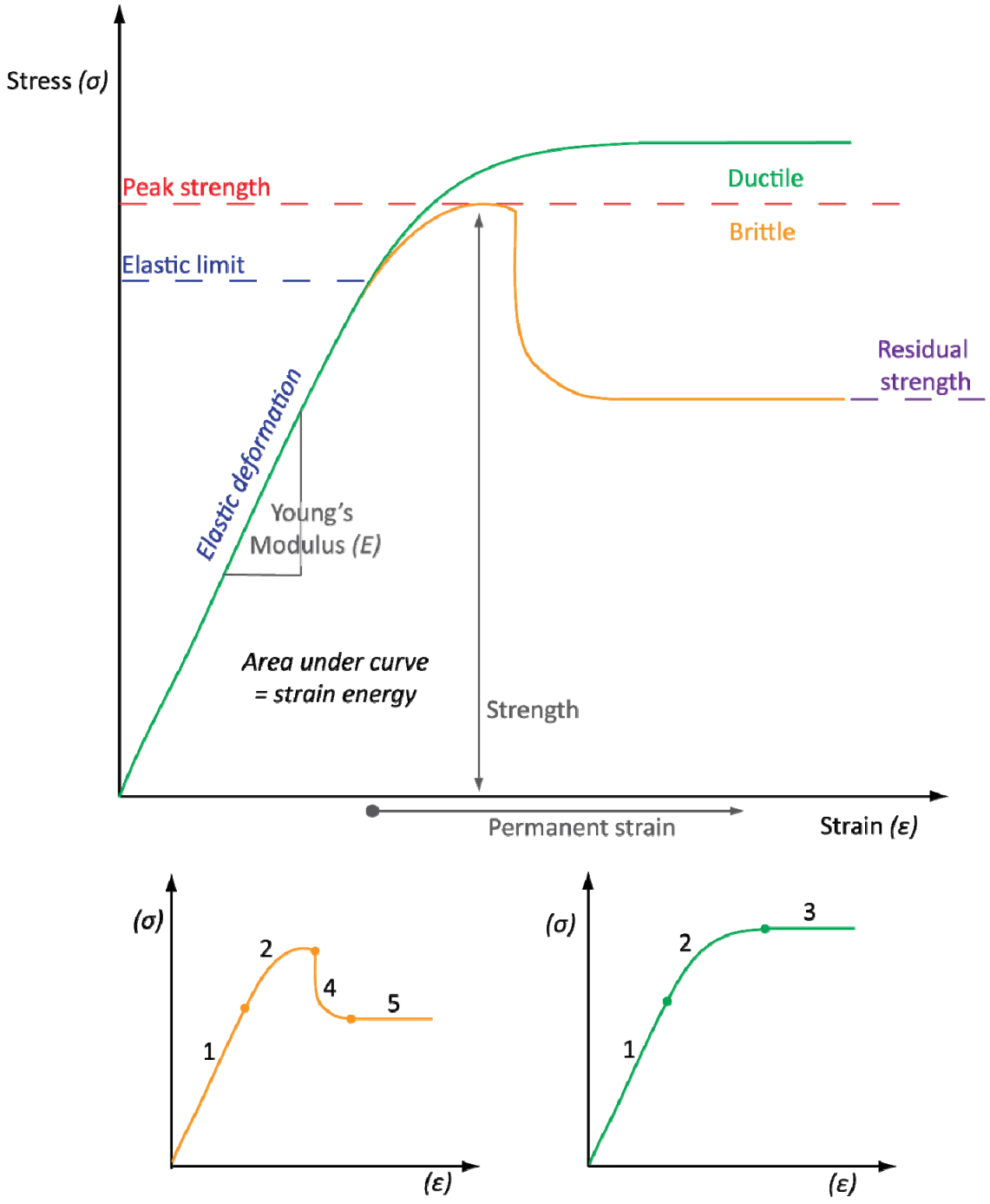

Figure 2.6: Stress path for a typical brittle (orange) and ductile (green) material: (a) stress- strain curve illustrating key mechanical parameters; (b) brittle deformation; (c) ductile deformation. For (b) and (c): stage 1= initial elastic phase, stage 2= elastic-plastic phase, stage 3= steady-state plastic deformation phase, stage 4= strain weakening phase, stage 5= residual, steady-state phase [(b) and (c) after (Petley and Allison, 1997 in Ng, 2007)].

Both materials initially deform elastically, a phase in which strain is recoverable (stage 1, figure 2.6(a) and (b)). When the elastic limit is reached, elastic-plastic deformation ensues as the weakest or most highly stressed bonds between particles permanently break (stage 2, figure 2.6 (a) and (b)) (Petley and Allison, 1997). Internal slip, dislocation and micro-fractures develop around weakened areas within the brittle mass, which fails when the stress path reaches material peak strength (i.e. the peak sustainable stress) (Petley et al., 2005b). During stage 4 (figure 2.6 (a)) strain localises on the tips of micro-fractures, initiating shear surface development through a gradual loss of shear resistance as the last inter-particle bonds between micro-fractures break, creating a rupture through the mass. This plastic deformation occurs rapidly, driven by the imbalance between shear stress and shear strength, caused by a sudden loss in cohesion (Kilburn and Petley, 2003). The material fails when the stress-path reaches residual strength, indicating a new steady-state for the material (stage 5, figure 2.6(a)). Ductile deformation is not limited by material peak strength; when under constant stress, plastic failure occurs during which particles in the material are restructured (stage 3, figure 2.6 (b)). No clear shear surface forms as strain cannot localise, so deformation is distributed throughout the mass (Petley et al., 2005a). Strain rate increases as the mass is progressively restructured and affected by pore water pressure fluctuations (Ng, 2007).

2.3.3.2. Progressive creep model: the brittle case

Terzaghi (1950) first identified the connection between material creep and landslides, recognising progressive deformation of the basal shear zone. This work illustrated the process of creep as a gradual decrease in factor of safety (i.e. the ratio of shear strength to shear stress) through time (Ng, 2007). A hillslope fails when shear stress and shear strength are in unity and the factor of safety equals one. Terzaghi's work was fundamental to understanding slope stability; providing insight into strain development and final failure. However it does not explain the mechanics of progressive deformation.

Bjerrum (1967) first described the process of progressive failure- recognising that landsliding in cohesive materials generally requires the shear zone to undergo a significant drop in resistance, transitioning from peak to residual strength (Petley et al.,

2005a). Bjerrum's model associates this behaviour to the formation of a continuous shear surface, re-scaling the mechanisms involved in brittle deformation (section 2.3.3.1) to operate over a hillslope. As inter-particle bonds break under stress, elastic strain energy is liberated, enabling localised plastic deformation. Stress redistributes with each microscopic failure; stress is concentrated on unsheared crack tips within the mass that gradually join to make a shear surface. As the proportion of unsheared material in the shear zone decreases, shear stress tends to infinity and deformation accelerates (Petley et al., 2008a). Bjerrum's work highlights the presence of "recoverable strain energy" in shearing materials (Bjerrum, 1967), facilitating progressive failure in unstable hillslopes.

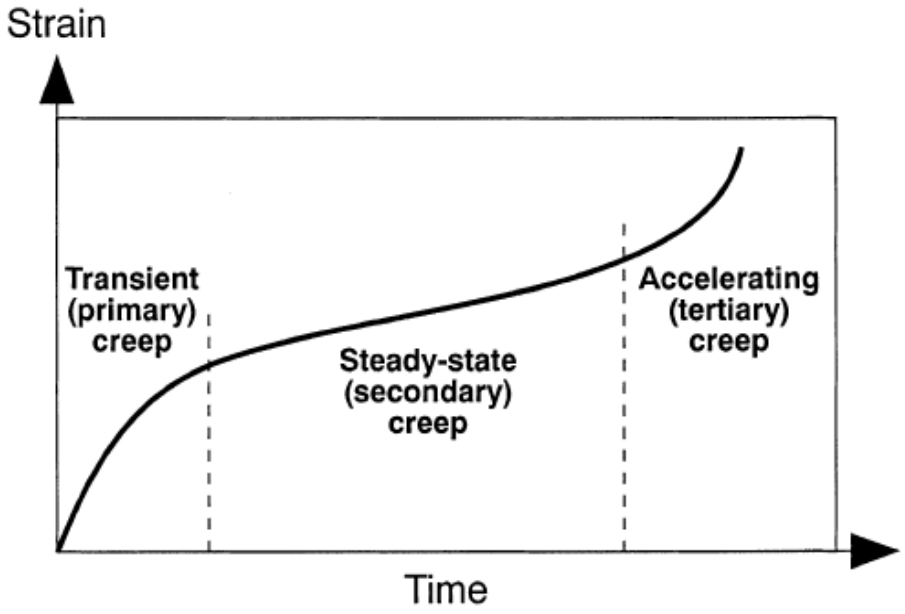

Figure 2.7: Three- phase creep model (Main, 2000 after ; Varnes, 1978)

Varnes (1978) described the progressive failure of materials under constant stress, using a three-stage creep model (figure 2.7). This builds on Bjerrum's understanding of shear surface formation and is consistent with patterns of precursory strain development observed in other natural phenomenon such as volcanic dyke propagation (Kilburn, 2003) - also involving the slow cracking of rock. The three phases of the model: primary (transient), secondary (steady-state) and tertiary (accelerating creep) are associated with the contrasting processes of strain hardening and strain softening, operating on a micro-scale within the rock mass (Martel, 2004). Strain hardening (also known as work hardening in materials science), is the strengthening of

a material by dislocation movements within the crystal structure (Callister and Rethwisch, 2010). Strain softening facilitates shear surface development and represents the gradual loss of shear resistance with strain after peak strength has been reached (Prevost and Hoeg, 1975). The three-phase creep behaviour is explained using a mechanics model (figure 2.8) adapted from those presented in Petley et al. (2005a) and Petley et al. (2005b). This illustrates progressive failure of an infinite slope in terms of time-dependant displacement and factor of safety. The mechanism of precursory micro-cracking is primarily underpinned by theories of damage accumulation in solids (Main, 2000), together with the results from laboratory reinflation tests (Petley et al., 2005b; Petley et al., 2005a; Petley et al., 2008a) and observations of the progressive dynamics of individual slope failures (Crosta and Agliardi, 2003).

Initially the slope is stable (figure 2.8, A); no features associated with instability are present although a weak layer exists within the mass. Primary creep represents the early stages of damage in which strain hardening mechanisms are progressively mobilised. Initial elastic deformation stretches molecular level bonds, the weakest of which break, rearranging atoms within the solid material (plastic deformation) (Kilburn and Petley, 2003; Petley, 2009). Under continued stress, the material becomes increasingly saturated with new dislocations (defects). This perhaps explains the observed initially high displacement rate of the primary creep stage and a decline in slope factor of safety (figure 2.8, B) (Petley and Rosser, 2009). As dislocations accumulate they serve as pinning points, altering the local stress field within the lattice and resisting internal plastic deformation; the material is strengthened (strain hardened), increasing the force required to produce new dislocations (Smith and Hashemi, 2006). A dominance of this process during the primary stage of creep appears to account for declining displacement rates as progressive failure advances towards the secondary phase (figure 2.8, B). Importantly it is noted here that primary creep in landslide mechanics remains the least understood phase of Varne's model (Varnes, 1983); interpretation is thus based on established concepts applied in other areas of materials science.

As shear forces overcome the elevated strength of inter-particle bonds, dislocations begin to nucleate, initiating micro-fracture development throughout the mass (Smith et al., 2006). Fluctuations in slope FoS during the primary creep stage

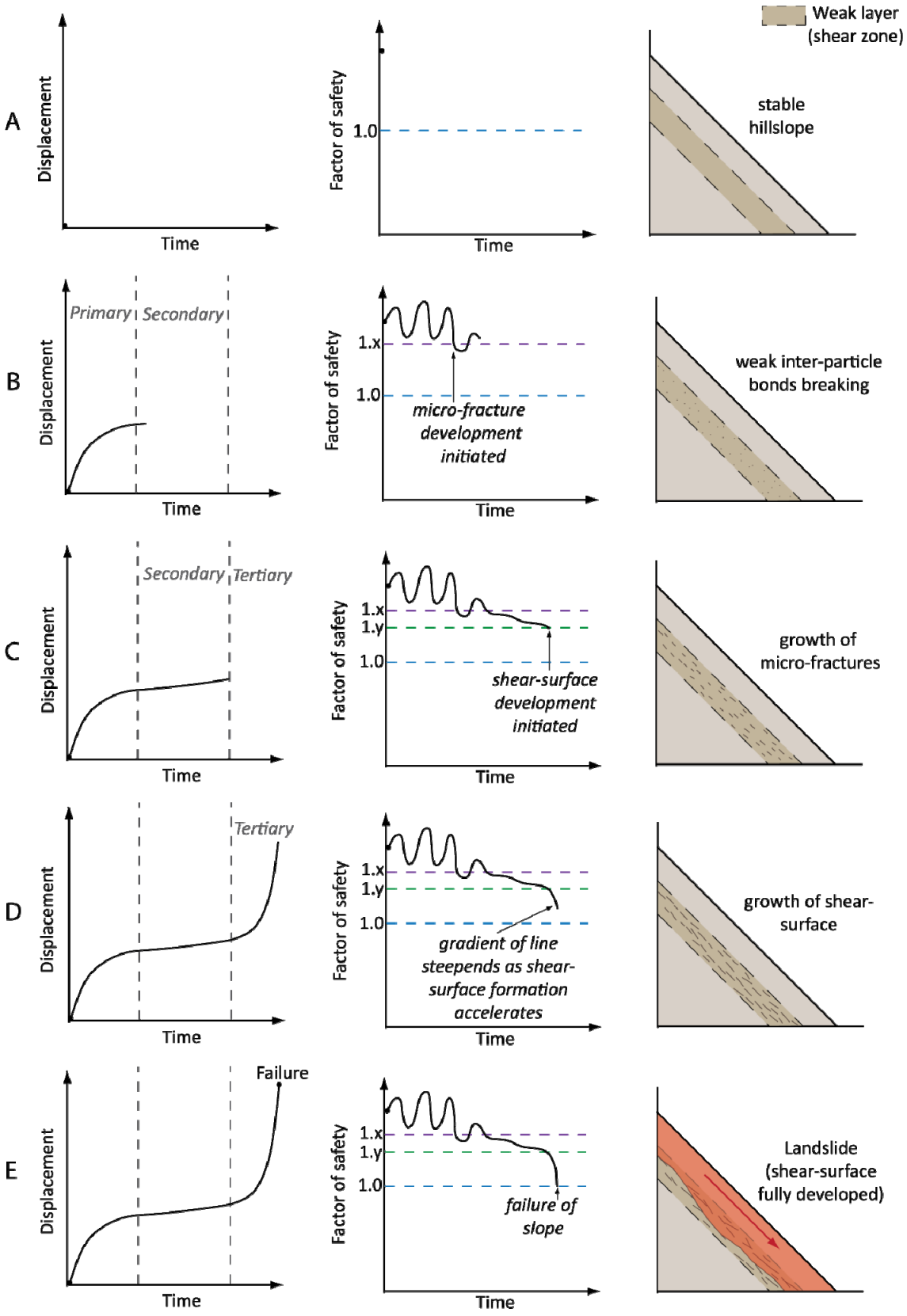

Figure 2.8: Pre-failure deformation mechanisms of brittle rock slopes adapted from fig.4, p. 203 (Petley et al., 2005a) and fig. 9 (Petley et al., 2005b)

represent the en-mass progressive strain hardening and dislocation of inter-particle bonds. Gradual damage accumulation within the slope decreases its stability. Petley et al. (2005a) highlight microfracture initiation as an important FoS boundary, propensiating further damage to the slope. Essentially stability at this point is recoverable if effective stress is reduced; many damaged slopes are thought to exist in an apparent stable state following a decline in local stress conditions.

Secondary creep represents a steady-state period of slow plastic deformation (Main, 2000). The weak zone of material (figure 2.8, C) remains under constant stress accumulating further damage resulting from a shifting balance of strain hardening and softening forces (Carey et al., 2007). Local hardening mechanisms focus on tiny material flaws (crack nuclei) and the tips of existing microfractures (Kilburn and Petley, 2003). Although surrounding material is initially strengthened under this process, the greater shear force required to overcome peak strength and create new dislocations, also enhances strain softening; once bonds break neighbours relax and release greater amounts of built up elastic strain energy, driving additional fracturing (Lawn, 1993). Initially deformation during the secondary phase is dominated by new crack formation, but progressively it becomes a function of crack growth (Carey et al., 2007). As material in the shear zone grows weaker an inflection point in the deformation-time graph is observed (figure 2.8, C). This represents a shift from the dominance of strain hardening to strain softening mechanisms (Petley et al., 2008a). Although crack growth is inherently stable during this period- fractures' remain isolated from one another and controlled by the magnitude of shear and effective normal stress- deformation begins to accelerate (Kilburn and Petley 2003). The progressive loss of cohesion and growth of microfractures reduces hillslope FoS to a second important boundary (figure 2.8, C). Here microfracture density becomes sufficiently high that neighbouring cracks begin to interact (Petley et al., 2005a). Strain softening mechanisms localise deformation on the unsheared material residing between crack tips (Cornelius and Scott, 1993). Shear stresses acting on this intact mass increase at a hyperbolic rate as the process becomes self-reinforcing (Petley et al., 2005a), driven purely by the elastic energy release of micro-scale dislocation- independent of changing stress conditions (Petley et al., 2005b). The initiation of this mechanism corresponds to the boundary between secondary and tertiary creep, also described as critical strain (Kilburn and Petley,

2003), it represents the point at which shear surface development is initiated within the weak layer of hillslope (shear zone).

Shear surface development is characterised by a hyperbolically increasing bulk displacement rate, corresponding to growing slope instability (decreasing FoS) and accelerating damage within the shear zone (figure 2.8, D). Whereas deformation during the primary and secondary creep stage is essentially ductile and distributed throughout the weakening mass, tertiary deformation is a brittle process localised by strain softening on a single plane within the shear zone (Main, 2000). In line with Bjerrum's (1967) model, final failure occurs when the deforming material reaches residual strength (figure 2.6). Just before this point, the area of uncracked material in the shear plane becomes infinitely small and shear stress becomes infinitely big (Carey et al., 2007). Figure 2.8(E) illustrates that catastrophic landsliding occurs when FoS reaches or is marginally below unity (1.0); the point at which shear stress exceeds shear strength and the failure plane fully forms (Petley et al., 2005a).

Griffith's criterion (Griffith, 1921) presents a two-stage feedback process to explain the failure of brittle materials. His work recognised the changing stability of crack growth driven initially by strain hardening (with negative feedback) but progressing to strain softening mechanism (with positive feedback) (Main, 2000). His equation $K = Y\sigma x^q$ (equation 1; Main, 2000, p.153), describes the stress intensity at the crack tip *(K)* as the product of the loading configuration/mode of failure constant *(Y)*, the applied stress at the boundary *(σ)*, the half-length of the crack *(x)* to the power of a crack growth stability constant *(q)*. When *q<0*, feedback is negative, however when *q>0* accelerating unstable crack growth occurs. Griffith provided insight into modelling the three stages of progressive failure proposed in Varne's (1978) model. Voight (1989) later proposed

$$\frac{dx}{dt} = [\mathrm{A}(1-\alpha)(\mathrm{t}-\mathrm{t}_0) + \frac{dx}{dt}_0^{(1-\alpha)}]^{\frac{1}{(1-\alpha)}}$$

[Equation 4 (Voight, 1989; p.201)]

In this case *x* represents displacement, *t* is time, and *A* and *α* are empirical constant. Importantly Voight (1989), with later verification from De La Cruz-Reyna and Reynes-Davila (2001), found that *α = 2* for movements of rock fracture in real systems (Petley

et al., 2005a). This provides a hyperbolically accelerating rate of strain accumulation, associated with the tertiary creep stage of Varne's (1983) model (Main et al., 1993).

Main (2000) developed a simple hybrid model for creep in brittle materials, following the work of Griffith (1921), Voight (1989) and Omori (1894); Omori presented a law for the temporal decay of earthquake aftershocks, relevant to the seismicity observed during micro-cracking of brittle materials.

$$\varepsilon(t) = \varepsilon_0[1 + \frac{t}{m\tau}]^m$$

[Equation 5 (Main, 2000, p.151)]

Equation 5 is used for strain rate, $\varepsilon(t)$, where τ is the ratio of initial crack length to rupture velocity; strain hardening dominates when *0 < m < 1*, whilst *m < 0* when strain softening controls microfracture development. Main's model recognises secondary creep as an emergent behaviour from the linear superposition of stable (transient) and unstable (accelerating) crack growth within a power law rheology (figure 2.7, Main, 2000). Although other authors have modelled progressive failure with different mathematical relationships (e.g. exponential form, Lawn (1993), a power-law is noted to best describe crack coalescence behaviour (Main, 1999).

Kilburn and Petley (2003) present a model for crack growth during accelerating creep, describing how microscopic deformation manifests to macroscopic bulk dilation and downslope displacement. Based on the assumptions that each crack event breaks a fixed distance of unbroken rock (by nucleating or cracking) and that bulk movements are proportional to the total rate of cracking, rates of downslope displacement during tertiary creep are given by,

$$\frac{dx}{dt} = (\frac{dx}{dt})_0 e^{\psi(x-x_0)}$$

[Equation 6 (Kilburn and Voight, 1998)],

where *x* represents displacement, t is time, suffix 0 denotes conditions when crack growth first dominates crack nucleation and ψ is an inverse length scale that depends on the applied stress, rock properties and geometry of the crack array. The term,

$$\psi = B\omega^2 S^2 \varphi \frac{(dN/dx)}{YkT}$$

[Equation 7 (Kilburn and Petley, 2003, p.26)]

where ω is an atomic stretching distance for breaking bonds at crack tips, *S* is the remote applied stress (due to the downslope weight component of the unstable slope), φ is the mean distance a crack extends during each step-like crack event, *Y* is young's modulus (see figure 2.6), *k* is Boltzmann's constant (relating energy to temperature), *T* is rock's absolute temperature, *B* is a dimensionless term incorporating Poisson's ratio (ratio of transverse strain to axial strain) for the deforming rock, the coefficient of friction along a crack's touching surfaces, and terms describing the geometry of the crack array (Lockner, 1993) and *dN/dx* denotes the number of crack events per unit area (Kilburn and Petley, 2003). The model describes slope behaviour beyond critical strain, importantly quantifying factors contributing to the rate of crack growth within the mass.

Varne's three-stage creep model is evaluated here with reference to an adapted conceptual model from Petley et al, (2005a) and Petley et al. (2005b). Figure 2.8 presents a hypothetical infinite slope to illustrate progressive landslide development. The hillslope may consist of soil or rock, however importantly both the general hillslope material and weak layer are cohesive; the hyperbolic acceleration of displacement during the tertiary creep stage is characteristic of brittle deformation (Main, 2000; Petley et al., 2008). Although the weak zone of material in this schematic maintains a consistent depth parallel to the slope surface, shear zones within natural hillslopes are generally more complex (Skempton and Petley, 1967): often discontinuous, occurring over different depths, composed of materials with varying mass strengths (section 2.3.1.2.) and exposed to distinct local stress conditions. Displacement-time and FoS-time graphs (figure 2.7) represent the entire slope at each stage of the model; theoretically the progressive development of failure is consistent throughout the shear zone because the slope modelled is infinite (Petley et al., 2005b). In reality, displacement rates may vary across a hillslope, reflecting local shear surface development (Petley, 2004; Terzaghi, 1950). Equally, FoS may vary spatially, with different sections of hillslope destabilising at different rates; local FoS may drop below

unity (1.0) as cracks coalesce but general slope FoS will remain above unity until the shear surface fully forms (Petley et al., 2005a). Application of the three-phase creep model to explain progressive failure in brittle materials is well established in damage mechanics. Behaviour has been verified using laboratory static-load tests (e.g. Petley et al. (2005a), Petley et al. (2005b), Petley et al. (2008a)), observed in field data (Carey et al., 2007; Petley and Rosser, 2006; Rose and Hungr, 2007) and modelled numerically (e.g. Crosta and Agliardi, 2003; Main, 2000; Voight, 1989). The physical mechanism of progressive failure outlined here underpins methods of strain-based landslide forecasting. This model will be discussed further in the context landslide movement data presented in chapter 4.

2.3.3.3. Ductile failures

As noted in section 2.3.3.1, ductile mechanisms are commonly found in materials with little or no inter-particle bonding at high effective stresses (Ng., 2007). Most non-cohesive soils are considered viscoelastic-plastic materials, whose behaviour when placed under stress is strongly controlled by grain size, packing, fabric and water content (Selby, 2005). Although ductile deformation is a process often associated with reactivated landslides, moving on pre-existing shear surfaces (Petley et al., 2002), shear zones may develop from non-brittle mechanisms in previously stable hillslopes. Work by Ng, K (2007) investigating deformation in residual soils suggested that the development of elastic strain during the initiation of primary creep was negligible for non-cohesive or heavily weathered materials. Application of Bjerrum's model (1967) to reinflation test results(Ng and Petley, 2009) indicated that the elastic strain energy required to advance progressive failure was absent from the weathered samples (Ng, 2007). In effect, such materials exist at residual shear strength, developing strain from inter-particle movement. Dilative soil behaviour, typically in response to elevated pore water pressures, loosens inter-particle contacts. Strain hardening mechanisms operate as soil particles subjected to shear, rearrange- either by push and climb or sliding movements (Wood, 1990)

Under constant stress crack nucleations form throughout the shear zone (Inkpen, 2005). If Main's model (Main, 2000) applies here, fractures should develop under strain softening mechanisms, driven by the release of elastic energy as new

dislocations form (Lawn, 1993). This positive feedback does not dominate deformation in the secondary and tertiary phase of non-cohesive material creep. Shear strength in soils is controlled primarily by inter-particle friction rather than cohesion (bonding) between particles (Powrie, 2004). The granular nature of soil prevents strain localising; deformation is distributed throughout the mass by generalised inter-particle sliding rather than contributing to shear surface development (Ng, 2007; Petley et al., 2005a). As the material internally is remoulded, strain rate accelerates exponentially (Petley et al., 2002). Unlike the brittle behaviour observed during shear plane development in cohesive materials, ductile deformation does not manifest in a sudden rapid bulk mass displacement; typically surface movements are slower during tertiary creep (Ng, 2007). Strain rate develops in response to changing stress conditions, particularly driven by fluctuations in pore water pressure. The chemical make-up of soil (i.e. mineral composition) governs its response to water penetration. Atterburg limits define whether the material will deform as a plastic or flow as a liquid (Selby, 2005). As water content increases within the mass, deformation accelerates in the shear zone generating a characteristic *surge* movement (Allison and Brunsden, 1990). Failure occurs when pore water pressure increase reduces soil strength below constant shear stress (Ng, 2007).

Although significant research has been undertaken within the engineering sector to understand deformation in non-cohesive soils using laboratory stress testing (Powrie 2004), mechanisms controlling patterns of pre-failure movement in hillslopes composed of such materials, are less well understood (Carey et al., 2007). Terzaghi (1950) highlighted that patterns of surface movement leading up to failure provide insight into processes occurring within the shear zone. Pre-failure strain accelerations were discussed by Petley et al., (2002), who noted key differences between slopes undergoing brittle and ductile deformation. The progression of creep in brittle materials is characterised by a power law (section 2.3.3.2), whereas strain develops at an exponential rate in ductily deforming materials (Petley et al., 2002). Importantly basal mechanisms evolve through time; Varne's (1978) three-phase model describes an essentially ductile process during secondary creep which becomes gradually dominated by strain softening leading to brittle deformation during the tertiary stage(Petley, 2004). Both cohesive and non-cohesive materials experience ductile or

plastic deformation during progressive failure. Under high pressures and temperatures, cohesive rocks and soils may deform in a purely plastic manner (Hudson and Harrison, 1997). Although these conditions generally exist at great depths from the surface, shear zones forming on weak rocks or soils at depth within a hillslope- leading to a deep-seated landslide- may alter their deformation behaviour from brittle to ductile in response to confining pressures. Ductile failures will not develop into catastrophic landslides (Rosser, 2010); strain rate is typically lower than that of failures driven by unstable crack growth (brittle) (Ng, 2007).

The self-reinforcing nature of brittle failure presents possibilities to forecast shear-plane development, using slope *strain-state* (section 3.4). Conversely, hillslopes deforming under ductile processes are considered in terms of landslide likelihood; based on an assessment of slope *stress-state* (Ng and Petley 2009) (section 3.3). Landslides are incredibly complex phenomena. Although deformation processes have been studied extensively within the laboratory, controls on progressive hillslope failure remain poorly understood (Rosser, 2010).

2.3.3.4. Preparatory and triggering factors

Interacting with elements pre-conditioning hillslopes to instability (outlined in section 2.3.1), preparatory factors reduce the margin of stability in a slope over time, without actually initiating final failure (Glade and Crozier 2005). Conceptually all hillslopes are located on a failure continuum, determined by physiographic setting, intact material strength (Hudson and Harrison, 1997) and the sequence, dynamics and intensity of environmental forcings (Densmore et al., 1997; Hertgarten, 2003; Rosser et al., 2007). Slopes accumulate *strain* or permanent damage over a variety of timescales, ranging from days to hundreds or perhaps thousands of years (Petley et al., 2008a). Some preparatory processes- for example weathering, tectonic uplift, regional climate change (table 1)- operate over long geological time scales, creating the general physiographic environment in which intact material is slowly damaged. The action of others- for example deforestation, rainfall, earthquakes (table 2) - is more immediate. These events or environmental forcings alter the rate at which a hillslope accumulates strain ordinarily within its physiographic setting. Basal mechanisms determine whether final slope collapse is controlled by self-reinforcing shear surface formation, following

from a critical strain or by the magnitude and frequency of stress events accelerating rates of deformation to a critical strain. Hillslopes composed of brittle materials initially develop strain in response to local physiographic mechanisms and environmental forcing events (during primary and secondary creep). Slope strain state evolves from zero to a critical threshold (peak strength), after which irreversible accelerating deformation develops (tertiary creep) resulting in catastrophic failure as effective shear strength falls to a residual value (Main, 2000; see sections 2.3.3.1 and 2.3.3.2). Hillslopes destabilising under ductile mechanisms also develop strain in response to stress, however failure occurs at critical *strain*- when a triggering event reduces shear strength below shear *stress*- rather than at the point of shear plane completion (section 2.3.3.3).

Local physiographic mechanisms (table 1) operate continuously to degrade hillslope material. Many of these processes fluctuate in intensity in response to seasonal cycles. Some are dependent on fluctuations in other variables; many chemical processes are modulated by temperature (Anderson and Anderson, 2010). All physiographic mechanisms reduce material strength increasing the effectiveness of subsequent environmental forcing events (table 2). In turn, periods of intense stress readily enhance physiographic mechanisms- effectively both preparatory processes act together in a symbiotic relationship to reduce hillslope strength. Intact material strength of slope composites is an important pre-condition to the rate of progressive hillslope failure (section 2.3.1.1). Figure 2.9 illustrates conceptually the process of strain accumulation, highlighting the differential response of various rock strengths to environmental forcing. Here material deformation is modelled on three-phase creep (Main, 2000; see section 2.3.3.2); critical strain represents the transition from secondary to tertiary creep leading to brittle failure. Rock resilience to damage defines the rate of *strain* accumulation under *stress* through time. The weakest material is sensitive environmental forcing; strain evolves and the slope reaches a critical strain state, triggering shear surface development. The strongest material responds only slightly to *stress* events; a small amount of deformation occurs (i.e. irreversible damage), but the slope remains fairly intact, hypothetically residing in the primary creep stage of progressive failure.

Physiographic mechanisms typically exert constant low level stress on a hillslope. Environmental forces act episodically, applying intense stress over discrete periods. For damage to accumulate, each stress episode must reduce effective material stress to a level equal or lower than that previously experienced (Petley et al., 2005b). In brittle materials this process of hysteresis is known as the Kaiser-stress memory effect (reviewed in Holcomb, 1993; Lavrov, 2005; Lockner, 1993); with each 'effective' stress episode the potential for catastrophic failure increases (Meredith, 2010). Under this model for cumulative damage a slope may exist for significant amounts of time just below critical strain state in the absence of an event of suitable magnitude to instigate the transition into tertiary creep (Rosser, 2010).

Pre-conditions and preparatory factors set the stage for triggering events, initiating accelerating shear-plane development and catastrophic failure in brittle materials (Rybar et al., 2002) and prompting sudden loss of strength in ductile deforming shear zones. Most landslides are triggered by one of three key factors: precipitation, seismicity or the action of humans (Petley, 2009). Water reduces shear strength triggering failure: in brittle materials water acts as a catalyst to crack growth (Kilburn and Petley, 2003), in ductile materials it saturates pore spaces, preventing further 'dilatant strengthening' (Anderson and Anderson 2010). High intensity, short duration rainfall events are particularly effective at triggering landslides (Guzzetti et al., 2008), although long duration low intensity rainfall and rapid snow or ice melt are also known to destabilise hillslopes (e.g. Guzzetti et al., 2009). Earthquakes generate strong ground shaking, reducing the cohesion and/or frictional strength of hillslope material through rockmass shattering or liquefaction (Meunier et al., 2008). Events of magnitude greater than M= 4.0 (Keefer, 1984) have been observed to trigger landslides, although it is noted that seismicity of any magnitude may reduce the effective shear strength of the hillslope. Seismic acceleration is intensified in mountain ranges as surface topography diffracts vertically incidient seismic waves (S-waves), amplifying ground accelerations towards ridge crests (Parker, 2009). This highlights the importance of hillslope morphology as a precondition to slope instability.

TYPE OF DAMAGE	PROCESS
Brittle	communition; initiation
Ductile	stratigraphic sequencing
Creep	sub-critical crack growth
Fatigue	low/high frequency loading/ unloading cycles (glaciations isostasy, pore-water pressure fluctuation, freeze-thaw, wet/dry, seismicity, salt cracking, plants)
Thermal (mechanical)	climate change; heating and cooling cycles
Tectonic	tectonic uplift; tectonic structures and lineaments; pre-conditioned damage due to faults, folds and in-situ stress
Anthropogenic	Human disturbance (i.e. footpath erosion, burst pipe)
Physio-chemical	weathering, hydrothermal alteration, corrosion
Geomorphic	lithology; local bedrock outcropping; fluvial incision promoting feedbacks from channel uplift to knick-point migration; glacial debutrassing/ incision; slope oversteepening by erosion activity; thermal cycling

Table 2.1: Types of hillslope damage resulting from physiographic processes operating in the local environment (modified from Brideau et al. (2009, table 1, p.31) and Rosser (2010))

TYPE OF DAMAGE	PROCESS
Fatigue	rainstorm; snowmelt
Thermal (mechanical)	extreme heating or cooling (i.e. sudden changes in temperature or extreme temperatures for time of year)
Tectonic	earthquake
Anthropogenic	deforestation; slope disturbance by human activity ; human modification; excavation or blasting
Geomorphic	fluvial incision (river in flood); sudden glacial collapse

Table 2.2: Types of hillslope damage resulting from environmental forcing events modified from Brideau et al. (2009 , table 1, p.31) and Rosser (2010))

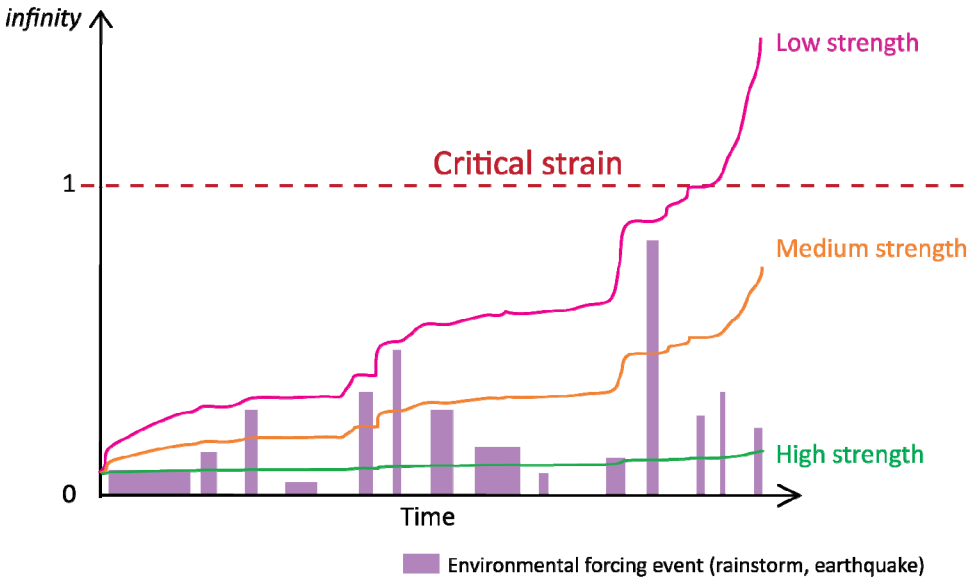

Figure 2.9: Conceptual mode of differential rock strain accumulation in response to environmental forcing events (adapted from Rosser (2010; figure 3.10, p.75) and Roberts (1977) in Selby (2005; figure 4.4 p.34))

Anthropogenic action is also a key contribute and triggering factor of hillslope failure. Relatively small increases in population density are seen to drive big increases in landslide density (number of events occurring per 1000 sq km) (Petley 2009). Landslides are typically triggered both by construction (e.g. road development)- often a result of poor engineering in marginal areas of rapidly urbanising centres (Smyth and Royle, 2000)- and quarrying (i.e. excavation), (Brideau et al., 2009).

Rock strength evolution is widely considered in slope-scale engineering geology (Main, 2000; Petley et al., 2008), leading to the concept that hillslope state lies within a failure continuum. Rosser et al. (2010) suggested that all slopes within a landscape reside at some point on a time-strain curve (figure 2.9) as a function of the ratio of accumulated damage versus the critical strain required for failure at each location. The adaptation of this model to represent three geological scenarios reflects observations by Korup (2008) that terrain over the long-term retains a fingerprint of geology, indicating that slope failure is fundamentally controlled by material strength and its deterioration. Under conditions of catastrophic trigger some slopes will fail in clearing events (Densmore et al., 1997) yet others remain superficially intact (Rosser, 2010). Failures are also observed to occur without an apparent trigger. Critically here is the idea that an event triggering failure in one slope may not collapse another, but instead

contribute to its damage accumulation history, increasing the susceptibility of failure in future events. Returning to an observation made earlier in this section, cohesive slopes may exist in a state close to critical strain for significant amounts of time, requiring only a small, potentially undetectable stress variation to initiate tertiary creep (Rosser, 2010). Some failures on slopes composed of non-cohesive materials have been known to lag behind critical stress events (e.g. rainstorm). Ng and Petley (2009) discuss this behaviour, recognising that although FoS may equal unity (1.0), actual slope failure is time dependent as material deformation (internal restructuring) must occur. The implication of these observations is that slope stability in both cohesive and non-cohesive materials is ultimately controlled by *strain*, rather than the conventional widespread use of *stress*, which develops in response to variable *stress-state* caused by local physiographic mechanisms and environmental forcing events (Rosser, 2010).

2.3.4. Modes of failure

Several landslide classification schemes exist to describe the style of hillslope movement after failure has been initiated. Most schemes are based on three key elements: the type of movement, the kind of material and the rate of movement (Varnes, 1978). The term 'landslide' (defined in section 2.1) is used to describe a complex array of different mass movements. The infinite slope model (section 2.2, figure 2.3) depicts stress balance for a sliding failure, however there a number of different styles through which hillslope materials are mobilised downslope. Table 3 outlines the classification scheme adopted in this thesis; figure 2.10 is given to add clarity to the principal categories. This landslide classification is based on the system proposed by Varnes (1978), taking into account modifications made by Cruden and Varnes (1996). The scheme was chosen because it emphasises movement style, rather than slope condition or movement rate. For the purposes of this research, an understanding of post-failure movement type is useful in deriving the nature of pre-failure creep; monitoring strain accumulation and forecasting shear plane development must account for the dimensionality and rotational attributes of movement. Importantly the mechanisms (brittle or ductile) and form of shear zone and slip-plane formation establish the style of slope failure whilst pre-conditions, preparatory processes and triggering factors destabilise the slope and govern the

velocity, water content and distribution of a landslide until it essentially stops (Picarelli et al., 2005b).

Type of movement			Type of material		
			Bedrock	Engineering soils	
				Predominantly fine	Predominantly coarse
Falls			Rockfall	Earth fall	Debris fall
Topples			Rock topple	Earth topple	Debris topple
Slides	**Rotational**		Rock slump	Earth slump	Debris slump
	Translation	**Few units**	Rock block slide	Earth block slide	Debris block slide
		Many units	Rock slide	Earth slide	Debris slide
Lateral spreads			Rock spread	Earth spread	Debris spread
Flows			Rock flow	Earth flow	Debris flow
			Rock avalanche		Debris avalanche
			(Deep creep)	(Soil creep)	
Complex and compound			Combination in time and/or space of two or more principal types of movement		

Table 2.3: Landslide classification based on Varnes (1978), modified to account for the later scheme proposed by Cruden and Varnes (1996)

2.3.5. Actively unstable slopes

Actively unstable slopes are those which are unable to withstand destabilising forces after first time failure, existing thus in an episodic state fluctuating between reactivation and suspension (see: Cruden and Varnes 1996). Reactivation occurs when all or part of a stationary but previously failed mass is involved in new movements along pre-existing shear surfaces (Lee and Jones, 2004). The style of movement and size of the new landslide body are dictated by the location of the relict slip surface (Picarelli et al., 2005). Materials within the shear zone of a reactivating failure are at residual strength, responding to local physiographic mechanisms and environmental forcings that the slope prior to failure could have resisted (Lee and Jones 2004). Reactivations are triggered much more readily than first time failure because less strain is required to reach the critical threshold for landslide initiation. Movements are typically slow, a

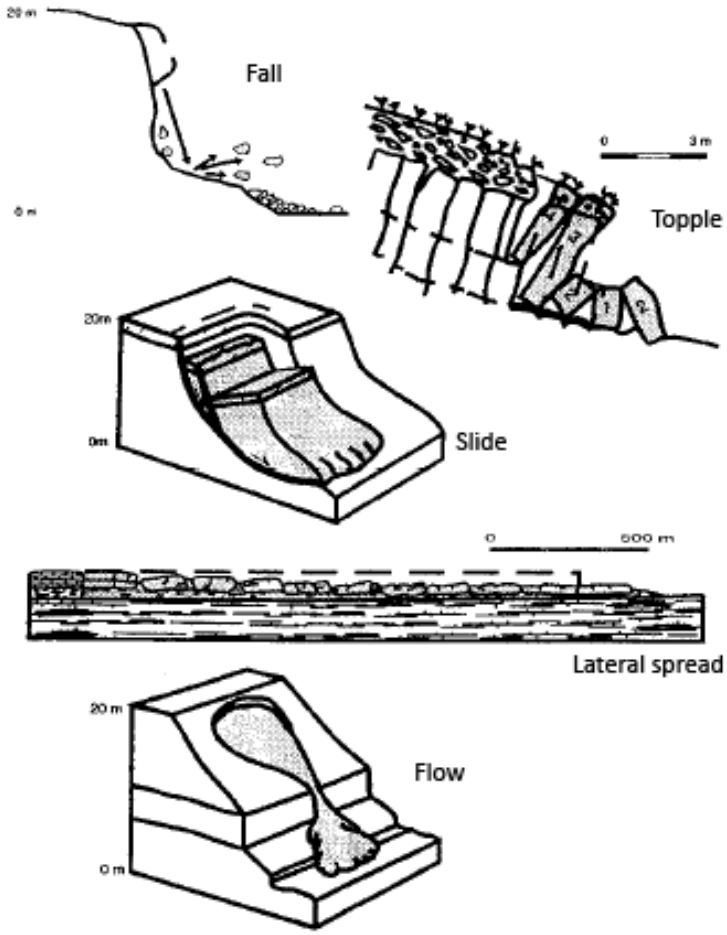

Figure 2.10: Principal categories of slope movement (Cruden and Varnes 1996)

characteristic shared by ductile failures undergoing periods of intermittent activity. Reactivations can evolve progressively driven by ductile mechanisms (section 2.3.3.3). Brittle failure governed by unstable crack growth does not occur in previously failed slopes unless a new shear surface is forming, in which case the sub-section of hillslope is considered a first time failure, operating within an actively unstable slope.

Perhaps this last statement best illustrates a common theme running through the processes described over the last chapter; landslides are incredibly complex phenomena. They develop from hillslopes differing in material intact strength and lithology, subjected to a veritable array of preparatory factors and responding to triggering events initiating critical strain and time-dependent material deformation. Following this, hillslopes may remain actively unstable within the landscape, creating a mosaic of landslide features of various ages and origins, conceptually existing at different points on a zero strain (stable) to critical strain curve (section 2.3.3.4). Pre-

failure strain accumulation in hillslopes provides an important precursor to catastrophic first time landsliding. Although a mechanistic understanding of brittle creep has been utilised to forecast the timing of final failure retrospectively (chapter 3), the technique has rarely been applied to progressively unstable hillslopes in advance of failure. Lack of understanding of the finer mechanisms governing unstable crack growth and the controls on tertiary creep rate within a 'real' hillslope is perhaps one explanation for the underuse and uncertainty surrounding this approach. Chapter 3 presents a review of the different methods available to forecast hillslope susceptibility to failure, focusing on strain-based techniques. Whilst chapter 4 analyses a compendium of published tertiary creep data, specifically comparing landslide characteristics (e.g. geology) to attributes of observed brittle deformation (e.g. velocity).

CHAPTER 3

Landslide predictability and the ‘inverse-velocity’ method

3.1. Introduction

The natural process of landsliding becomes hazardous when it has the potential to cause damage or harm to vulnerable elements (such as people or buildings) (Glade et al., 2005). In the context of a landslide risk management framework (figure 3.1.), the term hazard takes a more technical definition, "the probability of occurrence, within a specific period of time and within a given area, of a potentially damaging phenomenon" (Varnes (1983) in Corominas et al. (2003; p.421)). Within this framework unstable hillslopes are identified and assessed to establish appropriate risk management strategies. Landslide hazards may be avoided through effective planning and physical intervention- restricting new construction on vulnerable slopes and stabilising engineering work (slope restructuring, drainage). However, throughout the world, many people live on landslides (e.g. Taihape, New Zealand;(Massey, 2010) or in regions affected by numerous events (e.g. Hong Kong; Ng, 2007) presenting challenging mitigating conditions (Petley, 2009). In such cases, early warning and evacuation, based on the science of forecast and prediction offers a management strategy for those unavoidably exposed to landslide risk (Sarewitz, 2000).

The assessment of potential landslide location and timing is undertaken using either a *stress-based* or *strain-based* approach; or in certain cases a combination of the two (Petley et al., 2008a). This chapter initially reviews key differences between the two methods, before focusing specifically on the 'inverse-velocity method'. Developed from observations of pre-failure slope movements by a Japanese railway engineer, Saito (1969), this strain-based predictive method uses pre-cursory movements to derive the timing of hillslope failure from the linear regression of inverse-velocity plotted against time. Following from a detailed explanation of this technique (section 3.4.2.2.1); section 3.4.3 briefly overviews field methods used to record surface displacement data for inverse-velocity-time based prediction.

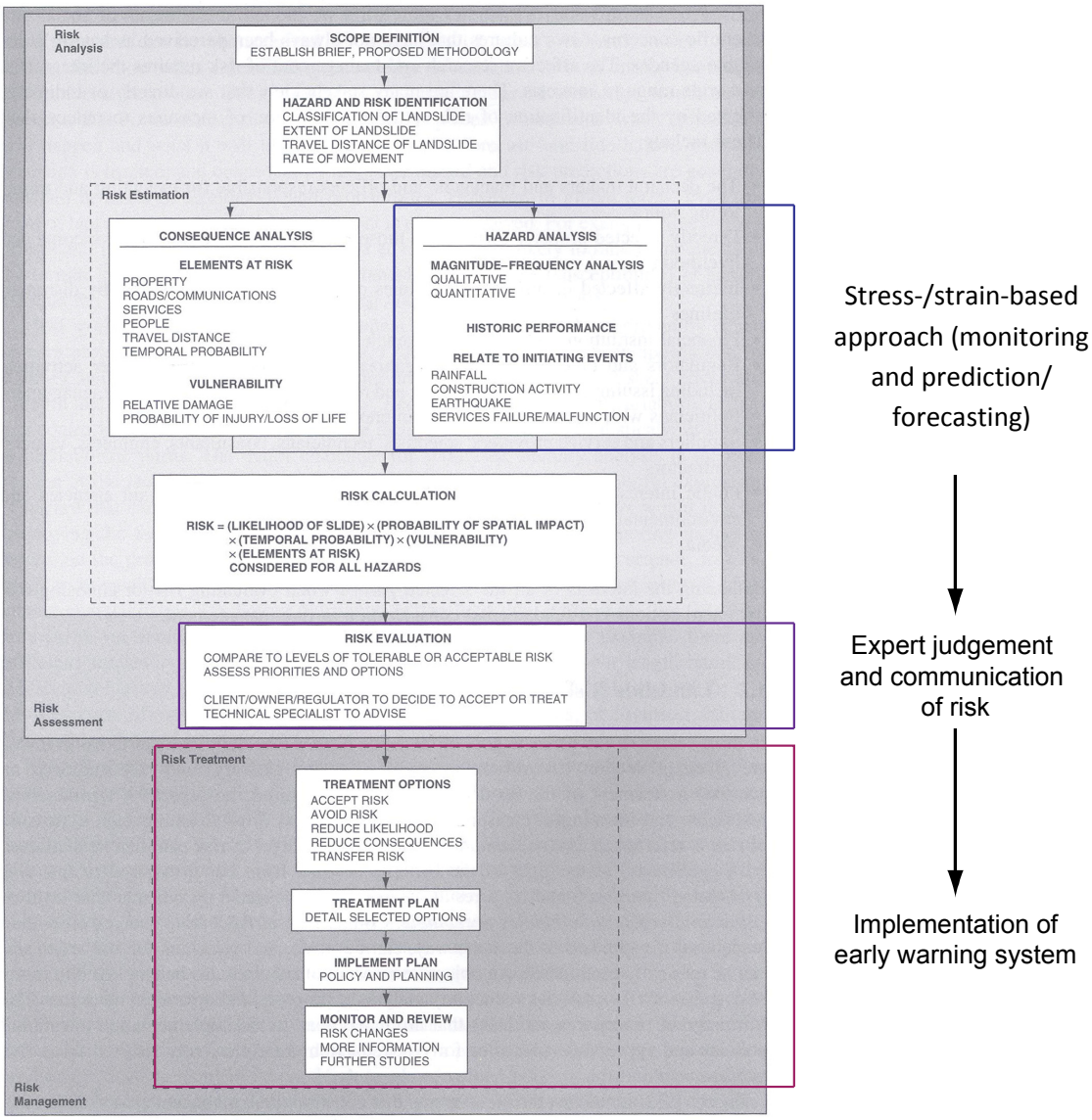

Figure 3.1: Landslide prediction and early warning in the context of landslide risk management (adapted from Australian Geomechanics Society, 2000 in Glade et al., 2005, p.10)

3.2. Prediction and forecasting

Prediction is defined as...

"... the foretelling of an event or condition and may be either absolute (an event with particular characteristics will occur at a particular place and time) or contingent (a particular event will occur if certain conditions are satisfied)" (Wilcock and Iverson, 2003), p.18)

The term forecast is a synonym of predict; however forecasting is concerned with probabilities rather than certainties (Webster (1986) in Krzysztofowicz (2001)). Both predictions and forecasts operate over varied timescales: short-, intermediate- and

long-term. Typically uncertainty is reduced as the lead-time to an event is reduced. Short term predictions give a precise indication of where, when and the magnitude of an event (Zschau and Küppers, 2003). A key element of forecasting is the role of expert judgement, which uses an empirical understanding of the natural system to decide the most probably projection of future behaviour. As forecast lead-time becomes shorter, 'chaos' within the system significant to the forecast output is overcome resulting in a reduction in the number of potential outcomes and an increase in the probability each result will occur (Armstrong, 2001). The more precise the prediction or forecast the greater its potential value to a decision maker (Sarewitz, 2000). Importantly in the context of a landslide risk management framework (figure 3.1), predictions and forecasts feed into early warning systems for people affected by the hazard. The process of...

Prediction → Communication → Use

(Sarewitz et al., 2000)

...is most effective when all three elements work holistically together.

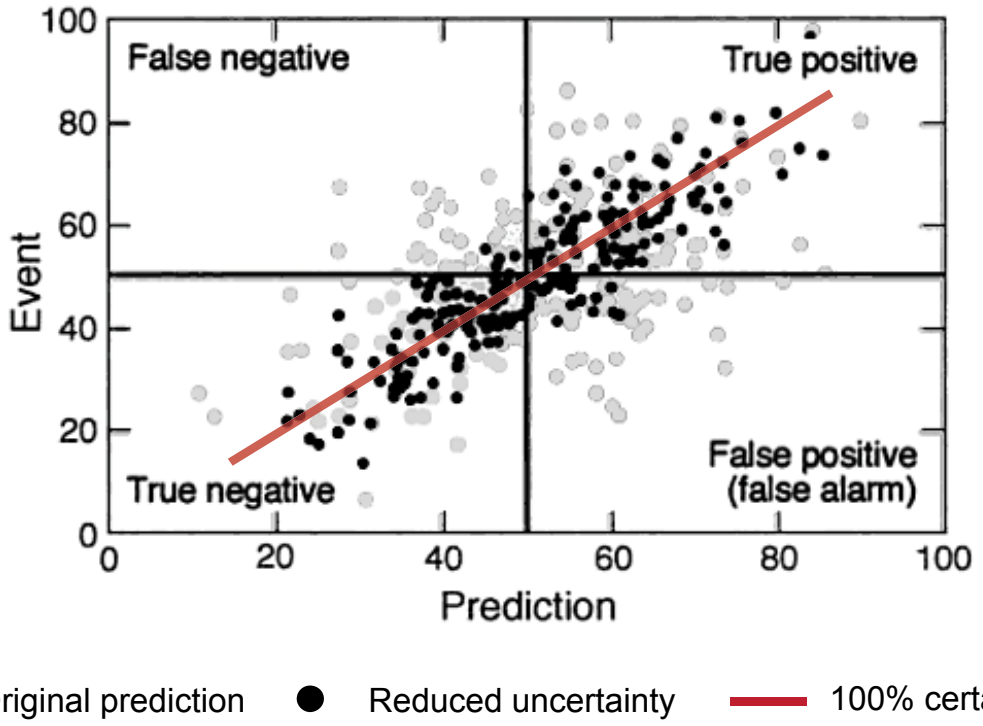

Figure 3.2: Taylor- Russell diagram with reduced uncertainty, adapted from Sarewitz et al. (2000; p. 45 and 50).

Critically, reducing uncertainty in the prediction stage of early warning, reduces the probability of communicating a false alarm (false positive) or failing to recognise precursors leading to a surprise event (false negative). The Taylor-Russell diagram, figure 3.2, provides a conceptual model for predictive certainty; as deviation from the linear-regression increases, the incidence of false positive and false negative predictions increases (Sarewitz et al., 2000). Overall uncertainty in prediction and forecasting is composed of two elements: *epistemic uncertainty*- knowledge of processes that influence events- and *aleatory uncertainty*- natural and unpredictable variation in the performance of the system (Daneshkhah, 2004). The following sections critically review *stress*- (section 3.3) and *strain- based* (section 3.4) approaches to landslide forecasting and prediction, highlighting sources of inherent epistemic uncertainty surrounding techniques and the applicability of each within an early warning framework.

3.3. Stress-based forecasting

Conventional *stress-based* approaches to landslide forecasting, relate the impact of preparatory and triggering factors to the stability condition of the hillslope. Landslide probability is assessed over different spatial scales; from global through to regional, and at a site-specific level. Different methods are more appropriate to each scale of investigation and these are outlined in the following sub-sections.

3.3.1. Global and regional assessment

Landslide forecasts made at a global and regional scale are typically generated from three key inputs:

1. A landslide inventory
2. A landslide susceptibility model
3. Trigger thresholds (rainfall intensity/ duration or earthquake magnitude)

Inventories are the simplest form of landslide mapping (Guzzetti et al., 1999), recording the location, extent and type (if known) of discernible failures in an area. Most maps are created at a 1:25,000- 1:1,000,000 scale (Baum and Godt, 2010), for landslides following a specific trigger event or as a general historical archive of slope failures over time in a region (Malamud et al., 2004). Inventories may be limited by the

spatial coverage or resolution of primary data. Traditionally aerial photographs are used to identify and delineate landslides (Cardinali et al., 1990); however following significant advances in remote sensing and image processing, satellite imagery is increasingly utilised when compiling an inventory (van Westen et al., 2006). Aerial photographs provide high resolution coverage capturing, in some cases, geomorphic activity over several decades. Satellite images, on the other hand, offer broader spatial coverage, regular acquisition, additional spectral information and are available in digital format (Lillesand et al., 2007). Critically, landslides must be manually identified from aerial photographs; a time and labour intensive process (Borghuis et al., 2007). Semi-automated object-based classification techniques have been used effectively on satellite data to delineate slope failures and indicate landslide type with a 76.4% recognition and 69.1% classification accuracy (Martha et al., 2010). Clearly neither method (manual or automated) is perfect, and both may result in cartographic errors and incomplete databases (Malamud et al., 2004), however they generate a wealth of data, providing a snap-shot on landscape *stress-state*; the foundations for a landslide susceptibility map. Several national inventories have been successfully developed, these include: Italy (Guzzetti, 2000), Hong Kong (Ho, 2004), Switzerland (Lateltin, 1997), France (Faure et al., 1988) and Colombia (Gonzalez, 1989). Work from such databases contributes to a global landslide record; a valuable resource when validating global and regional landslide susceptibility models (Dai et al., 2002).

Following the creation of a landslide inventory, the second required input is a susceptibility map. This highlights which slopes within a landscape are most vulnerable to landsliding and is based on factors preconditioning and preparing hillslopes for failure (see section 2.3.1. and 2.3.3.4 for examples of preconditioning and preparatory factors, respectively). Susceptibility assessments provide a measure of the likelihood of landsliding over an area using factor mapping (precondition/ preparatory) to indicate unstable ground, and past landslide inventories to associate instability factors with landsliding (Glade et al., 2005). This is known as the precedence approach to landslide susceptibility (Rice et al., 1969). Factors believed to contribute to slope instability and thus typically included in assessment are: geology, known fault proximity, slope angle, slope aspect, river channel proximity, land-use, road proximity, vegetation condition (Miller et al., 2009). This is by no means a complete list and variables are included on a

physical-basis if they are believed to improve the effectiveness of physiographic and triggering processes (for examples see section 2.3.3.4) on destabilising a slope. Using multi-temporal data sets to relate pre-failure landscape characteristics (earlier image) to landslide distribution (later image)- with images perhaps bridging a widespread trigger event (e.g. earthquake)- provides a basis on which to determine regional landslide susceptibility. A number of different approaches are used to explore relationships between variables and landslide occurrence (Gunther et al., 2004). Statistical approaches include bivariate regression (Keefer, 2000), multiple regression (Yin and Yan, 1988), logistical regression (Chung and Fabbri, 1999), principle component analysis (Baeza and Corominas, 2001), discriminant analysis (Carrara et al., 1991) and susceptibility indexing (Parise and Jibson, 2000). Heuristic (qualitative) approaches are also used if theoretical models relating landslide susceptibility to destabilising factors (Dai et al., 2002) are available, however the subjectivity inherent to such methods limits result reproducibility (Barredo et al., 2000). Although considered more appropriate for regional scale landslide susceptibility mapping (Dai et al., 2002), statistical techniques can be applied in a black-box manner, with inadequate appreciation of the mechanics of the physical processes involved, leading to coarse or misleading regression correlations (Ho et al., 2000).

Unless insufficient data is available, most susceptibility models are based on the precedence that landslides will occur when geo-environmental conditions that led to past slope failure, are replicated (Hervás and Bobrowsky, 2009). As with landslide inventories, the quality and nature of information used to build the model will determine the accuracy with which landslide probabilities are assigned (Dai et al., 2002). Both inventories and susceptibility maps are limited within their time-frame of acquisition. To account for continual changes in terrain as susceptible material is mobilised and slope resistance increased, assessments must undergo frequent revision (Glade et al., 2005). This is both a costly and difficult task, especially if a region, geomorphically, is highly active. In addition, assessments are spatially constrained within the region where the precedence was established; application in areas beyond this will contain inherent uncertainty (Dai et al., 2002).

Landslide susceptibility models indicate the location of vulnerable slopes in a landscape based on the action of preconditioning and preparatory factors, however

estimates of landslide probability depend on both conditioning and triggering variables (Godt et al., 2009). Threshold analysis identifies the nature and intensity of conditions associated with landslide initiation in the past and compares these with conditions that did not trigger movement (Hutchinson, 2001). Trigger events are both natural and anthropogenic however the latter are difficult to assess on a threshold basis; precipitation and seismicity are key variables commonly considered in global and regional scale landslide forecasting (Glade et al., 2005).

Rainfall thresholds are devised on the assumption that direct relationships exist between landslide occurrence and precipitation quantity (intensity and duration) (Dai et al., 2002). The technique is well used and thresholds have been developed for real-time landslide warning systems in a number of regions: US (Keefer et al., 1987), Hong Kong (Geotechnical Control Office, 1984), Italy (Panizza et al., 1996; Premchitt, 1994), South Africa (Garland and Olivier, 1993), the San Francisco Bay region (Keefer et al., 1987), Rio de Janeiro (D'Orsi et al., 1997), Nagasaki (Iwamoto, 1990), Jamaica (Ahmad, 2003), Piedmont region, Italy (Aleotti, 2004), La Honda regional Santa Cruz Mountains, California (Wilson and Wieczorek, 1995), Central mountains Puerto Rico (Larsen and Simon, 1993) and Seattle, USA (Chleborad, 2003; Godt et al., 2006). Global thresholds have also been published following the work of Caine (1980) by Innes (1983), Clarizia et al. (1996); Crosta and Frattini (2001); Cannon and Gartner (2005) and most recently Guzzetti et al., (2008). Alongside geographical extent, rainfall thresholds may be classified by the precipitation attributes used to establish critical limits: intensity-duration, total event, total event-duration and total event-intensity rainfall, where intensity-duration is most commonly used (Guzzetti et al., 2008). Thresholds are derived either physically using process-based models (e.g. Crosta (1998); Salciarini et al. (2008); Terlien (1998); Wilson and Wieczorek (1995)) or empirically from statistical analysis (e.g. Corominas (2000); Aleotii (2004); Frattini et al. (2009); Wieczorek and Glade (2005); Guzzetti et al. (2007, 2008)). Both methods create probabilistic limits for landslide occurrence under certain triggering conditions (Frattini et al., 2009), however the former uses spatially distributed stability models while the latter draws on detailed landslide inventories to relate past slope failures with precipitation conditions. Physical models are limited by environmental assumptions: antecedent rainfall is poorly accounted for by the steady-state pore pressure distribution and landscape scale

variations in morphology and geology are challenging to replicate (Frattini et al., 2009). Uncertainty inherent to approaches founded on database analysis is reduced as the size of the landslide inventory and its temporal range is increased (Guzzetti et al., 2008). Different recording procedures and inaccurate reporting also hinder threshold development (Glade, 1998). Landslide inventories derived from remotely sensed data- outlined earlier in this section- do not suffer from human reporting error, but are temporally limited by the frequency of available imagery.

Thresholds combine with meteorological data and precipitation forecasts, reporting on antecedent conditions and landslide susceptibility maps to evaluate slope failure probability under different trigger events (Baum and Godt, 2010). Precipitation data is provided in real-time both remotely from satellites (e.g. Tropical rainfall measuring mission (TRMM) and multi-satellite precipitation analysis (TMPA); Hong and Adler (2007)) and by rain gauge networks (Baum and Godt, 2010). Of the two systems, rain gauges present the greatest number of challenges when used in the context of landslide forecasting; they can vary in quality (Guzzetti et al., 2008), are not always located close to landslide activity (Brunetti et al., 2010) and may suffer technical difficulties when measuring very high intensity rainfall (Guzzetti et al., 2008). Antecedent conditions associated with pre-failure precipitation and soil moisture are equally important to ascertain as rainfall measurement (Guzzetti et al., 2007, 2008; Dahal and Hasegawa, 2008). The infiltration and evapotranspiration process is difficult to account for when developing rainfall thresholds (Saito et al., 2010). Several authors report adjusting thresholds after 48 hours of continuous precipitation, recognising this as the duration for which antecedent precipitation and soil moisture conditions become important for the initiation of landslides (Aleotti, 2004; Chleborad, 2003; Crozier, 1999; Glade et al., 2000).

Global rainfall thresholds provide a basis for landslide warning where regional thresholds are not available (Hong et al., 2007). However differences in the shape and scale of power law threshold curves defined for different climates indicate intrinsic uncertainty associated with the definition of a single minimum global threshold (Guzzetti et al., 2008) and results in false positive and false negative forecasts. Regional thresholds are climate specific: for mid-latitude climates rainfall intensity is more important whereas in mountainous areas and mild marine climates, rainfall duration is

most relevant to landslide initiation (ibid.). Although regional thresholds provide more accurate forecasts, they are not spatially explicit: rainfall trigger conditions are extrapolated over a wide area (Glade et al., 2005), orographic effects are not considered (Baum and Godt, 2010) and infiltration, when included in models, is oversimplified as a constant value (Reichenbach et al., 1998).

Rainfall thresholds are based on a number of assumptions, primarily that triggering and environmental conditions remain constant (Aleotti and Chowdbury, 1999). Earthquake triggers are not so well studied in terms of threshold analysis (Bommer and Rodŕiguez, 2002), but the principle static-state assumption transcends this technique also. Slope stability is assessed when subjected to peak ground accelerations for different return periods using a pseudo-static analysis (Dai et al., 2002). Although real-time earthquake warning systems are in place (e.g. USGS[2]) or under development (e.g. Crampin and Gao (2010)), "forecasting seismic waves is still at least several years away in seismology" (Hong and Adler, 2007; p. 3717). As technology advances, earthquake thresholds will become more useful to global and regional landslide forecasting. Rainfall thresholds are most relevant to shallow and wet flows, caused by increases in soil pore-pressure (Reid, 1994), whereas seismic events are likely to trigger more deep-seated failures. Importantly both types of threshold, rainfall and earthquake, rely on landslide susceptibility maps to deliver a temporal and spatial probability of landsliding (Ahmad and McCalpin, 1999), although exact landslide location from a particular storm is beyond threshold forecasting (Baum and Godt, 2010).

3.3.2. Site-specific assessment

Unstable slopes may be identified within the landscape from field-based observations. Signs of fresh cracking (particularly at the top of a slope), changes to slope surface (depressions, slump-like features), tree-trunk curvature or damage (if vegetated), bare-ground and (or) patches of fresh rock or loose sediment from localised small failures, and increased overland transport of sediment (visible in downstream water sources) are all indicative of hillslope instability. Site-specific approaches to landslide forecasting require a good geotechnical understanding of the slope, including its geology, structure, mass-strength and hydrology (Read, 2007). This

[2] http://www.usgs.gov/newsroom/article.asp?ID=2366&from=rss

provides an assessment of passive (pre-conditioning) factors and dynamic (preparatory) mechanisms setting up landslide activity (Baum and Godt 2010). Dynamic factors control slope *stress-state* and eventually trigger failure, thus it is important to monitor them and their effect on slope kinematics.

Direct instrumentation including piezometers (for porewater pressure), raingauges, snow gauges, thermometers and pressure cells are used to record the changing conditions on and within the hillslope (e.g. Angeli et al., 2000). This information feeds into models which evaluate static slope stability (Bromhead, 1996), providing a factor of safety (FoS) estimate (section 2.2). Slip-surface geometry- where possible derived from borehole investigations- determines whether an Infinite-slope Model (planar slip-surface, translational failures; Haefeli (1948); Skempton and Delory (1957)) or Slices Model (curved slip-surface, rotational failures; Kennedy (1970); Janbu (1957)) is used to establish FoS. Running a Monte Carlo simulation (or similar test) on the chosen model, produces an estimate of the *stress* conditions capable of destabilising the slope (Dai et al. 2002). Relating this to key triggering variables such as rainfall, allows thresholds to be defined past which failure is more likely. One particularly good example of this widely applied technique is to the Mam Tor landslide, Derbyshire. Here rainfall thresholds were established from past kinematic records by relating periods of significant movement to local precipitation. Both antecedent conditions (750mm during May to November) raising local groundwater tables to a critical level, and winter events (210mm in a calendar month between November and February) expected to trigger slope movements were accounted for (Waltham and Dixon, 2000). This approach is an improvement on that used to establish regional scale thresholds, because landslide location is known. Forecasts are thus purely temporal, relying on meteorological or seismic projections, but not susceptibility maps to situate probable failure.

Critically site-specific approaches are limited by man-power requirements to carry out repeat field surveys and the assumptions inherent to 2D stability models. Direct instruments provide only point-based measurements that are further generalised when input into calculations (Selby, 2005). Complex infiltration processes are not properly accounted for, particularly since slope heterogeneity is poorly considered; complexities such as differential geology (and permeability), micro-

structures (cracking) and vegetation are not included. More complex models such as the Combined Hydrology and Slope Stability Model (CHASM^{TM}) consider the coupling between water and slope composition as a series of units within a Slices framework (e.g. Anderson et al. (1988)). Although providing a better representation of hillslope heterogeneity, such models still represent slopes in 2D, assuming *shear stress* parallel to and *normal stress* at right angles to the slip-plane along an infinite length of slope, rather than bounded by scarp and toe processes. Attempts to increase complexity with a third dimension are often limited by computational power and available input data, particularly given the sub-surface nature of key variables (Selby, 2005). Estimates of friction and cohesion, used to calculate the effective shear strength, also pose problems. Typically these are derived from laboratory *stress* tests or rock mass rating schemes- such as Hoek and Brown's Geological Strength Index (Hoek et al., 2002)- providing values from intact samples which are difficult to relate to a fragmented slope, or using expert judgement that naturally incurs high levels of subjectivity (Read, 2007).

Ultimately landslides are complex three-dimensional features that are difficult to replicate in computer form (Brunsden, 1999). *Stress-based* methods of forecasting, both over a global or regional- scale, and at a site-specific level, provide useful estimates of landslide probability and timing, given a certain magnitude of trigger event (typically rainstorm). However this technique assumes slopes fail when exposed to a significant forcing event, such as high intensity rainfall. Importantly, the work of Bjerrum (1967) and others has recognised the progressive nature of failure, whereby damage is accumulated within the slope to a critical point before collapse is initiated; this mechanism is particularly relevant to materials deforming in a brittle manner (section 2.3.3.4). *Stress-based* methods do not account for the damage history of slopes and the ability of small insignificant *stress* variations to trigger catastrophic failure (Rosser, 2010). *Strain-based* techniques discussed in the following section utilise patterns of pre-cursory movement- a manifestation of *strain* accumulation- to predict failure timing, irrespective of hillslope *stress-state*.

3.4. Strain-based forecasting and prediction

Strain-based approaches to landslide forecasting utilise patterns of pre-cursory movement to indicate the spatial extent and development of hillslope failure (Petley 2009). Although techniques are typically applied on a site-specific basis, regional-scale assessments are used to probabilistically characterise the future landslide hazard within a particular landscape (Guzzetti et al., 2007). The following section (3.4.1) briefly addresses the use of event magnitude-frequency distributions to indicate impending slope collapse over a regional-scale. Site-specific approaches utilise patterns of pre-cursory rockfall (or small localised failures), seismicity and displacement to predict hillslope shear-failure. Section 3.4.2 discusses forecasting methods based on this phenomenon; focus is given to developments surrounding pre-failure creep and the application of the Inverse-velocity Method to landslide prediction (section 3.4.2.2).

3.4.1. Regional assessment

Landslide magnitude-frequency distributions derived from inventories (section 3.3.1) provide a useful approach for hazard managers attempting to forecast the impact of significant environmental forcing events on the landscape (Malamud et al., 2004). The approach is discussed under the umbrella of *strain-based* forecasting because it focuses on the scale of slope-failure events (i.e. landslide area as an expression of *strain*) rather than linking changing *stress* conditions to slope stability. Distributions typically follow an inverse-power law over several orders of magnitude when plotted in log-normal space (e.g. Dai and Lee (2001)). Importantly, data frequently departs from the expected trend at small magnitudes (usually under 10,000m^2), creating a rollover effect (Malamud et al., 2004). Following observations that this effect also occurred at the other end of the magnitude spectrum, Guthrie et al. (2007) argued patterns of landslide distribution were strongly related to physiographic variables- slope, slope distance and the distribution of mass within the landslide- rather than purely a function of data biasing during inventory assembling. This physical constraint is still not fully understood (Corominas and Moya, 2008), leading to uncertainties when 'expected' landslide magnitude-frequency distributions are extrapolated from inverse-power law functions. Additional to this, the quality of

forecasts rely on the completeness of inventory data determined by the spatial resolution of imagery, temporal range of the dataset, the method of landslide classification (manual/automated) and the experience of the assembler (Corominas and Moya, 2008; Guthrie and Evans, 2007). Further uncertainties in defining landslide magnitude and accounting for long-term changes in physiographic processes within the local environment, add additional complexity to the utility of magnitude-frequency relationships. Ultimately, forecasts are not spatially explicit, nor stand-alone from meteorological or limited real-time earthquake warnings, relying on these to indicate future environmental forcing events that are expected to generate significant landslide activity. In this manner, magnitude-frequency distributions are commonly used alongside *stress-based* susceptibility maps and event thresholds.

3.4.2. Site-specific assessment

In common with site-specific *stress-based* approaches, unstable slopes should first be identified and delimited (where possible) in space, before appropriate monitoring instrumentation is installed (Petley, 2009). Glastonbury and Fell (2000) described the main pre-cursors to failure exhibited by slopes. In order of perceived occurrence these are: (1) cracking, (2) localised failures and rockfalls, (3) an increased level of micro-seismicity and (4) alterations in the hydrological regime surrounding the slide. Each of these pre-cursors reflects the manifestation of accumulating *strain* in the hillslope. The utility of site-specific patterns of localised detachments (or failures) and micro-seismicity to forecasting are briefly discussion, leading to a more detailed overview of the predictive tools derived from pre-failure surface displacement (section 3.4.2.2).

3.4.2.1. Localised failure and micro-seismicity

The occurrence of pre-cursory phenomena such as localised detachment (rockfall) and seismicity increase as the lead time to a large landslide event decreases (Suwa, 1991). Accelerations often follow a power-law (Amitrano et al., 2005) reflecting the process of progressive failure as strain accumulates within the hillslope (Rosser, 2010; refer to section 2.3.3.2). Rockfall magnitude-frequency distributions provide an estimate- in a similar manner to regional scale patterns- of the number of small events expected to occur before a larger failure. Landslide forecasts are based on the

increasing magnitude of events through time, reflecting the accumulation of strain and irreversible damage to the rock (or soil) mass. Advances in terrestrial remote sensing over the last decade have provided instrumentation capable of capturing three-dimensional surface data to fine spatial resolutions (e.g. Hapke et al. (2005)). Sequential Digital Terrain Models (DTMs) generated from raw field data, are compared to calculate rockfall volumes and indicate areas of maximum relative strain (Rosser et al., 2007). Currently instrumentation does not provide continuous coverage of a rockface, relying on repeat site visits to collect data. This limits the capacity to forecast the timing of large rockfall events; the temporal resolution of data collection may be too sparse to capture signs of imminent failure and collapse.

Seismic networks have been used effectively to detect cracking and related rockfall on cliffs, particularly in coastal regions (e.g. Helmstetter and Garabois (2010)). The formation, growth and coalescence of cracks give rise to elastic waves (Amitrano et al., 2010). Differentiating the frequency of seismicity have shown two major signals: (1) steady-state energy release from fracture growth, and (2) high energy events representative of material shedding (Got et al. 2010). Also known as a 'seismic crisis', high level seismicity typically triggered by an environmental forcing event, provides a precise record of localised failure (Helmstetter and Garabois 2010). Low-level seismicity provides the better estimate of slope strain-state, reflecting the gradual accumulation of damage within the rock mass, rather than rapid stress induced fluctuations in short-term stability. Given this, the increase in magnitude of both signals provides a basis on which to forecast the immanency of widespread slope failure (Got et al. 2010).

Although promising, seismic- and rockfall-based forecasts are difficult to implement. Very few active slopes are instrumented and installations of sensor networks require heavy field maintenance, an unrealistic venture for long-term monitoring or slopes with poor access (Helmstetter and Garambois, 2010). Monitoring systems must be bespoke to the physiography of the site, specifically reflecting local geology (Hardy, 2003). The magnitude of pre-failure seismicity and shedding (or rockfall) is a product of the intact strength and resistance of the slope to local stress factors (Rosser et al., 2007). In order to capture events (particularly seismically), it is important to install equipment capable of detecting movements within the expected

magnitude and in locations of lithological instability. Similar to regional scale distributions, magnitude-frequency patterns of local rockfall (and seismicity) typically contain a 'rollover' for smaller events; indicative of the limited resolution of instrumentation (Helmstetter and Garambois 2010). This uncertainty, alongside the expense and man-power required to install and operate monitoring, is the key drawback of forecasting based on these pre-cursors, and one that should be addressed with instrumentation development.

3.4.2.2. Accelerating strain

> "Displacement rate is commonly considered the best indicator of the failure process"
>
> (Rose and Hungr 2007, p.308).

Hillslopes undergoing shear-failure typically exhibit pre-cursory creep reflectant of material deformation within the slope (Ng, 2007) (refer to section 2.3.2 for a more detailed explanation). Crosta and Agliardi (2003) outline three approaches to studying pre-failure creep:

(1) The micro-mechanical approach
(2) The rheological-mechanical approach
(3) The empirical approach

The micro-mechanical method (Mitchell et al., 1968) aims to relate creep behaviour to molecular scale processes (Crosta and Agliardi, 2003). The approach is typically integrated within distinct element models, used to evaluate the stability of slopes composed of granular materials, from parameters defining inter-particle friction and particle stiffness (Calvetti and Nova, 2004). The technique, although useful for soil slopes, has limited applicability to developing rockslides.

The rheological-mechanical approach fits idealised mathematical laws- derived from laboratory testing- to estimate the motion of deforming hillslopes (Hungr, 2009). Mechanical models consisting of springs, dashpots and sliding blocks (figure 3.3) are used as analogues to represent elements of 'ideal' material behaviour: elastic, viscous and plastic respectively (Selby, 2005). Combinations of these simple models (e.g. visco-elastic) are used to describe the rheological response of *stressed*

materials. Although this provides a good, albeit simple, representation of the micro-scale deformation process, models are rarely used to give temporal prediction due to the complexity and detail of data required (Crosta and Agliardi, 2003). Numerical models utilise rheological laws to simulate slope failure under different *stress* conditions, providing probabilistic forecasts of failure mode and thresholds on stability (Hungr et al., 2005). In common with other modelling applications, landslide models are limited by the availability of good quality data, often requiring inputs that are not routinely measured (Stead et al., 2006). This may lead to reductionist approaches when defining model structures and thus only a simple abstraction of reality is processed (Wainwright and Mulligan, 2004); limiting the utility of computation outputs.

The third approach holistically evaluates pre-failure slope movements using empirically or semi-empirically derived models describing the expected performance of the system (Hungr et al., 2005). Over the last 50 years, several authors have proposed mathematical functions (linear, exponential or power law) for modelling displacement-time relationships during the tertiary stage of pre-cursory creep (see section 2.3.3.2), these include work by Saito (1965; 1969), Kennedy and Niermeyer (1970), Zavodni and Broadbent (1980), Varnes (1983), Zvelebil , Cruden and Masoumzadeh (1987), Glawe and Lotter (1996), and Zvelebil and Moser (2001). Most of these authors utilise measures of *strain* or *strain-rate* to characterise slope behaviour; it is suggested this parameter is more appropriate than displacement or velocity when comparing movements of vastly differing magnitudes (Bonnard and Glastonbury, 2005). *Strain* describes deformation in terms of *relative* displacement; expressed as dilation (volume change) or distortion (shape change), or a combination of the two (Park, 2004) (see section 2.3 for greater detail). The parameter is calculated from measurements of slope displacement using either change in length of a reference line (extension) or change in angle between two reference lines (shear strain) (ibid). The dimensionality of the measurement (1D, 2D or 3D) will depend on the instrumentation and set-up from which data is derived (discussed further in section 3.4.2.4).

Most mathematical models for creep use *strain* or *strain-rate* alert thresholds to indicate imminent failure, extrapolating from records to predict collapse timing (e.g. Zavodni and Broadbent (1980) or Cruden and Masoumzadeh (1987)). Fundamentally

this approach assumes that slope deformation is accelerating to collapse. The concept of progressive failure (discussed in section 2.3.3.2) substantiates this assumption for hillslopes composed of brittle material that have entered the tertiary stage of the *Three-phase creep model* (Main, 2000) (see section 2.3.3.2). Materials deforming in a ductile manner respond to *stress* fluctuations in the final phase of failure more readily than brittle materials (see section 2.3.3.3). This results in deviances from predicted behaviour, whereby empirical models fail if slope *stress*-state is reduced, leading to an episodic stick-slip creep behaviour (Bonzanigo et al., 2001) and higher incidence of false positive predictions (for example Hiem (1932) at Kilchstock, Swiss Alps in Hungr et al. (2005)). Glastonbury and Fell (2002) thus concluded that no single mathematical function could adequately model all types of failure mechanism due to fundamental differences in shear zone deformation.

3.4.2.2.1. The Inverse-Velocity Method

Although there is no universally accepted equation for accelerating creep rates in geo-materials, a growing body of work has developed and applied Saito's (1965, 1969) observations that hillslopes undergoing accelerating creep exhibit linearity in log time- log *strain-rate* space (figure 3.3). Saito equated *strain-rate (ε)* to...

$$\varepsilon = \frac{a}{(t_r - t)^n} \qquad \textit{[Equation 8; Saito (1969)]}$$

... where *a* is constant, *t* is time from the beginning of tertiary creep and t_r is time of failure. When *n=1* data is modelled using a log function ("pure Saito"), however when *n≠1* data is modelled using a power function ("generalised Saito") (Glastonbury and Fell, 2002). Saito (1965) was perhaps the first to attempt to predict time of slope collapse from displacement data. This coincided with the work of Skempton (1964), Bjerrum (1967) and Bishop (1967) who contributed to present understanding of the progressive failure concept (see 2.3.3.2) for brittle materials. Saito's (1965) observations utilise the pattern of accelerating deformation during tertiary creep, as a precursor to slope collapse (Petley et al., 2008a). Beyond critical *strain* crack growth dominates under *strain-softening* mechanisms, leading to shear- surface formation (see section 2.3.3.2). This process is reflected in the linearity observed by Saito (1965, 1969). Catastrophic hillslope collapse occurs when a failure plane fully forms (Petley et al., 2005a), and may be predicted from Saito's log time- log *strain-rate* model using a

linear fit on data; extrapolating the trend to its y-intercept (figure 3.3) providing an estimated time of slope failure. Predictions become more reliable as the lead time between data and failure reduces (Saito, 1969).

Voight (1989) and Fukuzono (1990) developed Saito's method, providing significant improvements to predictive techniques founded on the concept of accelerating creep. Fukuzono (1985) experimentally derived a time-dependent failure relationship using measurements of inverse-velocity- time; moving from Saito's *strain-rate* parameterisation. Three functions were fitted to lab data (concave, convex and linear; figure 3.4) defined using *equation 9* and the constants *A* and *α*.

$$V^{-1} = [A(\alpha - 1)]^{\frac{1}{\alpha}-1}(t_f - t)^{\frac{1}{\alpha}-1}$$

[Equation 9; reproduced from Rose and Hungr, (2007)]

Here V^{-1} is inverse-velocity, t_f is the time of failure and t is time. Both *A* and *α* are constants representing material characteristics for constant boundary conditions (Crosta and Agliardi, 2003). *α* is a dimensionless parameter controlling the sensitivity of accelerating activity (figure 3.4) and *A* is a positive constant controlling the shape of the curve; and is dependent on the value of *α* constant (Cornelius and Scott 1993). Of the three models, Fukuzono (1985) concluded that the tertiary stage of creep is best characterised by a linear trend in inverse-velocity-time space, where *α=2*. Final failure (t_f) reflects the point at which the linearity is extrapolated to cross the x-axis (figure 3.4), or where inverse-velocity equates to zero (Carey et al., 2007); since velocity cannot be infinite, realistic predictions are made just before the point of inception (Petley et al., 2005a).

Fukuzono's (1985) approach was validated theoretically by Voight (1989), who found values of *α* to range between 1.7 and 2.2, and corroborating earlier empirical models. Cornelius and Scott (1993) demonstrated conclusively that *α ≈2* is characteristic of tertiary creep, using records from Mount St Helens (USA) and Vajont (Italy) to link the empirical function to real-world observations. Following laboratory work by McGuire and Kilburn (1997), Kilburn and Voight (1998) presented a differential equation characterising crack growth in brittle materials (equation 6, section 2.3.3.2). Differentiating this equation with respect to time (equation 10) and then

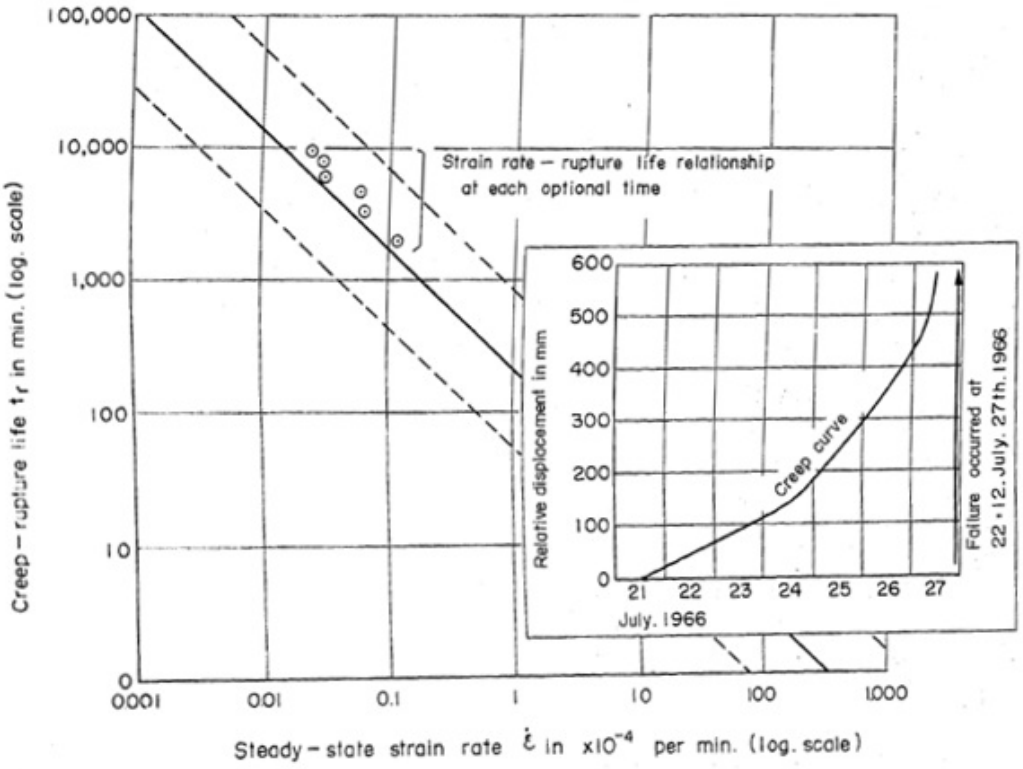

Figure 3.3: Field measurement with an automatic strainmeter at Asamushi landslide (reproduced from figure 1, Saito (1969; p.677))

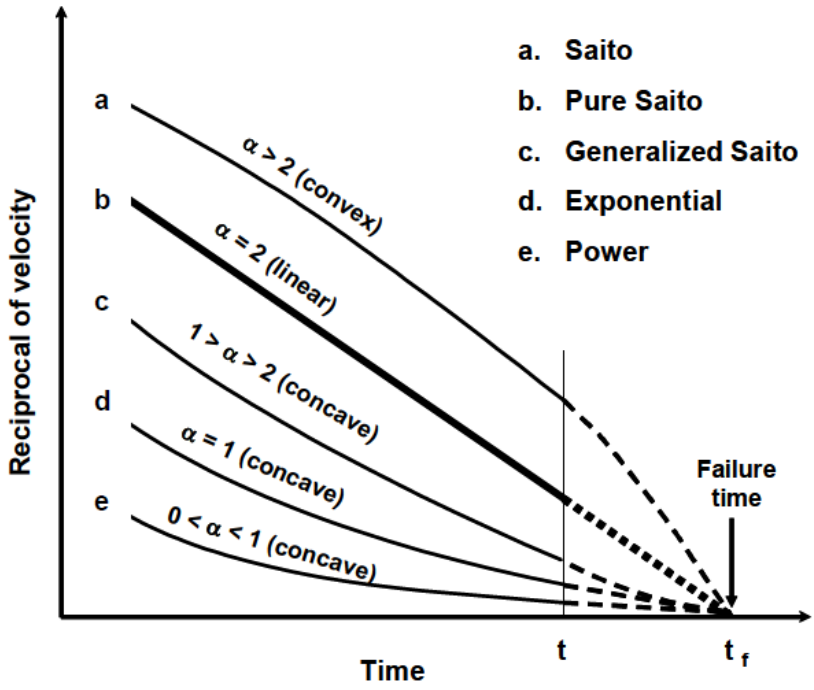

Figure 3.4: Inverse-velocity versus time relationships preceeding slope failure (reproduced from figure 2.15, Ng (2007; p.34) after Fukuzono (1985))

integrating it, provides a function (equation 11) describing patterns of accelerating creep in inverse-velocity-time space mechanistically, giving consideration to the physical basis of Fukuzono's original model.

$$\frac{d^2x}{dt^2} = \lambda\frac{dx}{dt} + \psi(\frac{dx}{dt})^2$$

[Equation 10, adapted from Kilburn and Voight 1998; see section 2.3.3.2 for terms]

$$\frac{dx}{dt}^{-1} = (\frac{dx}{dt})_0^{-1} - \psi(t - t_0)$$

[Equation 11, adapted from Kilburn and Voight 1998; see section 2.3.3.2 for terms]

Here inverse-velocity, previously V^{-1} is represented by the term $\frac{dx}{dt}^{-1}$. Kilburn and Voight's (1998) work marks a key development in the theory of accelerating creep.

The slow cracking model proposed by Kilburn and Voight (1998) was first applied to landslides by Petley et al. (2002). This work verified linearity in inverse-velocity-time space for hillslopes undergoing brittle shear failure (figure 3.5a), using data from the Selborne slope- cutting experiment (for further details, see section 4.). Several unsuccessful applications of Saito's principles to unstable hillslopes (e.g. Hungr et al., (2005); Angeli et al. (1989)), have raised questions on the validity of the approach (Qin et al., 2001). Petley et al. (2002) noted differences in the trend generated by inverse-velocity-time data, inferring that processes of deformation within the basal shear zone, control patterns of pre-cursory creep. Kilburn and Voight's (1998) equation assumes that mean rates of pre-collapse movement are proportional to rates of cracking (Kilburn and Petley, 2003). As discussed, linearity is attributed to the *stress* transfer process during crack growth (Main et al., 1993), which leads to patterns of accelerating deformation as rupture surfaces form (Petley et al., 2008a). The process is associated with first time failure of soil or rock slopes composed of cohesive materials (section 2.3.3.2). Shear zones deforming in a ductile manner, either sliding on existing surfaces (reactivation) or purely under strain-hardening mechanisms (crack nucleation), observe an asymptotic trend in inverse-velocity-time space (figure 3.5a; Petley et al., 2002). This trend is also evident during primary and secondary creep in slopes that eventually fail under brittle mechanisms (Carey et al., 2007).

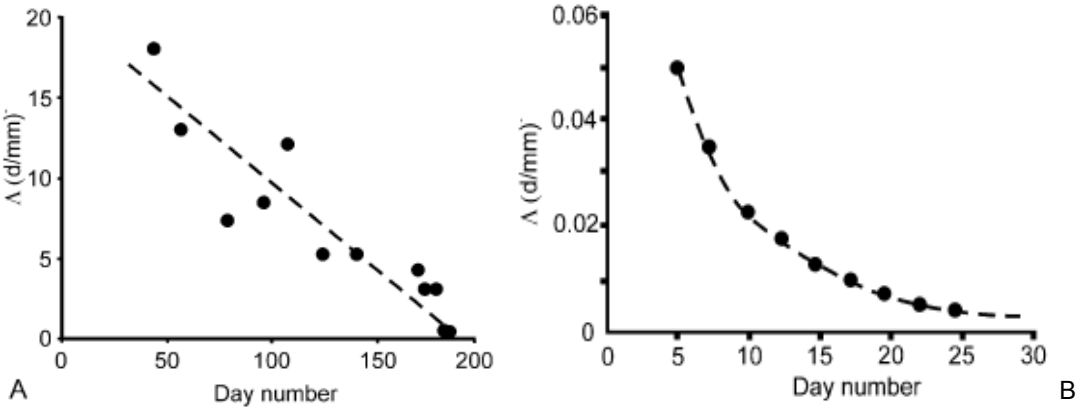

Figure 3.5: (A) Inverse-velocity-time trend for hillslopes undergoing brittle shear failure (Data from Inclinometer 8, Selborne landslide, reproduced from figure 2A, Petley et al. (2002); p.720). (B) Inverse-velocity-time trend for hillslopes undergoing ductile deformation in the shear zone (Data from Abbotsford landslide, New Zealand, reproduced from figure 3B, Petley et al. (2002; p.721)).

The inverse-velocity method, quantified by *Equation 11*, is a valid tool for the prediction of landslides deforming in a brittle manner (Petley and Rosser, 2006). Although this and earlier formulations of Saito's principle have only been applied to a limited number of unstable hillslopes (Mufundirwa et al., 2010; Rose and Hungr, 2007; Carey et al., 2007; Petley and Rosser, 2006; Kilburn and Petley 2003; Petley et al., 2002; Zvelebil and Moser 2001; Hungr and Kent, 1995; Suwa, 1991; Zvelebil, 1984; Kennedy and Niermeyer, 1970; Saito, 1969), mostly retrospectively, the technique has proven robust for these examples. Founded on the concept of progressive damage accumulation in slopes (section 2.3.3.2; Brideau et al., 2009), Saito's observations are supported by the time dependency of pre-cursory localised failures and rockfall (section 3.4.2.1) (Rosser, 2010). The inverse-velocity method is the only predictive technique- both *strain-based* or *stress-based*- to provide an estimate of failure timing (Glastonbury and Fell 2000). Although instabilities must be identified, delineated and monitored, application of the method does not require site-specific tailoring or rely on an alert threshold- as is the case with other empirical functions (Petley et al., 2008a). Since the majority of landslide related deaths are caused by sudden catastrophic first time failures (Petley et al., 2005b) either rainfall or seismically triggered, the contribution this technique could make to landslide science is significant.

3.4.3. Methods of monitoring displacement

Monitoring instrumentation limits the accuracy of landslide predictions derived from the Inverse-velocity Method, and other strain acceleration techniques. Precise measurements of displacement are required to capture the sub-centimetre creep rates of pre-failure hillslope deformation (Bhandari, 1988). Several instruments exist to record slope movements, these may be grouped into the broad categories (1) type of measurement (point/surface) and (2) location of the measurement (surface/ sub-surface), and are reviewed in table 3.1.

The most long-standing and well-used methods involve simple point-based direct instrumentation, such as inclinometers and extensometers. Point-based instruments are capable of recording millimetre displacements to a high precision and accuracy, however they provide only limited coverage of the hillslope (McHugh and Girard, 2002). Many such techniques involve equipment that is directly installed onto the slope. This requires careful planning and strategic placement of the device in a location where motion is expected to occur, based on geological conditions (Angeli et al., 2000). Differential GPS and total EDM surveying are two more advanced point-based techniques, facilitating greater surface coverage dependent on the number of reflectors or receivers deployed over the surface. However although both techniques operate with an element of remoteness, their targets are subject to damage by landslide activity.

Remote monitoring overcomes problems associated with manually installing (and maintaining) direct instruments on steep unstable terrain (Lim, 2006). Including both passive and active sensors mounted on satellite, airborne or terrestrial platforms, remote techniques are diverse but commonly collect a number of points across the slope surface, providing greater coverage for motion detection. Satellite techniques such as Differential InSAR, may be limited by spatial and temporal resolution (Petley et al., 2002), however terrestrial systems such as the laser scanner, provide high resolution, high density data at temporal resolutions dependent from the frequency of site-visit. Importantly data is not collected continuously, unless a system is permanently installed. The majority of techniques reviewed in table 3.1 measure surface displacements. Although these movements are easier to record (Petley, 2004),

Type of measurement	Location of measurement	Instrument	Description	Typical resolution/ accuracy	Positives	Negatives	References
Point	Surface	Extensometer/ strain-meter	Measures linear movement across two reference points (up to ~30m apart) on the hillslope surface. If installed across and perpendicular to existing tension cracks extensometers can measure relative movements between a stable and unstable area of slope. Type Wire (tape) Borehole (rod)	Measurement repeatability= 0.10mm Display resolution= 0.01mm (e.g. CEP digital tape extensometer[1])	• High measurement precision • High temporal resolution (near-continuous) • Relatively easy installation • Rugged design • Long installation life • Not affected by atmospheric conditions • Low power consumption	• Directional • Limited spatial coverage (singular line of displacement measured) • Intense movements can snap wires and damage rods • Affected by temperatures below freezing • Distortions in measurement if tilting occurs	Angeli et al. 2000; Husaini and Ratnasamy (2001)
Point	Surface	Crack-gauge/ meter (jointmeter)	Similar principle to extensometer; measures the linear movement across a crack. Type Mechanical Electrical	Measurement repeatability= 0.3mm Resolution= 0.15mm (e.g. DGSI VW crackmeter[2])	• High measurement precision • High temporal resolution (near-continuous) • Low-cost • Relatively easy installation • Not affected by atmospheric conditions • Low power consumption	• Limited crack span (typically only a few centimetres) • Directional • Limited spatial coverage (singular profile of displacement measured) • Damaged if twisted • Affected by temperatures below freezing	Chelli et al., (2006)
Point	Sub-surface	Inclinometer (tiltmeter)	Measures changing angle (tilt) with respect to an artificial vertical (or horizontal) start horizon. Installed below ground to capture sub-surface movements. Instrument captures movement along a 5-8m profile.	3µradians (e.g. LCF-196 Dual Axis Precision Borehole inclinometer[3])	• High measurement precision • High temporal resolution (near-continuous) • Robust against shocks and vibration • Locate shear zone(s) • Determine whether a shear zone is planar or rotational • Not affected by atmospheric conditions or temperature change (unless extremely hostile) • Low power consumption	• Limited spatial coverage (singular profile of displacement measured) • Requires borehole installation • Damaged if significant movement in the shear zone • Relatively short installation life if slope movements are significant (of the magnitude of metres) • Casing set-up (i.e. length relative to instrument) can cause problems • Expensive	Chelli et al., (2006)
Point	Surface	Total station (EDM) survey	Measurements are made to and between survey markers (or reflectors) spread across the surface of the unstable slope. Manual instruments require on-	Angular resolution= 2” RMSE distance measurement (prism mode)=	• Large spatial coverage • Three dimensional movement vectors • Capable of recording a wide range of movement magnitudes	• Temporal resolution may be limited if manually operated EDM used • Measurement precision decreases with range • Affected by atmospheric conditions	Kalaugher et al., (2000); e.g. Tessina landslide (Petley et al., 2005c)

			site operation by a field worker. Automated systems seek and record reflector locations.	2mm + 2ppm (e.g. Trimble S3 Total Station[4])	• Main EDM unit is remote from landslide activity (capable of measuring distances ~5000m) • Records differential movements between points across the slope • Low power consumption	(reflector detection and measurement accuracy) • Reflectors may be damaged or hidden by localised failures • Coverage depends on number of points included	
Point	Surface	Differential GPS	A reference base station is located over a known point (i.e. Ordnance Survey benchmark) on stable ground. 'Moving' stations are distributed over the unstable slope. The changing positions of the 'moving' stations are recorded in relation to base station, which provides a highly accurate stable reference point. Movement vectors are calculated between 'moving' points, and between the reference station and 'moving' points.	Measurement precision and accuracy in position and height dependent on number of factors. ~5mm horizontal, ~10mm vertical accuracy achievable with post-processing (e.g. Leica GPS1200+[5])	• High measurement precision (optimal at 24 hours, but degrades with time due to variations in satellite constellations and multipath effects) • Three-dimensional movement vectors • Does not require direct line of sight between the 'moving' stations and the base station • Base station may be situated up to ~5km away • Measurements between 'moving' and reference stations are not weather or light dependent • Lower maintenance than other point-based systems	• Limited temporal resolution if GPS isn't permanently installed and automatically recording. • Access issues for 'moving' station installation • Power supply required if permanently installed • Local geophysical conditions (mountains or forest) may limit satellite detection and create multipath errors • Complicated post-processing unless automated • Expensive • Different horizontal and vertical resolutions	e.g. Super-Sauze earthflow (S.Alps, France) (Malet et al., 2002; Tagliavini et al., 2007)
Surface	Surface	Differential InSAR	Satellite-based. Uses two SAR images to create an interferogram of the surface. Images obtained using repeat pass (one antenna, two acquisitions) or single pass (two antennas, one acquisition) methods. Target to sensor distance is calculated from phase signals. Differential SAR compares sequential interferograms (captured at different times); calculating displacement from differences in the phase component of each image.	Imaging resolution~ 3m depending on set-up (e.g. RADARSAT-2[6])	• Capable of detecting large and small movements • Remote data capture • Near global data available from 1994 • Two-dimensional surface monitoring • Three-dimensional movement vectors • Maintained by data providers • Large spatial coverage	• Limited temporal resolution • Can be expensive if data not released • Problems with geometrical distortions/ view direction (i.e. areas in shadow) • Restricted by time lapse between images (decorrelation occurs if surface changes are too great) • Volume decorrelation if two SAR images capture from different acquisition geometry • Decorrelation if two SAR images captured through different atmospheric conditions • Accuracy of time measurement • Problems if surface changes between	e.g. Frank slide, Canada, Singhroy et al. (2005); Corsini et al. (2006)

			Satellites ERS-1/2, JERS-1, Envisat ASAR, Space shuttle (SIR-A/B, Shuttle Radar Lab, Shuttle Topography Mission), and RADARSAT-1/2			data collection e.g. vegetation change • Complicated processing procedure • Complex movement signals to interpret • Power supply required • Limited capture parameters	
Surface	Surface	Ground-based InSAR	Ground-based InSAR uses the same technique as the former satellite-based approach. The instrument employs a single pass method; two radar antennas are mounted on a linear rail, horizontally sliding to form a synthetic aperture. Phase variations are directly related to ground displacement along the sight-line of the radar system. Spatial resolution is controlled by the aperture spacing and target distance.	Spatial resolution depends on distance between the radar and target LISA system has an expected precision lower than 0.3mm for distances ~150m (Antonello et al., 2004)	• High measurement precision; capable of millimetre displacement detection between SAR images • Instrument may be situated a few metres to several kilometres from target slope • Operates independently of weather and light conditions • High temporal resolution (although not continuous) • Flexible operation and capture parameters (i.e. may be set up to capture less frequent images for slower moving slopes) • High range (~3km) • Large spatial coverage • Remote data capture • Two-dimensional surface monitoring • Three-dimensional movement vectors • More appropriate view-direction than satellite systems	• Restricted by time lapse between images (decorrelation occurs if surface changes are too great) • Some instruments (high frequency) are very sensitive to surface state change, resulting in loss of coherence • Problems with atmospheric artefacts • Limited range of velocity detectable, up to a few decimetres per hour • Very expensive overhead costs • Problems if surface changes between data collection e.g. vegetation change • Complicated processing procedure • Power supply required • Requires line-of-sight	Catani et al. (2005); Corsini et al.(2006); Antonello et al. (2004); Noferini et al. (2007)
Surface	Surface	Terrestrial Photogramm- -etry	Photographs are taken from two exposure stations to create a stereo pair. Stations are triangulated using an EDM, providing local coordinates. Differential GPS relates local units to a geographic coordinate system. Sequential stereo pairs, captured periodically of the site provide a time series of surface change. Features on deforming sections of the surface are	~0.03m at ~70m range (Lim et al., 2005)	• Two-dimensional surface monitoring • Three-dimensional movement vectors • Remote data capture • Cheaper than other surface techniques • Provides additional photographs of the slope surface • Processing may be automated • More appropriate view-direction than airborne systems	• Limited temporal resolution, relies on manual collection (non-continuous measurement) • Undulating and/or steep slopes present difficult viewing angles for photography • Requires line-of-sight • Changing light and weather conditions (and cliff appearance) during single acquisition may affect photograph matching • Complete surface evaluation is	Bhandari (1988) (e.g. Mussoorie-chamba bypass landslide Lim et al. (2005))

			tracked to calculate movement vectors.			unpractical, check points used across the slope to overcome this. Point location dictates DEM resolution	
Surface	Surface	Terrestrial laser scanning (LiDAR)	Operates in a similar manner to an EDM unit, however the laser beam is directed across the slope surface using a horizontally rotating base unit and vertically tilt mechanism. A systematic pattern of points are collected providing range measurements between the scanning instrument and the target surface. Most systems are based on the time-of-flight principle. Points are interpolated into a DEM and sequential DEMs may be compared.	5mm precision, 3mm accuracy at 100m range (e.g. Riegl VZ-400[7])	• Two-dimensional surface monitoring • Three-dimensional movement vectors • High measurement precision • Remote data capture • High point sampling rate across surface • More appropriate view-direction than airborne systems • May be integrated with a camera to provide photography • Capable of detecting large and small movements • Not prevented by light conditions (data may be collected in the dark) • Data may be collected over 600m range (new systems)	• Limited temporal resolution, relies on manual collection (non-continuous measurement) • Errors generated by edge effects from laser footprint averaging • Requires line-of-sight • Expensive overhead costs • Point-precision dependent on surface characteristics (limited by wet or dark surfaces), angle of incidence to the surface, weather and dust. • Surface reflectivity governs scanner range • Power supply required • Undulating slopes present difficult viewing angles • Problems if surface changes between data collection e.g. vegetation change	e.g. Puigcercos landslide, Catalonia, Spain (Abellán, 2009)
Surface	Surface	Airborne LiDAR (light detection and ranging)	Airborne LiDAR uses the same instrument (and principles) as a terrestrial application, however is this is combined with a differential GPS and IMU (inertial measurement unit) which relates data acquisition to geographic coordinates, adjusting for in-flight tilting.	Mean horizontal error~ ±38.5cm, mean relative vertical error~ 1.8 ± 4.8cm (e.g. Optech ALTM-2050; Xharde et al. (2006))	• Two-dimensional surface monitoring • Three-dimensional movement vectors • Remote data capture • Not prevented by light conditions (data may be collected in the dark) • Large spatial coverage	• Limited temporal resolution • Requires line-of-sight • Spatial resolution perhaps too coarse for fine creep movements • Errors generated by vegetation • Hugely expensive costs due to flight chartering • Point-precision dependent on surface texture and weather. • Steep slopes present difficult viewing angles • Complicated processing procedure	e.g. Gaspé Peninsula, Canada (Xharde et al., 2006)

Table 3.1: Evaluation of instrumentation commonly used to monitor hillslope displacement.

[1] http://www.cep.com.sg/pdf/tapeextensometer.pdf
[2] http://www.slopeindicator.com/pdf/vw%20crackmeter%20datasheet.pdf
[3] http://www.leveldevelopments.com/PDF_Documents/LCF-196.pdf
[4] http://trl.trimble.com/docushare/dsweb/Get/Document-469042/022543-492A_TrimbleS3_DS_0110_sec.pdf
[5] http://www.servco1.com/Site/Instrument%20PDF's/GPS%20Systems/SmartRover%20&%20GPS1200/GPS1200_TechnicalData_en.pdf
[6] http://www.radarsat2.info/about/features_benefits.asp
[7] http://www.riegl.com/uploads/tx_pxpriegldownloads/10_DataSheet_VZ400_20-09-2010.pdf

it is important to consider the sub-surface accumulation of strain in the landslide mass and how accurately surface deformation represents this (Petley et al., 2002).

Monitoring is a powerful tool for landslide kinematic analysis if data is collected in an effective, comparable manner (Angeli et al., 2000). Incorrect instrument choice or installation may lead to inaccurate or false results (Abramson and Lee, 1996). Accuracy and durability are important attributes to monitoring devices, often resulting in a number of systems being installed to maintain coverage of the site beyond the damage life of a single system (e.g. Chelli et al. 2006). Few recent complete reviews exist evaluating the relative merits of landslide monitoring techniques. Most are confined within key engineering geology textbooks such as Dunnicliff (1993), Kliche (1999) and Hustrulid (2000), predominantly covering traditional point-based direct methods. Less literature exists, comparing remote monitoring devices, although Delacout and others review the state of landslide remote sensing in 2007 (Delacout et al. 2007). Over the last 5 years- since this publication- a number of rapid technological developments particularly in ground-based InSAR and terrestrial laser scanning have arisen to provide the geological community with more accurate and precise slope surface measurements. In the context of *strain-based* prediction and the Inverse-velocity Method, new monitoring tools provide better quality data leading to improvements in the prediction of landslide failure time. Although this review is by no means comprehensive, it provides a good starting point when selecting slope instrumentation, and will be returned to in the discussion of published deformation data (chapter 5).

Instrumentation is the main limiting factor and source of error involved in the Inverse-Velocity Method. However the technique also relies on several other assumptions, that…

(1) the slope is deforming in a brittle manner
(2) deformation mechanisms operating in the shear zone manifest representative patterns of measurable surface displacement
(3) the landslide accelerates continuously to failure (Borsetto et al. 1991), exhibiting a linear trend in inverse-velocity-time space during the tertiary creep phase.

Fundamentally, the limited published applications of the Inverse-Velocity Method *a-priori* to actively deforming brittle hillslopes highlights the *epistemic uncertainty* and thus reduced confidence in applying this technique to determine landslide failure time. Although *stress-based* threshold techniques indicate a higher probability of slope collapse within a region or for a pre-identified unstable mass, *strain-based* site-specific approaches- singularly the Inverse-Velocity Method- provide an estimate of failure timing based on pre-failure *strain* accumulation. Understanding this technique better, particularly in light of the complexities of different slopes and the *aleatory uncertainty* this naturally entails, is an important frontier in landslide science. Failure timing is arguable the most significant parameter when mitigating against landslide loss (Rosser et al,. 2007), particularly when early warning systems are the only viable management solution.

The following chapters address two key aspects of uncertainty surrounding the Inverse-Velocity Method. Chapter 4 presents a database of tertiary creep examples collated from a number of published pre-failure datasets; all of which derive from unstable hillslopes that collapsed under brittle mechanisms. Importantly this chapter discusses *aleatory uncertainty* generated by variations in tertiary creep parameters (i.e. duration); further postulating from these results possible physical causes of diverse behaviour and the impact this has on developing a monitoring technique applicable to a wide range of different slopes. Chapter 5 discusses results in the context of monitoring, recommending the most appropriate method of monitoring deforming hillslopes in the context of feeding data into the Inverse-velocity method leading to failure prediction.

CHAPTER 4

Tertiary creep database

4.1. Introduction

The Inverse-velocity method provides an estimate on failure timing based on pre-failure strain accumulation (section 3.4.2.2.1). Although some studies have been successful in applying the technique to unstable hillslopes, others have not, for reasons that remain poorly understood. The 'black box' nature of this method, results specifically from the lack of understanding surrounding the physical mechanisms that control variations in the linear trend in inverse-velocity-time space. Developed from the fundamental work of Bjerrum (1967) and Main (2000), Petley et al. (2005b) presented a mechanics model for landslide systems (figure 2.7) to explain the physical processes operating in-slope; manifesting as three-phase creep behaviour preceding collapse (section 2.3.3.2). The model provides a good conceptual basis for slopes undergoing brittle shear failure, however its generic form does not constrain slope specific factors controlling the nature and shape of creep curves (Federico et al., 2002; Fell et al., 2000; Hutchinson, 2001); and in turn the duration and linearity of inverse-velocity-time data.

Recent work has focused on understanding the relationship between micro-scale deformation processes and macro-scale strain development. Laboratory testing of intact slope samples (section 2.3.1.1.) provides measurements of the strength and behaviour of material under different stress conditions. Although this brings useful insight into the mechanism (e.g. brittle) controlling material failure; as discussed in chapter 2, it is an abstraction from reality that does not account for the discontinuous heterogeneity of most hillslopes. Variations in inverse-velocity behaviour result from the complexity of real landslide systems. Macro-scale displacement data from actively failing slopes captures shear zone deformation within the context of slope heterogeneity. A significant body of published deformation data is available, yet to date there has been no attempt to collate a catalogue of landslide deformations from a large number of sites to examine emergent behaviour; notably variations in and controls on movement prior to failure. Collation of published data provides a platform on which to examine different patterns of tertiary creep and consider the effect of associated slope characteristics- such as geology- on basal shear zone mechanisms.

4.1.1. Criteria

The inverse-velocity method is a valid tool for the prediction of landslides deforming under brittle shear failure (Petley et al. 2008a; see section 3.4.2.2.1). Criteria must be set in line with this when collating published landslide displacement data. Although all pre-cursory behaviour to slope collapse is interesting, this study is specifically focusing on landslides to which the inverse-velocity method may be applied to data retrospectively. Examples must conform to the following criteria:

(1) **Shear zones must be deforming under a predominantly brittle mechanism**. This is identified from descriptions of slope geology, damage history; whether the event is a first-time failure with a clear shear surface; if the slope is shown to accelerate to failure; additionally if crack growth is discussed as a mechanism by the author of the source in which data is presented.
(2) **Slopes must have fully failed and collapsed**. The tertiary stage of creep may have an incredibly short duration, and it is important to capture the final pre-failure movements of the landslide.
(3) **Movement data must be present in the source** (e.g. article) in graphical or tabular form

Following a brief methodology (section 4.2) outlining how the database was compiled, variations in the dataset are presented and discussed considering the: (1) spread of slope characteristics (e.g. slope gradient) across the examples, (2) tertiary creep variations and, (3) implications this has on measuring surface displacement and applying inverse-velocity based predictions to *real* failing slopes.

4.2. Methodology

Landslide science has generated an increasing number of publications in recent years, responding to growing numbers of fatal events, economic costs and technological innovation facilitating greater understanding of mass wasting processes. Slope displacement data is often included in studies focusing on specific localities. Although results are presented in a number of locations including books, journal articles, conference papers, blogs, professional research body websites, postgraduate

theses (Masters and PhD) and commercial reports; this study initially focused on articles within ten peer-reviewed journals (table 4.1).

JOURNAL	DATES	WEB-LINK
Journal of Geology	Sept 1973-Aug 2010	http://geology.gsapubs.org/
Journal of Geomorphology	July 1987-Aug 2010	http://www.elsevier.com/wps/find/journaldescription.cws_home/503334/description#description
Earth Surface Process and Landforms	Jan 1976-Aug 2010	http://onlinelibrary.wiley.com/journal/10.1002/(ISSN)1096-9837/issues
Nature Geoscience	Jan 2008-Aug 2010	http://www.nature.com/ngeo/index.html
Engineering Geology	Aug 1965-Aug 2010	http://www.elsevier.com/wps/find/journaldescription.cws_home/503330/description#description
Landslides	Mar 2004-Aug 2010	http://www.springerlink.com/content/1612-510X
Natural Hazards	Mar 1988-Aug 2010	http://www.springerlink.com/content/0921-030X
International Journal of Rock Mechanics and Mining Sciences	Jan 1997-Aug 2010	http://www.elsevier.com/wps/find/journaldescription.cws_home/256/description#description
Quarterly Journal of Engineering Geology and Hydrogeology	Sept 1967-Aug 2010	http://qjegh.lyellcollection.org/
Environmental Geology	Jan 1975-Aug 2010	http://www.springerlink.com/content/0943-0105

Table 4.1: Journal information

The ten journals were chosen as a starting point to scope the availability of pre-failure deformation data. They are all peer-reviewed, meaning that article publication

is regulated by professionals working in the same or similar fields, indicating that it is a quality and credible piece of research. Articles in each journal were searched online (see table 4.1) using combinations of key words from box A 'AND' box B (figure 4.1). Only papers available on the internet (i.e. within the dates specified in table 4.1) were included in the search, however most journals now contain an archive from the date of first issue release. This is useful in providing access to a broad spectrum of data, collected using different methods and under different motivations.

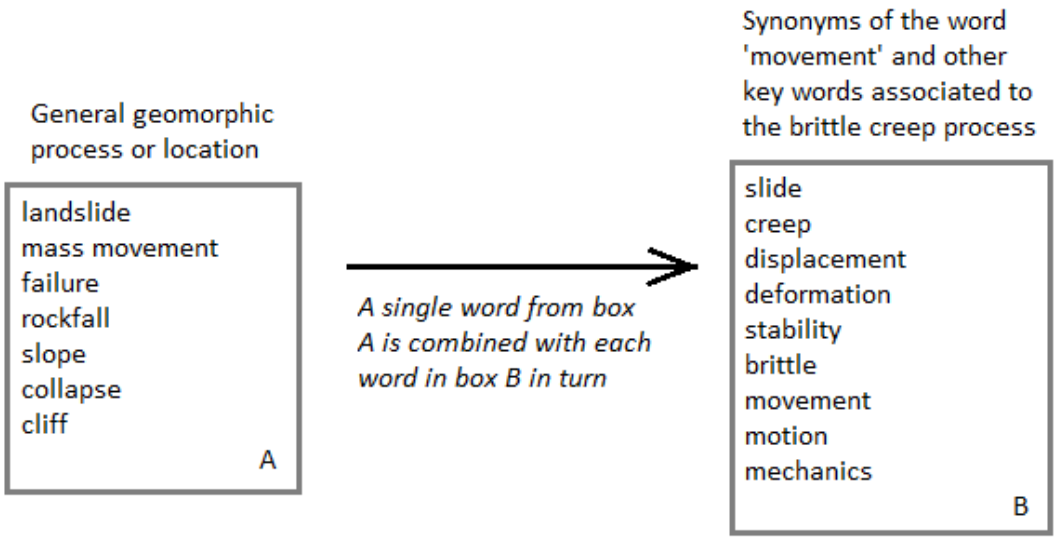

Figure 4.1: Keyword 'search' framework

The search method generated over 6,000 article returns, all of which were exported into an Endnote database. The number of returns was reduced by removing irrelevant studies (e.g. submarine landslides) then the remaining articles were visually skimmed and kept if they contained any form of displacement data. 158 articles contained landslide movement data. Of these 56 papers contained data from slopes believed to be deforming under brittle shear-failure. Only 8 articles provided displacement data that captured the moment of slope collapse. This disappointing result- only 5% of articles that contained data were appropriate to the database criteria- raises questions as to whether displacement data is simply not included in publications, or if it is not readily collected from landslides deforming under the brittle-shear mechanism. Importantly only 14% of slopes evolving in this manner were recorded to collapse, indicating, perhaps, that the instability had been identified and mitigated before failure (although this is not clear from the publications in question).

The limited number of examples also questions the choice of 'scoping' journals. Given that "samples are often considered small if their size is under 30" (Porkess, 2005)it would benefit the database for the 'net' to be cast a little wider. A number of papers referenced in chapters 2 and 3 contain landslide movement data that satisfies the search criteria. Although many of these were from published texts that would have encountered a peer-review, some are conference articles that have not necessarily gone through this process. Nevertheless the research provides a further 10 examples for the database.

Bonnard and Glastonbury (2005) presented time to collapse- strain rate data for a number of excavated slopes, however the lack of information on slope length restricted conversion to displacement and thus inclusion of the examples. The data had originated from two published technical reports, (Glastonbury and Fell, 2000)and (Glastonbury and Fell, 2002). These studies presented a database of just over 100 landslides. 13 of the examples fell within the search criteria specified in section 4.1.1; although most slopes in the reports were first-time failures only a few had collapsed (it is noted that others exhibited significant displacement without collapsing).

All 31 examples collected from the different sources were presented graphically. Data was scanned in from hard copies or captured using the snapshot tool in Adobe, then digitised within SigmaScan software. Associating the limits of graph axes to the local grid within SigmaScan provides a reference on which to re-scale 'picked' data points from local coordinates (x, y) to original graphical values; thus extracting data from the published graphs. To assess the accuracy of this technique, the Vajont original raw data set was acquired (Kilburn, 2011), from which figure 4.2 (a) was generated and published in Kilburn and Petley (2003; p.27). It is noted that this paper is one of few which considers, linearity in an *inverse-velocity-time* plot of data. The 'time' variable is presented on a 'time to failure' scale, where the last data point (considered the point of failure) occurs at zero time; this conversion was used for all 31 examples. Comparing the original raw values to those digitised (figure 4.2, (b-c)), one derives that data was extracted with high accuracy (R^2=1). The maximum error on *time* data is 0.1 days. The published data was deliberately plotted by the authors using circles of a diameter (~2 days) to represent the <5% estimated error on measurement rates (Kilburn and Petley, 2003; figure 6). This however results in the 0.1 day

imprecision in the digitised data (figure 4.2(a));graphs containing 'cross' markers have the least digitising error.

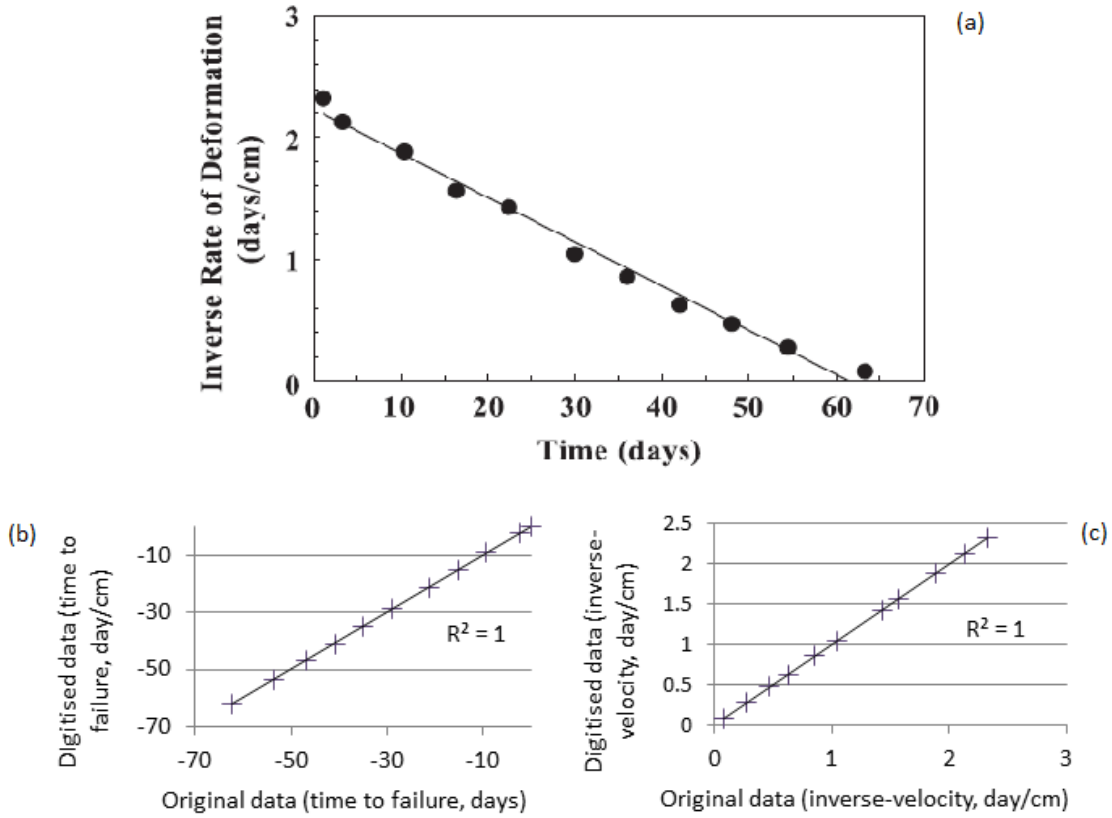

Figure 4.2: (a) Inverse rates of horizontal slope movement before the catastrophic collapse of Mt. Toc into the Vajont reservoir (reproduced from Kilburn and Petley (2003); p.27, fig. 6). (b) Correlation of *time-to-failure* data. (c) Correlation of *inverse-velocity* data.

Landslide displacement is presented in a variety of forms: (1) displacement-time, (2) cumulative displacement-time, (3) velocity-time or (4) inverse-velocity-time; and a number of units, i.e. hours, days, mm, cm etc. For this study units will be converted to days (time), mm (displacement), mm/day (velocity), mm/day2 (acceleration) and days/mm (inverse-velocity); as used by Petley et al. (2002). When data was presented in form (2) the displacement for each time step was calculated. Velocity and inverse-velocity was derived for data in the form of (1) and (2) using equation 12 (Box 4.1). For such examples velocity is associated to the mid-time between each displacement measurement. Inverse-velocity is calculated using equation 13 (Box 4.1). Where data is in form (4), velocity measurements are derived

from 1/inverse-velocity. Displacement is calculated from data in the form (3) and (4) using equation 14 (Box 4.1).

$$velocity = \frac{displacement}{time} \quad \textit{[Equation 12]}$$

$$inverse - velocity = \frac{1}{velocity} \quad \textit{[Equation 13]}$$

$$displacement = velocity \times time \quad \textit{[Equation 14]}$$

Box 4.1 Conversion equation

Nine of the thirty-one data sets were digitised from *inverse-velocity-time* graphs (form 4). It is assumed here- given the context of these specific papers- that all values presented were within the tertiary creep range. Some authors have used R^2 as an indicator of tertiary creep onset; Petley and Rosser (2009) employed a value of 0.9 to indicate a confident linear fit on data. Other examples, such as data from the Selborne slope cutting (figure 3.5 (a)), are fitted with an R^2 value of 0.806 (table 4.2(b)). It must be assumed that the *time* duration of these graphs corresponds to the full period of tertiary creep, where authors have identified the transition into self-reinforcing crack development (section 2.3.3.2) using linearity in *inverse-velocity-time* space. This assumption is verifiable for cases such as Vajont, where displacement measurements are also published, but not for examples such as Barrick Gold's Betze-Post open pit mine (southwest slope) Rose and Hungr (2007) who have only included measurements within their defined tertiary creep period.

For data digitised from *displacement-time* (forms 1 and 2) or *velocity-time* (form 3) graphs, the onset of tertiary creep is identified using an R^2 value of greater than or equal to 0.8, when points are plotted in *inverse-velocity-time*. This was chosen to reflect the minimum fit value (0.806) derived from the nine examples published in form 4 graphs (discussed briefly above). The remaining twenty-two examples were plotted on *inverse-velocity-time* graphs, fitted with a linear regression which was re-evaluated as points were removed; reducing the duration of data but increasing the R^2 value until it is above 0.8. Figure 4.3 provides a graphical example of this process.

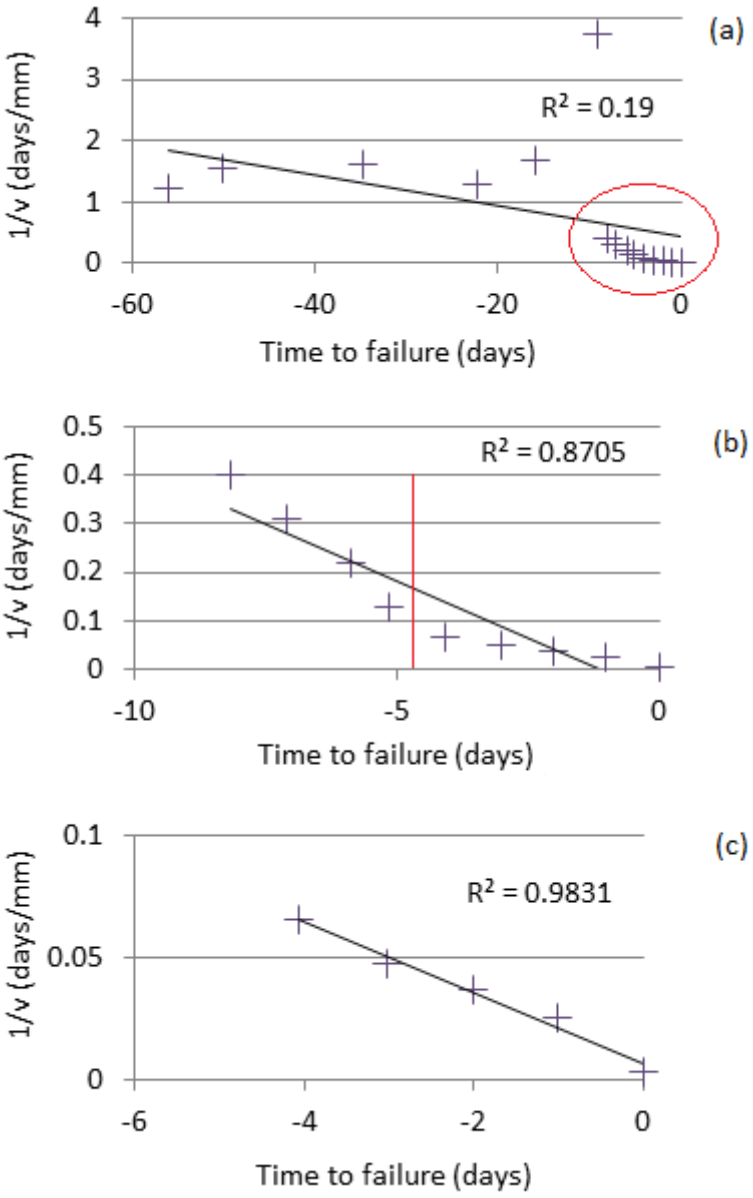

Figure 4.3: Ota Mura landslide data plotted in *inverse-velocity-time* (from Petley and Rosser (2009)) (a) Complete data set. (b) Data 10 days to failure. (c) Final creep phase

The Ota Mura example highlights one of the challenges of working with 'real-world' measurements. The final period of rapid acceleration, characteristic of tertiary creep is defined in this data by the clustering of points close to zero *time* and low *inverse-velocity* values- circled in figure 4.3 (a). Although the linear fit for the final ~10 days of data has an R^2 value greater than 0.8, closer inspection of the points indicate that the trend shifts ~4 days to failure (marked by the red line, figure 4.3 (b)). Possible physical mechanisms controlling trend shifts in creep movements are discussed in chapter 5 within the context of results from the wider database. For this study, only data following the last significant change in behaviour (figure 4.3 (c)) will be kept from examples containing gradient shifts between clear periods of linearity (as displayed in figure 4.3 (b)).

Linear trends in figure 4.3 were fitted to data without fixing the x-axis intercept (in common to published examples). Although the database provides an opportunity to evaluate the accuracy and precision of failure forecasting using the Inverse-velocity method (this will be discussed with chapter 5), results are primarily focused on gaining more insight into the variability of pre-failure creep to inform slope deformation monitoring (section 4.1). Considering this, it seems more appropriate to fit a linear trend whose intercept coincides (in *time*) with the last data point; i.e. fix the x –axis intercept at zero, recognised as the point of landslide failure. Crucially this is based on the assumption that the final measurement in published graphs, corresponds to the point of slope failure, and not the last sampling interval before failure. Given though that it is more likely to relate to the latter, based on the typical set up of slope monitoring equipment (section 3.4.3), an error margin equivalent to the sampling interval will be considered in discussions (chapter 5) when evaluating data fitted with a fixed x-axis intercept.

No unstable slope is entirely alike in terms of material composition, geological structure, geometry and physiographic setting. Differences in slope form and situation are likely controls on tertiary creep variability; however this has not yet been explored in past publications. For each example in this database, attributes including month of failure, geology of slope, vegetation condition, failure size, pre-failure slope gradient, failure trigger and whether a slope was formed natural or cut (i.e. mining) will be recorded- where possible- and considered alongside tertiary creep parameters (e.g. duration). Although a description of the landslide was included in most publications used, it did not always include all details listed above. Where possible other papers recording the same site were referred to. A lack of standard reporting of slide geometry meant it was not possible to include a full spectrum of measurements (e.g. length) in the database. The most commonly used descriptors were area and volume; volume has been chosen to represent size in this study. For slides where volume is unknown but area is given, volume is estimated using equation 15 and the scaling exponents from Larsen et al. (2010).

$$V = \alpha A^{\gamma}$$

[Equation 15, reproduced from Larsen et al. (2010)]

Here *V* represents volume, *A* represents area which depends on scaling exponent *γ* and intercept *α*. Larsen et al. (2010) recently reviewed the scaling of this model presenting values *γ= 1.1-1.3* for shallow soil slides and *γ= 1.3-1.6* for bedrock failures. To ease analysis, volume was classified by magnitude (see below) to give a broad idea of relative landslide size.

VOLUME (M^3)	LANDSLIDE SIZE
1 < x ≤ 1,000	1
1,000 < x ≤ 100,000	2
100,000 < x ≤ 1000,000	3
1,000,000 < x ≤ 10,000,000	4
10,000,000 < x ≤ 1,000,000,000	5

Table 4.2: Landslide size classification

Detailed geology is summarised under the categories soft rock, hard rock or clay (soil) using typical mean uniaxial compressive strength (UCS) values for the predominant slope material (Look, 2007). Hard rocks are those with a UCS value over 100 MPa (Singh and Goel, 1999). This is a very basic method of classifying slope geology and material strength, and does not account for slope heterogeneity, structural features or accumulated damage (i.e. under physiographic mechanisms, section 2.3.3.4). However, publications typically contained only minimal descriptions of slope pre-failure condition and this simplistic classification provides a clear method of broadly differentiating slopes by geology with limited information. Glastonbury and Fell (2000) and Glastonbury and Fell (2002) were able to more fully investigate material properties of the slope failures contained in their databases, by visiting each site and testing samples in the laboratory. Unfortunately this was not possible here, and is unlikely to be an option for most researchers drawing on vast amounts of secondary data derived from different global locations.

The slope attributes and tertiary creep parameters are listed for each example in tables 4.3(a) and 4.3(b). Methods of monitoring and total monitoring period are also included where disclosed in the original publication.

4.3. Results

This section presents data from thirty-one examples of tertiary creep, digitised from published pre-failure slope deformation data (see section 4.2). The database is summarised in tables 4.3(a) and 4.3(b). This includes slope characteristics (e.g. pre-failure gradient), factors preparing collapse (e.g. causes), failure timing (e.g. month), tertiary creep parameters (e.g. duration), and monitoring methods. Clear from these tables is the diversity of failures contained within the database. The distribution of examples under different slope characteristics is presented in section 4.3.1 and discussed in chapter 5. This initial overview focuses on common pre-condition, preparatory and triggering factors that have led to instability and collapse of slopes in the database.

Pre-failure tertiary creep variations are presented in section 4.3.2. Each movement parameter is addressed beginning with *cumulative displacement-time* curves, leading to *velocity-time* curves and finally the *inverse-velocity-time* projection of data. Results are considered alongside slope and failure characteristics, with the aim of relating these to variations in tertiary creep. The accuracy and precision of the Inverse-velocity method is considered by fitting linear trends to data, from different time periods before failure (section 4.3.3). Results are discussed in chapter 5 under the following framework:

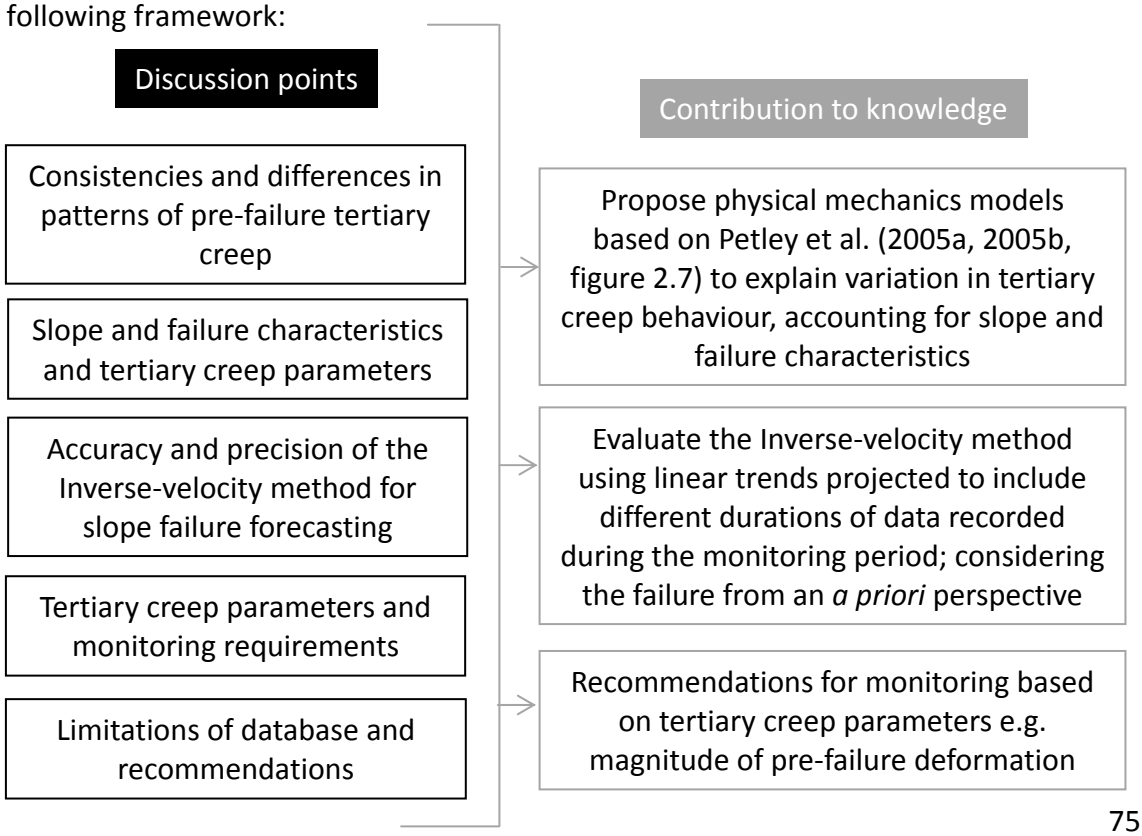

		BACKGROUND				GEOLOGY				GEOMETRY		
ID	**NAME**	**Reference**	**Location**	**Failure Month**	**Failure Year**	**General Geology (material)**	**Material Strength**	**Mechanism Comments**	**Vegetated**	**Volume (m^3)**	**Size Rating**	**Average Pre-failure Slope Gradient (deg)**
1	Selbourne slope cutting	(Petley et al., 2002)	England	7	1989	Soil	Clay	Roto-translational	No	18413	2	49
2	Liberty Pit mine	(Rose and Hungr, 2007)	USA	.	.	Rock	Hard	.	No	7000000	4	33
3	Barrick Gold's Betze-Post open mine	(Rose and Hungr, 2007)	USA	8	2001	Rock	Hard	Compound	No	18000000	5	27
4	Un-named slope	(Rose and Hungr, 2007)	USA	.	.	Rock	Soft	Toppling	No	1000000	4	45
5	Barrick Gold's Betze-Post open pit mine (southwest)	(Rose and Hungr, 2007)	USA	6	2005	Rock	Hard	.	No	2000000	4	38
6	Vajont landslide	(Belloni and Stefani, 1987; Kilburn and Petley, 2003)	Italy	10	1963	Rock	Hard	Roto-translational	Yes	270000000	5	25
7	New Tredegar	(Carey et al., 2007)	Wales	4	1930	Rock	Soft	Roto-translational	No	1935574	4	.
8	Ota Mura	(Petley and Rosser, 2006)	Japan	8	2004	Rock	Soft	Translational	Yes	65000	2	35
9	Lijiaxia landslide	(Bai et al., 2008)	China	10	1998	Rock	Soft	Translational	Yes	1530000	4	26
10	Xintan landslide	(Keqiang and Sijing, 2006)	China	6	1985	Rock	Soft	Translational	Yes	30000000	5	23
11	Bomba landslide	(Picarelli et al., 2005b)	Italy	.	.	Soil	Clay	.	No	.	.	.
12	Roesgrenda slide A	(Okamoto et al., 2004)	Norway	3	2000	Soil	Clay	Roto-translational	Yes	2000	2	40
13	Saleshan landslide	(Siqing and Sijing, 2000)	China	3	1986	Rock	Soft	Roto-translational	No	200000	3	20
14	Eskihisar coal mine wall	(Ulusay and Aksoy, 1994)	Turkey	9	1989	Rock	Soft	Roto-translation	No	45017	2	60
15	Randa rockslide	(Bonnard et al., 1995)	Switzerland	5	1991	Rock	Soft	Translational	Yes	7000000	4	50
16	Asamushi landslide	(Saito, 1969)	Japan	7	1966	Rock	Soft	.	Yes	100000	3	.
17	Un-named rockmass	(Mufundirwa et al., 2010)	Japan	.	.	Rock	Soft	.	No	500	1	.
18	Excavation A	Unpublished reports [1]	Australia	6	1950	Rock	Soft	Translational	No	150000	3	35

19	Teifer Mine	(Thompson and Cierlitza, 1993)[1]	Australia	10	1992	Rock	Soft	Translational	No	86000	2	50
20	Tuckabianna West	(Thompson, 1993)[1]	Australia	.	.	Rock	Soft	Translational	No	125000	3	32
21	Chuquicamata Mine- East Wall	(Kennedy and Niermeye, 1970)[1]	Chile	.	.	Rock	Soft	Compound	No	600000	3	45
22	Smoky River Mine	(Martin, 1993)[1]	Canada	.	.	Rock	Soft	Compound	No	314000	3	65
23	Delabole Quarry	(Boyd et al., 1973)[1]	England	.	.	Rock	Soft	Toppling	No	50000	2	67.5
24	Afton Mine	(Reid and Stewart, 1986)[1]	Canada	6	1986	Rock	Hard	Toppling	No	2800000	4	40
25	Hogarth Pit	(Brawner and Stacey, 1979)[1]	Canada	6	1975	Rock	Hard	Toppling	No	200000	3	44
26	Luscar Mine-50A2 Pit	(Wylie and Munn, 1978)[1]	Canada	.	.	Rock	Soft	Toppling	No	5600000	2	30
27	Roberts Pit	(Coates et al., 1979)[1]	Canada	9	.	Rock	Soft	Rotation	No	1200000	4	45
28	Nevis Bluff	(Brown et al., 1980)[2]	New Zealand	6	1975	Rock	Soft	Rotation	No	32000	2	66
29	Ryan and Call slide 2	(Ryan and Call, 1992)[1]	Mexico	7	.	Rock	.	Translational	No	.		75
30	Kennecott#1	(Zavodni and Broadbent, 1980)[1]	USA	.	.	Rock	.	Translational	No	4800000	4	33
31	Labe Canyon	(Zvelebil and Moser, 2001)	Germany	1	1984	Rock	Soft	Toppling	Yes	1360	2	85

Table 4.3 (a): Tertiary creep database: slope history and deformation behaviour. When information is unavailable cell is marked with a dot (.)

[1] in *Glastonbury and Fell (2002)*

[2] in *Glastonbury and Fell (2000)*

		SLOPE HISTORY			DEFOMORATION BEHAVIOUR						
ID	NAME	Natural or man-made slope	Cause	Trigger	Type of Monitoring	Monitoring Duration (days)	Tertiary Phase				
							Total Displacement (mm)	Duration (days)	Maximum Rate (mm/day)	R^2	$\frac{1}{v}$ gradient
1	Selbourne slope cutting	Man-made	Groundwater	Groundwater	Inclinometer	400	32	150.36	2.19	0.806	-0.1063
2	Liberty Pit mine	Man-made	Slope redesign	Blasting	.	.	1502	101.85	155.67	0.857	-0.0064
3	Barrick Gold's Betze-Post open mine	Man-made	Slope redesign, rainfall, groundwater	Groundwater	Inclinometer	1100	2895	43.54	295	0.990	-0.0011
4	Un-named slope	Man-made	Slope structure, slope redesign, groundwater	Groundwater	Extensometer	10	3080	8.23	1021.98	0.918	-0.0008
5	Barrick Gold's Betze-Post open pit mine (southwest)	Man-made	Groundwater, slope structure	Loading (other slide)	Surface survey	5	527	4.5	488.33	0.903	-0.0046
6	Vajont landslide	Natural	Groundwater, reservoir, rainfall	Groundwater	Surface monument	1185	1372	63.35	130.67	0.986	-0.0035
7	New Tredegar landslide	Man-made	Groundwater, slope redesign, blasting	Groundwater	Peg network	70	376	15.49	81.75	0.941	-0.0082
8	Ota Mura	Natural	Groundwater, rainfall	Rainfall	Extensometer	222	259	7.99	81.75	0.816	-0.0383
9	Lijiaxia landslide	Man-made	Groundwater, slope redesign, reservoir	Groundwater	Surface monument	113	92	14.25	7.38	0.810	-0.0383
10	Xintan landslide	Man-made	Groundwater, loading	Rainfall	Survey lines	3085	32146	357.91	858.72	0.889	-0.0007
11	Bomba landslide	Man-made	.	.	.	.	51195	8.43	99670.06	0.807	-0.0001
12	Roesgrenda slide A	Natural	Groundwater	Groundwater	Extensometer	852	1429	0.29	31.23	0.81	-1.7635
13	Saleshan landslide	Natural	Groundwater	Rainfall, groundwater	.	662	1358	144.5	16269.55	0.937	$-3.00\ e^{-06}$
14	Eskihisar coal mine wall	Man-made	Groundwater, slope redesign, slope structure	Groundwater	Tension crack meters	10	33133	433.8	429.36	0.935	-0.0002
15	Randa rockslide	Natural	Earthquake, snowmelt, temperature	Loading (other slide)	Surface survey	21	7966	10	9642.86	0.808	-0.0005

			fluctuations								
16	Asamushi landslide	Natural	.	.	.	7	1562	1.36	7922.41	0.804	-0.0041
17	Un-named rockmass	Man-made	Rainfall, excavation, slope structure	Structural complexity	Extensometer	185	50	0.016	13882.58	0.912	-0.1156
18	Excavation A	Man-made	Pipe ruptures, excavation, rainfall	Rainfall	Surface survey	21	721	13.63	104.08	0.8079	-0.0402
19	Teifer Mine	Man-made	Excavation	Excavation	Surface survey	250	10233	144.65	657.21	0.8054	-0.0129
20	Tuckabianna West	Man-made	Excavation	Excavation	Surface survey	38	167	46.21	256.59	0.8835	-0.2535
21	Chuquicamata Mine- East Wall	Man-made	Earthquake, excavation, blasting	Excavation	Surface survey	145	51393	109.75	3885.24	0.8314	-0.0006
22	Smoky River Mine	Man-made	Snowmelt, mining	Mining	Surface survey	270	2742	84.68	128.08	0.8245	-0.0147
23	Delabole Quarry	Man-made	Excavation	Excavation	Tension crack meters	7700	8276	3171.45	3.99	0.8104	-0.0165
24	Afton Mine	Man-made	Excavation, blasting	Excavation	Surface survey	62	47877	9.82	134164.56	0.8294	-0.0018
25	Hogarth Pit	Man-made	Excavation, blasting, rainfall, snowmelt	Rainfall	Extensometer	290	82297	243.28	7098.55	0.8447	-0.0019
26	Luscar Mine-50A2 Pit	Man-made	Excavation, high seasonal piezometric pressures	Mining, Loading (other slide)	Extensometer	375	97825	338.71	897.62	0.897	-0.0014
27	Roberts Pit	Man-made	Excavation	rainfall	Surface survey	147	63	126.17	8.03	0.8157	-1.0405
28	Nevis Bluff	Natural	Road construction, freeze-thaw cycles, rainfall	excavation	Surface survey	300	5890	26.76	2619.88	0.8149	-0.0379
29	Ryan and Call slide 2	Man-made	.	.	Surface survey	80	12353	65.14	2617.08	0.8064	-0.0195
30	Kennecott#1	Man-made	.	.	Tension crack meters	696	4591	24.97	1999.8	0.815	-0.0193
31	Labe Canyon	Natural	Road construction	.	Rod dilometer	758	1150	102.03	109.675	0.8137	-0.1599

Table 4.3 (b): Tertiary creep database: slope history and deformation behaviour. When information is unavailable cell is marked with a dot (.)

[1] in *Glastonbury and Fell (2002)* .[2] in *Glastonbury and Fell (2000)*

4.3.1. Slope characteristics

This section overviews the distribution of examples under the context of specific slope characteristics, e.g. pre-failure slope gradient, to provide a sense of data provenance. Understanding preferential settings for brittle shear plane deformation (i.e. features common to slopes in this database), or turning this on its head and using slope characteristics to indicate when tertiary creep has been successfully captured in the past, gives useful insight into the type of slope on which to focus future monitoring.

The majority of slopes in the database were man-made (figure 4.4), rather than natural. Such slopes were cut during mining, quarrying or construction work. The average pre-failure gradient of man-made examples, ~40 degrees, was similar to natural sites, ~42 degrees. All landslides (for which pre-failure gradient was known) occurred on slopes greater than 20 degrees (figure 4.5); nearly half the examples (~44%) occurred on slopes greater than 45 degrees. It is noted that for 4 cases, the pre-failure slope gradient was unknown.

Over 85% of landslides in the database occurred on rock slopes (figure 4.6 (inset)). Of these 65% were classified as soft rock, 19%, hard rock and 6% unclassified (due to lack of information in the publication) (figure 4.6). Failures occurring on soil slopes were all composed of clay dominated material; only one of the four slopes was natural. All hard rock slopes were natural; however the majority (three out of every four) soft rock slopes were man-made. None of the hard rock failures originated from slopes with gradients over 44 degrees (figure 4.7). Landslides derived from soft rock slopes showed the greatest distribution of slope gradients (ranging from 20 to 85 degrees), whilst all failures occurring in clay (soil) came from steep slopes of 40 degrees or above (figure 4.7). Six examples were not included in this comparison due to the absence of either material strength or pre-failure gradient information.

Factors preparing slopes for failure (figure 4.9) and triggering collapse (figure 4.8) were derived from descriptions of landslide development in publications and broadly put into categories such as “groundwater” with reference to table 2.1 and 2.2. It is noted that two landslides had several triggers and eighteen examples developed under multiple preparatory factors, highlighting the complexity of

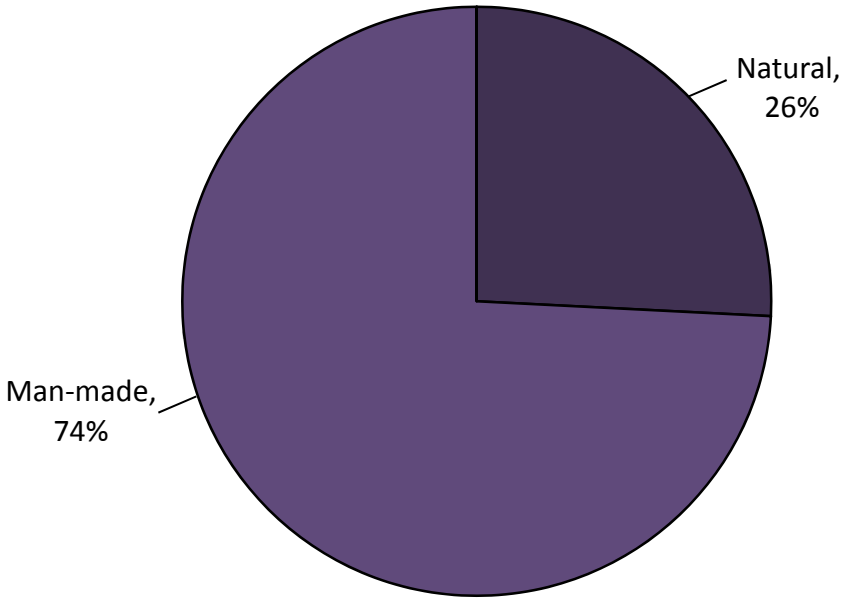

Figure 4.4: Slope type (man-made or natural)

Figure 4.5: Distribution of pre-failure slope gradients

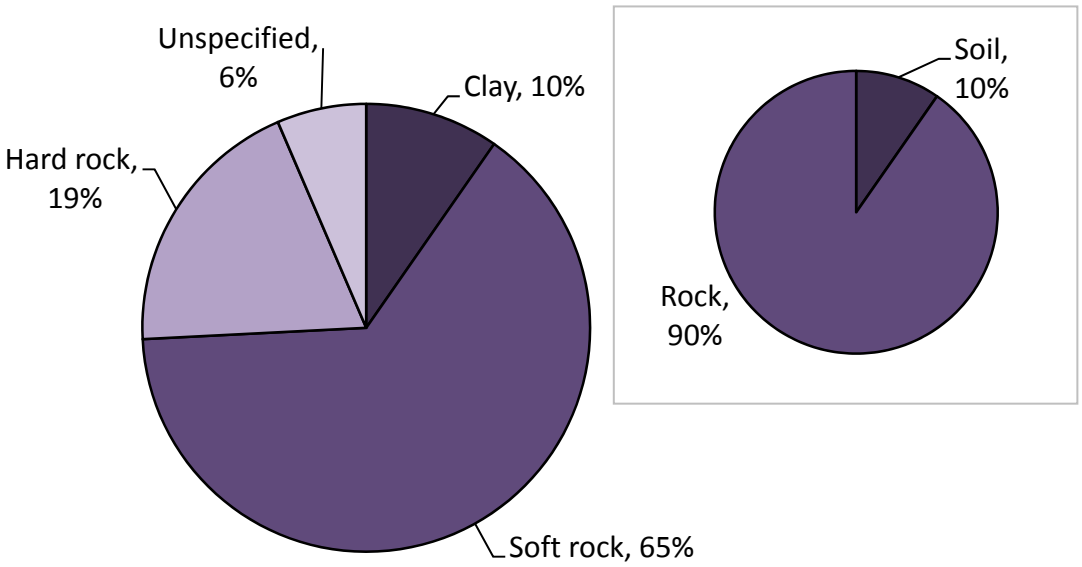

Figure 4.6: Slope material strength. [Inset] General hillslope geology

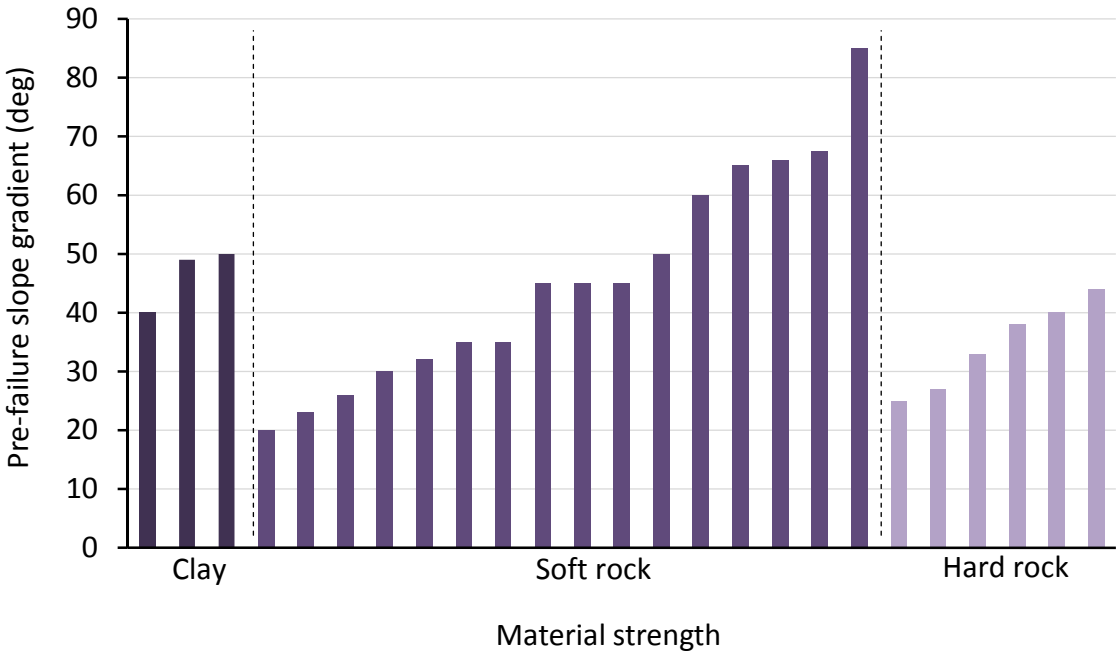

Figure 4.7: Distribution of pre-failure slope gradient sub-divided by material strength

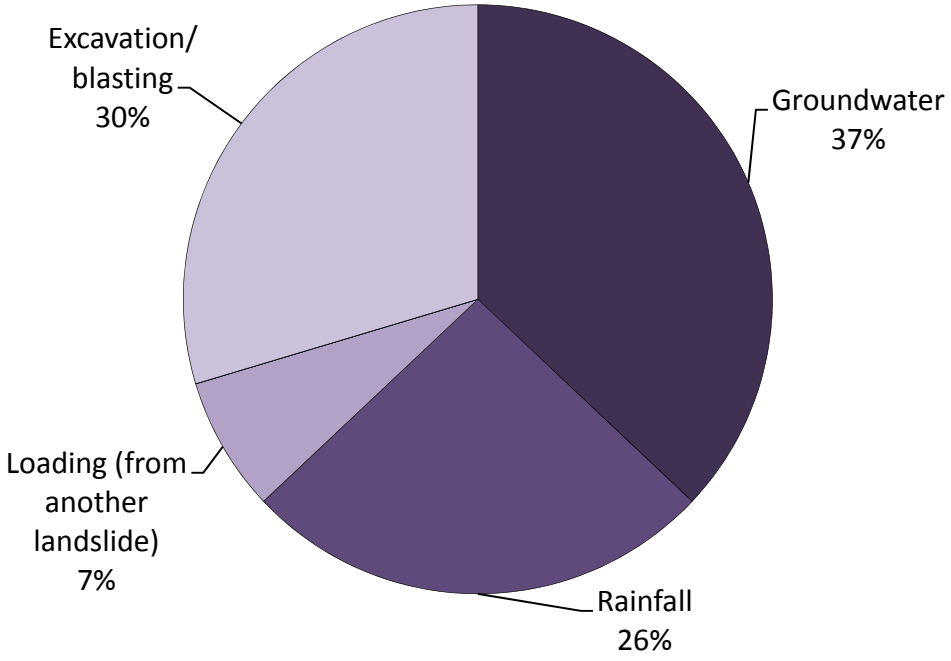

Figure 4.8: Factors triggering slope collapse

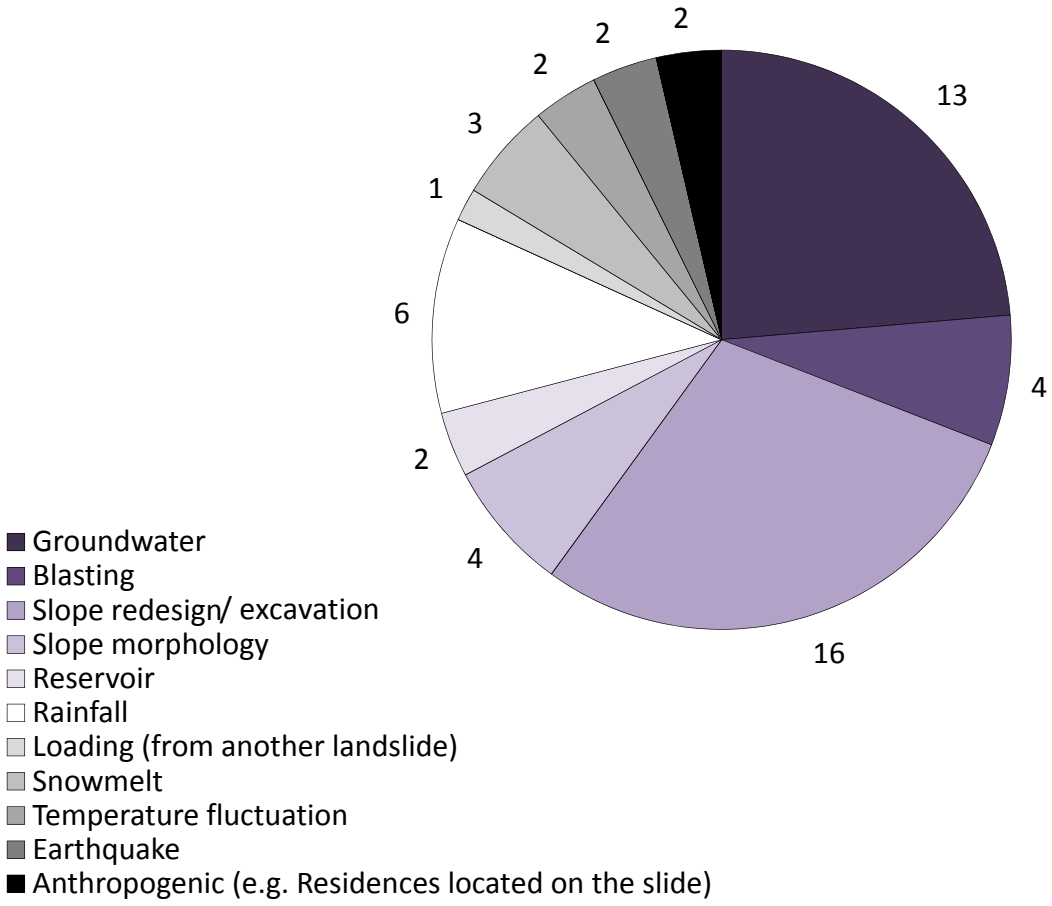

Figure 4.9: Preparatory factors to slope failure. Pie chart labels represent number of slopes within each category

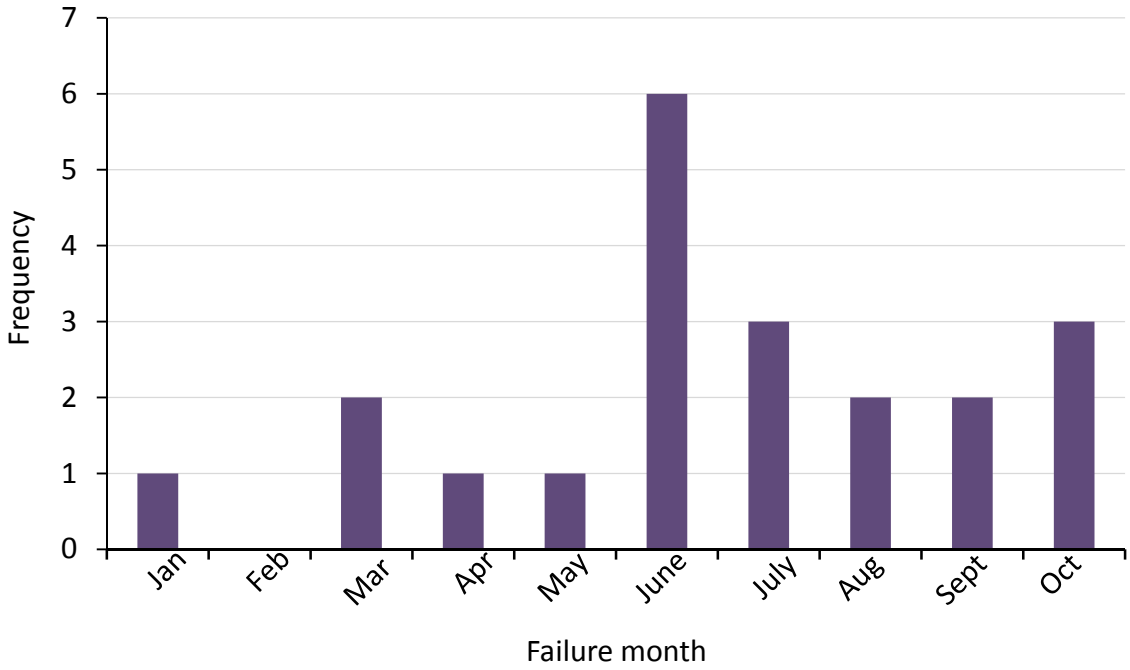

Figure 4.10: Month during which slopes collapsed

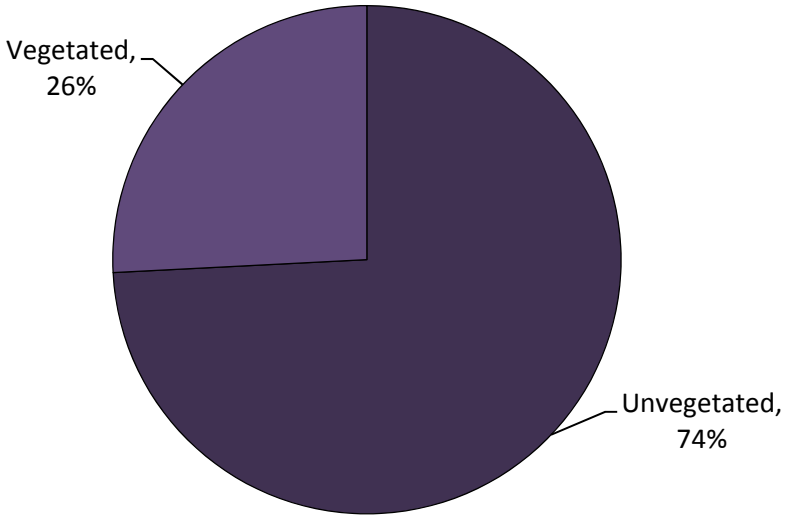

Figure 4.11: Slope vegetation

physiographic processes acting to damage and destabilise slopes, just within the twenty-seven examples presented here (no information was available for 4 of the failures).

Figure 4.8 shows that 63% of landslides were triggered by some sort of water action. No failures in this database were triggered by an earthquake. Only 30% of examples were triggered by excavation or blasting, even though 74% of slopes were man-made (figure 4.4). Saleshan landslide (id 13) was triggered by both groundwater and rainfall, whilst at Luscar Mine- 50A2 pit (id 26) the slope collapsed from mining activity and loading (from another slide or block of material) (table 4.1 (b)).

Two-thirds of the landslides developed under multiple preparatory factors. It is noted that this information was not available for four of the examples. Sixteen slopes were affected by slope redesign/ excavation, whilst twenty-four slopes were affected by some form of water *stress* (i.e. groundwater, rainfall, reservoir levels or snowmelt) (figure 4.9). Twenty-two of the examples were affected by anthropogenic activity (i.e. blasting, slope redesign, reservoir, anthropogenic), which correlates closely to the number of man-made slopes (totalling twenty-three). The Selborne slope cutting (id 1) is the only man-made slope not destabilised by anthropogenic activity; this experimental slope was brought to failure by controlled pore-pressure recharge (Cooper et al., 1998). Interestingly, two slopes survived earthquakes, but final failure was reported to be triggered by loading from another landslide (Randa rockslide, id 15) and excavation (Chuquicamata Mine- East Wall, id 21). Only 25% of landslides triggered by groundwater, involved preparatory rainfall, although all failures triggered in this way recognised the role of groundwater in destabilising the slope over long timescales. Reservoirs were the main cause of 25% of failures triggered by fluctuating groundwater levels. The failure involving snow melt was triggered by loading from another slide, rather than groundwater. 50% of rainfall triggered landslides involved groundwater, the other 50% developed under antecedent rainfall; note that Ota Mura (id 8) involved a combination of both preparatory factors.

Most slopes collapsed in June (figure 4.10), broadly though the majority of failures occurred between June and September inclusive (thirteen of the twenty-one examples for which failure month is known). Rainfall was the most common trigger for

failures occurring in June; 50% were triggered in this way. Ten of the eleven failures occurring between June and September (where preparatory and/or triggering factors were known) developed under the influence of some form of water action. The other slope (Teifer Mine, id 19) failed under of excavation and blasting. Surprisingly, the examples whose failure month was unknown (but causal and trigger factors are described) involved slope excavations; sites which are usually heavily monitored and documented due to health and safety.

As expected given the number of man-made sites, 74% of landslides originated from un-vegetated slopes (figure 4.11); all failures triggered by excavation occurred from un-vegetated hillslopes. Two man-made slopes were vegetated before failure (Lijiaxia landslide, id 9 and Xintan landslide, id 10); both failed under groundwater stress. Only one hard rock slope was vegetated (Vajont landslide, id 6); the majority of soft rock slopes were un-vegetated (fourteen of twenty).

This section has summarised common slope characteristics within the database and how they interrelate. Results are discussed in chapter 5.

4.3.2. Tertiary creep variations

Thirty-one examples of pre-failure tertiary creep were collated in the database (table 4.3). Patterns of slope deformation are compared in the following section. Data is presented in three formats: (1) cumulative displacement-time (figures 4.12 to 4.28), (2) velocity-time (figures 4.29 to 4.38) and (3) inverse-velocity-time (figures 4.39 to 4.42). Projecting the different derivatives of the measured movement provides a broad set of results on which to assess variations in pre-failure slope behaviour. Visualised on composite graphs (all landslide examples; figures 4.12(a), 4.29(a) and 4.39), the numerical range of key creep parameters such as duration, total displacement and maximum velocity define the design and requirements of instrumentation used to monitor unstable slopes. Although data from individual sites is referred to when illustrating the minimum and maximum bounds of creep parameters (figures 4.13, 4.14, 4.17, 4.18, 4.30, 4.31), results focus on characterising general patterns of deformation, relating these to slope composition and setting (introduced in section 4.3.1).

Figure 4.12(a) presents the cumulative displacement of each slope through time. Immediately it is clear that that the process of tertiary creep is operating over very different time scales; the inset (figure 4.12(a)) depicts the cluster of examples that lie close to zero time. The unstable slope at Delabole quarry (id=23; figure 4.13) has crept over a duration of 3,171.45 days whilst the rockmass discussed in Mufundirwa et al., (2010) (id=17; figure 4.14) deformed over only ~37 minutes (0.026 days). Figure 4.15 presents the distribution of tertiary creep duration across all thirty-one examples. Results are plotted on a kernel density graph, which accurately smoothes the distribution of data using kernel density estimation- in this case derived from the Epanechnikov kernel. Most landslides occurred within 500 days of tertiary creep; mean duration equates to 156.88 days and data is distributed with a large standard deviation of 566.92 days. Although the data is positively skewed, the duration of deformation at Delabole quarry (id=23; figure 4.13) gives the distribution a long tail; 97% of data is contained within the first ~14% of the maximum creep period in the database. Removing this example, the mean tertiary creep duration falls to 56.39 days, with a standard deviation of 93.09 days. The inset graph (figure 4.15) presents creep duration on a log scale for each slope failure. Most failures occurred after 1 to 100 days- 2 orders of magnitude- of tertiary deformation (20 failures).

The magnitude of creep leading to slope collapse ranges from 32 mm (id=1; figure 4.18) to 95.21m (id=26; figure 4.17). Figure 4.16 presents a kernel density graph for total displacements recorded within the database. Similarly to the duration data, results show a positive skew towards smaller displacement values; ~52% of failures occurred after less than 15m of deformation. The mean total displacement is 12.64m, around which a standard deviation of 22.63m describes the spread of data. The inset on figure 4.16 shows that only 8 slopes deformed more than 10m before failure. Considering just those examples which failed within three magnitudes of displacement (23 in total), the mean and standard deviation reduce to 2.4m and 2.9m respectively.

Comparing the patterns of displacement accumulation is difficult given the large ranges of creep duration and total displacement exhibited within the database. Normalising data (rescaling the duration and total displacement of each example to start at 0 and end at ±1) provides a projection from which to analyse the shape of the cumulative displacement-time plots (figure 4.12(b)). It is clear that unstable slopes

deform differently in the tertiary creep phase. Some of the examples show exponential increases in slope displacement (e.g. Luscar Mine 50A2 pit; id=26), whilst others accumulate displacement more steadily (near linear form) (e.g. Ryan and Call slide 2; id=29). The hypsometric integral- ratio of area beneath the curve to total graph area- was calculated for each example to better characterise patterns of slope displacement through time. Results are presented on a kernel density graph (figure 4.19), showing the range (0.131 to 0.56) and distribution of calculated values. A value under 0.425 indicates a concave cumulative displacement-time plot, where 0 is maximum concavity (Allison and Higgitt, 1998). Hypsometric integrals greater than 0.575 are used to describe convex curves; 1 is the maximum convexity. Although the value 0.5 represents a linear accumulation of displacement through time, the definition is buffered within the range 0.425 to 0.575 (Allison and Higgit, 1998); examples with this hypsometric integral are considered concavo-convex.

The majority of examples (~71%) have concave cumulative displacement-time graphs (figure 4.19). This is reflected by the mean hypsometric integral value of 0.347, and standard deviation, 0.127. Concavity suggests that the rate of displacement is increasing with time. This behaviour is depicted in all four individual cumulative displacement-time graphs (figures 4.13, 4.14, 4.17, 4.18); Luscar Mine 50A2 pit (id=26) is the most convex example with a hypsometric integral of 0.131, whilst Delabole Quarry (id= 23) tends more to concavo-convex form with an integral value of 0.319. Although data is skewed towards smaller hypsometric integral values, the low kurtosis measure of 0.049 does not indicate a strong leptokurtic distribution. The remaining nine examples are spread evenly across the concavo-convex range, with a slight peak around 0.514 (figure 4.19). Given that tertiary creep by definition is a period of accelerating displacement (section 2.3.3.2) the proportion of examples showing signs of steady-rate deformation is perhaps surprising and will be discussed further in chapter 5.

Correlation between total displacement and tertiary creep duration is very weak (figure 4.20). The fit is not described well by linear (R^2= 0.002) or logarithmic (R^2= 0.009) regressions. Although analysis of the complete database shows little correlation between these attributes, linear regressions carried out on a sub-set of examples, defined by specific slope characteristics, have produced greater r-squared estimates

(table 1, appendix). Where the mode of failure is known (26 examples; figure 4.21), the coefficient of determination between total displacement and duration ranges from 0.647 (translational) to 0.835 (roto-translational) for slopes involving rotational or translational movements (19 examples). This suggests that longer creep periods result in greater amounts of displacement before slope failure. There was no significant correlation between total displacement and duration, within the toppling failure subset.

The triggering conditions of twenty-one of the thirty-one failures are known (section 4.3.1). 58% of these examples were triggered by either rainfall or groundwater, and show a strong correlation between total displacement and tertiary creep duration; rainfall correlates with an r-squared value of 0.929 and groundwater, 0.859 (table 1, appendix). The amount of displacement leading to the collapse of slopes by water *stress* is highly likely to relate to the duration of creep. All failures triggered by groundwater or rainfall involved one or both of these factors during the pre-failure destabilisation period (section 4.3.1). This implies that slope's previously deforming in response to fluctuating groundwater or rainfall conditions during the primary and secondary stages of pre-failure creep (section 2.3.3.2), may display different patterns of tertiary phase displacement in comparison to those sites with no past history of deformation induced by water *stress*.

High coefficients of determination are derived from the linear regression of total displacement- duration for larger failures in the database (table 1, appendix). The distribution of landslide volumes- across the twenty-nine examples where information is known- is positively skewed with a long tail resulting from the exceptionally large Vajont landslide (figure 4.22), during which 270Mm^3 of material was mobilised. 90% of the landslide volumes included in the kernel density estimation were under 10Mm^3. The mean failure volume including all examples, 12,042,113m^3 is an order of magnitude larger than that calculated excluding all failures above 10Mm^3 (1,200,819m^3). The standard deviation also reflects the distortion particularly large landslide volumes have on resultant descriptive statistics describing the general distribution of data; 50,021,575m^3 for all twenty-nine examples, compared to 2,042,490m^3 for those below 1Mm^3.

To ease analysis of such a broad range of volumes, landslide size was classified by magnitude (table 4.2). The inset of figure 4.22 highlights the distribution of data across these classes, showing bi-modal groups, size 2 ($1.0e^3 \leq x < 1.0e^5$ m^3) and size 4 ($1.0e^6 \leq x < 1.0e^7$ m^3), containing 62% of all known examples. The correlation between total displacement and tertiary creep duration for landslides classified in size 2 is weak (R^2= 0.014), however those in size 4 show a stronger attribute relationship (R^2=0.715). Those landslides greater than 10Mm^3 produced an r-squared value of 0.848, although it is noted that only three data points were involved in the regression. Overlooking this, the strength of linear correlation between total displacement- duration appears to depreciate with landslide size (table 1, appendix), suggesting that the volume of unstable material is dominant in controlling the rate of pre-failure slope displacement. This is unsurprising, given that landslides of greater mass involve larger driving forces (figure 2.1) acting to destabilise material downslope.

The linear and log regressions of total displacement- volume (figure 4.23) and duration-volume (figure 4.24) derived coefficients of determination, ranging from 0.002 to 0.0174. Independently the parameters total displacement and duration do not correlate with landslide volume. Given that the smaller landslides (size 2) presented a very low r-squared (0.014) from the regression of total displacement-duration, but larger landslides (size 4 and 5) showed improved correlation values of 0.715 and 0.845 respectively (as discussed above), it is interesting to isolate the larger volumes from the correlations presented in figure 4.23 and 4.24. The linear regression of total displacement- volume>1,000,000m^3 and duration-volume>1,000,000m^3, however did not show significant improvements on the coefficient of determination: 0.0106 and 0.1164, respectively. This suggests that for larger landslides the duration of tertiary creep is likely to indicate the amount of relative total displacement, i.e. longer time periods leading to greater amounts of deformation. It does not however suggest that larger landslides will generate greater amounts displacement over a given duration than smaller failures.

The magnitude of shear *stress* (figure 2.2) is derived not only from the mass of unstable material, but also the angle of slope. All failures- for which gradient information is known (27 examples) - in the database occurred on slopes greater than 20 degrees (figure 4.5). Considering the linear regression of total displacement-

duration sub-set by slope angle (table 1, appendix) highlights that for all failures except those occurring on 30 ≤ x < 40 degrees the coefficient of determination is weak, ranging from 0.006 to 0.121. The seven landslides derived from slopes between 30 ≤ x < 40 degrees showed good correlation between total displacement and tertiary creep duration; r-squared value of 0.829. Figures 4.25 and 4.26 isolate each tertiary creep parameter (duration and total displacement), regressing these against pre-failure slope angle. Table 4.4 includes the complete and stepped- where gradient is grouped into 10 degree intervals- r-squared values derived from total displacement-pre-failure slope gradient and duration-pre-failure slope gradient regressions.

	all	Pre-failure slope gradient (degrees)			
		20 ≤ x < 30	30 ≤ x < 40	40 ≤ x < 50	60 ≤ x < 70
Number of landslides	27	5	7	7	4
Total displacement-slope gradient	0.0089	0.0505	0.418	0.0534	0.7721
Duration-slope gradient	0.0758	0.8664	0.561	0.3308	0.2311

Table 4.4: R-squared values for the linear regressions of total displacement-slope gradient and duration-slope gradient. 50 ≤ x < 60, 70 ≤ x < 80, 80 ≤ x < 90 (degrees) were omitted from this table because the groups contained 2 or less failures.

The results from the regressions displayed in table 4.4 show the opposite pattern to those generated for the equivalent analysis sub-setting examples by volume. Here data has shown a weak coefficient of determination for the linear correlation of total displacement-duration, total displacement-slope gradient and duration-slope gradient. However sub-sets of the latter two regressions present better fits; specifically total displacement- slope gradient for those failures derived from 60 ≤ x < 70 degree (0.7721) and duration- slope gradient for those failures derived from 20 ≤ x < 30 degree (0.8664). Given the isolated and unrelated nature of these stronger r-squared values it is difficult to draw conclusions from them.

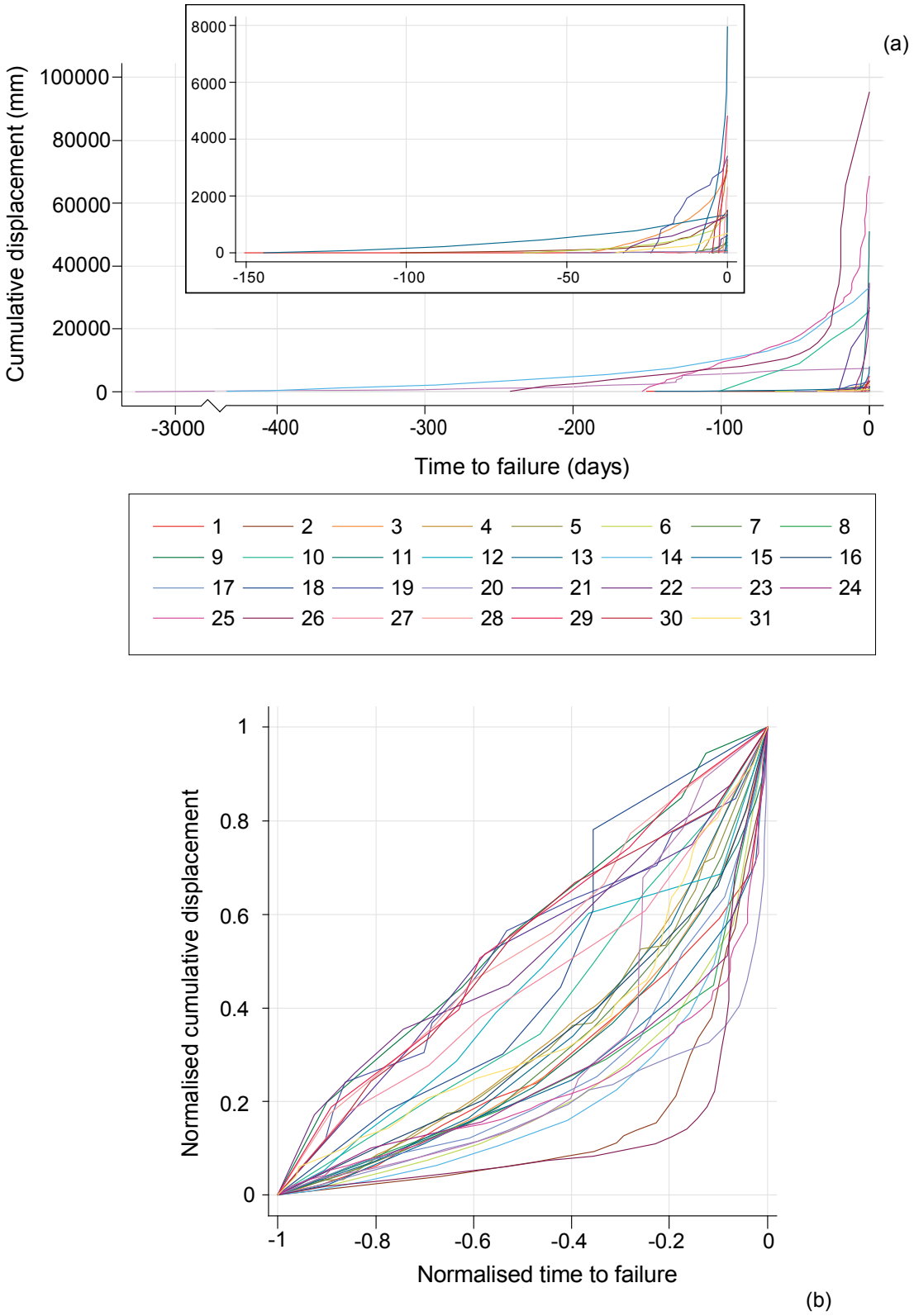

Figure 4.12: (a) Cumulative displacement- time data from the tertiary stage of creep. [Inset] Cumulative displacement-time data for failures whose total displacement is less than 10,000 mm; also excluding landslide ID 23. (b) Normalised cumulative displacement- normalised time data from the tertiary stage of creep

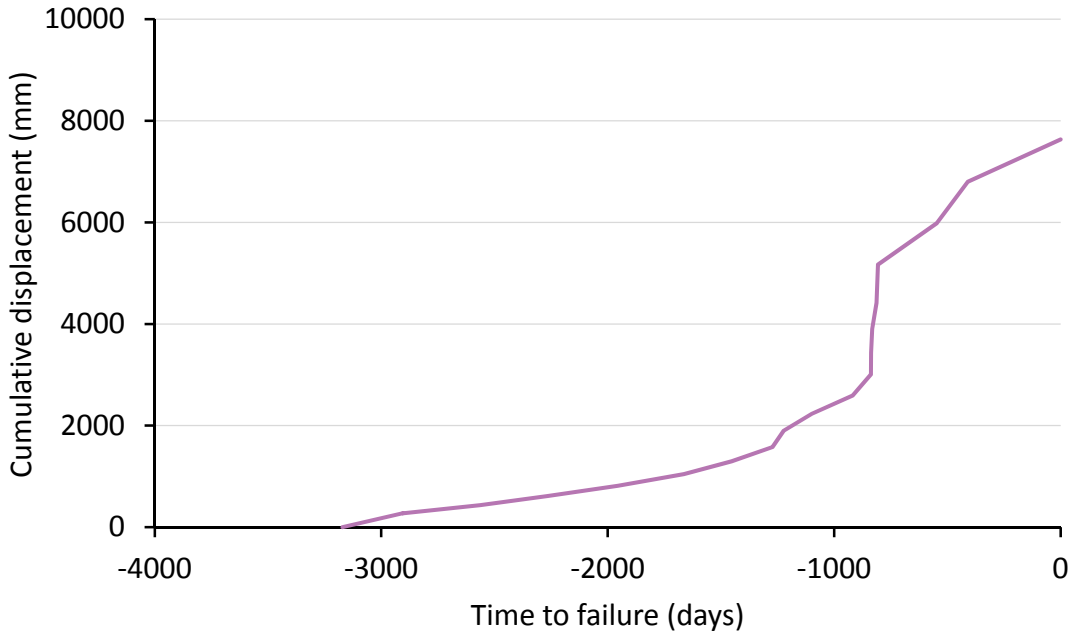

Figure 4.13: ID= 23 Cumulative displacement-time data from the tertiary stage of creep

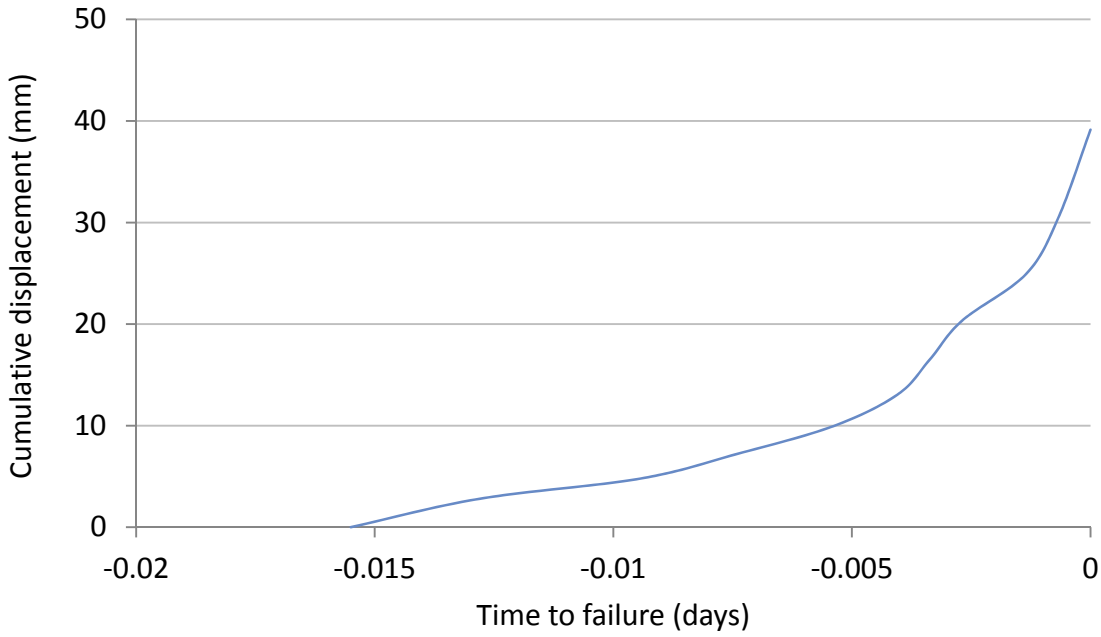

Figure 4.14: ID= 17 Cumulative displacement-time data from the tertiary stage of creep

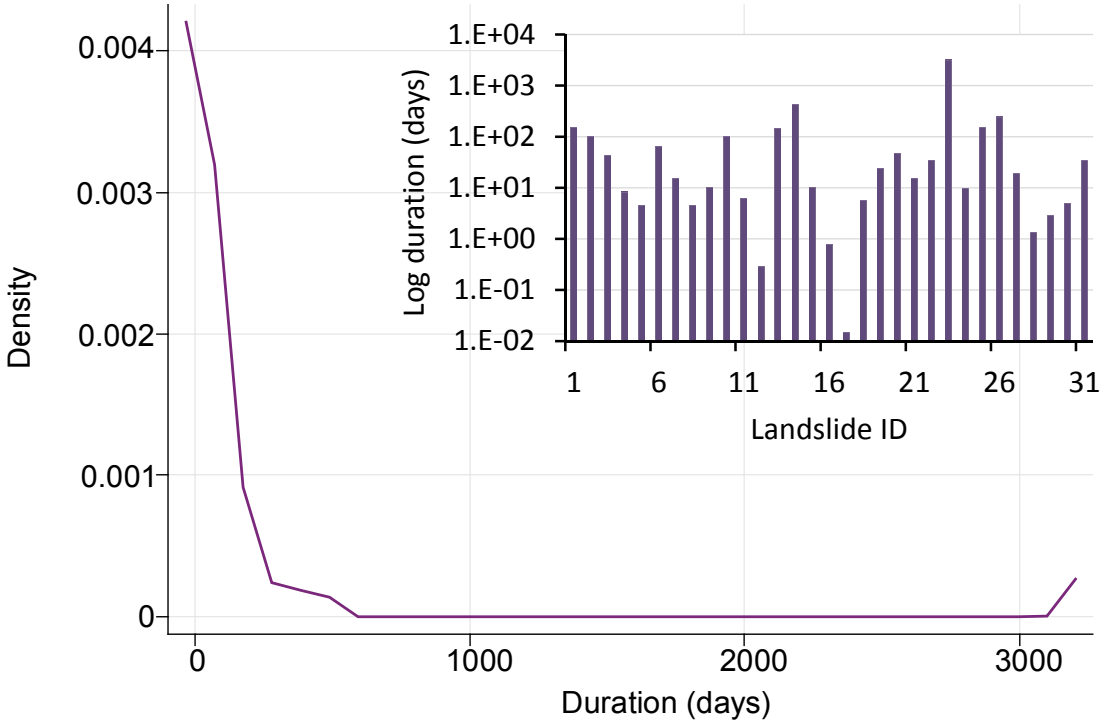

Figure 4.15: Kernel density estimate of duration. [Inset] All duration by landslide ID.

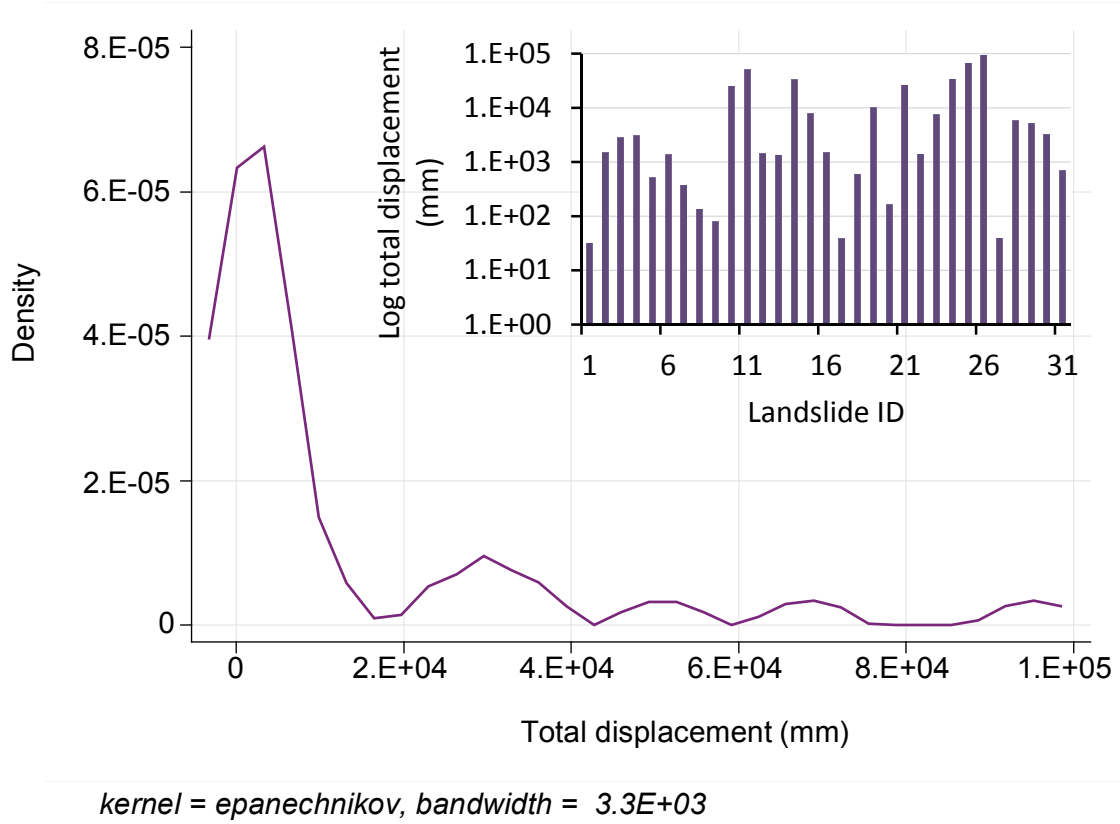

Figure 4.16: Kernel density estimate of total displacement. [Inset] All total displacement by landslide ID.

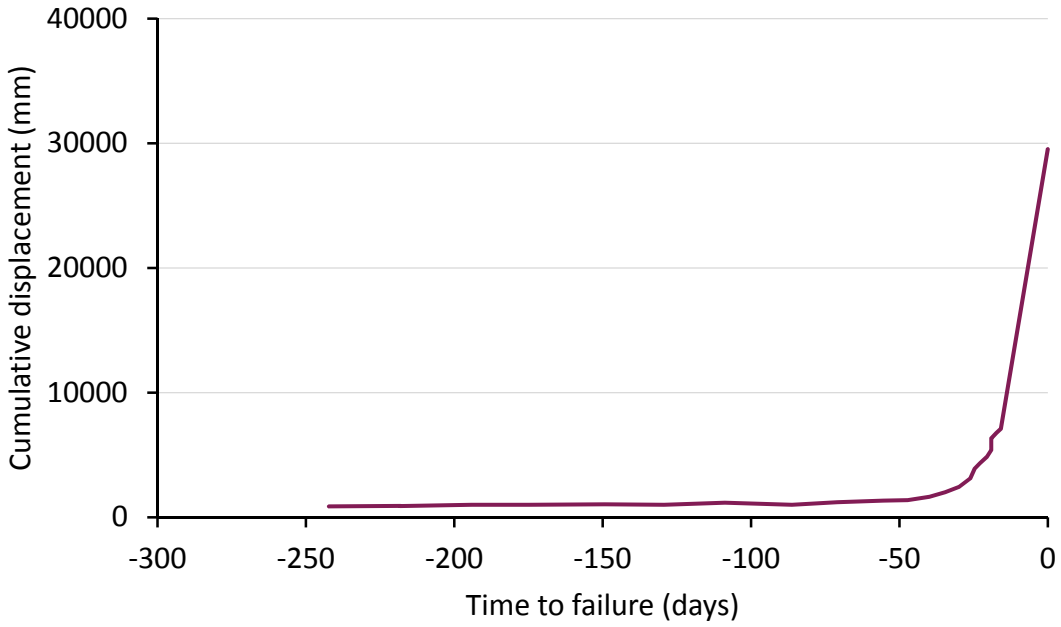

Figure 4.17: ID=26 Cumulative displacement time data from the tertiary stage of creep

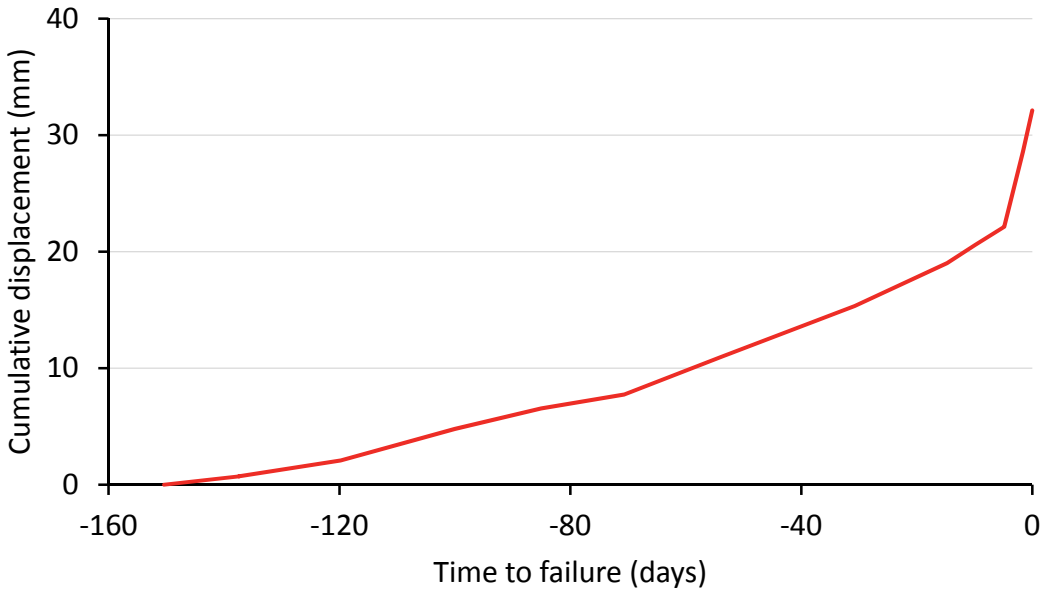

Figure 4.18: ID= 1 Cumulative displacement time data from the tertiary stage of creep

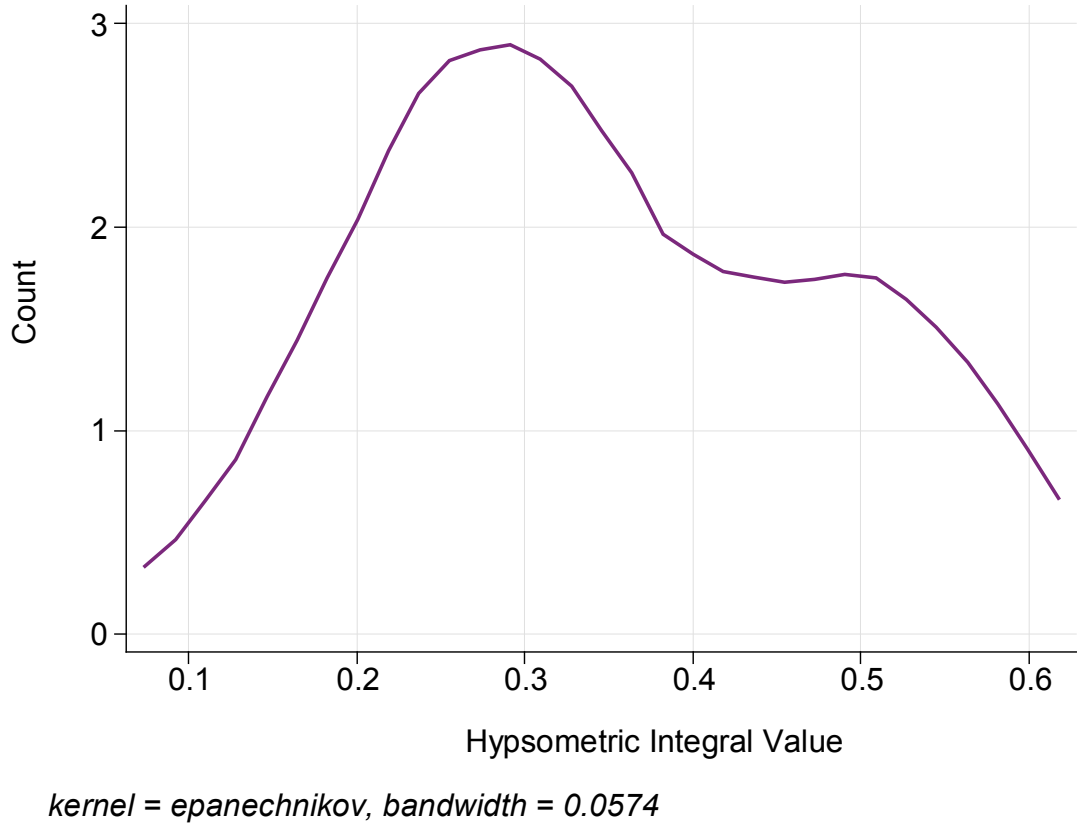

Figure 4.19: Kernel density estimate of hypsometric integral values distribution across the database (all)

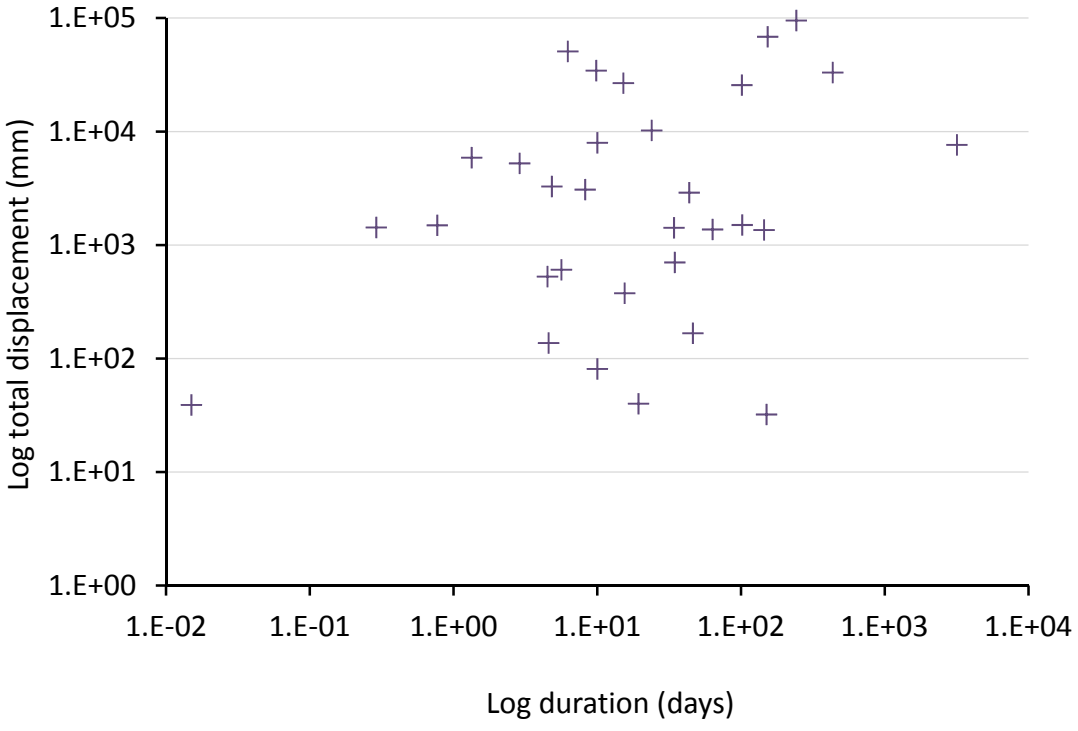

Figure 4.20: Scatter plot: total displacement- duration

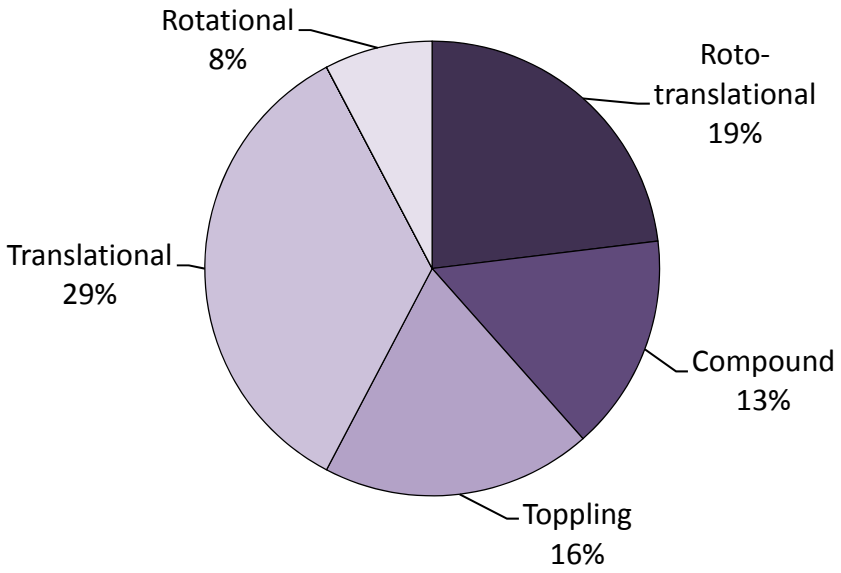

Figure 4.21: Mode of failure

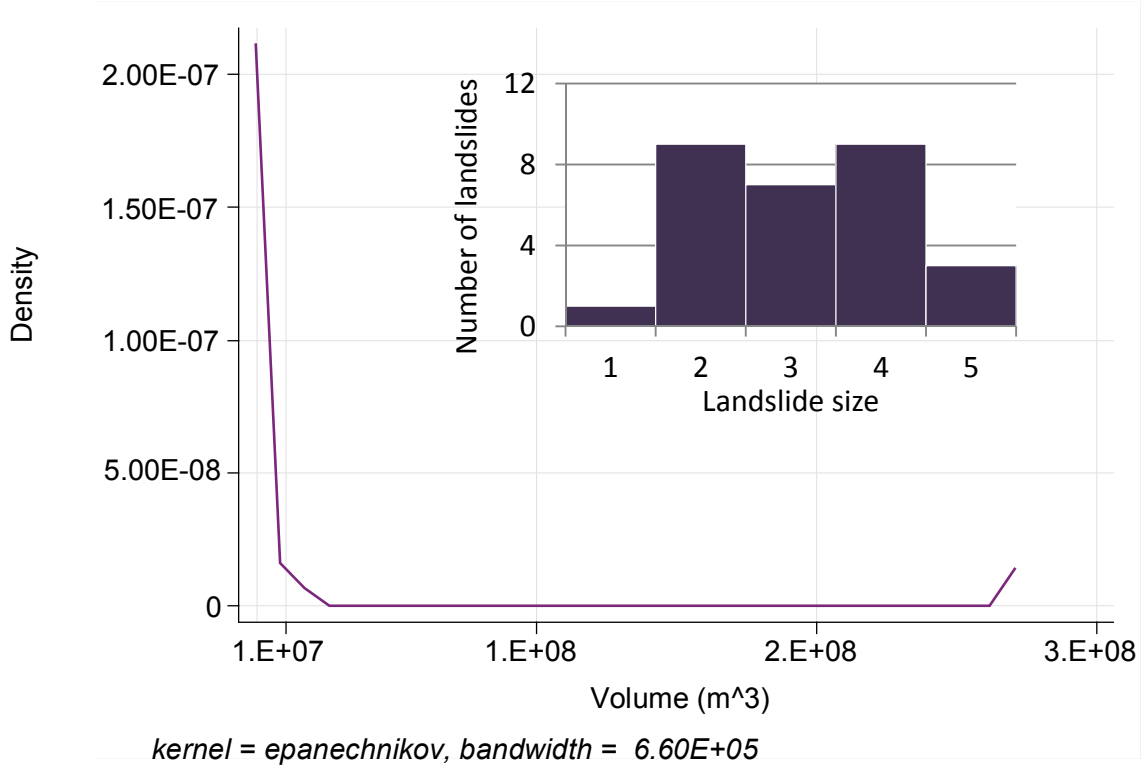

Figure 4.22: Kernel density estimate of landslide volume. [Inset] Landslide size distribution (where 1, 1 ≤ x < 1.0E+03; 2, 10.E+03 ≤ x < 1.0E+05; 3, 1.0E+05 ≤ x < 1.0E+06; 4, 1.0E+06 ≤ x < 1.0E+07; 5, 1.0E+07 ≤ x < 1.0E+09)

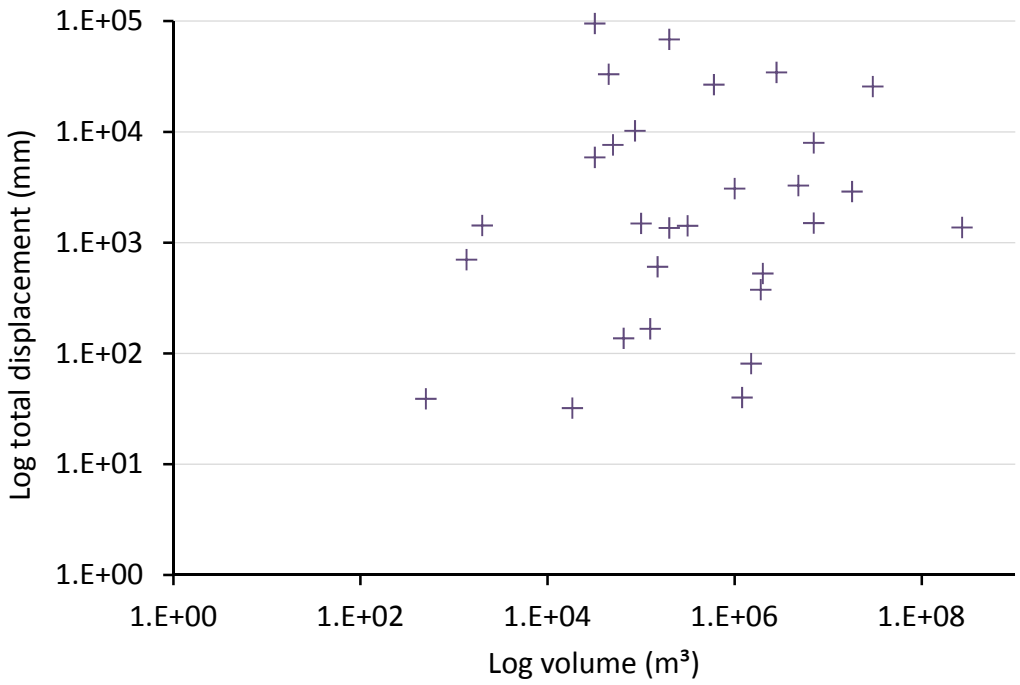

Figure 4.23: Scatter plot: total displacement- volume

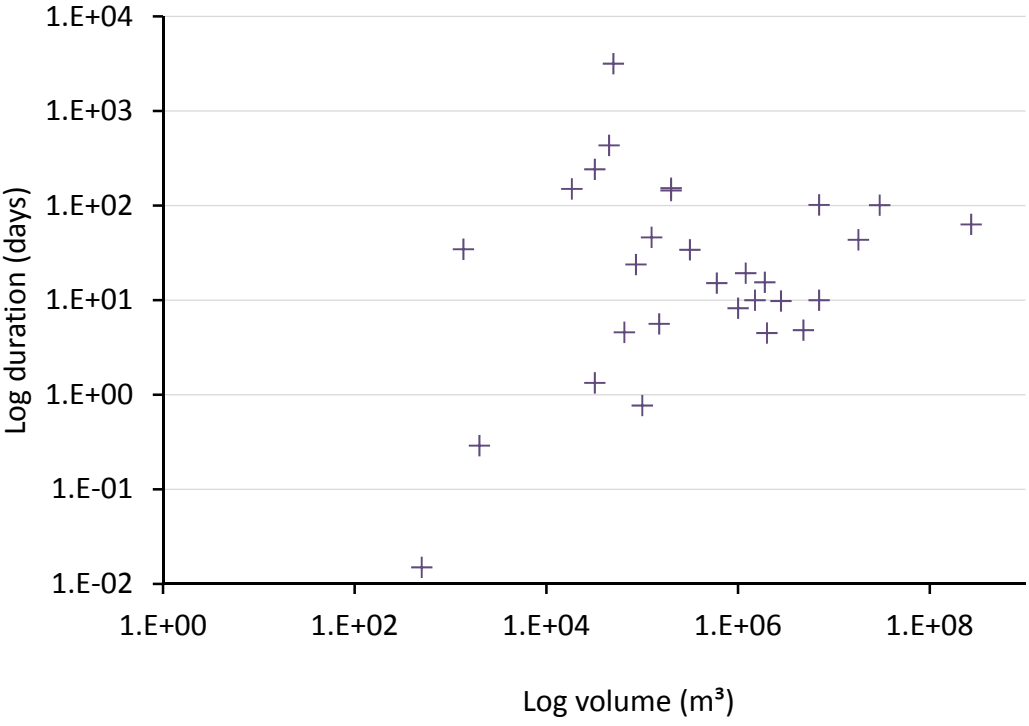

Figure 4.24: Scatter plot: duration- volume

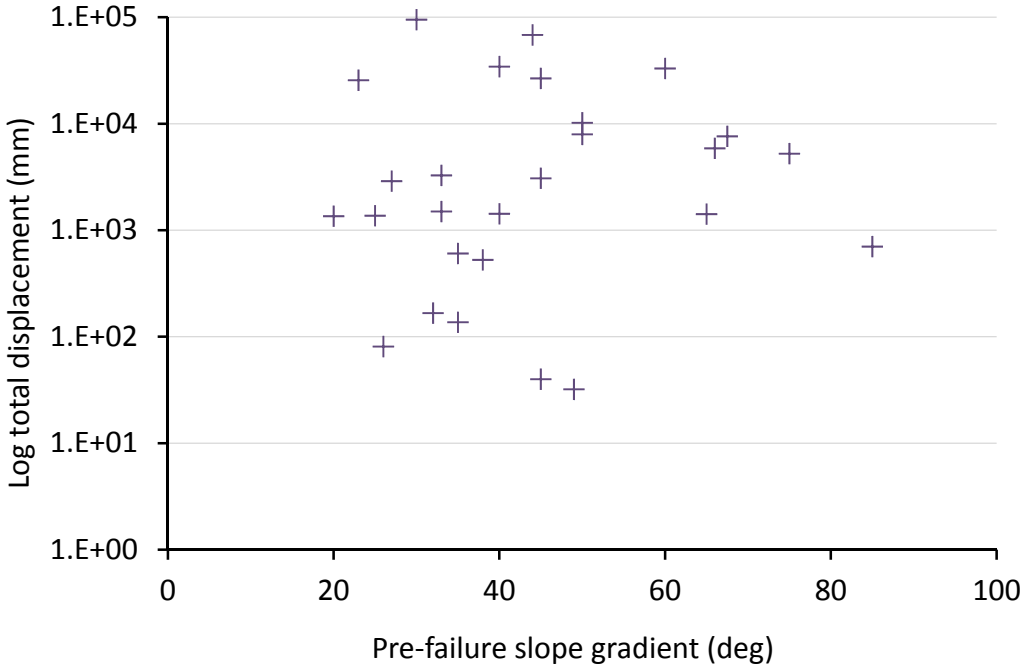

Figure 4.25: Scatter plot: total displacement- pre-failure slope gradient

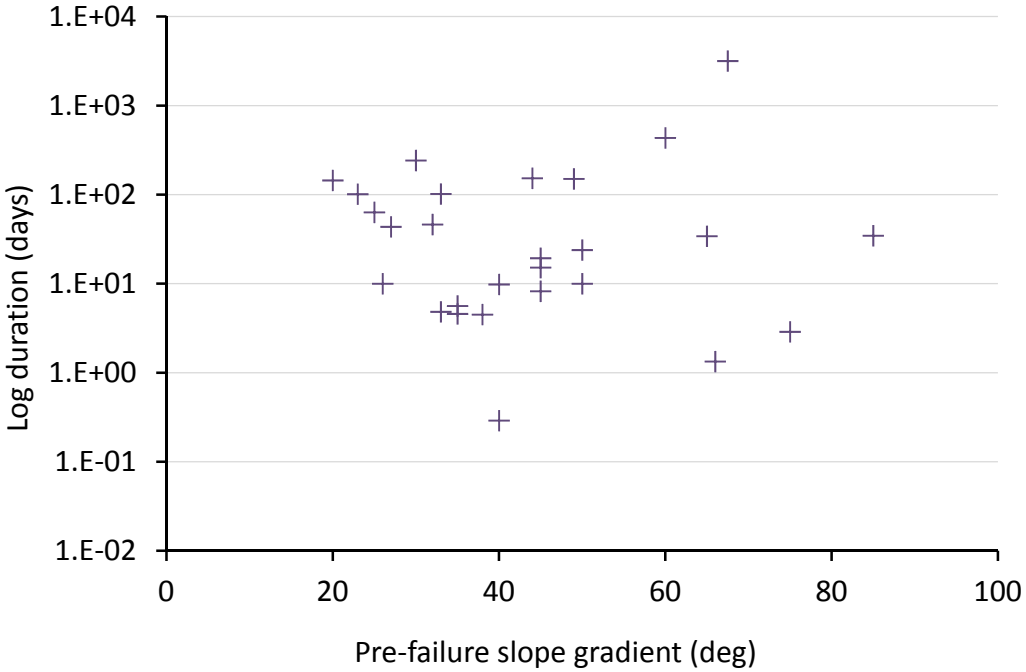

Figure 4.26: Scatter plot: duration- pre-failure slope gradient

Figure 4.27(a) presents the velocity of displacement on each slope through time. As discussed earlier with reference to figure 4.12(a), tertiary creep operates over a large spread of time scales (figure 4.15); duration ranges from ~37 minutes (0.026 days; figure 4.14) to 3,171.45 days (figure 4.13). It is clear from the plot of Saleshan landslide (id=13) data in figure 4.27(a) and Eskihisar coal mine wall data (id=14) in the inset of figure 4.27(a) that some of the examples do not terminate at zero time. This is due to the conversion method between cumulative displacement-time and velocity-time used for digitised examples in the form of (1) and (2) (see section 4.2 for explanation); whereby the mid-time between each displacement measurement is related to calculate velocity. The highest 'maximum velocity' recorded before failure was 1341.65 m/day (134,165 mm/day) from the Afton mine collapse (id=24, figure 4.28). This was measured after ~9.79 days of creep, during which the average velocity of displacement equated to 154.65 m/day (15,465.25 mm/day). The Selborne slope cutting failure presented the lowest 'maximum velocity': 2.19 mm/day (figure 4.29). Deformation occurred at an average velocity of ~0.49 mm/day over a period of 143.89 days.

The distribution of 'maximum velocity' across all thirty-one examples in the database (figure 4.30) shows that most failures (27 examples) did not travel faster than 10 m/day (10,000 mm/day) during the period of tertiary creep (inset figure 4.30). Although the mean 'maximum velocity', 9.8 m/day (9,828.26 mm/day) falls within the first four magnitudes of the distribution, in common with the majority of the data, the standard deviation is large, 29.22 m/day (29,218.91 mm/day), reflecting the highest and lowest recorded velocity values (figures 4.28 and 4.29, respectively). Removing the long tail on data by recalculating statistics to consider the 27 examples below 10 m/day reduces the mean to 1.55 m/day (1,545.41 mm/day) and standard deviation to 3.38 m/day (3,382.15 m/day). However this mean is still somewhat greater than the median of the entire dataset, 0.49 m/day (488.33 mm/day), reflecting the positive skew that remains in the distribution even when outlying values are removed.

Figure 4.31 depicts the relationship between duration and maximum creep velocity (by id). There is no significant correlation between variables; r-squared values resulting from linear and log regressions of the data equate to 0.07 and 0.1148 respectively. Values from the regression of total displacement- maximum velocity

(figure 4.32) are equally low (linear r-squared= 0.114, log r-squared= 0.12). Linear regressions were carried out on sub-sets of data grouped by slope and failure characteristics (as before with cumulative displacement-time) for the two maximum velocity based relationships depicted in figures 4.31 and 4.32. Table 1 (appendix) contains the r-squared values resulting from all correlations. Although the coefficient of determination between maximum velocity and duration remained insignificant for all but two sub-sets (size 5 landslides = 0.716 and pre-failure slope gradients $20 \leq x < 30$ degrees = 0.636), the values derived from the regression of maximum velocity-total displacement indicated some significant correlations that stood out from otherwise weak relationships. Slopes composed of clay (3 examples) showed a strong correlation between maximum velocity and total displacement; r-squared value of 0.967. Failures that occurred in a compound manner (3 examples; table 2.3, section 2.3.4, p.) also presented a high coefficient of determination, 0.972; as did large 'size 5' landslides (3 examples), 0.974. It is noted that the three sub-sets contained different examples; the only data overlap is Barrick Gold's Betze-Post open mine (id=3), that is both a compound and large ($1.E+07 \leq x < 1.E+09$). Although the specific correlations mentioned above are strong, they are between small groups of examples, i.e. three data points, suggesting that the high coefficients of determination are a result of small sample size rather than a strong maximum velocity-total displacement correlation.

Assessing the strength of relationship between the median and maximum velocity of each example provides a general insight into the uniformity of creep acceleration behaviour broadly across the database. Figure 4.33 presents this data. The median is used instead of mean velocity here, because it is robust in characterising the rate of creep at the same relative position in time (50^{th} percentile) irrespective of extremely large (outlying) values, common to the final data points of rapidly accelerating unstable slopes. The coefficient of determination resulting from the linear regression of median velocity- maximum velocity was low, 0.368, indicating only a very weak correlation between these parameters. The lack of uniform connectivity between velocity during the middle and end of creep indicates that slopes across the database are exhibiting different patterns and rates of acceleration.

Patterns of acceleration during the tertiary stage of creep may be characterised using Voight's (1989) model parameters (equation 4, section 2.3.3.2), α and A. These

constants represent material characteristics for time invariant external conditions (i.e. load and temperature) (Crosta and Agliardi, 2003) (discussed in section 3.4.2.2.1 in the context of Fukuzono's (1985) inverse-velocity- time relationships). Given that the duration and velocity of tertiary creep spans several orders of magnitude when considering the entire database of examples, data has been normalised (figure 4.27(b)). Hyperbolic curves were fitted to the rescaled data using equation 16 in Matlab's curve fitting toolbox.

$$y = [A \times (1-\alpha) \times (x) + y_f^{1-\alpha}]^{\frac{1}{(1-\alpha)}}$$

[Equation 16; adapted from equation 9 for Matlab Curve fitting]

The term $(t_f\text{-}t)$ is simplified here with x (or time to failure) because the time of failure in every case is zero. Velocity ($\frac{dx}{dt}$), is represented by y in this equation where y_f is the velocity at zero time (or failure). Importantly this equation is valid under the condition $\alpha > 1$; A and y_f boundaries are set at zero and infinity (lower and upper) for the curve fitting procedure, and α is restricted between 1.001 and infinity (lower and upper). Curves were fitted to data using a robust regression, which considers the absolute distance between data and is most robust against outlying values. Table2 (appendix) contains the output α mean, α range, A mean, A range, y_f mean, y_f range and r-squared value for each hyperbolic fit.

It is noted that the α range for the curves fitted to several creep examples were 'fixed at bound'. This indicates that the best hyperbolic fit for certain sets of data was found when α=1.001, or the lower bound defined for the fitting procedure. When α=1, data shows an exponential relationship, based on Voight's (1989) parameters (figure 3.4, section 3.4.2.2.1). Exponential curves were fitted to all creep examples using equation 17, where the constants A and y_f were calculated within the bounds zero and infinity.

$$y = \exp(A \times x) \times y_f$$

[Equation 17 for Matlab Curve fitting]

The r-squared value for each exponential fit, as well as the mean and range of constants A and y_f are summarised in table 3 (appendix).

The hyperbolic and exponential best fit curves for each creep example are collated and presented in figures 4.34 (a) and (b). Fitted under either model, results highlight the different acceleration trends exhibited by failing slopes during tertiary creep. The shape of each hyperbolic curve is defined by constants α, *A* and y_f. Drawing on specific examples, the failure with greatest maximum velocity, Afton mine (id = 24; figure 4.28) is fitted with an α value of 1.859 whilst the Selborne Slope Cutting failure (id = 1; figure 4.29) whose maximum velocity was the lowest at 2.19mm/day, was given a α value of 1.001 (or the lower bound value). Although the latter of these examples has been described with the α value expected to indicate exponential patterns of acceleration, the relatively low final velocity of 0.1344 within the normalised period of 0 to 1, results in a shallow curve gradient (figure 4.34(a)). Roesgrenda slide A (id = 12) also shows this pattern under the α value of 1.001. The Selborne Slope Cutting data is also fitted with a shallow exponential curve, and low final velocity value (0.1343), in common with four other examples (id = 15, 19, 24 and 31). The Roesgrenda slide A final velocity derived from the exponential fit is slightly higher (on normalised scale), 0.4072. One explanation for the appearance of these specific curves may be a sudden jump in the magnitude of velocity over a short period of time within the last few data points. This seems to be the case for the exponential examples, where accelerations during the final 0.1 units of time of tertiary creep range 16.19 mm/day^2 to 67.78 mm/day^2.

Figure 4.35 shows the mean and potential range of values of α used for each hyperbolic best fit. The Bomba landslide (id = 11) has the greatest α value, 2.969, whilst the Chuquicamata Mine- East Wall failure (id = 21) showed the greatest potential range of α, -7.561 to 19.68, from which a hyperbolic curve may be fitted. This example was one of seven whose potential range for the α constant was greater than 1. The distribution of α values is depicted in figure 4.36 by the kernel density plot. The distribution is positively skewed with a mean of 1.402, standard deviation of 0.410 and range between 1.001 and 2.969. Six examples (id = 1, 2, 4, 5, 12 and 13) were best fit with an α value of 1.001 indicating that the slope was likely to be accelerating in at an exponential rather than hyperbolic rate. Given that ~65% of examples were best fit with an α value less than 1.5, the tendency towards this exponential rate of acceleration was common within the overall database.

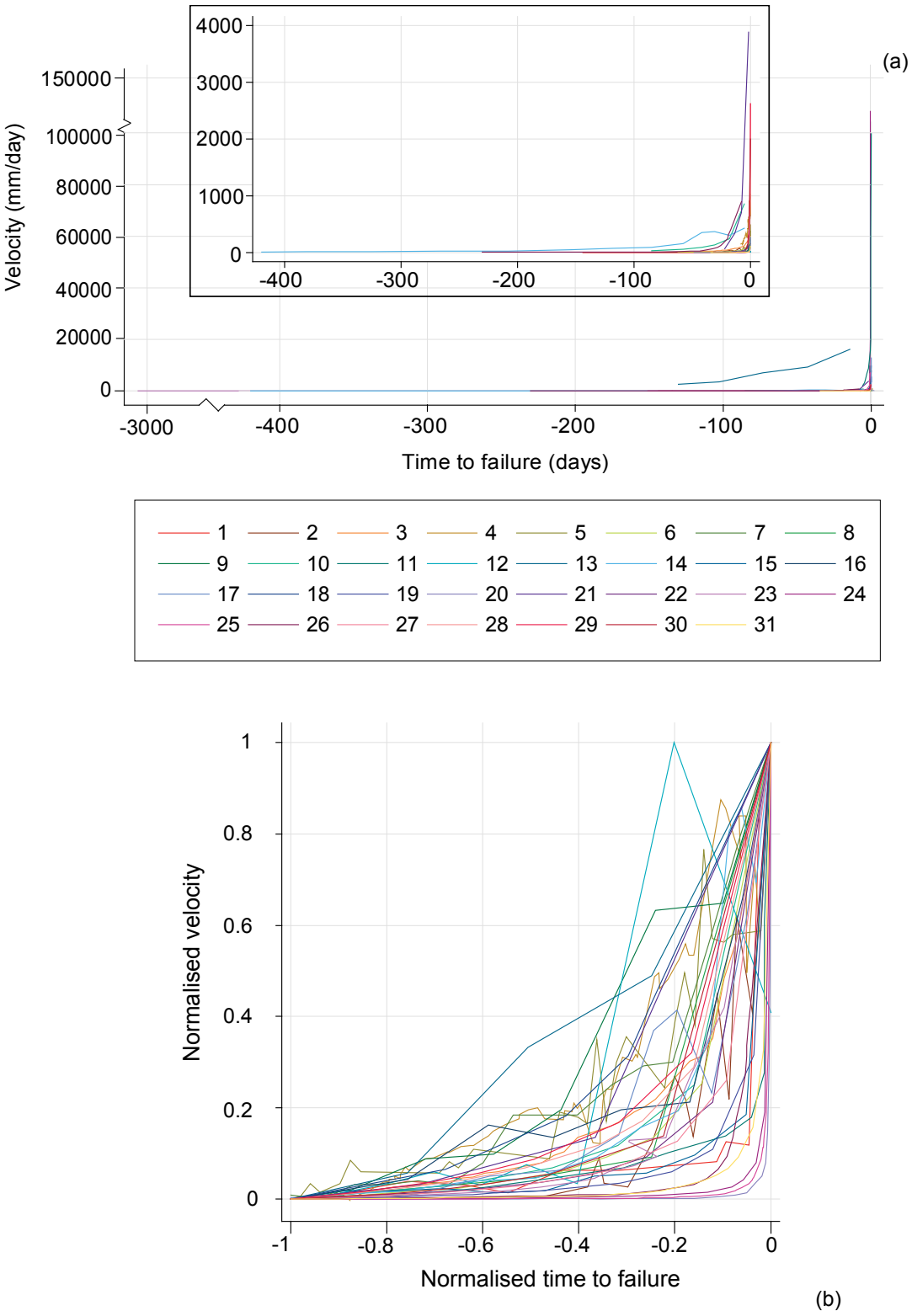

Figure 4.27: (a) Velocity-time data from the tertiary stage of creep. [Inset] Velocity-time data for failures whose maximum velocity is less than 5,000 mm/day; also excluding landslide ID 23. (b) Normalised velocity- normalised time data from the tertiary stage of creep

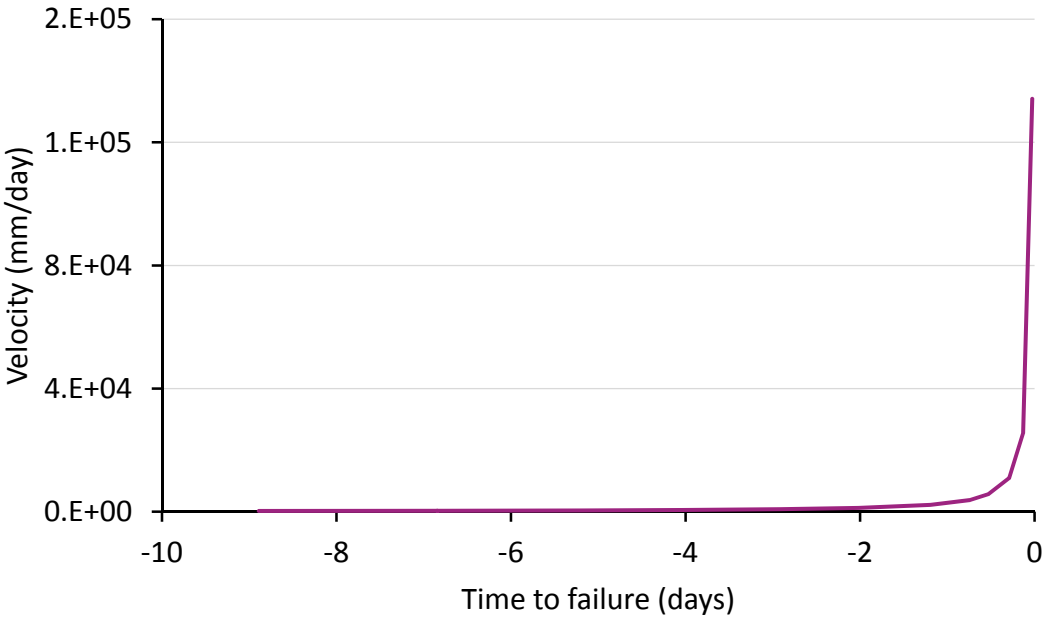

Figure 4.28: ID= 24 Velocity-time data from the tertiary stage of creep

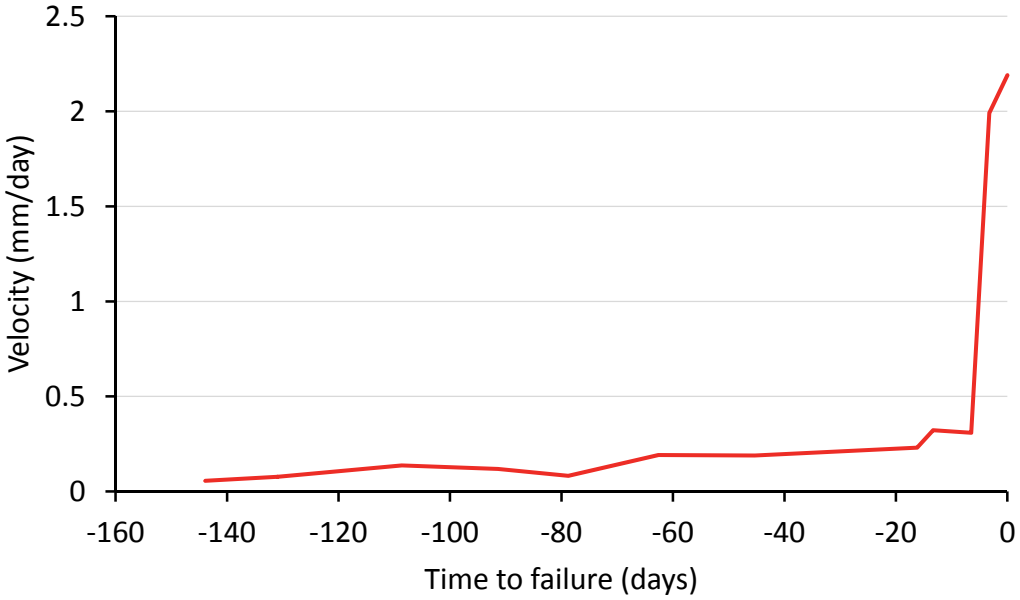

Figure 4.29: ID=1 Velocity-time data from the tertiary stage of creep

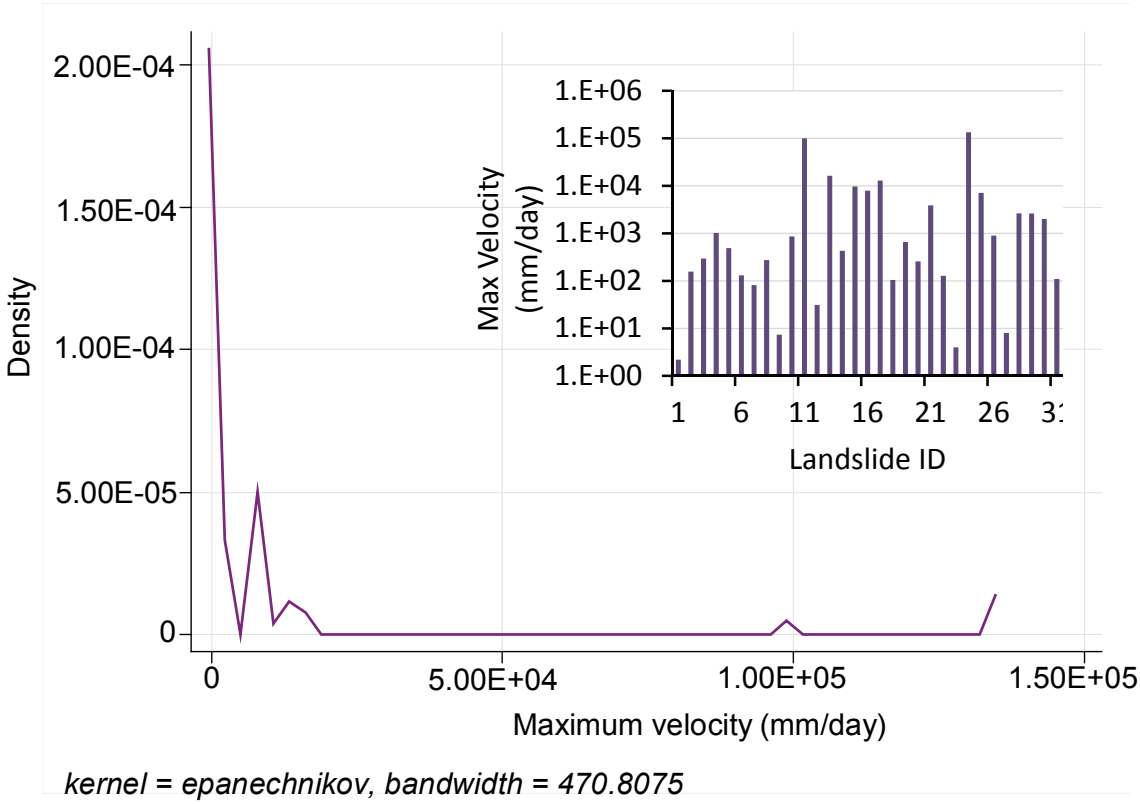

Figure 4.30: Kernel density estimate of maximum velocity. [Inset] All maximum velocity by landslide ID

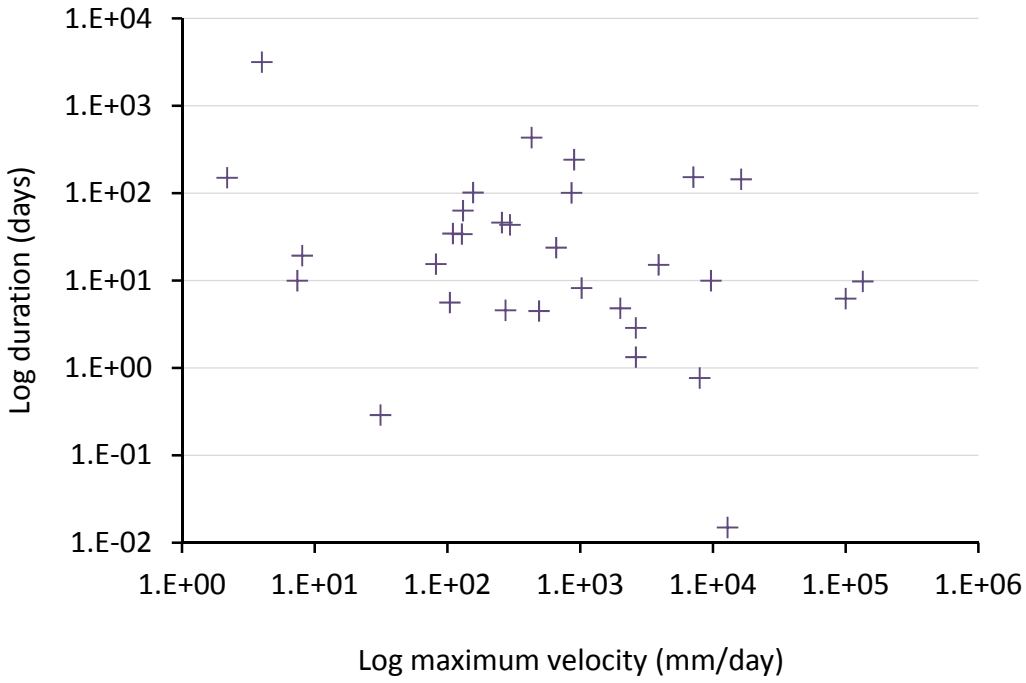

Figure 4.31: Scatter plot: duration- maximum velocity

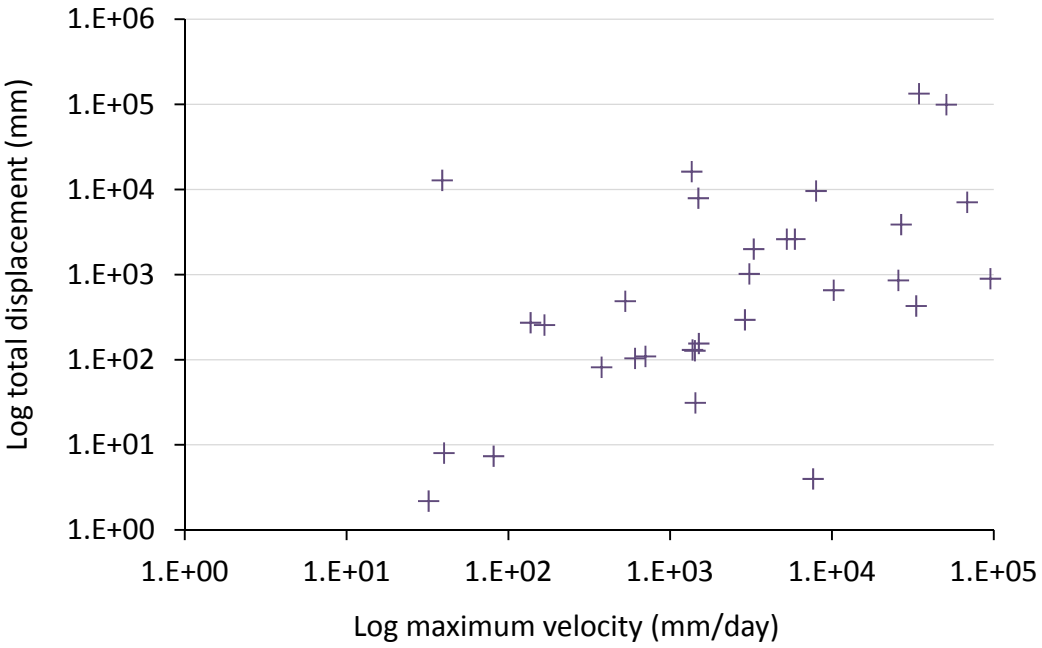

Figure 4.32: Scatter plot: total displacement- maximum velocity

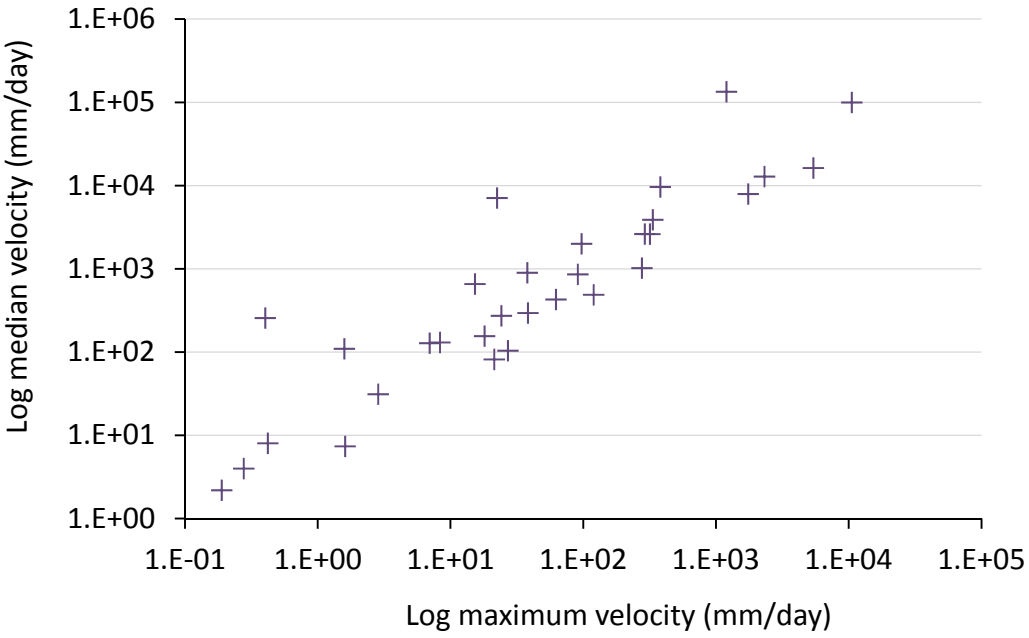

Figure 4.33: Scatter plot-: median velocity- maximum velocity

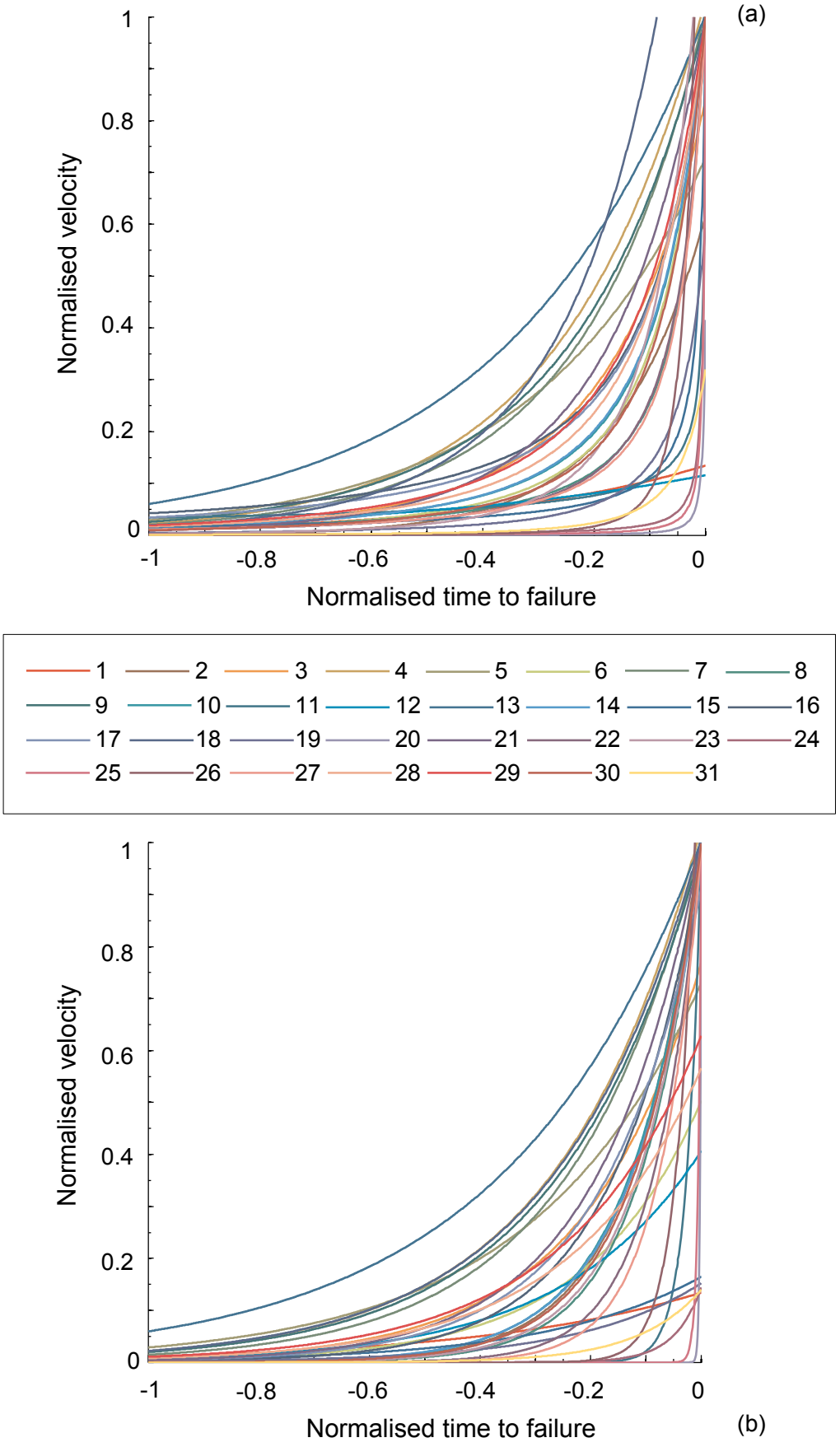

Figure 4.34: (a) Best-fit hyperbolic curves for normalised velocity- normalised time data

(b) Best fit exponential curves for normalised velocity- normalised time data

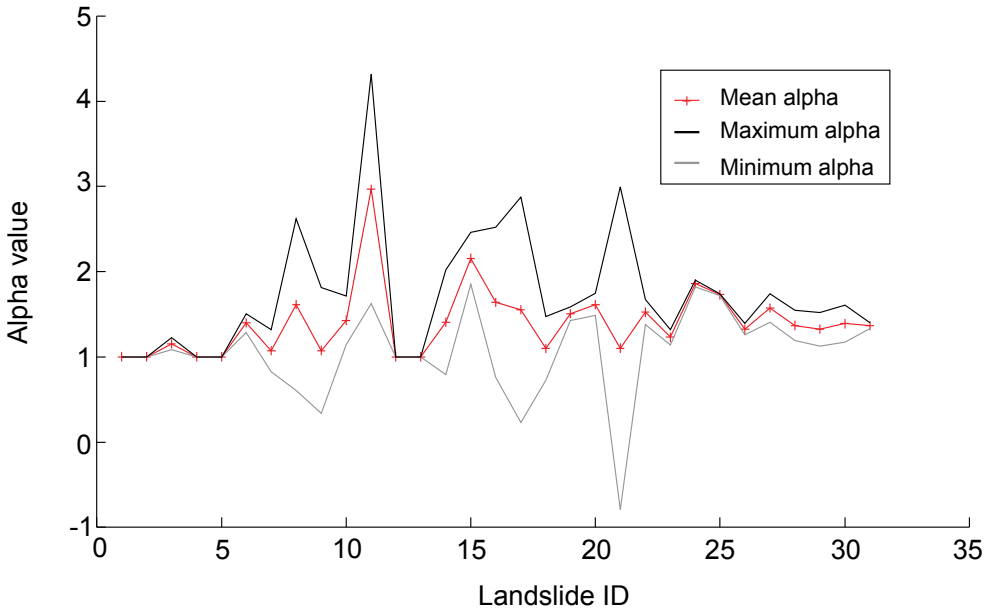

Figure 4.35: Mean, minimum and maximum α values, displayed by landslide ID. Note that data is discrete.

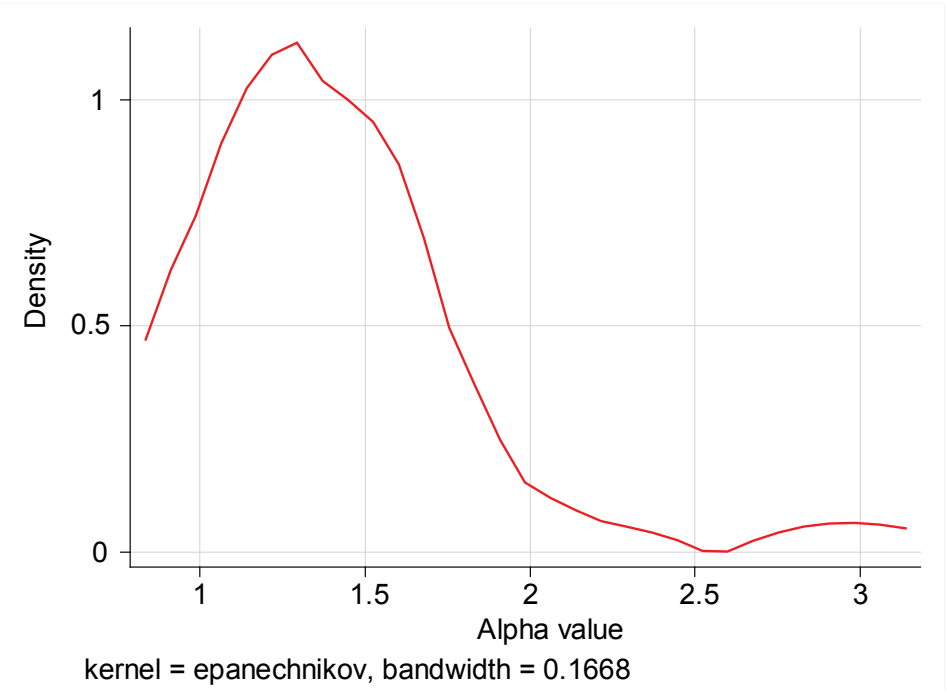

Figure 4.36: Kernel density estimate of the hypsometric α values

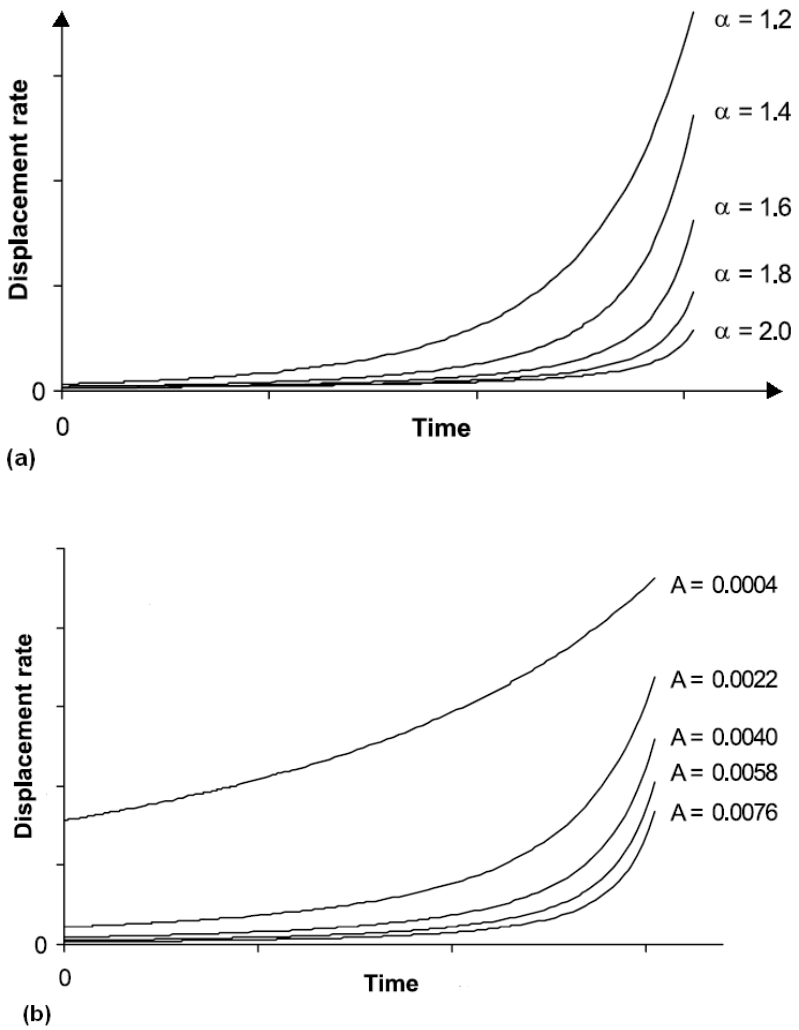

Figure 4.37: Results from the sensitivity analysis of Voight's parameters (a) α and (b) *A* on a displacement rate- time plot (Crosta and Agliardi, 2003, p.179)

The α constant controls the sensitivity of accelerating activity (Crosta and Agliardi, 2003), illustrated in figure 4.37(a) by the changing general steepness in curvature. Most curves (20 examples) were fitted with an α value between 1 and 2 (figure 4.38(b)). Nine examples were best fit with exponential curves (figure 4.39 (a)), whilst only two examples presented with α values greater than 2 (figure 4.39(c)); Labe Canyon (id=31) was fitted with the largest α constant of 2.969. Although examples are grouped by similar patterns of acceleration (whether exponential or hyperbolic ($1 < \alpha < 2$ or $\alpha \leq 2$)), there are clear differences in the change in acceleration rate as creep progresses. The constant *A* controls the shape of the curve (Crosta and Agliardi, 2003),

where greater values of *A* result in greater increases in the acceleration as time progress, leading to larger differences in curve gradient between -1 and zero time (figure 4.37(b)).

Figure 4.39 shows the mean and potential range of values of *A* used for each hyperbolic and exponential best fit. The linear regression between the exponential and hyperbolic values of *A* results in an r-squared of 0.5022. This value suggests that only a weak correlation exists between the constant *A* used for each of the two types of fit. Given that the dimensions of *A* depend on the value of α (Cornelius and Scott, 1993), it is not surprising that examples for which the best fit curve is exponential (i.e. α = 1.001 in the hyperbolic model), the values of *A* show better correlation, 0.753. The connectivity between these two constants is also shown by the value of *A* for the hyperbolic fit of Bomba landslide data (id = 11), 399.1; this example used the largest α and *A* constants of all curve definitions. The value for *A* in the exponential fit is significantly smaller at 38.51. The largest *A* constant used for an exponential curve is 418.7 (for Tukabianna West, id = 20). Although the *A* constant for the hyperbolic fit is similar, 403.8, the α value is not close to 1.001; it was best fit with a value of 1.613. This suggests that there is also correlation between the values *A* beyond curves fitted with an exponential (or 1.001 α value).

The distribution of hyperbolic and exponential *A* constants is different (figure 4.40). The mean hyperbolic value is 59.85, whilst the mean exponential is 26.80. Although the range of values is similar, the standard deviation of hyperbolic *A* constants is greater (119.80) than the exponential *A* constants (78.56). This is reflected in the broader peak of the hyperbolic data (density maximum of ~0.3), compared to the narrow peak of exponential values (~1.05 density). It is noted too that the potential range of *A* for each fit is smaller for exponential curves than hyperbolic (figure 4.40), reflective that the value of *A* for hyperbolic fits has the added complexity of α association (and the potential range of this constant).

Although the last velocity point for each example equated to 1 when the data was rescaled onto normalised axes, most of the curves predicted lower values of final creep rate (y_f; figure 4.41; 4.42). When the velocity at failure was less than 1, curves indicated generally lower rates of acceleration (figure 4.34); this was discussed earlier

in the context of the Selborne Slope Cutting (id = 1) example and others. The correlation between values of y_f for hyperbolic and exponential fits is weak, 0.3335, when all examples are included in the regression. The linear regression of data which correlate with the exponential model (or α = 1.001), showed stronger correlation between y_f values, with an r-squared value of 0.7941. As is the case with values of *A*, it is expected that the predicted velocity at failure (y_f) will be similar between models because both use exponential (or approximate exponential) fits on the data.

Figure 4.42 shows the difference in range between the hyperbolic and exponential y_f distributions. Although the predicted velocity at failure for hyperbolic curves spans a greater range (0.116 to 3.107), the standard deviation of 0.506 around mean 0.964 is smaller than for exponential data. Values for y_f spanned a smaller range (0.134 to 1.143), but are not so tightly distributed around the mean (0.793), where the density of values peaks at ~1.5 compared to peak density of 4 for hyperbolic data. Considering the distribution of values before the mean, it is noted that for five hyperbolic curves and seven exponential examples, the predicted failure velocity is less than 0.5 (normalised scale). This returns to earlier discussion on initial observations from figure 4.34, which suggested that sudden jumps in the magnitude of velocity over a short period of time within the last few data points may not be properly captured by the curves fitted to consider the entire dataset. Following from figure 4.37(b), it might be inferred that using a different value of *A* within the modelled range or choosing an alternative method of fitting data may predict higher y_f values better in line with raw measurements. Although this would be interesting to model, the value of α used for each 'best' fit curve, provides greater insight into the physical mechanisms driving creep (e.g. crack growth) (Kilburn, 2003). This is based on the different patterns of acceleration (exponential and hyperbolic) represented by values of α in the Voight model, and will be discussed further in the context of figure 2.8 (section 2.3.3.2) and slope characteristics, in chapter 5.

Characterising tertiary creep using Voight's model assumes that slope displacements are accelerating to failure (section 2.3.3.2). Returning to the normalised projection of velocity-time data (figure 4.27(b)), it is clear that several examples decelerate between measurement intervals (i.e. negative gradient in plot). These examples are discriminated in figure 4.43; twenty-one failures show acceleration to

collapse (figure 4.43(a)), but ten examples (id = 1, 2, 4, 5, 7, 12, 14, 17, 18, 23) display deceleration (figure 4.43(b)) of varying magnitudes. The most prominent of these (visually) is Roesgrenda slide A (id = 12), which exhibited a sharp deceleration of 994.57 mm/day^2 just before failure (figure 4.43(b)). Figure 4.44 shows the spread and range of acceleration and deceleration for the entire database. The largest recorded deceleration, 1.45e^{-05} mm/day^2, occurred at ~-0.2 normalised time during creep on the hillslope monitored by Mufundirwa et al. (2010) (id = 17). The deceleration involved a change of 12.845 m/day (12845.4 mm/day) in velocity over a short period of ~29 seconds, compared to 13.91 mm/day over the period of ~20 minutes.

There were 61 points of deceleration recorded in the database (and shown on figure 4.44), 11 points of steady velocity and 403 accelerating intervals recorded, highlighting that ~13% of intervals involved deceleration, whilst the majority ~85% involved acceleration. Accelerations ranged from 2.98e^{-05} mm/day^2 to 6.87e^{06} mm/day^2 and show a general increasing trend to failure (zero time). Given that the thirty-one examples in the database showed different magnitudes of displacement, velocity and thus acceleration/deceleration, it is useful to rescale the second derivatives of each example between 0 and 1 relative to the maximum rate of velocity change exhibited by each creeping slope. Figure 4.45 shows the relative acceleration and deceleration of each example as creep evolves to final failure. There is a clear increase in the magnitude of deceleration as time progresses to zero. The magnitude of acceleration also increases to failure; however for certain slopes the greatest rate of acceleration did not occur in the final moments of creep, but earlier in the tertiary phase. Although only clearly apparent for four examples (where acceleration = 1 before -0.2 time), other minor pulses of acceleration are seen across the database as slopes approach zero time. The slope data (id=17) presented in Mufundirwa et al. (2010) shows a fluctuating decelerating-accelerating pattern of creep with a gradual increase in the magnitude of velocity as time progresses. This behaviour is unexpected for the tertiary phase of failure and will be discussed further in the context of the physical mechanisms controlling slope deformation in chapter 5.

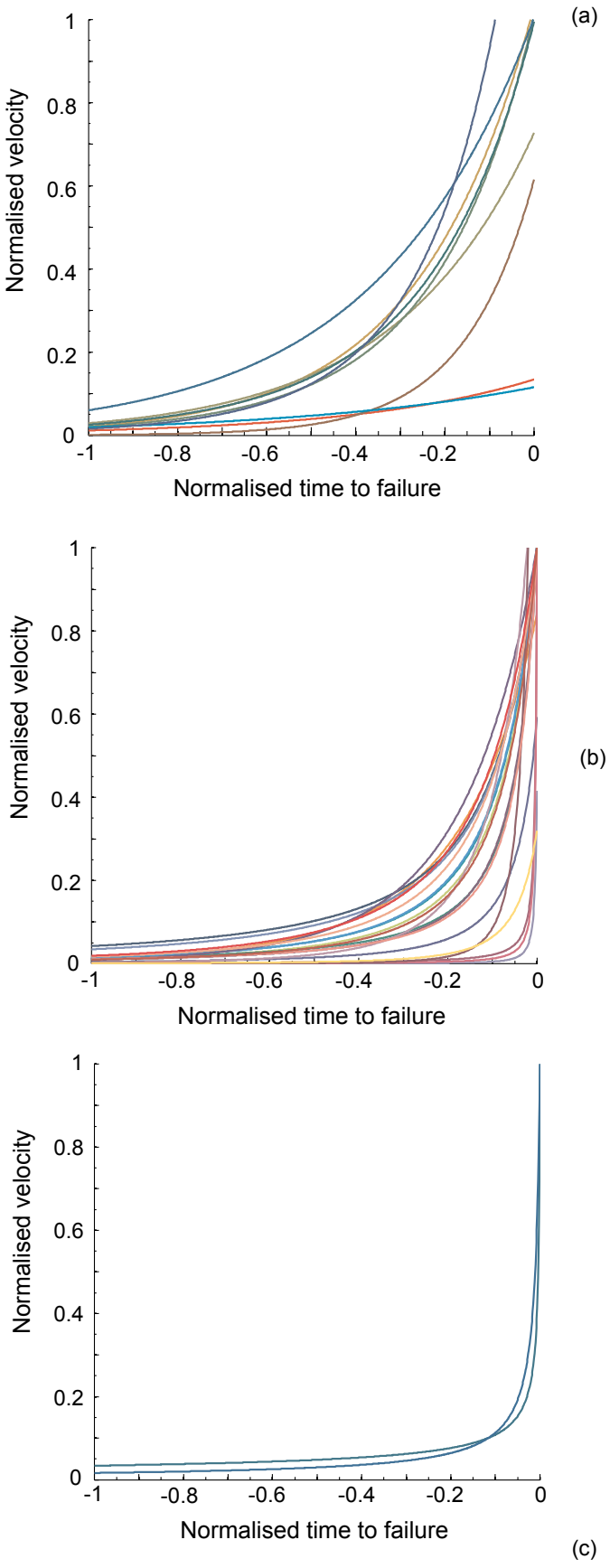

Figure 4.38: Best fit hyperbolic curves, separated by (a) α=1, (b) 1< α<2 and (c) α≥2

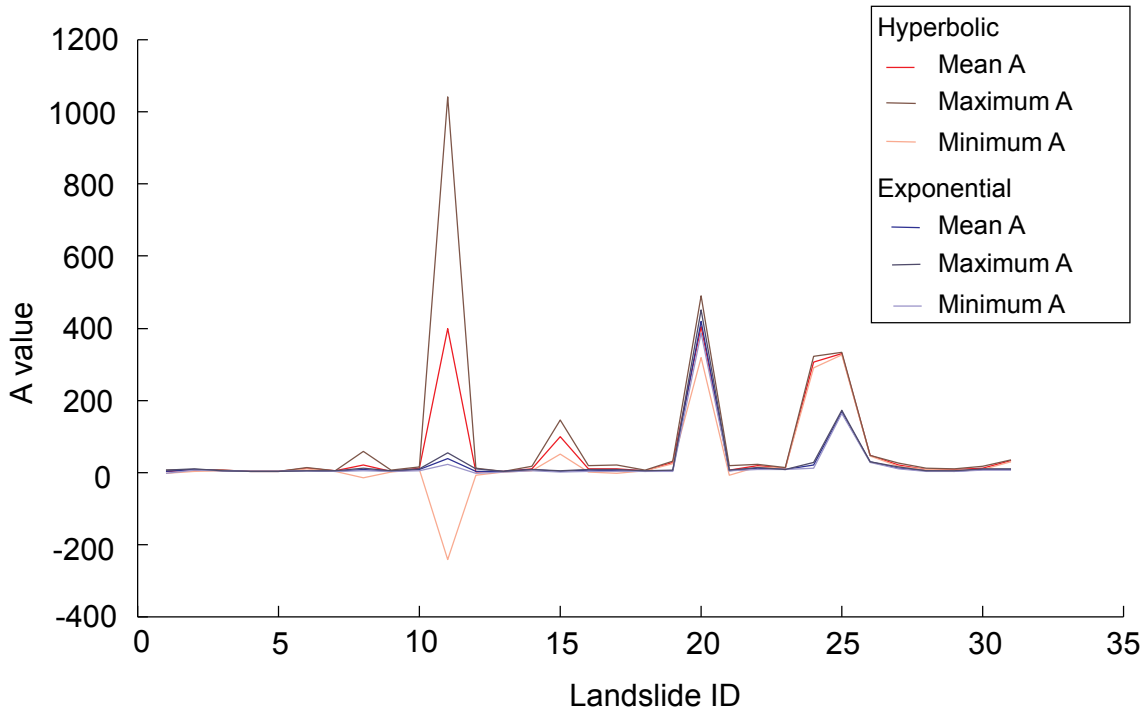

Figure 4.39: Mean, minimum and maximum A values, displayed by landslide ID. Note that data is discrete.

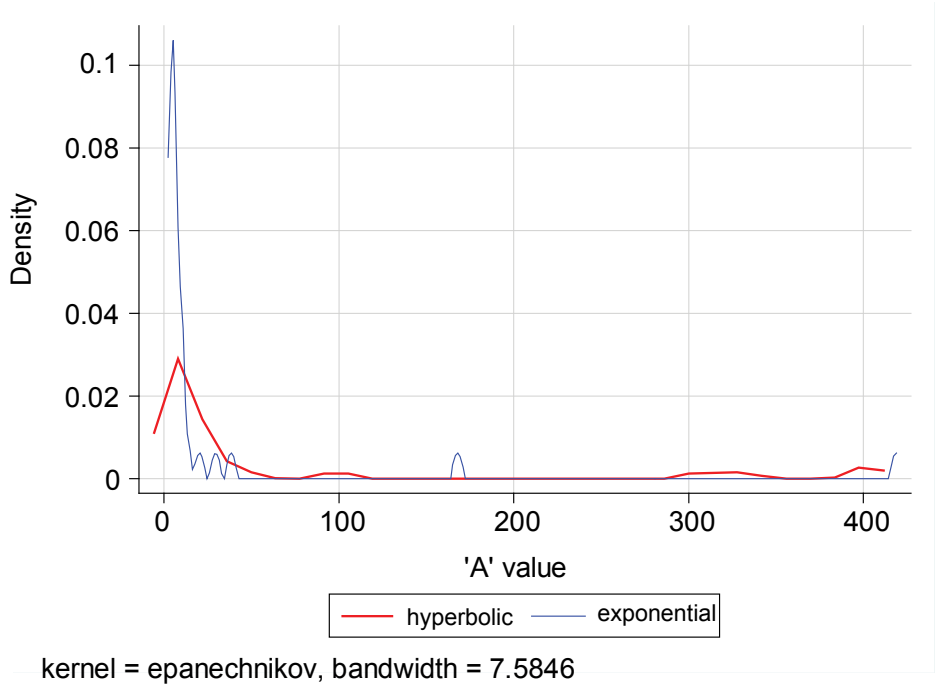

Figure 4.40: Kernel density estimate for values of *A* derived from hyperbolic and exponential fits

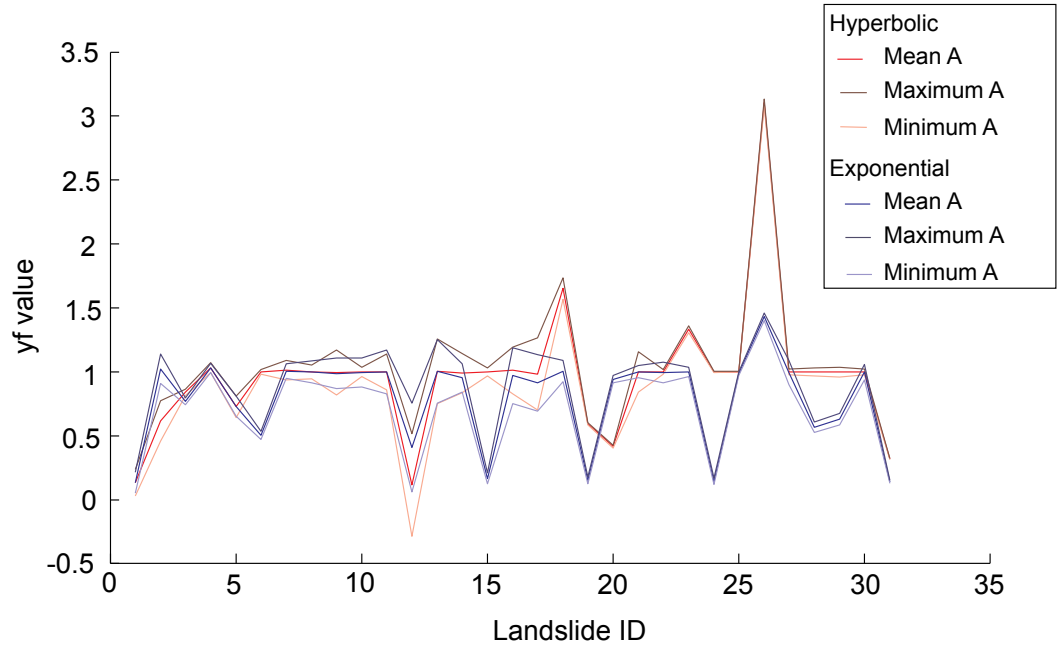

Figure 4.41: Mean, minimum and maximum y_f values, displayed by landslide ID. Note that data is discrete.

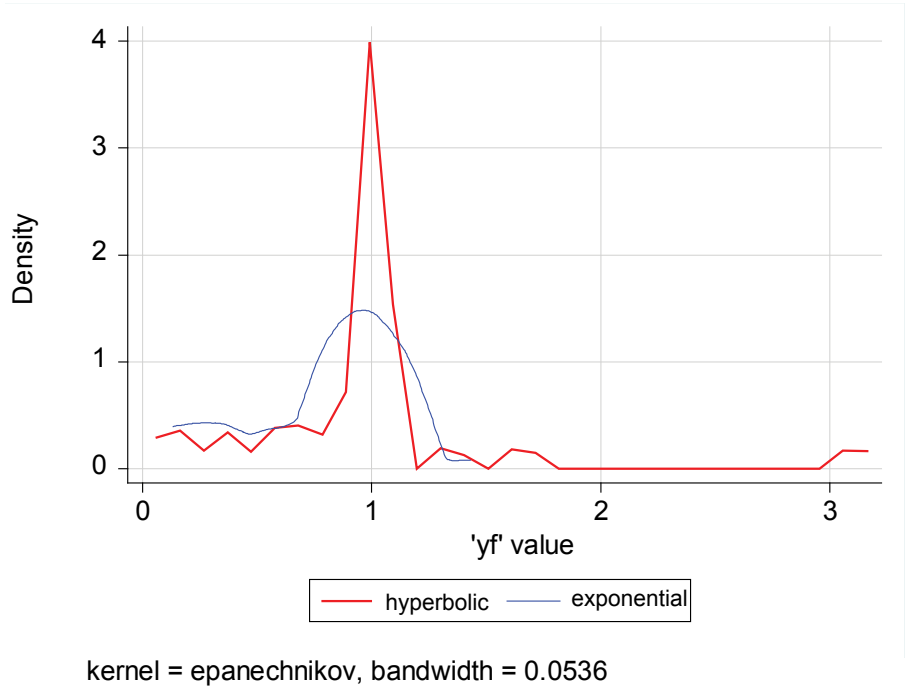

Figure 4.42: Kernel density estimate for values of y_f derived from hyperbolic and exponential fits

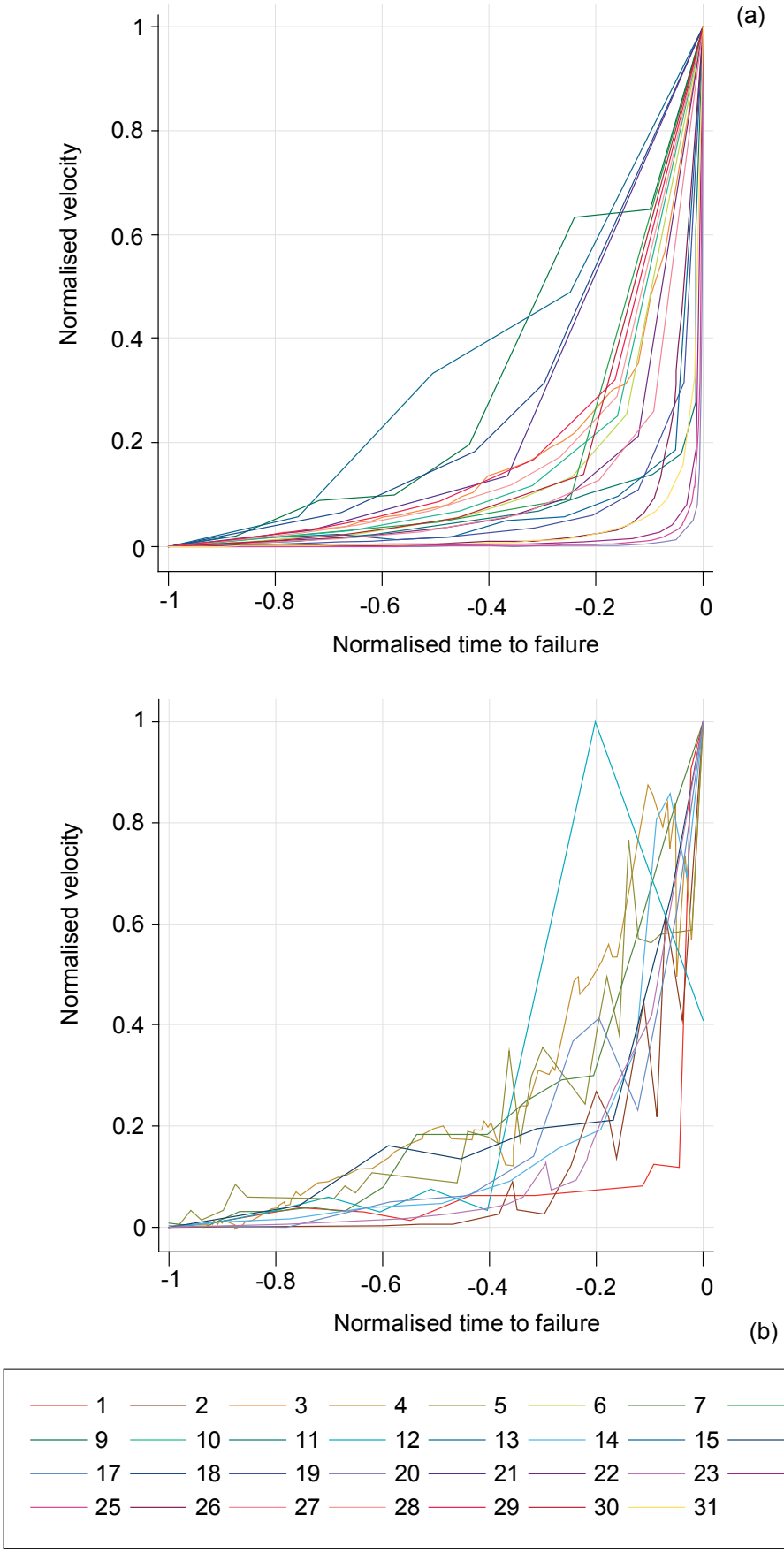

Figure 4.43: (a) Normalised velocity- normalised time data from the tertiary stage of creep (accelerating cases). (b) Normalised velocity- normalised time data from the tertiary creep stage (fluctuating cases).

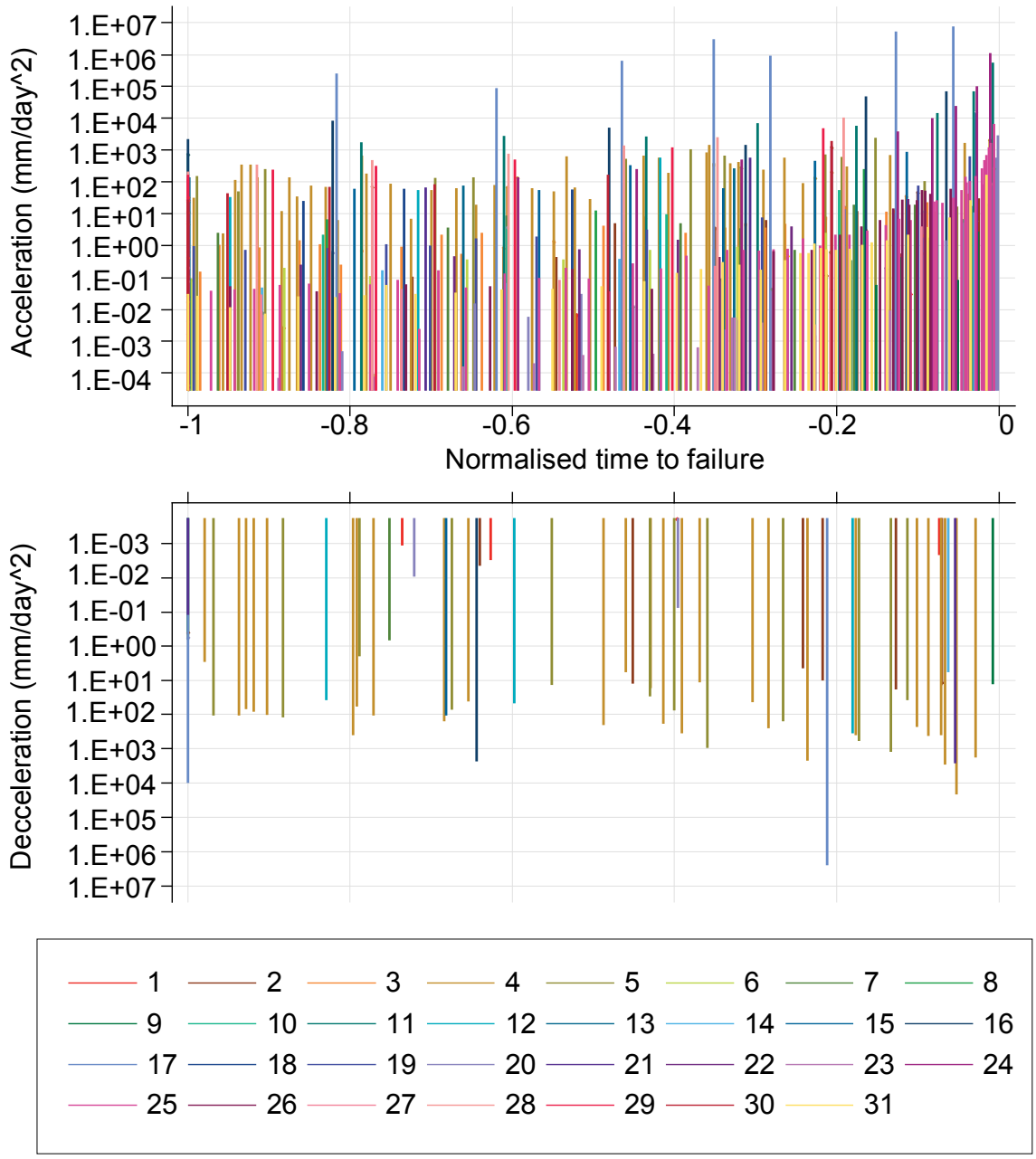

Figure 4.44: Drop-plots displaying values of acceleration and deceleration through time for all 31 database examples. Data values equating to zero mm/day^2 were removed from the plot to facilitate log scaling.

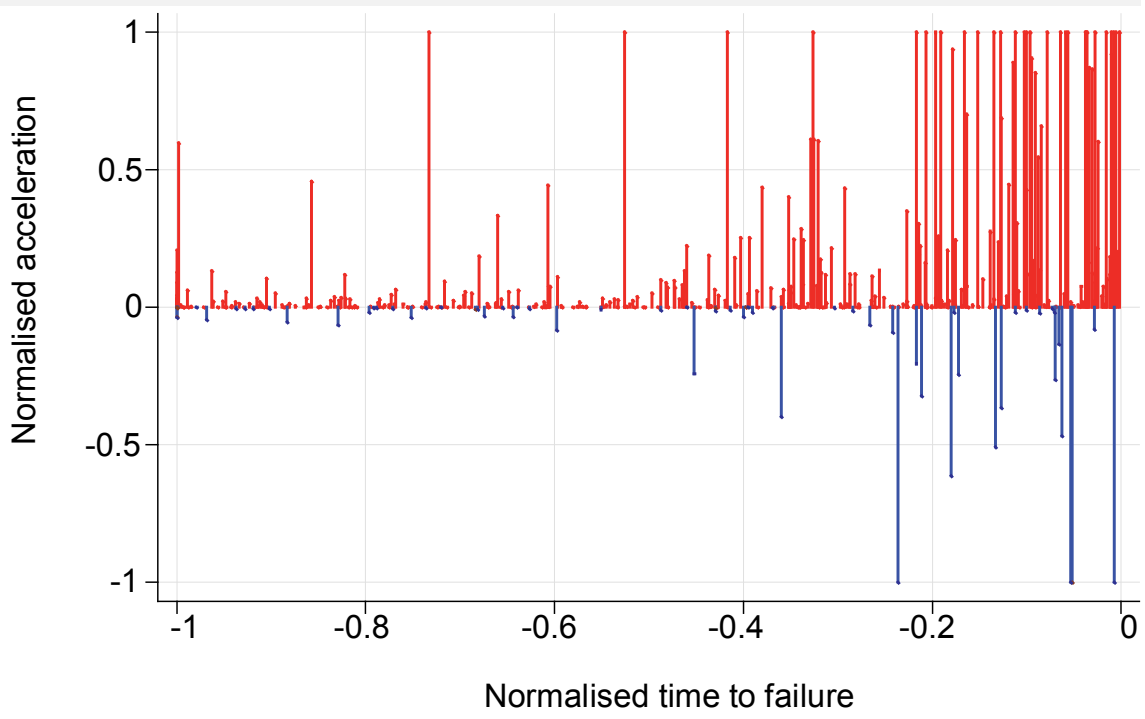

Figure 4.45: Positive (red) and negative (blue) values of acceleration re-scaled on normalised axes

Figure 4.46 compares the fits derived from the normal linear regression of inverse-velocity-time using a fixed x-axis intercept of zero (as discussed in section 4.2). Tertiary creep operates over different time periods and at different rates, ranging several orders of magnitude (figure 4.12 and 4.27). Coefficients of the linear fits range from $-3e^{-06}$ (Saleshan landslide, id=13) to -1.76 (Roesgrenda slide A), and are distributed around a mean of $-8e^{-02}$ with a standard deviation of 0.31. Figure 4.47 shows that most hillslopes are creeping at a rate close to 1 days/mm; however the distribution has slight bi-modality, distinguishing a second group of slopes accelerating at significantly greater rates, centred around ~-0.78 days/mm.

Although the criteria for the onset of tertiary creep is based on an r-squared value above 0.8, from the normal linear regression of inverse-velocity-time; the goodness of fit within the 31 database examples ranges from 0.81 (Selbourne slope cutting, id = 1) to 0.99 (Eskihisar coal mine wall, id = 19). This is best visualised when data is presented on normalised inverse-velocity- normalised time axes (figure 4.48). The differences in linear regression gradient (inset, figure 4.48) and distribution of data points around each fit indicate not only different rates but also different styles of tertiary creep. This transcends from observations of data projected in velocity-time

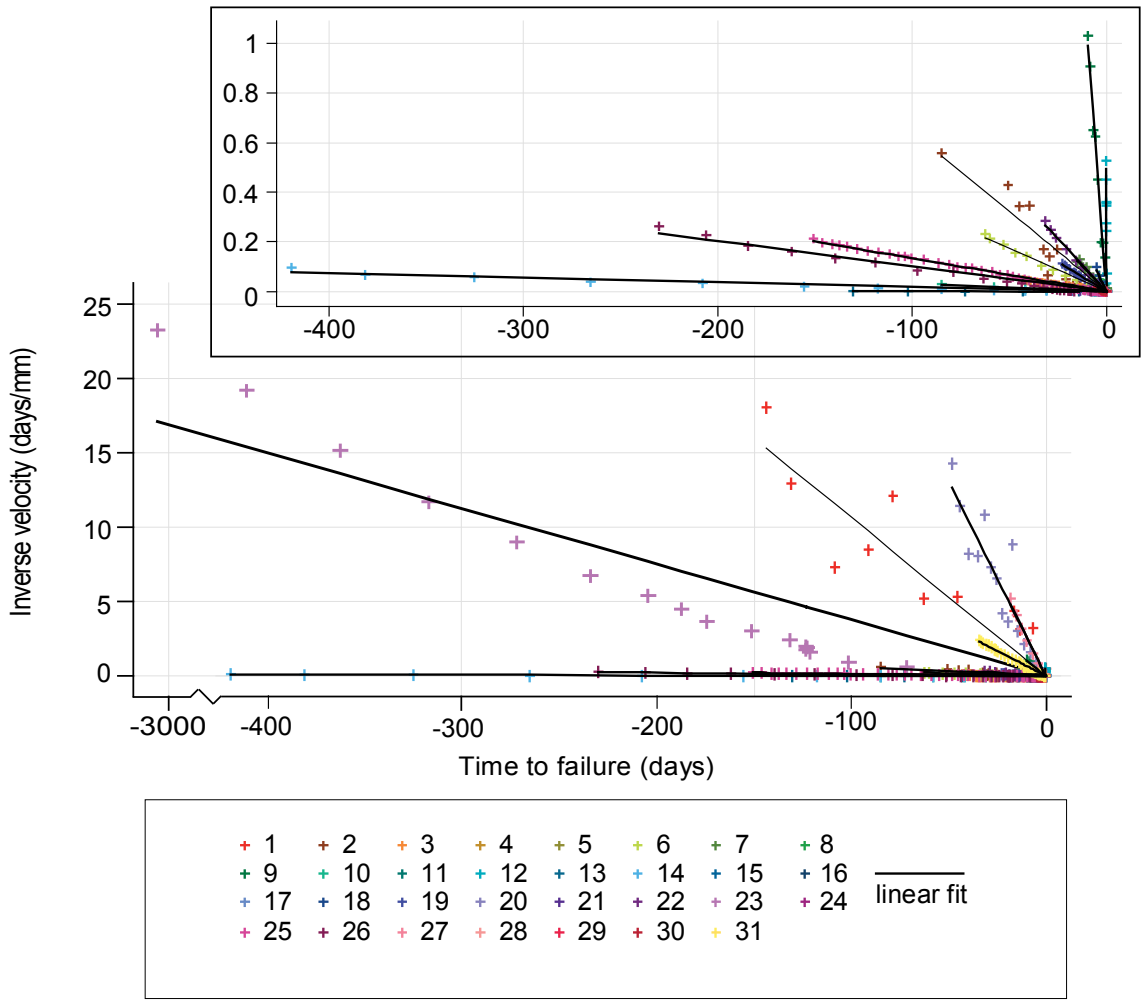

Figure 4.46: Inverse-velocity-time data from the tertiary creep stage. [Inset] Inverse-velocity- time data for failures whose maximum inverse- velocity is less than 1 days/mm; also excluding landslide ID 23.

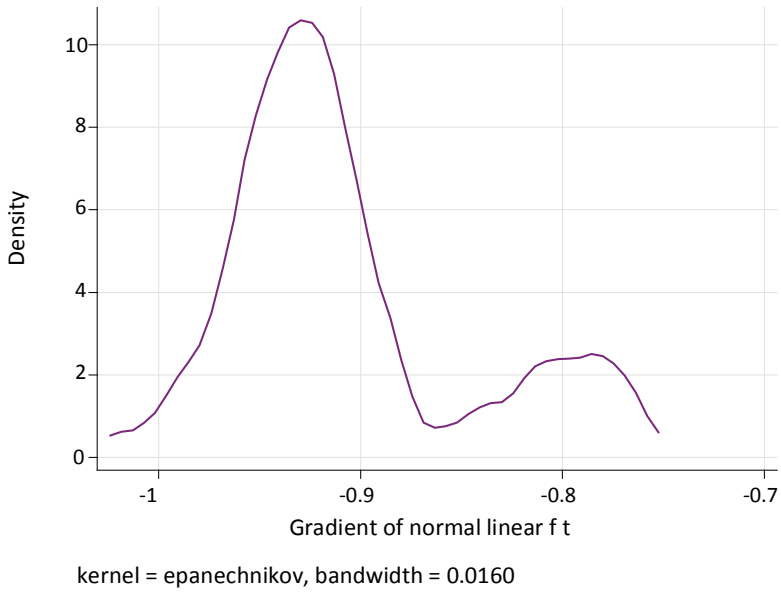

Figure 4.47: Kernel density estimate of normalised linear regression gradient of fit

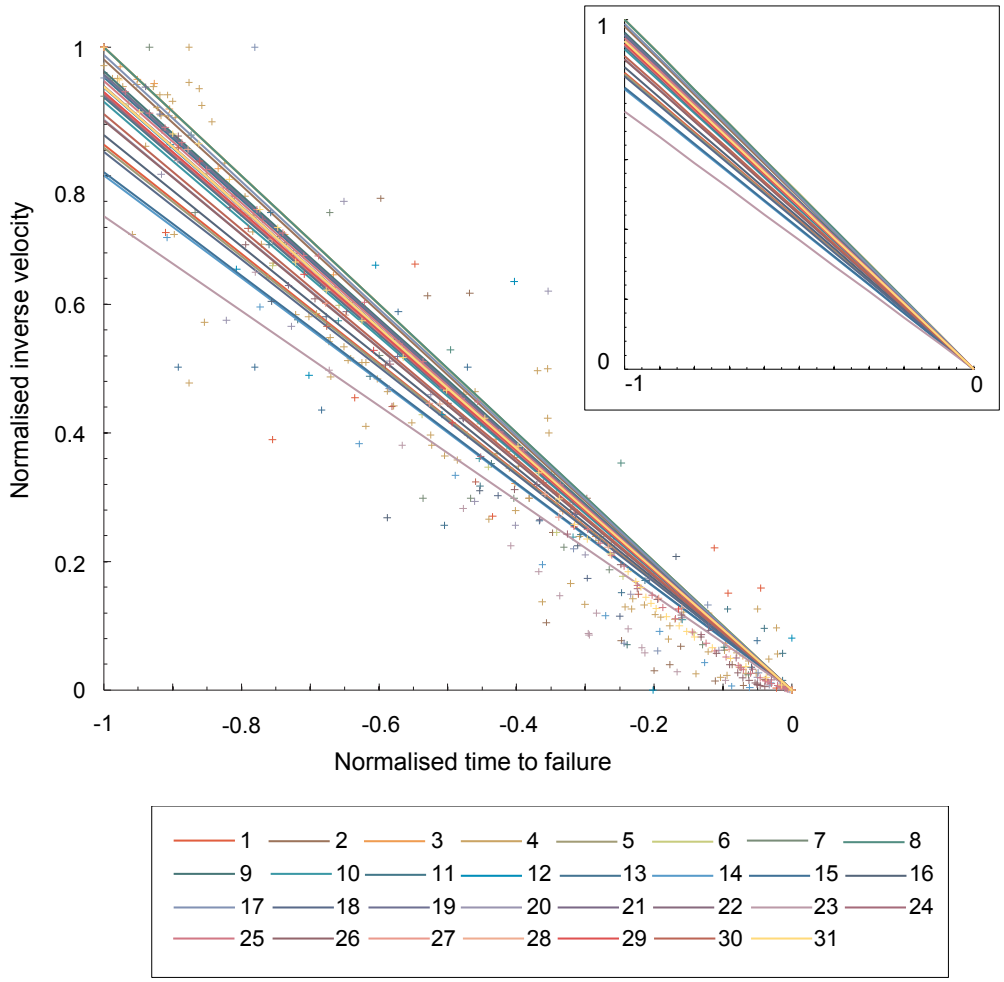

Figure 4.48: Normalised inverse-velocity- normalised time data from the tertiary creep stage. [Inset] Data displayed without normalised linear regression for clarity

space which presented a spread of acceleration trends (figure 4.38), characterised using Voight's parameters.

Normal linear regression of the coefficient and r-squared values resulting from the linear fits of inverse-velocity-time and the normal linear regression of creep duration and r-squared value, result in no significant correlation (0.148, 0.109 respectively). This suggests that the goodness of linear fit on inverse-velocity-time data does not relate to the rate of acceleration during or duration of, tertiary creep. Figure 4.9 presents the spread of residual values associated to the normal linear regression of inverse-velocity-time. 65% of residual values are negative, and show a clustering (48%

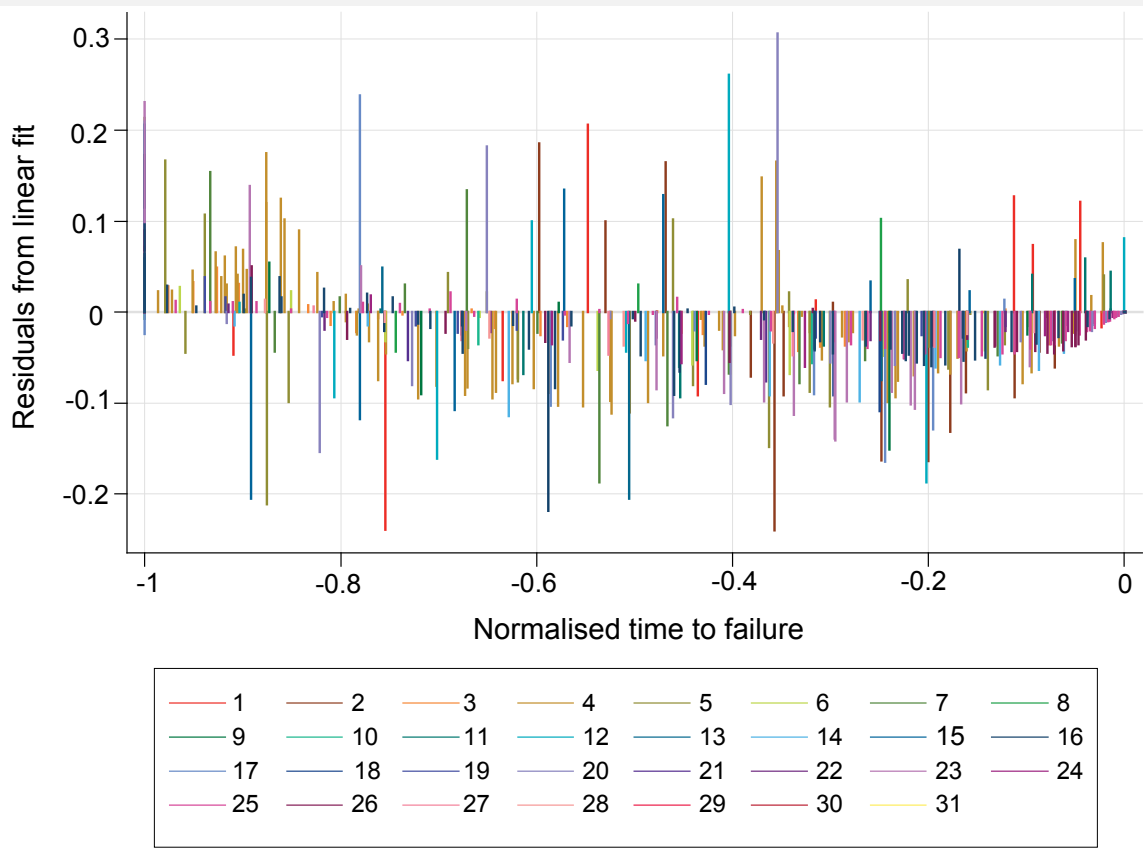

Figure 4.49: Residuals from the linear fit (normalised inverse-velocity- normalised time) plotted against normalised time.

of these) and decreasing trend in magnitude from -0.2 normalised time to the point of final failure. The negative residual values close to zero time indicate that the normal linear fit on data is over-estimating the time of final failure, whilst the positive residuals at this stage of creep suggest an underestimate. It is interesting that positive residual values cluster early in the creep phase between -1 and -0.8 normalised time. 54% of all positive residuals are located within this time frame, and average 0.064 ranging between 0.0024 to 0.2315. Examples, such as the 'unnamed slope' from Rose and Hungr (2009) (id=4), present clusters of positive residual values between -1 and -0.8, and clusters of negative residual values between -0.2 and 0. This indicates that a hyperbolic rather than a linear trend may best fit data.

Voight's (1989) model parameters were applied to characterise patterns of acceleration for data projected in normalised velocity- normalised time space (figure 4.34) using equations 16 and 17. An inverse of the hyperbolic function (equation 17) is

used to fit curves in Matlab's curve fitting toolbox to normalised inverse-velocity-normalised time projections of data

$$y = [A \times (1 - \alpha) \times (x) + y_f^{1-\alpha}]^{\frac{1}{(\alpha-1)}}$$

[Equation 18; adapted from equation 9 for Matlab Curve fitting]

This equation is valid under the condition α>1; A and y_f boundaries are set at zero and infinity (lower and upper) for the curve fitting procedure, and α is restricted between 1.001 and infinity (lower and upper). In common with the previous fitting procedure (16), curves were fitted to data using a robust regression, which considers the absolute distance between points and is most robust against outlying values. Table4 (appendix) contains the output α mean, α range, *A* mean, *A* range, y_f mean, y_f range and r-squared value for each hyperbolic fit.

Considering all 31 examples, the best fit α parameter (or mean α) ranges between 1.149 and 2.23. This indicates that all curves fall within a hyperbolically refined trend, rather than requiring exponential fitting. Figure 4.50 illustrates the resultant curves from the modelling procedure. The results are grouped by Generalised Saito ($1 < \alpha < 2$) and Saito ($\alpha = 2$) to Pure Saito ($\alpha > 2$), as outlined in figure 3.4. Only two examples fall within this latter grouping (figure 4.51(c)): Ota Mura landslide (id = 8), which is characterised by a Saito curve (α = 2.03), and Randa rockslide (id = 15), best modelled using a Pure Saito curve (α = 2.23). The spread of Generalised Saito fits (figure 4.51(b)) is predominantly α = 1.7 (86% of generalised examples), corroborating with Voight's (1989) values for α which ranged between 1.7 and 2.2.

A series of normal linear regressions were carried out between the mean α coefficient, and slope and failure characteristics such as landslide volume; this was undertaken in a similar manner to earlier assessment of the cumulative displacement-time data. Twelve different variables were considered (failure month, slope material and geology, failure mechanism, pre-failure gradient, vegetation condition, volume (and size), natural / man-made, creep duration, maximum rate, and total displacement), however no significant relationship between any attribute was derived from the analysis; r-squared values were not greater than 0.1 in all cases. This indicates

that similar tertiary creep behaviour may be observed on very different slope conditions and landslide scales. The Ota Mura landslide and Randa rockslide provide a useful example here. Creep behaviour at both sites was characterised by a mean α coefficient greater than 2 and the slides are similar in terms of pre-failure slope condition (i.e. both derived from un-vegetated soft rock slopes and failed in a translational manner over periods of time within one order of magnitude of each other (4.58 days and 10 days respectively). Despite some similarities, clear differences exist between the scale of landslide (65,000 m^3 and 7M m^3, respectively), maximum rate (273 mm/day and 9,643 mm/day, respectively) and total displacement (137 mm and 7,967 mm, respectively).

Figure 4.51 compares the goodness of fit r-squared values derived for each example from the normal linear regression and hyperbolic curve model. The coefficient of determination between the normal linear regression of these two parameters equates to 0.667, indicating that inverse-velocity-time data presenting a high r-squared value from the normal linear regression will tend to also have a good relative fit in the hyperbolic model. Where this is not the case, for example the outlier at approximately (0.86, 0.99) - Delabole Quarry (id = 23) - the hyperbolic model has a significantly better fit to data, indicating an α coefficient closer to 1; in this instance 1.566. There is a general tendency across the database for Voight's parameters to better model data than the normal linear regression. This is highlighted by the distribution of residual values (from all datasets) in figure 4.52. As expected, based on the method of model fitting, both sets of residual values are approximately normally distributed about the mean: 0.15 for the linear model and 0.002 for the hyperbolic curve. A greater number of residual values are between -0.1 and 0.1 for fits derived from Voight's parameters concurring with the higher coefficients of determination for hyperbolic fits observed in figure 4.51. In addition the spread of residuals over the duration of tertiary creep is different to those resulting from the normalised linear regression model. Although there is a clustering of residuals close to zero normalised-time, they are positive and of low value. Their presence indicates an under-prediction of failure time caused by a number of possible factors: (1) a poor fit of the hyperbolic curve over the entire creep duration, (2) an unexpected physical change in slope

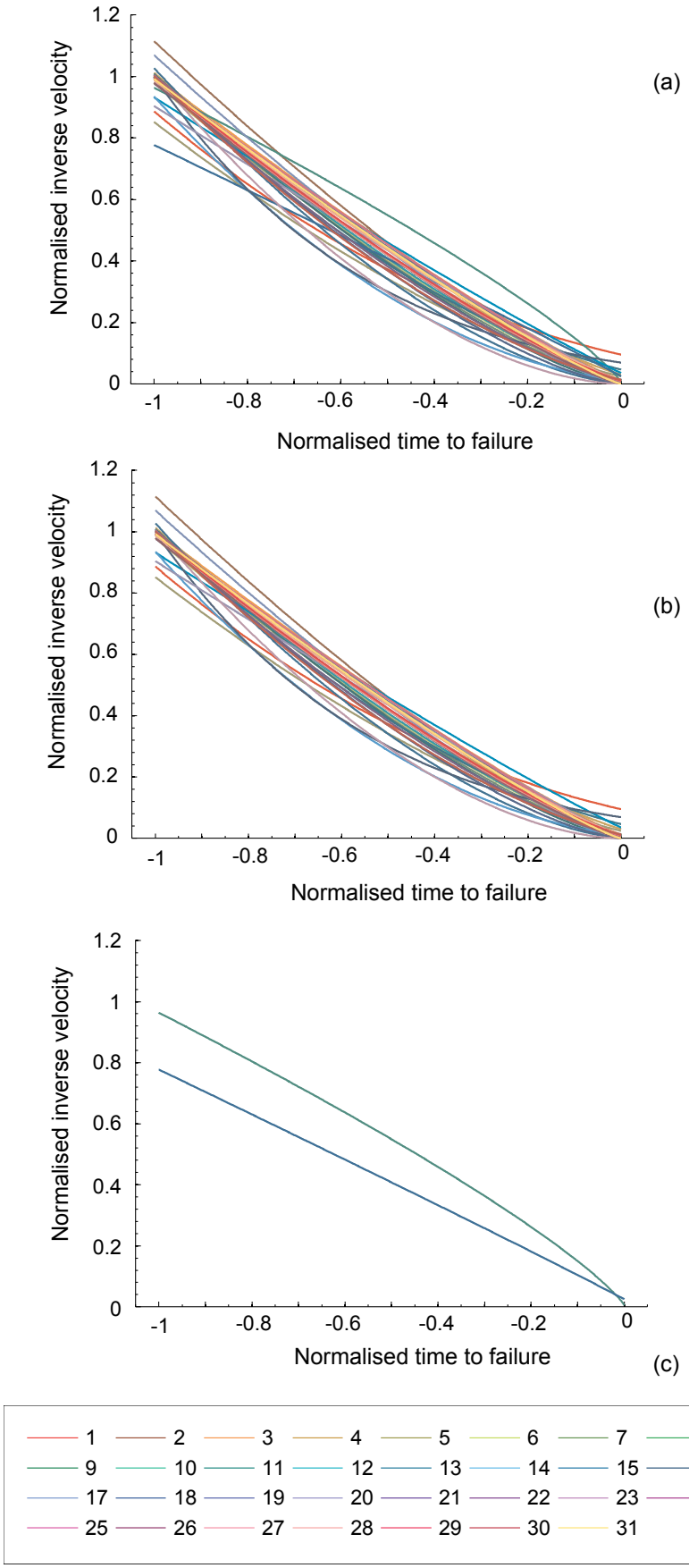

Figure 4.50: (a) Best fit hyperbolic curves of normalised inverse-velocity- normalised time data for the tertiary creep stage. (b) $\alpha < 2$. (c) $\alpha \geq 2$

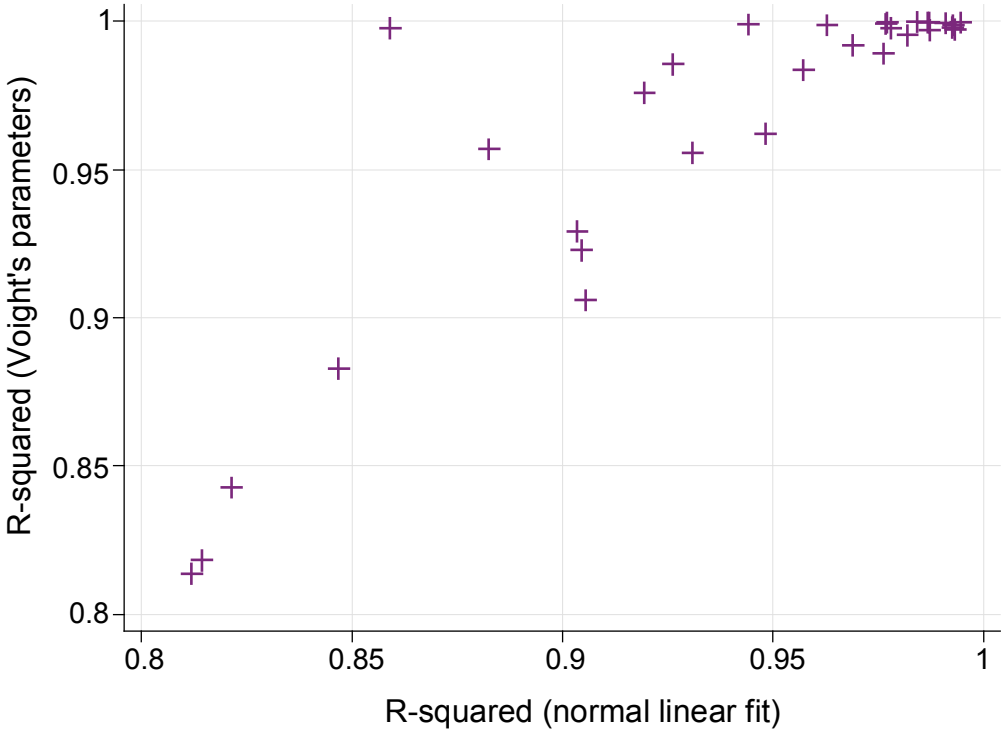

Figure 4.51: R-squared values from normalised inverse-normalised velocity-time data, corresponding to goodness of fit using Voight's parameters and goodness of fit using normal linear regression model.

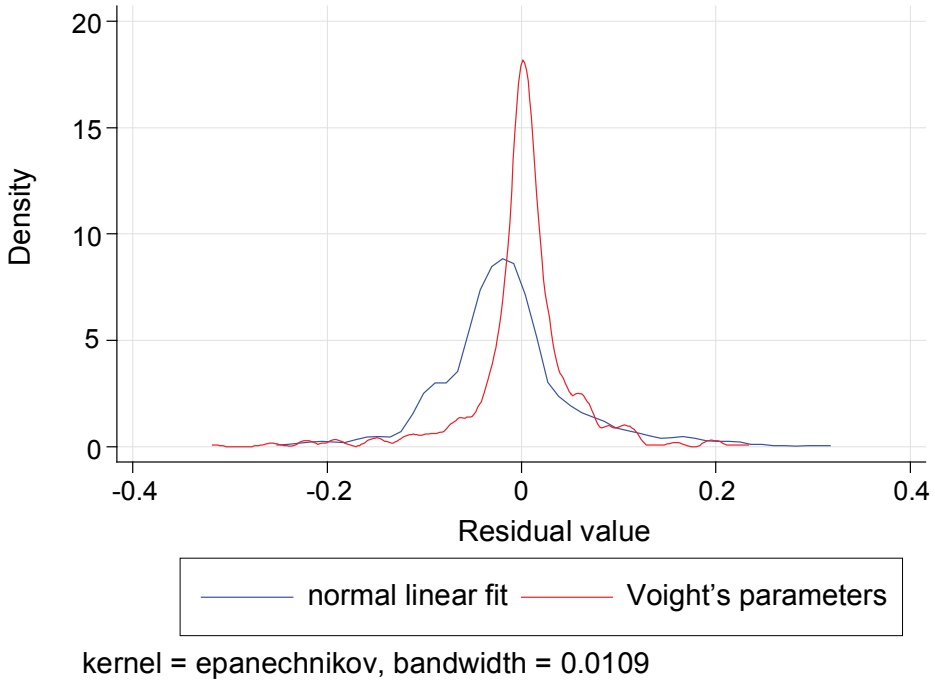

Figure 4.52: Kernel density estimates of the distribution of residual values resulting from the normal linear and Voight models fits for normalised inverse-velocity-normalised time data

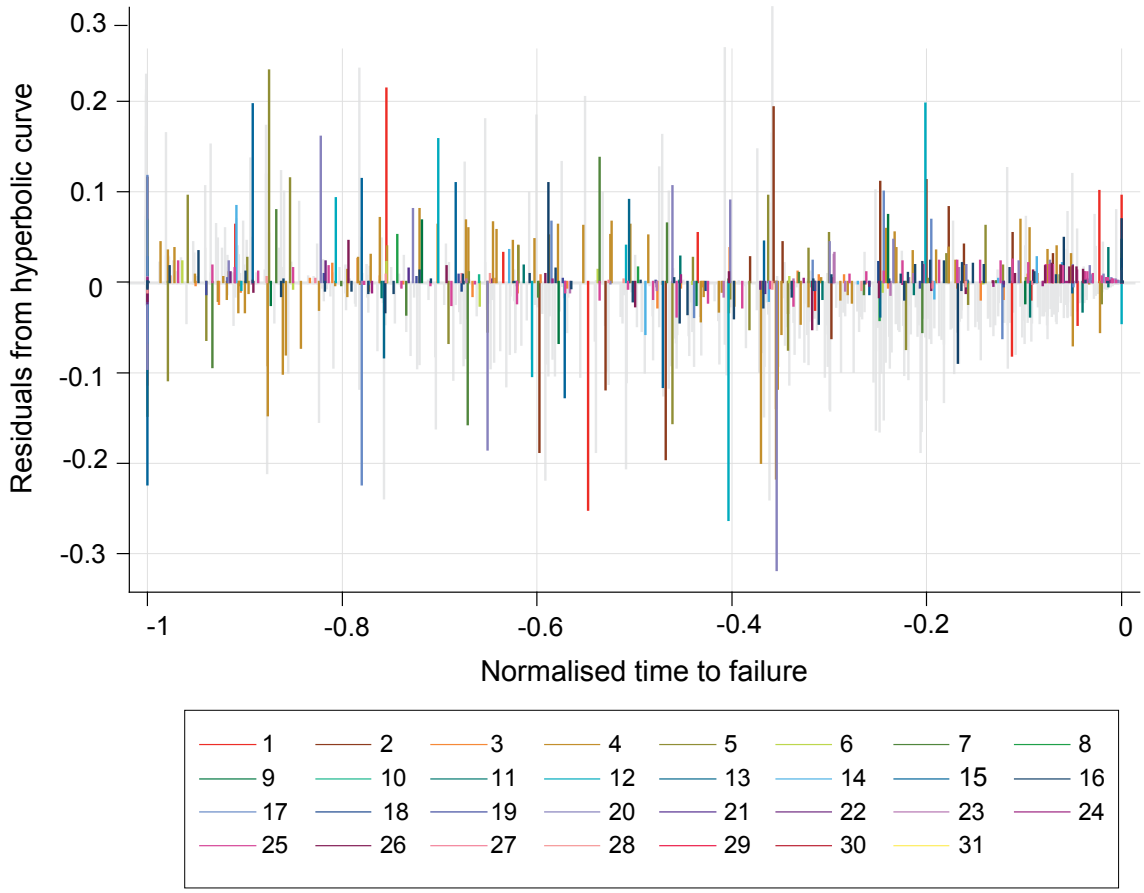

Figure 4.53: Figure 4.49: Residuals from the hyperbolic fits (normalised inverse-velocity- normalised time) plotted against normalised time. Residual values from the linear-fit (reference figure 4.49) are displayed in grey behind data to facilitate visual comparison.

behaviour that results in a deviation from the general deformation trend or (3) measurement error.

Inverse-velocity-time data is analysed retrospectively here to consider the variance in tertiary creep parameters and style, however if it is used to forecast failure then the point of slope collapse is unknown. The quality of fit and how it extrapolates from available movement records will affect the precision and accuracy of the forecast. The practical application of the Inverse-velocity method (normalised linear regression model) to forecast final collapse is considered in the following section (4.3.3)

4.3.3. Forecasting final failure

A normalised linear regression with 'no fixed x-intercept' was iteratively calculated by incrementally increasing the number of data points (minimum of three) included in the fit; simulating the growing acquisition of data through time common to monitoring an actively failing slope. Results are presented in figure 4.54 for each slope example. A normalised linear regression with 'fixed' x-intercept of zero was also calculated using the same procedure to provide a comparison between *a priori* and *retrospective* data analysis.

It is useful to visualise all thirty-one examples in this manner, which allows the overall evolution of forecast to be assessed. 61% of failures exclusively predicted the point of collapse before 'real' slope failure, providing a false positive early warning. 24% of examples however over-estimated creep duration. The minimum temporal range over which failure was predicted is 1.7 minutes (0.00118 days); 'un-named rockmass', Mufundirwa et al. (2010) (id = 17). This period corresponds to 8.32% of the total creep duration. In comparison, Delabole Quarry (id = 23) presented the broadest range for predicted final failure, 661.88 days. Although this is large in comparison to the minimum result, the duration of pre-failure creep on this landslide was the longest in the database at 3174.45 days. Thus the prediction period represents 21.77% of total creep duration. The temporal range over which failure is modelled for the 'unnamed slope' (id = 4) (Rose and Hungr, 2007) represents 573.1% of total creep duration. This is the greatest percentage gain from creep duration, accounting for 46.83 days range of prediction timings but only 8.23 days of tertiary creep. There is a significant relationship between creep duration and total temporal forecast range, but not creep duration and forecast range as a percentage of total tertiary creep period. The coefficient of determination from the normal linear regression of these variables results in an r-squared value of 0.974 and 0.004 respectively. This indicates that although long periods of tertiary creep are likely to result in a greater range of failure predictions, no relationship drawing together the proportionality of this period to creep duration exists.

The coefficient of determination of the normalised linear regression (no 'fixed' x-intercept) of inverse-velocity-time improves as the time to 'real' slope failure reduces

(figure 5.5). All examples reach a goodness of fit of 0.6 (r-squared) by -0.35 normalised time to failure; all but four examples (id = 1, 12, 15 and 20) have an r-squared value of 0.8 or above by -0.75 normalised time to failure. If the criteria for onset of tertiary creep (r-squared = 0.8) used to define this database, was applied in the forecasting context, 87% of slopes would be identified as entering tertiary creep within the first 25% of this phase (from its retrospective delineation). One critical point to draw on is the example (Tuckabianna West, id = 20), which presents an r-squared value of 0.81 at ~-0.5 normalised time, but this then drops to 0.6. Although the goodness of fit from this point improves to failure, it is important to recognise that fluctuations in the r-squared statistic may result in incorrect empirical interpretations; in this case it may be implied that tertiary creep had not in fact onset at ~-0.5 normalised time. Fluctuations in the r-squared parameter result from the inclusion of data with significant residual from the previous linear fit. The minimum range of r-squared values calculated from a single creep example, equated to 0.0018 (Ota Mura landslide, id = 8); r-squared ranged between 0.982 and 0.984, displaying a consistently good fit on data. Interestingly the alpha value derived for this example from the hyperbolic model (figure 4.50) is the highest within the database ($\alpha = 2.23$), corresponding to a convex fit with data. Given that $\alpha = 2$ is linear (Pure Saito), it would be expected that creep patterns tending to an α value close to 2 will perform better when normal linear regression is applied to forecast failure. However there is no relationship between the modelled α value (from Voight's parameters) and the range of r-squared values derived as the fitting iteratively progresses in time.

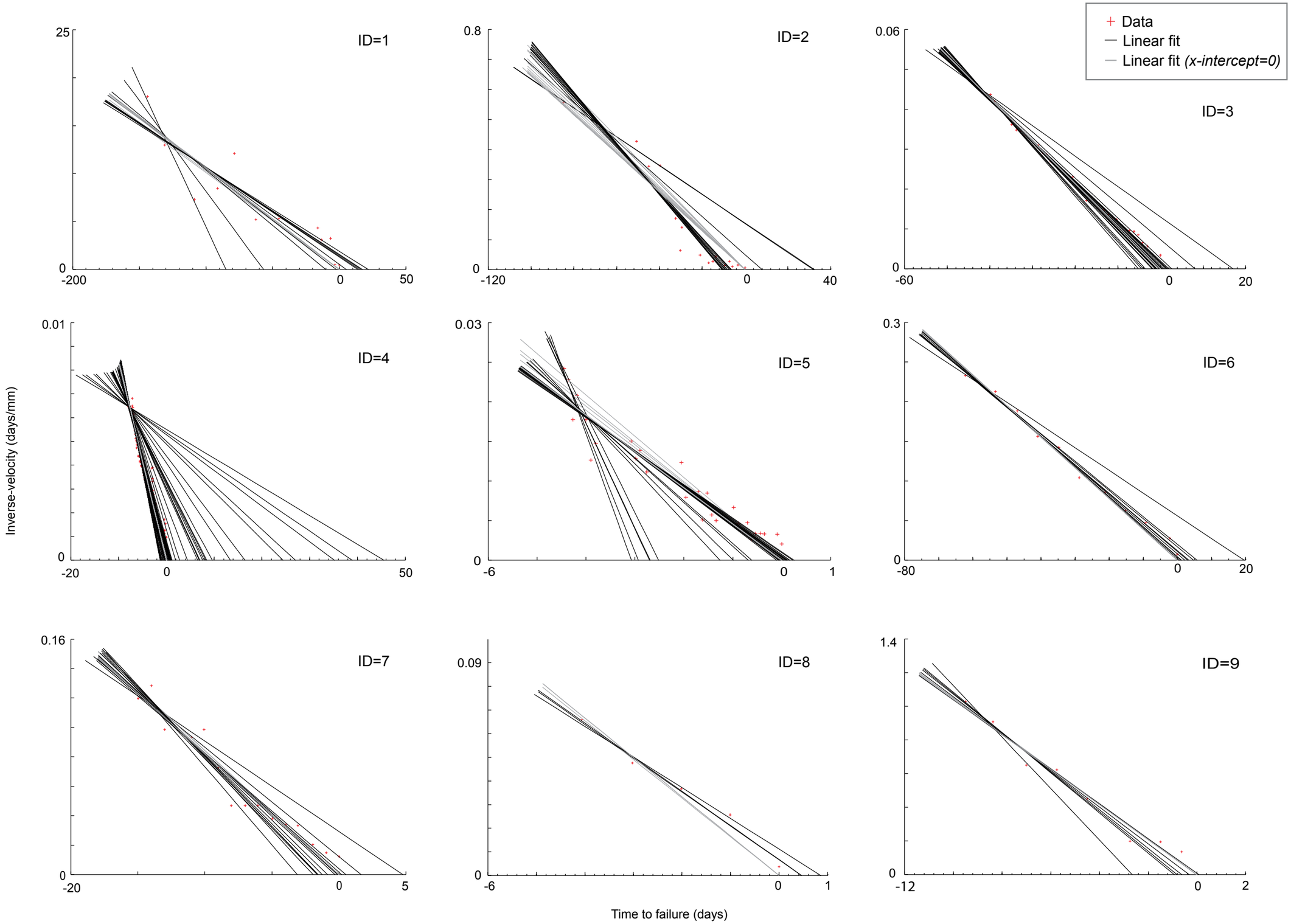

Figure 5.54:(a) Results from the iterative normal linear regression (grey corresponding to 'fixed' x-intercept) procedure carried out on inverse-velocity-time data. Landslide examples are presented on individual axes.

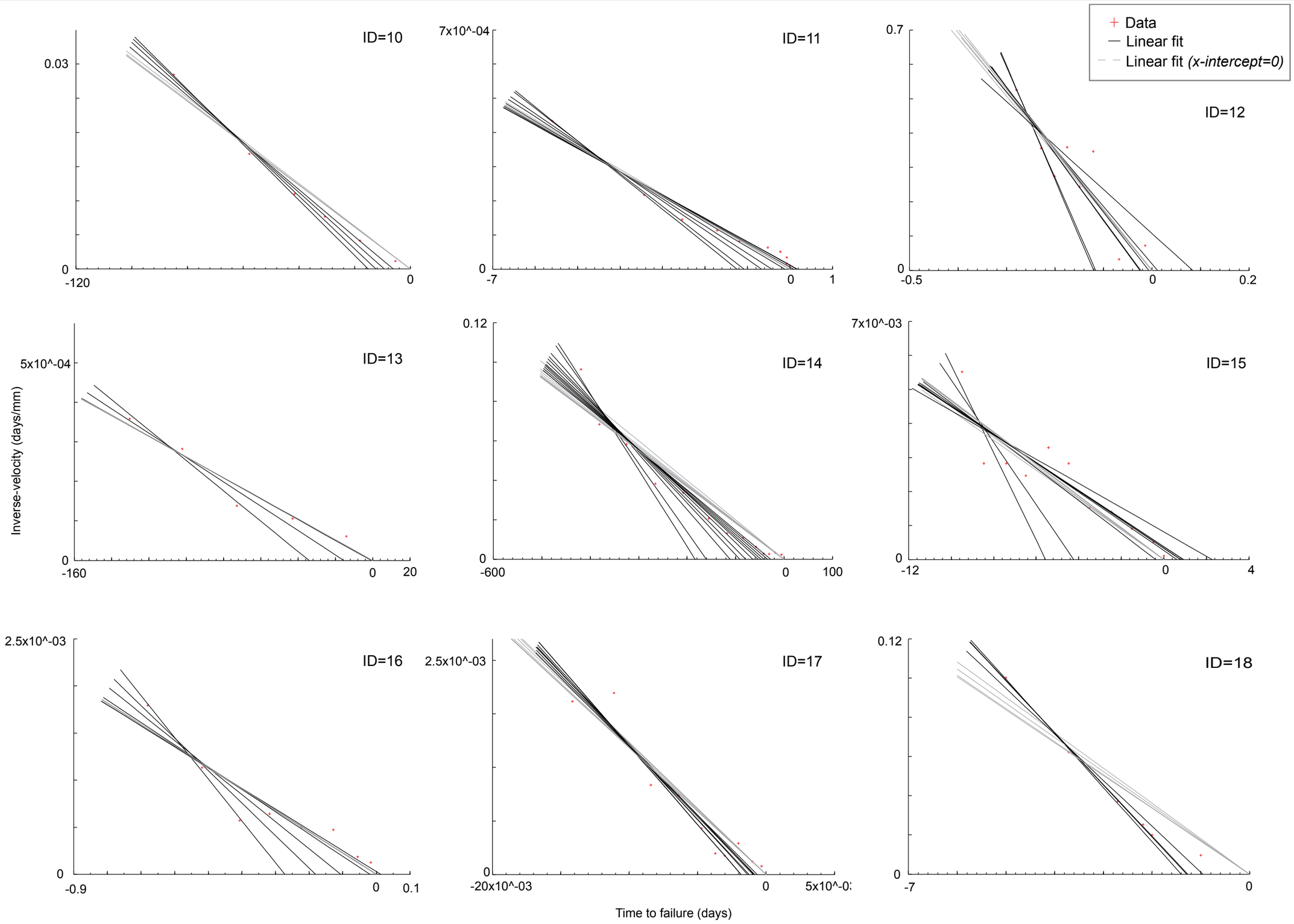

Figure 5.54:(b) Results from the iterative normal linear regression (grey corresponding to 'fixed' x-intercept) procedure carried out on inverse-velocity-time data. Landslide examples are presented on individual axes.

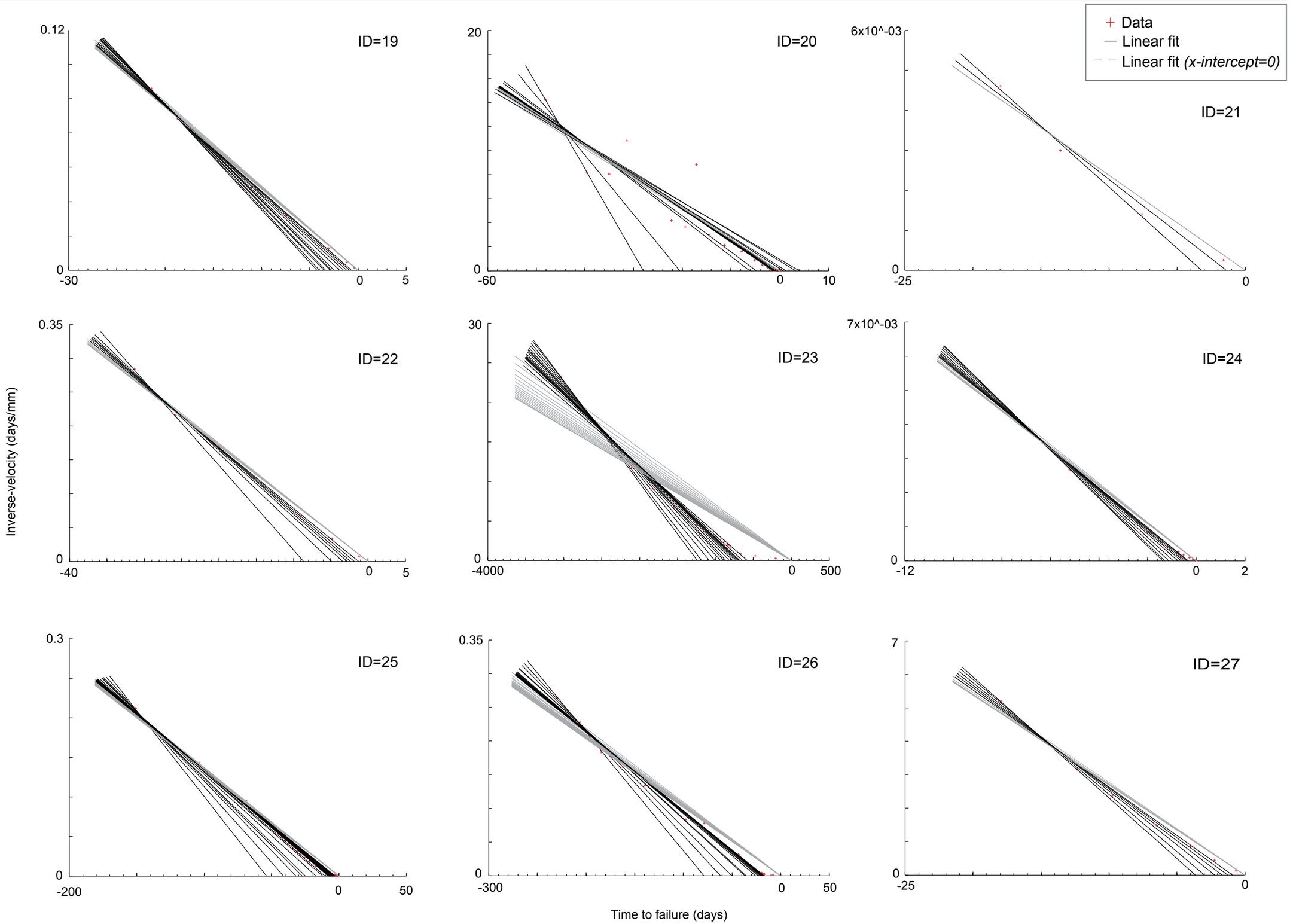

Figure 5.54:(c) Results from the iterative normal linear regression (grey corresponding to 'fixed' x-intercept) procedure carried out on inverse-velocity-time data. Landslide examples are presented on individual axes.

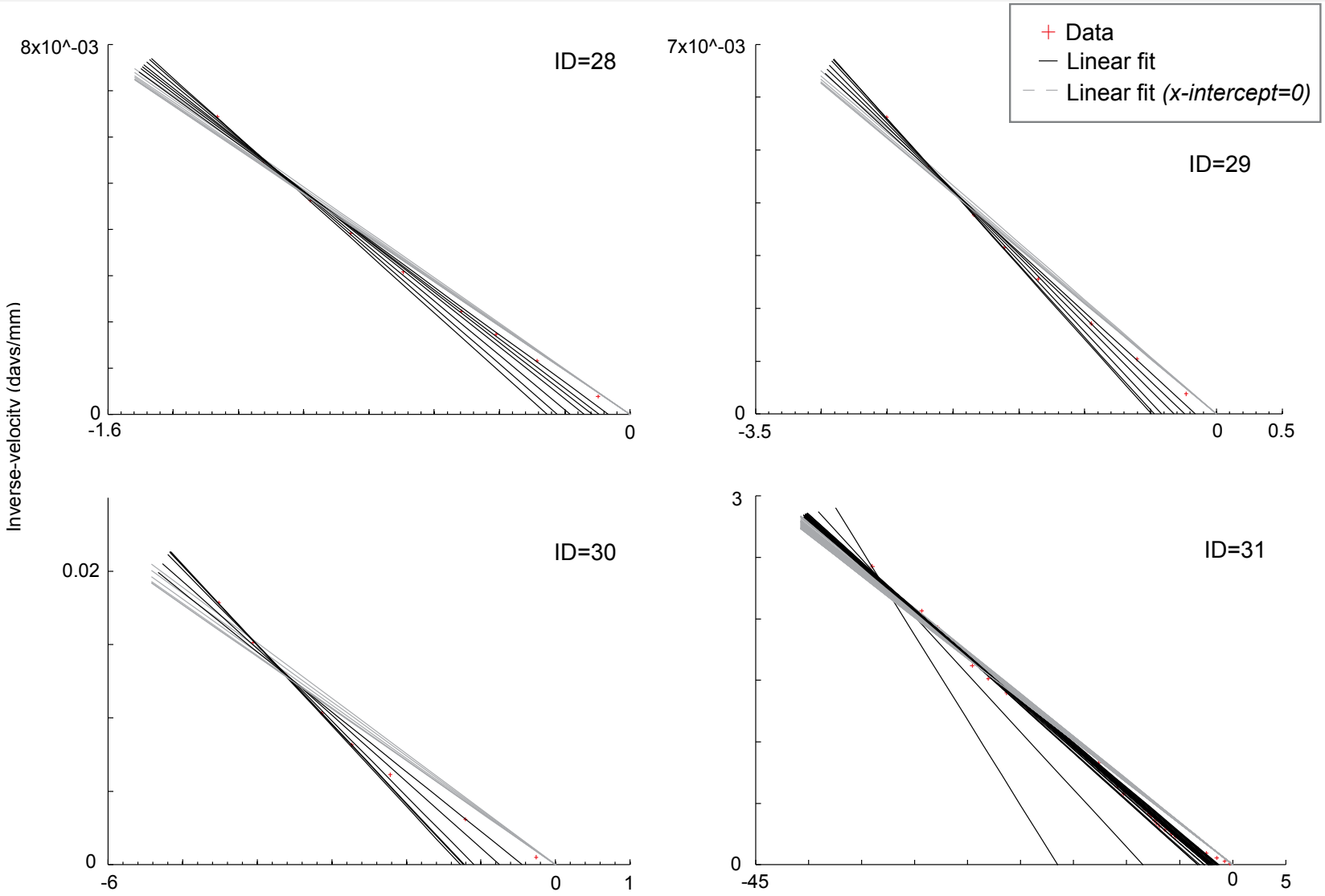

Figure 5.54:(d) Results from the iterative normal linear regression (grey corresponding to 'fixed' x-intercept) procedure carried out on inverse-velocity-time

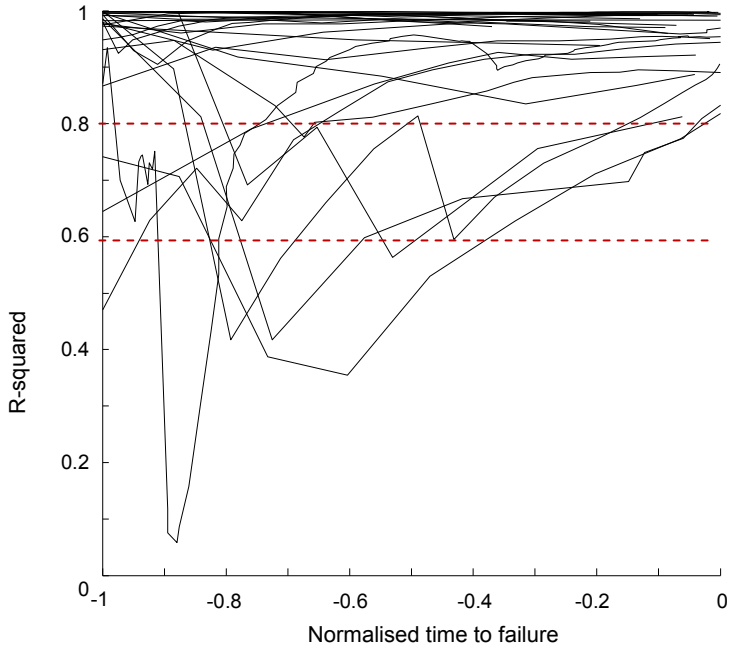

Figure 5.55: Summary of changes to the r-squared statistic through normalised time resulting from the normal linear regression of inverse-velocity-time data. All 31 examples are accounted for on this plot.

This section presented data from thirty-one examples of tertiary creep, digitised from published pre-failure slope deformation data. Results presented considered the variation in slope characteristics (section 4.3.1), patterns of deformation within this tertiary phase (section 4.3.2) and the accuracy of *a priori* applications of the Inverse-velocity method to forecasting. Results will be discussed in chapter 5 .

CHAPTER 5

Discussion

5.1. Introduction

This chapter returns broadly to the main aim and objectives of the thesis (chapter 1). Sections 5.2 discuss key results from the tertiary creep database presented in chapter 4. Following from this, section 5.3 evaluates the uncertainties involved in applying the Inverse-velocity method to forecasting and early warning. These findings inform section 5.4, which considers ground-based monitoring procedures potentially capable of detecting pre-failure deformation. Within this section a case study is used to preliminarily highlight research challenges involved in applying the proposed instrumentation within the field of small movement detection. Section 5.5 briefly reviews the limitations of records within the tertiary creep database. Discussions will be concluded in chapter 6.

5.2. Variations in tertiary creep

The collation of published data provides a platform on which to examine different patterns of tertiary creep and consider the effect of associated slope characteristics- such as geology- on basal shear zone mechanisms. Key observations were made from the tertiary creep database, each of which are listed and then discussed below.

(1) The duration of tertiary creep examples range between ~37 minutes (0.026 days) and 3,171.45 days
(2) During this period, slopes displaced between 32 mm and 95.21 m (95,211 mm)
(3) Rates of deformation range between 2.19 mm/day and 1341.65 m/day (134,165 mm/day)
(4) Slopes exhibited different styles of acceleration which may be characterised by the parameters of Voight's (1989) model.
(5) There are no significant relationships between patterns of tertiary creep and pre-failure slope attributes

Although the duration of tertiary creep ranged from tens of minutes to thousands of days, most landslides occurred following less than 500 days of pre-failure final phase deformation. The duration of tertiary creep highlights the timescales over which slopes accumulate strain. Given that the final phase of creep is a period of acceleration and the primary and secondary stages of the model are considered transient and steady-

state periods of deformation (figure 2.7), creep durations of 3,171.45 days (for example) infer years worth of pre-failure movement before reaching critical strain, particularly if local physiographic mechanisms are relatively steady (section 2.3.3.4).

Petley et al. (2005a) suggest that the period of development of progressive failure depends on the material involved and the size of the landslide. Typically 85% of the failures in the database occurred from rock slopes, however no significant correlations were found relating creep duration to geological strength (section 4.3.1). Slopes composed of clay showed a high coefficient of determination between maximum velocity and total displacement (r-squared = 0.967), indicating that sub-grouping slopes by characteristic identifies specific patterns of behaviour from the wider database of examples. Whilst these relationships are interesting, it is important to be critical about the basic method of classifying slopes in the database within the bounds of hard rock, soft rock and clay descriptors. Importantly publications typically only contained minimal information on the pre-failure condition of slope (section 4.2). Aleatory uncertainty is introduced both on the grounds of source information and classification within simplistic geological bounds. Classifications of geological strength or rock mass ratings (RMR) do not capture the uniqueness and complexity of slopes in which destabilising forces act anisotropically to reflect the frictional strength and structure of the mass (section 2.3.1). In common to this thesis, Glastonbury and Fell (2002) found no apparent relationship between strain and their choice of rock mass rating. Given that intact material properties have a strong bearing on deformation parameters in laboratory testing (section 2.3.1), it may be suggested that slope structures supersede observed empirical relationships between material strength, and creep duration, maximum velocity and total displacement.

Although Petley et al. (2005a) detail landslide size as a key contribute to creep duration, results from this database suggest that the mode of failure has more significance to total displacement-duration creep parameters. Glastonbury and Fell (2000) indicated that toppling failures exhibited the greatest relative strain prior to collapse and translational failures the least. The higher coefficients of determination between the normalised linear regression of total displacement-duration for translational and roto-translational slides (section 4.3.2), suggest that acceleration patterns during creep are less erratic than for toppling examples. The complexity of

toppling movements, which may involve a degree of flexure (Duncan, 2004), potentially explaining the large differences in maximum displacement rate, 8.03 mm/day and 2619.88 mm/day, observed between the toppling failures in the database.

Pre-failure slope movements are dependent on basal deformation processes (Petley et al., 2002). The thirty-one database examples exhibited a range of different patterns of displacement through time (e.g. figure 4.12). This was initially evaluated using the hypsometric integral of each normalised cumulative displacement-normalised time plot. Results were distributed around a mean value of 0.347 with a standard deviation of 0.127 (figure 4.19) reflecting that ~71% of examples presented with a concave cumulative displacement-time curve, characteristic of accelerating displacement. Acceleration curves were derived from velocity-time data using equations 16 and 17, which calculated the best hyperbolic and exponential fit following from the work of Fukuzono (1985), validated by Voight (1989). Curves were also derived using equation 18 from the inverse-velocity-time projection of data. Importantly there are striking differences between the α coefficient from fits on the same series of data (but in different projections). This constant controls the sensitivity of accelerating activity (Crosta and Agliardi, 2003) by the changing general steepness in curvature and should remain the same in this instance. There is a poor correlation (r-square of 0.0079) between the velocity-time and inverse-velocity-time constants used for each curve suggesting the former parameterisation of data is not reflective of the latter. There are several possible reasons for this: (1) decimal precision errors from the conversion of data into inverse-velocity and subsequently onto a normalised scale or (2) the treatment of strong fluctuations in data close to zero time (i.e. it was commented that strong location fluctuations in points may not have been properly modelled by the velocity-time curve, section 4.3.2); together these potential errors contribute to computational problems similar to those noted by Borsetto et al. (1991). Exploring these further is beyond the scope of this thesis, however results from the inverse-velocity-time series present a good fit to all datasets and values of α are predominantly within the range anticipated (1.7 to 2.2) in light of Voight's (1989) validation work.

Constants defining curves represent the material characteristics for time invariant external conditions (i.e. load and temperature) (Crosta and Agliardi, 2003), and provide insight into physical mechanisms driving creep (Kilburn, 2003). Cracking dominated by crack growth is characterised by an $\alpha \approx 2$, representing linearity (Pure Saito) in inverse-velocity-time data (Voight, 1989; Crosta and Agliardi, 2003). The transition from exponential ($\alpha<1$) to hyperbolic ($\alpha=1$ to 2) patterns of deformation indicates a shift from creep dominated by crack nucleation to uncontrolled fracture propagation (Kilburn, 2003). Although Petley et al. (2005a) characterise tertiary creep as the point at which micro-fracture density becomes sufficiently high that neighbouring cracks begin to interact (section 2.3.3.2), landslides in this database are characterised by α values ranging from 1.15 to 2.23, indicating that the failure of some slopes is in part controlled by fracture density rather than purely coalesce and propagation. Importantly it is recognised that slopes are characterised on a sliding scale between crack nucleation (essentially ductile) and growth (brittle), and that processes are operating at different spatial scales from sub-microscopic to macro-fractures (Kilburn, 2003). Although generalised physical controls on patterns of creep may be postulated, the finer mechanics of individual basal shear zones is difficult to elucidate; particularly given the epistemic uncertainty around basal- surface landslide interactions and the provenance of most slope data.

5.3. Accuracy and precision of the Inverse-velocity method for slope forecasting

In the context of landslide forecasting it is critical to understand the effect deviation from linearity in inverse-velocity-time has on the accuracy of applying the Inverse-velocity method. 86% of examples in the database were modelled with an α constant greater than 1.7. Although residual values (figure 4.9) indicated that Voight's (1989) parameters rather than a linear fit better models data (figure 4.5.1, section 4.3.3), the Inverse-velocity method based on normalised linear regression, is easier to extrapolate to failure (Rose and Hungr, 2007). Preferentially, the effect of forcing linearity typically results in pre-failure warnings of collapse; 61% of failures would produce false-positive early warnings if considered *a priori* to collapse. This is common to observations by Mufundirwa et al. (2010) who indicate that the initial convex nature of most inverse-velocity-time plots results pre-emptive "unsafe predictions".

In terms of early warning, problems are most acute when models produce false negative forecasts (i.e. over-estimate creep duration), or generate large shifts in predictions, reflecting either (1) changes in slope behaviour (Ota Mura landslide, Petley and Rosser, 2009) or (2) instrumental error (Crosta and Agliardi, 2003). Tertiary creep for the database of examples was defined by an r-squared threshold of 0.8, from the normal linear regression of inverse-velocity-time using a fixed x-intercept through the point of final slope collapse. Delimiting this phase during *a priori* forecasting produces different creep durations than when data is considered retrospectively (figure 4.53). The r-squared threshold was chosen as criteria for tertiary creep in the database following the precedent of past published examples (e.g. Petley et al., 2002). When considered *a priori*- whereby incremental data points were included in the regression to simulate 'real-time' forecasting- tertiary creep was identified on 87% of slopes within 25% of the 'actual' retrospectively defined creep duration (figure 5.55). Four examples did not reach the 0.8 r-squared threshold until just before slope collapse.

Considering this, a more relaxed threshold of 0.6 r-squared is proposed for *a priori* assessment to capture the onset of self-reinforcing crack development. This would also reduce confusion associated with sudden changes in deformation behaviour, within the tertiary phase; Tuckabianna West (id = 20) for example showed a significant reduction in goodness of fit halfway through the creep period. Problems arise however if this threshold is relaxed and used to interpret deformation when the physical mechanisms operating in the basal shear zone are unclear. Ductile deformation at the shear zone displays an asymptotic trend (figure 3.5 (a)) which cannot be modelled in the same manner as brittle failure, because it is not controlled by strain localisation and crack growth (section 2.3.3.3). Weakening the r-squared threshold may result in an un-meaningful forecast of non-brittle slopes.

Monitoring of unstable slopes to supply data for the Inverse-velocity method needs to be initiated as soon as a potential failure is identified. As tertiary creep progresses the estimate of failure time improves (Saito, 1969). Importantly monitoring must be adaptable and increase measurement rate as the slope accelerates. This is crucial in order to update predictions of failure in line with significant changes in deformation behaviour (Rose and Hungr, 2007). Calculating the appropriate degree of

uncertainty associated to failure forecasts addresses statistical errors associated to normal linear regression and the quality of monitoring data. The former have been discussed briefly in chapter 4 and earlier in section 5.2, section 5.3 discusses monitoring considerations and challenges in the context of applications of the Inverse-velocity method.

5.4. Monitoring challenges

Although the Inverse-velocity method has been successfully applied to a number of different sized brittle failures derived from an array of settings (chapter 4); challenges are faced identifying, delineating and monitoring instabilities to provide representative data for the forecasting of slope collapse (Petley et al., 2008a). Informed from the analysis of 31 examples of tertiary creep and in consideration of variations in pre-failure slope characteristic the following requirements are proposed ranked in order of importance, for monitoring instrumentation used to detect final phase movements:

(1) Spatial accuracy to ~10mm

For soil slopes, the minimum total displacement within the database during tertiary creep was identified as 32 mm (Selborne slope cutting, id = 1). Taking 'three', as the minimum number of points on which to calculate a normal linear regression, this value of displacement is divided to produce a minimum magnitude for spatial instrument accuracy of ~10mm. For rock slopes, the minimum total displacement is 39mm (un-named slope in Japan, id = 17), and thus indicates a value of similar magnitude, ~13mm, for monitoring spatial accuracy.

(2) Continuous measurement (high repeat rate ~10 minutes)

The minimum creep duration within the database was ~37 minutes (0.026 days) (id = -17). Following the same approach as used to recommend spatial accuracy, this value is divided by three to produce a maximum repeat rate of ~10 minutes. More importantly, instrumentation should have flexibility in acquisition rate to gradually increase measurements in response to accelerating activity. This is an important reflection on the nature of pre-failure creep which follows an exponential or hyperbolic acceleration curve (section 5.2).

The first two monitoring recommendations result from the minimum observed values of total displacement and total duration, in the database of 31 failures. The conditions proposed here are for a universal instrument capable of monitoring any of the landslides in this database, however it is recognised that these are not definitive limits for pre-failure slope deformation. Identifying slope conditions resulting in higher rates of pre-failure deformation will refine judgement on the necessary spatial accuracy and measurement repeat rate of instrumentation. Although relationships between slope characteristics and movement parameters were not evident in the database some assumptions may be made based on published literature.

Landslides composed of bedrock are likely to have a larger volume than soil slides covering the same surface area because their scar geometry is defined by hillslope structure (section 2.3.1.2) rather than soil availability (Larsen et al., 2010). This leads to shallow soil slides and deeper bedrock failures. Referring to figure 2.1, an object (or landslide) of greater volume will move faster than an object of smaller volume on the same slope, when the density and shape of the two object are the same. At a simple level increasing landslide volume is likely to increase slope deformation rate. Landslide geometry is also a key player here, primarily controlling the amount of tertiary displacement. Considering two landslides of identical surface area and material, but of different depths; the deeper shear-surface would take longer to form because more material has to be deformed for micro-fractures to coalesce as a failure plane (section 2.3.3.2). This suggests that increasing the size of the shear surface increases the duration of tertiary creep, and also the total slope displacement dependent on sub-surface landslide geometry. Furthermore, steepening the slope gradient (and associated failure plane) is likely to increase deformation rate by increasing the driving force destabilising the hillslope (box 2.1).

Considering geometrical landslide characteristics separately provides a simplistic theoretical expectation for relative rates of pre-failure creep. However progressive hillslope failure is a function of a multitude of different interacting conditions (i.e. physiographic setting, slope material, and the sequence, dynamics and intensity of environmental forcings; see section 2.3.3.4). Until the intricacies of different controls on slope stability are better understood, it is difficult to propose instrument parameters for spatial accuracy and repeat rate, specific to certain slope

attributes (such as mode of failure). For this reason a conservative approach is taken and the minimum values for total displacement, and duration within the database are recommended.

(3) Surface-based capture

The Selborne slope cutting experiment (Cooper et al., 1998) highlighted that different parts of a slope undergo different amounts and patterns of deformation; in this case cracks propagated outwards from the centre of the shear plane, resulting in a mechanical lag in deformation at the backscarp. The kinematic variability and complexity of landslides is best captured using surface based measurement (Angeli et al., 2000).

(4) Ground-based view angle

The majority of failures within the database occurred from gradients over 45 degrees. Greater spatial coverage on steep slopes such as these is gained using ground-based data capture (Rosser et al., 2008). Positioning instruments to overcome the effects of ground cover (e.g. vegetation) and occlusion when dealing with complex surface geometry, is challenging and may require multiple perspectives to fully capture a scene (Petrie and Toth, 2008a). Slopes with gentler gradients may require elevated monitoring positions, and benefit from view angles closer to a bird's eye perspective. Importantly ground-based measurements are easily repeated, compared to satellite or aerial capture which does not permanently monitor a site.

(5) Long duration fixture

The longest duration of tertiary creep within the database was 3,171.45 days (Delabole Quarry, id = 23). As discussed in section 5.2, this indicates significantly long periods of deformation, particularly if the instability is detected before entering the tertiary phase. Long duration fixtures must be robust against long resident times. Remote monitoring overcomes the problems associated with manual installation and maintenance on unstable terrain (Lim, 2006), particularly in the context of permanent instruments.

Section 3.4.3 reviews methods of monitoring movement on hillslopes. Table 3.1 provides a useful guide on which to select instrumentation that satisfies as many of the desired monitoring requirements- outlined above- as possible. Importantly there is currently no 'magic' instrument that automatically fulfils everything required. Terrestrial laser scanners, terrestrial photogrammetry and ground-based InSAR all provide surface-based data from a ground-based set-up. Of these instruments, terrestrial laser scanning (TLS) is the most promising technology for permanent landslide monitoring; processing may be automated for a 'batch' of data (unlike terrestrial photogrammetry) and it is lower cost than a ground-based InSAR system.

Although applications of this instrument to unstable slopes are far reaching, few publications (Abellán, 2009; Araiba, 2006; Monserrat and Crosetto, 2008; Schwalbe et al., 2008; Teza et al., 2007; Tsakiri et al., 2006) have attempted to extract 3D displacement vectors from TLS data. Achieving high precision measurement hinges on having a good understanding of data acquisition, processing and propagating errors resulting from each methodological step. Typically acquiring data based on time-of-flight (Fröhlich and Mettenleiter, 2004; Staiger, 2003), medium to long range (distance <200m) terrestrial laser scanners capture surface information in dense three-dimensional point clouds (x,y,z) with an additional reflex intensity value (Feng and Roshoff, 2004). Table 5.1 outlines a processing framework for point cloud data from acquisition to analysis, providing a useful summary on which to discuss and recommend further work to develop methods of monitoring pre-failure slope creep that recognise the scale of behaviour (based on observations in chapter 4) and result in appropriate data on which to apply the Inverse-velocity method.

Exploring each element of table 5.1 further is beyond the scope of this thesis; its presentation here is to highlight three key points:

(1) The complex and numerous sources of potential error within a processed TLS data set
(2) Currently no automated method exists to derive 3D movement vectors from surface data

	Sources of measurement error		References
(1) ACQUISITION	**TLS instrument**	Consistency of optical transmission efficiency (laser power)	(Höfle and Pfeifer, 2007; Pfeifer et al., 2007)
		Laser wavelength	(Petrie and Toth, 2008bb)
		Accuracy of system to detect return signal from laser pulse	(Petrie and Toth, 2008a)
		Size of receiving lens	
	Geometrical factors	Instrument position in relation to slope (range, incidence angle)	(Höfle and Pfeifer, 2007; Korpela, 2008; Rosser et al., 2007)
		Slope surface texture (lithology, wetness, vegetation)	(Lichti and Harvey, 2002; Rosser et al., 2007; Rosser et al., 2005)
	Environmental factors	Ambient light	(Starek et al., 2006)
		Airborne particles	(Rosser et al., 2007)
		Temperature	(Baltsavias, 1999)
	Geodectic network	Differential GPS accuracy	(Field, 2004)
		Instrument and target height measurement	(Petrie and Toth, 2008a)
(2) PROCESSING	**Georeferencing data within geodectic network**	Point accuracy of target scan	(Habib, 2008)
		Differential GPS accuracy	(Field, 2004)
	Scan co-registration	Stability of benchmarks	(Borghuis et al., 2007)
		Robustness of statistical method (e.g. ICP)	(Teza et al., 2007)
	Data filtering to remove topographically irrelevant features (non-ground points)	If manual: human interpretation of scene	(Lim, 2006)
		If automated: robustness of surface fitting procedure	(Prokop and Panholzer, 2009)
	Interpolation of point cloud	Method (e.g. kriging)	(Martha et al., 2010)
		Density of point cloud	(Lichti and Jamtsho, 2006)
(3) ANALYSIS	**Dimensionality of measurement**	The benchmark method, cloud-to-cloud comparison method and shaded relief image correlation method only produce 2D movement vectors but are automated	(Travelletti et al., 2008)
		Least squares method calculates 3D displacement vectors but requires manual point selection	(Monserrat and Crosetto, 2008)
	Failure geometry	Surface expression of basal *strain*	(Rosser et al., 2008)
		Mode of failure (see table 2.3)	(Jaboyedoff et al., 2009)
		Small slope fragments superseding wide scale slope movements	(Hungr et al., 2005)

Table 5.1: A framework for acquiring, processing and analysing terrestrial laser scanning data

(1) Measurements of surface velocity are difficult to interpret in the context of the inverse-velocity method because of the lack of epistemic understanding of surface expressions of basal *strain*

In order to achieve continuous (or near-continuous) measurement, a permanent TLS system should be installed to monitor slope deformation. This has not yet been attempted and the first two key points above highlight research hurdles for establishing a permanent set-up. Interaction of the laser pulse with the local environment and target object affect the precision of the distance measurement. Monitoring environmental variables at site that affect measurements and adjusting TLS data to account for changing conditions (Tsakiri et al., 2006) will improve data precision. Importantly understanding the magnitude of error resulting from variance in different elements (i.e. ambient light) using laboratory and field calibration tests, may reduce the degree of data correction required if resulting errors are within a tolerable limit. Critically calibrating data does not overcome the fundamental problem that some slopes may deform faster than the sampling resolution of the TLS; this can only be overcome with technical improvements to instruments to increase the speed of data capture.

Although TLS is not strictly a continuous measurement system because it requires a period of time (dependent on: instrument, point density, point averaging, scanning range and scan area) to capture data it has the capability to generate hundreds of point clouds per day of the same deforming surface if permanently installed. Working with such vast data sets requires automation however, as noted in table 5.1, deriving 3D movement vectors from surfaces currently requires an operator to manually delimit failure geometry (Montserrat and Crossetto, 2008). Further research is required to develop a practical method that automates this process.

Figure 5.1 highlights the spread of instrumentation used to collect data included in the deformation database (chapter 4). Only 29% (total survey, surface monuments and peg networks) of landslides were monitored by a surface-based measurement method, and the point density of these surveys was sparse compared with TLS capabilities. Importantly point-based instruments are installed relative to an area of stability (i.e. extensometer positioned over back scarp of slope failure) allowing

movement to be tracked in a discrete location, and plotted in simple displacement-time graphs (section 3.4.3). Resulting data sets from surface-based remote measurements are complex and difficult to interpret, particularly given the need to delimit the geometry of moving parts on a hillslope. Developing numerical and physical models to investigate slip-plane surface interactions in different types (failure geometry, mode and lithology) of deforming slope will better facilitate the application of the Inverse-velocity method to surface-based measurements.

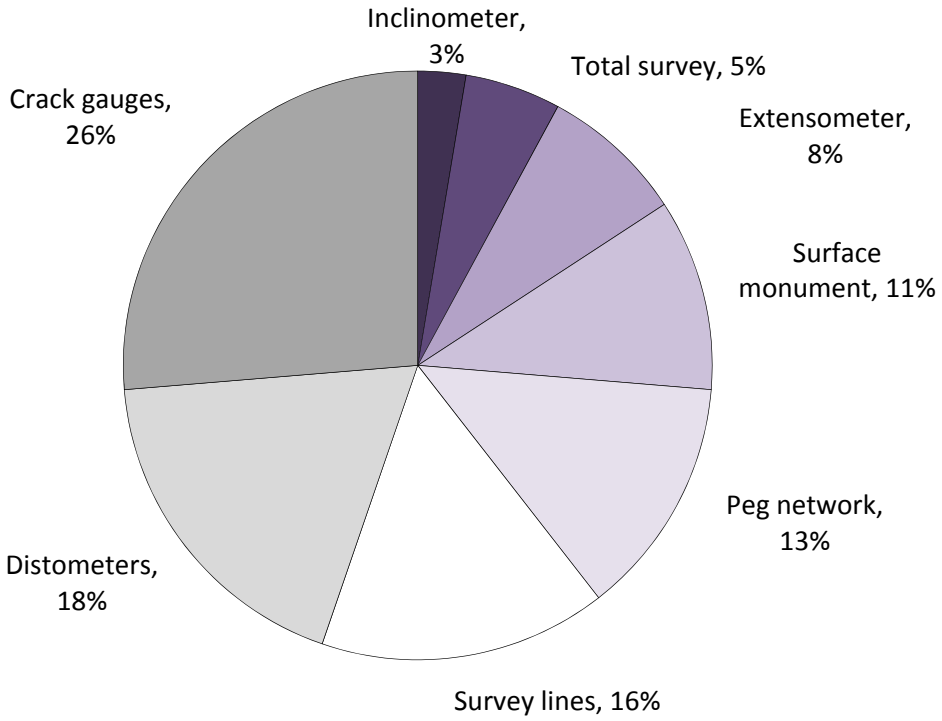

Figure 5.1: Monitoring method

Monitoring requires careful planning (Angeli et al., 2000); the most appropriate instrument for the situation, correct installation and the ability to use measurements to forecast future slope collapse, and provide early warning to vulnerable populations. TLS is a promising instrument for slope monitoring if further research is invested in developing data acquisition and processing, as discussed above. One of the main disadvantages however of this approach is cost. The majority of failures in the database (table 4.3) occurred in countries with a 'very high' level of human

development[3], indicating that they have capacity to invest in slope monitoring. Consistently Asia accounts for ~80% of annual global landslide fatalities (Petley, 2008b). Further analysis of the Asia-Pacific region between 2006 and 2008 (Ho, 2004) indicates that countries with a particularly acute number of fatal events are classified with 'low' or 'medium' levels of human development[3]. The HDI[4] measure only encompasses one direct economic indicator (GNIpc[5]) but it gives a sense of available national investment for landslide monitoring infrastructure. Cheaper simple solutions are likely to be more achievable in lesser developed regions, and based on this recognition, research is recommended to extend findings from complex technical monitoring installations (such as TLS) to inform effective affordable slope set-ups that generate data appropriate to forecasting models (such as the Inverse-velocity method).

5.5. Limitations of tertiary creep database

Although collations of secondary data provide useful tools to assess generalised behaviour in a system, it is important also to appreciate data limitations and the constraints this has on associated findings. Critically there are distinct limitations tied up with using secondary sources. Inconsistencies in reporting, particularly of slope attributes, such as detailed geology, limited the assessment relating patterns of tertiary deformation to failure characteristics. Returning to the slope factor of safety model, figure 2.1, it is noted that key parameters such as the angle of internal friction, ordinarily collected in lab-based tests when assessing a single site, are not present in the database. Field verification of large numbers of sites would be a costly and time intensive venture. Conflicting this, authors typically reported in great detail physiographic mechanisms initiating failure. This type of qualitative data was difficult to encompass into a numerically based database, leading to groupings and loss of information

Reporting bias can propagate through results (Guzzetti et al., 2008) and inconsistencies in terms caused problems when identifying brittle failures from ductily

[3] http://hdr.undp.org/en/countries/
[4] HDI: Human development index
[5] GNIpc: Gross national income at purchasing power parity per capita

deforming slopes. A lack of published examples fulfilling the database criteria indicates that either: (1) data of this nature isn't published (i.e. most slopes were man-made indicating industry rather than academic interests) or (2) monitoring rarely captures pre-failure deformations. Although the number of journals included in the initial 'search' may have been extended and other sources looked into (section 4.2), the return rate on useful articles from the search procedure was low, 0.1%. The limited number of examples made it difficult to compare with significance, patterns of tertiary creep from similar magnitude (for example) landslides.

Inconsistencies between monitoring approaches, notably coverage and resolution raise questions about the comparability of results. Importantly the onset of tertiary creep is may have been missed from records, leading to questions on creep duration, particularly in the context of those examples published in inverse-velocity-time. Both the process of digitising and conversion (between displacement- velocity) result in small precision errors (~0.1 day, section 4.2) which propagate through data. The full impact of these errors, particularly on curve modelling has not been fully investigated within this thesis.

Sections 5.2 to 5.5 discussed results presented in chapter 4 within the context of landslide monitoring and failure forecasting. Chapter 6 concludes the thesis summarising findings critical to each objective and the overall project aim.

CHAPTER 6

Conclusion

The results of this study will be summarised by revisiting the research objectives outlined in chapter 1. Recommendations for future research will be included in the evaluation of each directive.

Objective 1: To build a database of pre-failure deformations for collapsed slopes, to assess variables contributing to and controlling the nature of pre-failure strain accumulation

Using past precedent and current understanding of patterns of pre-failure deformation, a database of thirty-one examples of tertiary creep was assembled from a literature search of over 6,000 papers.

Key findings and contribution to knowledge:

- Extending previous publications which compared only a limited number of deforming slopes, the database is the first of its kind to collate a statistically significant number of tertiary creep examples to compare and contrast patterns of behaviour. Critically this provides validation data for empirical models describing brittle deformation driven by crack growth (Voight, 1989; Kilburn and Petley, 2003).
- Tertiary creep delineated using the criteria outlined in section 4.2 ranged between ~37 minutes and 3,171.45 days. Two key points arise from this:
  (1) Tertiary creep occurs at very different temporal scales
  (2) Long periods of tertiary creep, as observed in this database, indicate that slopes may destabilise and deform for many years before final collapse.
- Only very weak correlations exist between tertiary creep parameters and slope characteristics, although the limitations of attribute data, namely the secondary provenance, are discussed as bringing bias into the assessment.
- Collating data from different sources highlighted the lack of standard reporting of key site characteristics, this was particularly evident between industry-based reports and scientific papers.

Recommendations for future research:

- Extend the database to include more examples (if available) of pre-failure deformation data

- Carry out 'site-based' verification visits to better constrain slope characteristics, particularly local detailed geology of more recent failures
- To carry out primary data collection of similar unstable slopes using the same method of collection, to provide comparative data on which to consider relationships between patterns of deformation and characteristics of failure

Objective 2: To identify patterns of tertiary creep which may reflect physical deformation mechanisms

The 'inverse-velocity method' utilises the normal linear regression of inverse-velocity-time to extrapolate to the point of slope collapse. Alternative models (Voight, 1989) have been proposed to describe the transition from critical strain to slope collapse. Hyperbolic curves based on Voight's parameters were fit to data using the least-squares method in Matlab.

Key findings and contribution to knowledge:

- Applied to inverse-velocity-time data, the model α parameter varied between 1.15 and 2.23. Most examples (86%) fell within the bounds of $1.7 < \alpha < 2.2$ for brittle creep (as validated by Voight (1989).

- Relating results to physical mechanisms proposed by Kilburn (2003) it is shown that too differing degrees pre-failure deformations are dominated by either crack nucleation ($\alpha \approx 1$) or crack growth ($\alpha \approx 2$). Although the former is often discussed in the context of ductile shear zones (Petley et al., 2002), some examples within the database that fulfilled the 'tertiary creep criteria' for brittle deforming slopes, were characterised with α values closer to 1.

- There are no significant relationships between patterns of tertiary creep and pre-failure slope attributes. This is based on the limited slope attribute data reported in publications (refer above to objective 1).

- Hyperbolic parameters calculated for the velocity-time projection of data did not corroborate with those derived from inverse-velocity-time projections. Observations by Borsetto et al. (1991) suggest computational errors may exist in the fitting procedure. Although this means results from this section of work

must be treated with consideration of this potential error, it also shows that inverse-velocity-time rather than velocity-time is the best projection for data when assessing patterns of accelerating creep behaviour.

Recommendations for future research

- Some serious questions remain about the detailed mechanisms of failure development and their manifestation in terms of strain.
- Sensitivity analysis of the different Voight (1989) parameters is needed using 'real landslide data' to assess the extent to which model predictions are a reflection of measurement interval and 'chaotic' behaviour possibly derived from instrumental error
- Consideration of the differences between velocity-time and inverse-velocity time fits should be undertaken to gain a better understanding of computational errors intrinsically tied into the empirical model
- To assess relationships between movement attributes and slope characteristics using more sophisticated statistical models, particularly if the database is extended

Objective 3: To assess the application of the inverse velocity method to brittle failing rock slopes for purposes of forecasting and early warning

The 'inverse-velocity method' was applied to database records in an *a priori* manner, to simulate forecast of slope collapse. Defined retrospectively examples provided a useful test case to assess the reliability of predictions extrapolated from normal linear regressions of inverse-velocity-time data.

Key findings and contribution to knowledge:

- Slopes deforming in a brittle manner are more likely to predict slope collapse 'too soon' as a false positive prediction, than overestimating the duration of tertiary creep; based on results from the database.
- The onset of tertiary creep is harder to delimit when considering data *a priori* to failure; although this final phase of acceleration was identifiable in 87% of failure, within the first 25% of their 'retrospectively defined' creep duration.

- The inverse-velocity method has proven robust across a broad range of failures, pre-failure conditions and with data derived from a variety of instrumentation.

Recommendations for future research

- The transition from secondary to tertiary creep requires a more robust definition, reflective of the different physical mechanisms operating in the shear zone.
- The observed preferentiality towards false-positive forecast requires further investigation drawing on a greater number of examples.

Objective 4: To consider the constraints on ground-based remote sensing for monitoring pre-failure movements

Results from the database were considered in the context of available instrumentation. Five key recommendations were made for pre-failure deformation detection and monitoring. Measurements would benefit from instrumentation capable of:

(1) Spatial accuracy to ~10 mm
(2) Surface-based capture
(3) Continuous measurement (high repeat rate ~10 minutes)
(4) Ground-based view angle
(5) Long duration fixture

Terrestrial laser scanning is discussed as the most promising method of capturing pre-failure deformation. Reviewing the steps involved in acquiring, processing and interpreting data however highlight key areas for further research and development before TLS can be employed to permanently monitor slope failure.

Key research challenges:

- To calibrate errors in TLS measurement with different environmental and geometrical conditions using lab and field testing, with the aim of correcting data to improve its precision.
- To increase the capture rate of data by installing a permanent TLS system to monitor an unstable slope. To additionally instrument this slope to directly

measure deformation of high resolution but limited spatial extent, to provide a comparative dataset on which to compare the 'gain' in precision through point-cloud processing.

- To establish an automated processing procedure capable of delimiting the extent and mode of movement across a slope- this should also account for multiple points of differential movement
- To model shear-zone to surface interactions, in order to establish the representativeness of surface measurements in the context of physical mechanisms operating within the slope.
- To extend findings from future TLS monitoring installations to develop simple slope instrumentation, that is an affordable and generates data appropriate for forecasting and early warning.

The overall aim of this thesis was to (1) build a database on the nature of pre-failure acceleration from published examples of monitored failing slopes; and (2) using observations from this database, to consider the methodological constraints on detecting movement in the context of applying the inverse-velocity method for failure prediction.

The collation of a tertiary creep database has provided interesting insight into the range of scales pre-failure deformation operates over. It has generated quantitative data to instruct monitoring practise and evaluated the evolving accuracy of landslide forecast derived using the inverse-velocity method. Given the limited number of examples in the study, it has been difficult to relate slope characteristics to patterns of pre-failure deformation, however observed trends in acceleration conform well with cited literature (Voight, 1989). It is recommended in conclusion that database work using secondary sources should be extended and site validation of specific recent examples be undertaken. The contribution improved monitoring and early warning could make based on insight gained through retrospective failure analysis is significant.

Appendices

	All	Material strength			Failure type					Natural/man-made		Triggers				Size				
		Clay	Soft Rock	Hard Rock	Roto-translational	Compound	Toppling	Translational	Rotational	Natural	Man-made	Groundwater	Rainfall	Loading from other landslides	Excavation/ blasting	1	2	3	4	5
Total displacement v duration	0.0016	0.1980	0.0034	0.2966	0.8346	0.7165	0.0514	0.6473	.	0.0706	0.0000	0.8591	0.9285	.	0.0148	.	0.0136	0.3029	0.7153	0.8479
Max velocity v duration	0.0070	0.1362	0.0241	0.1762	0.0026	0.5550	0.0782	0.0365	.	0.3538	0.0104	0.0232	0.1923	.	0.0260	.	0.1166	0.4278	0.0263	0.7164
Max velocity v total displacement	0.1144	0.9665	0.0197	0.1112	0.0260	0.9716	0.0083	0.0198	.	0.0746	0.1076	0.0083	0.2851	.	0.5777	.	0.2872	0.0198	0.0527	0.9743

	Pre-failure slope gradient							Vegetation	
	20<=x<30 deg	30<=x<40 deg	40<=x<50 deg	50<=x<60deg	60<=x<70 deg	70<=x<80 deg	80<=x<90 deg	No	Yes
Total displacement v duration	0.1046	0.8285	0.1208	.	0.0061	.	.	0.0001	0.5718
Max velocity v duration	0.6360	0.0016	0.0574	.	0.2299	.	.	0.0113	0.1045
Max velocity v total displacement	0.0438	0.0498	0.0965	.	0.0251	.	.	0.1042	0.0059

Appendix table 1: R-squared values from the linear regression of different movement attributes (total displacement, max velocity and duration)

ID	*a* (mean)	*a* (min)	*a* (max)	α (mean)	α (min)	α (max)	y_f (mean)	y_f (min)	y_f (max)	R^2
1	2.465	-2.114	7.043	1.001	1.001	1.001	0.1344	0.03007	0.2387	0.9498
2	6.357	3.694	9.02	1.001	1.001	1.001	0.6157	0.4578	0.7736	0.8847
3	6.057	5.547	6.567	1.153	1.083	1.223	0.8404	0.8161	0.8648	0.9968
4	3.888	3.682	4.094	1.001	1.001	1.001	1.032	0.9935	1.07	0.9712
5	3.227	2.617	3.836	1.001	1.001	1.001	0.7278	0.6452	0.8104	0.9307
6	12.62	10.94	14.29	1.397	1.286	1.508	0.9997	0.9802	1.019	0.9993
7	4.561	3.468	5.654	1.072	0.8265	1.318	1.011	0.9346	1.088	0.9346
8	21.3	-15.31	57.92	1.614	0.6072	2.62	1	0.9452	1.055	0.9996
9	4.225	1.272	7.177	1.075	0.3386	1.812	0.9946	0.8172	1.172	0.974
10	11.7	8.043	15.37	1.428	1.143	1.714	0.9998	0.9621	1.037	0.9994
11	399.1	-241.8	1040	2.969	1.622	4.317	0.9998	0.8588	1.141	0.9691
12	1.794	-7.977	11.57	1.001	1.001	1.001	0.1157	-0.2852	0.5167	0.7095
13	2.818	1.399	4.238	1.001	1.001	1.001	1.004	0.7518	1.257	0.9691
14	11.19	5.239	17.14	1.405	0.7893	2.021	0.9892	0.8368	1.142	0.9686
15	98.84	51.68	146	2.156	1.852	2.46	0.9999	0.9686	1.031	0.9983
16	10.31	2.003	18.62	1.639	0.7601	2.519	1.011	0.83	1.193	0.9698
17	9.88	-1.835	21.59	1.554	0.231	2.876	0.9835	0.703	1.264	0.8899
18	5.607	4.61	6.603	1.097	0.7234	1.47	1.652	1.569	1.736	0.9969
19	28.2	24.96	31.45	1.504	1.426	1.583	0.5929	0.5823	0.6035	0.9997
20	403.8	318.3	489.3	1.613	1.483	1.743	0.4154	0.4052	0.4256	0.9995
21	6.061	-7.561	19.68	1.101	-0.7922	2.994	1	0.8432	1.157	0.9998
22	19.46	15.84	23.09	1.523	1.376	1.67	0.9998	0.9799	1.02	0.9995
23	12.84	11.77	13.9	1.229	1.14	1.318	1.332	1.304	1.361	0.9972
24	306.7	290.8	322.7	1.859	1.82	1.897	1	0.9964	1.004	1
25	329.7	326.1	333.3	1.729	1.719	1.738	0.9999	0.9979	1.002	1
26	47.1	45.96	48.23	1.323	1.256	1.391	3.107	3.08	3.134	0.9972
27	21.66	17.59	25.73	1.572	1.404	1.741	0.9997	0.9764	1.023	0.9995
28	9.522	7.692	11.35	1.368	1.191	1.545	0.9993	0.9675	1.031	0.9987
29	8.093	6.401	9.784	1.324	1.126	1.522	0.9991	0.9613	1.037	0.9986
30	13.16	8.96	17.36	1.39	1.171	1.608	0.9999	0.9759	1.024	0.9995
31	33.05	30.63	35.47	1.365	1.332	1.398	0.3195	0.316	0.3231	0.9999

Appendix: Table 2: Coefficients for hyperbolic curves fitted to velocity-time data

ID	a (mean)	a (min)	a (max)	y_f (mean)	y_f (min)	y_f (max)	R^2
1	2.457	-1.087	6	0.1343	0.05332	0.2152	0.9697
2	8.253	6.77	9.736	1.024	0.9088	1.138	0.9478
3	4.716	4.492	4.94	0.7702	0.7444	0.796	0.9946
4	3.879	3.686	4.071	1.03	0.9947	1.066	0.9747
5	3.241	2.659	3.823	0.7305	0.6516	0.8094	0.937
6	4.861	4.359	5.364	0.5036	0.473	0.5343	0.9979
7	4.235	3.847	4.623	1.005	0.9489	1.061	0.989
8	9.259	5.796	12.72	0.9996	0.9119	1.087	0.9969
9	3.917	2.957	4.878	0.9879	0.8688	1.107	0.9821
10	7.852	5.696	10.01	0.9942	0.8828	1.106	0.9911
11	38.51	22.76	54.26	1.001	0.8296	1.172	0.94
12	4.048	-2.079	10.18	0.4072	0.05929	0.7552	0.8183
13	2.828	1.429	4.227	1.005	0.7564	1.253	0.9702
14	7.725	5.872	9.579	0.9526	0.8409	1.064	0.9746
15	3.635	1.859	5.411	0.1648	0.1221	0.2075	0.994
16	6.262	3.082	9.443	0.9703	0.7533	1.187	0.9313
17	5.525	2.984	8.065	0.9126	0.691	1.134	0.8909
18	3.83	3.274	4.386	1.006	0.9235	1.089	0.9945
19	4.507	2.907	6.107	0.1524	0.1259	0.1789	0.9968
20	418.7	386.4	450.9	0.9415	0.9121	0.9708	0.9959
21	5.423	4.502	6.344	0.9998	0.952	1.048	0.9996
22	11.68	9.06	14.3	0.9953	0.9131	1.078	0.9898
23	8.91	8.46	9.36	0.9988	0.9637	1.034	0.9952
24	20.37	12.45	28.3	0.1438	0.1186	0.169	0.998
25	168	164.2	171.8	0.987	0.9732	1.001	0.9978
26	29.57	28.77	30.37	1.43	1.399	1.46	0.9961
27	13.2	10.05	16.35	0.9937	0.8997	1.088	0.989
28	4.293	3.779	4.807	0.5665	0.5272	0.6059	0.9974
29	4.102	3.576	4.629	0.6291	0.5854	0.6727	0.9974
30	8.37	6.672	10.07	0.9985	0.9378	1.059	0.9955
31	8.697	7.517	9.876	0.1399	0.1268	0.1529	0.9972

Appendix: Table 3: Coefficients for exponential curves fitted to velocity-time data

ID	*a* (mean)	*a* (min)	*a* (max)	α (mean)	α (min)	α (max)	y_f (mean)	y_f (min)	y_f (max)	R^2
1	0.2383	-0.9004	1.377	3.41	-3.666	10.49	1.499	-2.35	5.348	0.8429
2	0.8512	0.09032	1.612	2.279	1.461	3.098	4097	-4.02E+07	4.02E+07	0.8831
3	0.8341	0.7559	0.9123	2.174	2.093	2.256	25.03	-9.697	59.76	0.9979
4	0.6445	0.4256	0.8634	2.43	2.1	2.759	5.509	-1.728	12.75	0.9621
5	0.5343	0.06914	0.9995	2.52	1.556	3.483	4.957	-10.54	20.45	0.9228
6	0.7317	0.5567	0.9067	2.318	2.098	2.537	19.3	-51.21	89.8	0.9978
7	0.7284	0.168	1.289	2.347	1.61	3.084	24.62	-389.3	438.6	0.9558
8	1.173	0.5484	1.798	1.813	1.304	2.321	2877	-2.05E+05	2.11E+05	0.9892
9	0.7404	-0.043	1.524	2.359	1.371	3.346	1645	-1.10E+07	1.10E+07	0.9836
10	0.7205	0.5891	0.8519	2.344	2.174	2.513	13.71	-12.27	39.69	0.9997
11	0.4596	0.2015	0.7177	2.785	2.113	3.457	2.616	0.2826	4.95	0.992
12	0.8114	-0.7577	2.381	2.097	0.429	3.765	15.98	-237.6	269.5	0.8139
13	0.6217	-2.502	3.745	2.617	-2.475	7.71	16.06	-1848	1880	0.9759
14	0.4296	0.08539	0.7737	3.005	1.938	4.071	3.066	-2.657	8.79	0.9855
15	0.7712	-0.0243	1.567	1.971	0.9017	3.04	49.58	-811.9	911	0.8182
16	0.05041	-0.4747	0.5756	7.601	-28.94	44.14	1.063	0.3077	1.819	0.9569
17	0.8152	-0.3382	1.969	2.292	0.9982	3.586	2285	-1.86E+07	1.86E+07	0.9293
18	0.6952	0.2822	1.108	2.443	1.883	3.002	451	-4.62E+05	4.63E+05	0.9991
19	0.8187	0.7665	0.8709	2.191	2.134	2.249	25.98	0.07514	51.88	0.9996
20	0.8618	0.5327	1.191	2.054	1.636	2.473	8564	-1.16E+07	1.16E+07	0.9061
21	0.6612	-1.064	2.386	2.451	-0.04453	4.947	9.799	-203.6	223.2	0.9992
22	0.8168	0.675	0.9586	2.181	2.028	2.334	33.02	-80.98	147	0.9987
23	0.5703	0.4476	0.693	2.758	2.503	3.013	1126	-1.17E+07	1.17E+07	0.9979
24	0.7753	0.7399	0.8106	2.28	2.234	2.327	34.07	-3.943	72.07	0.9998
25	0.8835	0.8381	0.9288	2.12	2.069	2.171	7687	-2.27E+06	2.29E+06	0.9973
26	0.8034	0.6976	0.9091	2.224	2.085	2.363	4106	-3.27E+06	3.28E+06	0.9953
27	0.7451	0.6598	0.8304	2.297	2.188	2.406	15.49	-3.684	34.66	0.9996
28	0.7877	0.6861	0.8894	2.225	2.109	2.34	19.86	-13.03	52.74	0.9994
29	0.7524	0.6539	0.8509	2.284	2.165	2.403	15.55	-6.959	38.05	0.9995
30	0.5857	0.4063	0.7651	2.591	2.279	2.902	5.385	-1.927	12.7	0.9989
31	0.8532	0.7705	0.9358	2.164	2.076	2.252	4801	-2.44E+06	2.45E+06	0.997

Appendix: Table 4: Coefficients for hyperbolic curves fitted to inverse-velocity-time data

References

Abellán, A., 2009. Improvements in our understanding of rockfall phenomenon by Terrestrial Laser Scanning. Emphasis on change detection and its application to spatial prediction, Universitat de Barcelona, Barcelona.

Abramson, L.W. and Lee, T.S., 1996. Slope stability and stabilization methods. John Wiley, New York, 629 pp.

Ahmad, R., 2003. Developing early warning systems in Jamaica: rainfall thresholds for hydrological hazards, National Disaster Management Conference, Ocho Rios, St Ann, Jamaica.

Ahmad, R. and McCalpin, J.P., 1999. Landslide susceptibility maps for the Kingston metropolitan area, Jamaica: with notes on their use. Organization of American States general secretariat, unit for sustainable development and environment USAID-OAS Caribbean disaster mitigation project. UDS Publication Unit for disaster studies. Department of Geography and Geology, The University of the West Indies, Mona, Kingston, Jamaica.

Aleotti, P., 2004. A warning system for rainfall-induced shallow failures. Engineering Geology, 73: 247-265.

Aleotti, P. and Chowdbury, R., 1999. Landslide hazard assessment: Summary review and new perspective. Bulletin of Engineering Geology and the Environment, 58: 21-44.

Alexander, D., 2004. Vulnerability to Landslides. In: T. Glade, M. Anderson and M.J. Crozier (Editors), Landslide Hazard and Risk. John Wiley & Sons, Ltd, pp. 175-198.

Allison, R.J. and Brunsden, D., 1990. Some mudslide movement patterns. Earth Surface Processes and Landforms, 15(4): 297-311.

Allison, R.J. and Higgitt, D.L., 1998. Slope form and associations with ground boulder cover in arid environments, northeast Jordan. Catena, 33(1): 47-74.

Amitrano, D. et al., 2010. Microseismic activity analysis for the study of the rupture mechanisms in unstable rock masses. Natural Hazards and Earth System Sciences, 10(4): 831-841.

Amitrano, D., Grasso, J.R. and Senfaute, G., 2005. Seismic precursory patterns before a cliff collapse and critical point phenomena. Geophysical Research Letters, 32(8).

Anderson, M.G., Kemp, M. and Lloyd, D.M., 1988. Applications of soil water finite difference models to slope stability problems. In: G. Bonnard (Editor), Fifth

International Landlside Symposium. Balkema, Rotterdam, Lausanne, pp. 525-530.

Anderson, R.S. and Anderson, S.P., 2010. Geomorphology: The Mechanics and Chemistry of Landscapes. Cambridge University Press, Cambridge, 637 pp.

Angeli, M.G. et al., 1989. Examples of landslide instrumentation (Italy). Proceedings of the Twelfth International Conference on Soil Mechanics and Foundation Engineering, Vol 3, 1531-1534 pp.

Angeli, M.G., Pasuto, A. and Silvano, S., 2000. A critical review of landslide monitoring experiences. Engineering Geology, 55(3): 133-147.

Antonello, G. et al., 2004. Ground-based SAR interferometry for monitoring mass movements. Landslides, 1(1): 21-28.

Araiba, K., 2006. Study on the method for detecting and monitoring of pre-failure deformation in slope, Proceedings of the Interpraevent International Symposium Disaster Mitigation of Debris Flows, Slope Failures and Landslides, Niigata, Japan, pp. 581- 589.

Armstrong, J.S., 2001. Principles of forecasting: a handbook for researchers and practitioners. Springer, 849 pp.

Baeza, C. and Corominas, J., 2001. Assessment of shallow landslide susceptibility by means of multivariate statistical techniques. Earth Surface Processes and Landforms, 26(12): 1251-1263.

Bai, J.G., Lu, S.D. and Han, J.S., 2008. Importance of study of creep sliding mechanism to prevention and treatment of reservoir landslide. In: Z. Chen, J. Zhang, Z. Li, F. Wu and K. Ho (Editors), Landslides and Engineered Slopes: From the Past to the Future. CRC Press: Taylor & Francis Group, Xi'an, China, pp. 1071-1076.

Baltsavias, E.P., 1999. Airborne laser scanning: basic relations and formulas. ISPRS Journal of Photogrammetry and Remote Sensing, 54(2-3): 199- 214.

Barredo, J.I., Benavides, A., Hervás, J. and van Westen, C.J., 2000. Comparing heuristic landslide hazard assessment techniques using GIS in the Tirajana basin, Gran Canaria Island, Spain. International Journal of Applied Earth Observation and Geoinformation, 2: 9-23.

Baum, R.L. and Godt, J.W., 2010. Early warning of rainfall-induced shallow landslides and debris flows in the USA. Landslides, 7(3): 259-272.

Bell, R., Glade, T. and Danscheid, M., 2006. Challenges in defining acceptable risk levels. In: W.J. Ammann, S. Dannenmann and L. Vulliet (Editors), RISK21- Coping with Risks due to Natural Hazards in the 21st Century: Proceedings of the Risk21 Workshop, Monte Verita, Ascona, Switzerland, 28 November-3 December 2004. Taylor and Francis, pp. 77-87.

Belloni, L.G. and Stefani, R., 1987. The vajont slide: instrumentation- Past experience and the modern approach. Engineering Geology, 24(1): 445-474.

Bhandari, R.K., 1988. Special lecture- some practical lessons in the investigation and field monitoring of landslides Landslides, Vols 1-3, 1435-1457

Bishop, A.W., 1967. Progressive failure- with special reference to the mechanism causing it, Proc. Geotechnical Conference, Oslo, pp. 142- 50.

Bjerrum, L., 1967. Progressive failure- with special reference to the mechanism causing it. Journal of the Soil Mechanics and Foundations Division of the American Society of Civil Engineers, 93: 1-49.

Bommer, J.J. and Rodŕiguez, C.E., 2002. Earthquake-induced landslides in Central America. Engineering Geology, 63(3-4): 189-220.

Bonnard, C., Fell, R., Mc Innes, R. and Leroi, E., 2005. Risk assessment and management, International Conference on Landslide Risk Management, Vancouver, Canada.

Bonnard, C. and Glastonbury, J., 2005. Risk assessment for very large rock slopes In: O. Hungr, R. Fell and R. Couture (Editors), Landslide risk management: proceedings of the International Conference on Landslide Risk Management, Vancouver, Canada, 31 May-3 June 2005. Taylor & Francis, pp. 335-350.

Bonnard, C., Noverraz, F., Lateltin, O. and Raetzo, H., 1995. Large Landslides and Possibilitiesof Sudden Reactivation. Felsbau, 13(6): 400-407.

Bonzanigo, L., Eberhardt, E. and Loew, S., 2001. Hydromechanical factors controlling the creeping Campo Vallemaggia landslide, Proceedings of Landslides-Causes, impacts and countermeasures, Davos, Switzerland.

Borghuis, A.M., Chang, K. and Lee, H.Y., 2007. Comparison between automated and manual mapping of typhoon-triggered landslides from SPOT-5 imagery. International Journal of Remote Sensing, 28(7-8): 1843-1856.

Borsetto, M. et al., 1991. An application of Voight empirical model for the prediction of soil and rock instabilities. In: D.H. Bell (Editor), Proceedings of the 7th

International Symposium on Landslides. Balkema, Rotterdam, Christchurch, pp. 335-341.

Boyd, J.M., Hinds, D.V., Moy, D. and Rogers, C., 1973. Two simple devices for monitoring movements in rock slopes. Quarterly Journal of Engineering Geology and Hydrogeology, 6(3-4): 295-302.

Brawner, C.O. and Stacey, P.F., 1979. Hogarth pit slope failure, Ontario, Canada. In: B. Voight (Editor), Rockslides and Avalanches. Elsevier, Amsterdam, pp. 691-707.

Brideau, M.A., Yan, M. and Stead, D., 2009. The role of tectonic damage and brittle rock fracture in the development of large rock slope failures. Geomorphology, 103(1): 30-49.

Bromhead, E., 1996. Slope stability modelling: an overview. In: R. Dikau, D. Brunsden, L. Schrott and M. Ibsen (Editors), Landslide Recognition: Identificaiton, Movemnet and Casues. John WIley & Sons Ltd, Chichester, pp. 231-235.

Brown, I., Hittinger, M. and Goodman, R., 1980. Finite element study of the Nevis Bluff (New Zealand) rock slope failure. Rock Mechanics, 12: pp. 231-245.

Brunetti, M.T. et al., 2010. Rainfall thresholds for the possible occurrence of landslides in Italy. Natural Hazards and Earth System Sciences, 10: 447-458.

Brunsden, D., 1999. Some geomorphological considerations for the future development of landslide models. Geomorphology, 30(1-2): 13-24.

Caine, N., 1980. The rainfall intensity-duration control of shallow landslides and debris flows. Geografisker Annaler A, 62: 23-27.

Callister, W.D. and Rethwisch, 2010. Materials science and engineering Wiley, UK, pp.885 pp.

Calvetti, F. and Nova, R., 2004. Micromechanical approach to slope stability analysis. In: F. Darve and I. Vardoulakis (Editors), Degradation and Instabilities in Geomaterials, CISM Courses and Lectures no.461. Springer, Wien, pp. 235-254.

Cannon, S.H. and Gartner, J.E., 2005. Wildfire-related debris flow from a hazards perspective. In: M. Jakob and O. Hungr (Editors), Debris flow Hazards and Related Phenomena. Springer Berlin Heidelberg, pp. 363-385.

Cardinali, M., Guzzetti, F. and Brabb, E.E., 1990. Preliminary map showign landsldie deposits and related features in New Mexico, US Geological Survey Open File Report.

Carey, J.M., Moore, R., Petley, D.N. and Siddle, H.J., 2007. Pre-failure behaviour of slope materials and their significance in the progressive failure of landslides. In: R. McInnes, J. Jakeways, H. Fairbank and E. Mathie (Editors), Landslides and Climate Change: Challenges and Solutions. Proceedings and Monographs in Engineering, Water and Earth Sciences. Taylor & Francis Ltd, London, pp. 207-215.

Carrara, A. et al., 1991. GIS techniques and statistical-models in evaluation landslide hazard. Earth Surface Processes and Landforms, 16(5): 427-445.

Catani, F., Casagli, N., Ermini, L., Righini, G. and Menduni, G., 2005. Landslide hazard and risk mapping at catchment scale 2005 Arno River basin. Landslides, 2(4): 329-342.

Chelli, A., Mandrone, G. and Truffelli, G., 2006. Field investigations and monitoring as tools for modelling the Rossena castle landslide (Northern Appennines, Italy). Landslides, 3(3): 252-259.

Chleborad, A.F., 2003. Preliminary Evaluation of a Precipitation Threshold for Anticipating the Occurrence of Landslides in the Seattle, Washington, Area, US Geological Survey Open-File Report 03-463.

Chung, C.J.F. and Fabbri, A.G., 1999. Probabilistic prediction models for landslide hazard mapping. Photogrammetric Engineering and Remote Sensing, 65(12): 1389-1399.

Clague, J.J. and Evans, S.G., 1994. Formation and failure of natural dams in the Canadian Cordillera. Geol. Surv. Can. Bull., 464

Clarizia, M., Gullà, G. and Sorbino, G., 1996. Sui meccanismi di innesco dei soil slip. In: F. Luino (Editor), International Conference Prevention of Hydrogeological Hazards: the Role of Scientific Research. L'Artistica Savigliano pub., Alba, pp. 585-597.

Coates, D.F., Yu, Y. and Gyenge, M., 1979. A case history of pit slope design, Proceedings Fourth International Congress on Rock Mechanics, Montreaux, Switzerland, pp. 591-595.

Cooper, M.R., Bromhead, E.N., Petley, D.J. and Grant, D.I., 1998. The Selborne cutting stability experiment. Geotechnique, 48(1): 83-101.

Cornelius, R.R. and Scott, P.A., 1993. A materials failure relation of accelerating creep as empirical description of damage accumulation. Rock Mechanics and Rock Engineering 26(3): p.233- 252.

Corominas, J., Copons, R., Vilaplana, J.M., Altimir, J. and Amigo, J., 2003. Integrated landslide susceptibility analysis and hazard assessment in the principality of Andorra. Natural Hazards, 30(3): 421-435.

Corominas, J. and Moya, J., 2008. A review of assessing landslide frequency for hazard zoning purposes. Engineering Geology, 102(3-4): 193-213.

Corominas, J. et al., 2000. Measurement of landslide displacements using a wire extensometer. Engineering Geology, 55(3): 149-166.

Corsini, A. et al., 2006. Space-borne and ground-based SAR interferometry as tools for landslide hazard management in civil protection. International Journal of Remote Sensing, 27(12): 2351-2369.

Crampin, S. and Gao, Y., 2010. Plate-wide deformation before the Sumatra-Andaman earthquake. Submitted to Pure and Applied Geophysics.

Crosta, G., 1998. Regionalization of rainfall thresholds: an aid to landslide hazard evaluation. Environmental Geology, 35(2-3): 131-145.

Crosta, G.B. and Agliardi, F., 2003. Failure forecast for large rock slides by surface displacement measurements. Canadian Geotechnical Journal, 40(1): 176-191.

Crosta, G.B. and Frattini, P., 2001. Rainfall thresholds for triggering soil slips and debris flow. In: A. Mugnai, F. Guzzetti and G. Roth (Editors), Proceedings 2nd EGS Plinius Conference on Mediterranean Storms, Siena, pp. 463–487.

Crozier, M.J., 1986. Landslides: causes, consequences and environment. Taylor and Francis, Kent.

Crozier, M.J., 1999. Prediction of rainfall-triggered landslides: A test of the antecedent water status model. Earth Surface Processes and Landforms, 24(9): 825-833.

Cruden, D.M., 1991. A simple definition of a landslide. Bulletin of the International Association of Engineering Geology, 43: p.27- 29.

Cruden, D.M. and Masoumzadeh, S., 1987. Accelerating creep of the slopes of a coal-mine. Rock Mechanics and Rock Engineering, 20(2): 123-135.

Cruden, D.M. and Varnes, D.J., 1996. Landslide types and processes. In: A.K. Turner and R.L. Shuster (Editors), Landslides: Investigation and Mitigation. Transp Res Board, , pp. p.36- 75.

D'Orsi, R.N. et al., 1997. Rio-Watch: The Rio de Janeiro landslide watch system, Proc. 2nd PSL Pan-Am Symp. on Landslides, Rio de Janeiro, pp. 21-30.

Dahal, R.K. and Hasegawa, S., 2008. Representative rainfall thresholds for landslides in the Nepal Himalaya. Geomorphology, 100(3-4): 429-443.

Dai, F.C. and Lee, C.F., 2001. Frequency-volume relation and prediction of rainfall-induced landslides. Engineering Geology, 59(3-4): 253-266.

Dai, F.C., Lee, C.F. and Ngai, Y.Y., 2002. Landslide risk assessment and management: an overview. Engineering Geology, 64(1): 65-87.

Daneshkhah, A.R., 2004. Uncertainty in Probability Risk Assessment: A Review, University of Sheffield, Sheffield, UK.

De la Cruz-Reyna, S. and Reyes-Davila, G.A., 2001. A model to describe precursory material-failure phenomena: applications to short-term forecasting at Colima volcano, Mexico. Bulletin of Volcanology, 63(5): 297-308.

Densmore, A.L., Anderson, R.S., McAdoo, B.G. and Ellis, M.A., 1997. Hillslope Evolution by Bedrock Landslides. Science, 275(5298): 369-372.

Dictionary, W.s.N.N.C., 1986. Marriam-Webster Inc., Springfield Massachusetts.

Dieterich, J.H., 1978. Rock friction and earthquake precursors. Bulletin of the American Physical Society, 23(1): 75-75.

Duncan, N., 2004. Rock slope engineering: civil and mining. Taylor & Francis, UK.

Dunnicliff, J., 1993. Geotechnical instrumentation for monitoring field performance. Wiley-IEEE, 608 pp.

Faure, R.M. et al., 1988. Xpent, expert system in slope stability. Landslides, Vols 1-3, 625-629 pp.

Federico, A., Fidelibus, C. and Interno, G., 2002. The prediction of landslide time to failure- a state of the art., 3rd International Conference for Landslides, Slope Stability & Safety of Infra- Structure, Singapore, pp. 167-180.

Fell, R., Hungr, O., Leroueil, S. and Riemer, W., 2000. Keynote lecture- geotechnical engineering of the stability of natural slopes, and cuts and fills., Proceedings of the Geoengineering Conference, Melbourne, Australia, pp. 21-120.

Feng, Q.H. and Roshoff, K., 2004. In-situ mapping and documentation of rock faces using full-coverage 3D laser scanning techniques. International Journal of Rock Mechanics and Mining Sciences, 41(3): 379-379.

Field, H.L., 2004. Landscape surveying. Cengage Learning.

Frattini, P., Crosta, G. and Sosio, R., 2009. Approaches for defining thresholds and return periods for rainfall-triggered shallow landslides. Hydrological Processes, 23(10): 1444-1460.

Fröhlich, C. and Mettenleiter, M., 2004. Terrestrial Laser Scanning- New Perspectives in 3D Surveying. In: M. Thies, B. Koch, H. Spieker and H. Weinacker (Editors), ISPRS VIII/2 'Laser-Scanners for Forest and Landscape Assessment' International archives of photogrammetry, remote sensing and spatial information sciences., Freiburg, Germany, pp. 7-13.

Fukuzono, T., 1985. A new method for predicting the failure time of a slope, Proceedings of the 4th International Conference and Field Workshop on Landslides, Tokyo, Japan, pp. 145- 50.

Fukuzono, T., 1990. Recent studies on time prediction of slope failure. Landslide News, 4: 9-12.

Garland, G.G. and Olivier, M.J., 1993. Predicting landslides from rainfall in a humid, sub-tropical region. Geomorphology, 8(2-3): 165-173.

Geotechnical Control Office, G., 1984. Prediction of Soil Suction for Slopes in Hong Kong. Report No. 1/84, Hong Kong Government, Hong Kong.

Glade, T., 1998. Establishing the frequency and magnitude of landslide-triggering rainstorm events in New Zealand. Environmental Geology, 35(2-3): 160-174.

Glade, T., Anderson, M. and Crozier, M.J. (Editors), 2005. Landslide Hazard and Risk. John Wiley & Sons, Ltd, 175- 198 pp.

Glade, T., Crozier, M.J. and Smith, P., 2000. Applying probability determination to refine landslide-triggering rainfall thresholds using an empirical “Antecedent Daily Rainfall Model”. Pure Appl. Geophys., 157(6/8): 1059–1079.

Glastonbury, B. and Fell, R., 2000. Report on the analysis of rapid natural rock slope failures. , Universiyt of New South Wales, Sydney, Australia.

Glastonbury, B. and Fell, R., 2002. Report on the analysis of the deformation behaviour of excavated rock slopes, University of New South Wales, Syndey, Australia.

Glawe, U. and Lotter, M., 1996. Time prediction of rock slope failures based on monitoring results. In: K. Senneset (Editor), Landslides, Proceedings of 7th International Symposium on Landslides. A.A.Balkema, Rotterdam.

Godt, J.W., Baum, R.L. and Chleborad, A.F., 2006. Rainfall characteristics for shallow landsliding in Seattle, Washington, USA. Earth Surface Processes and Landforms, 31(1): 97-110.

Godt, J.W., Baum, R.L. and Lu, N., 2009. Landsliding in partially saturated materials. Geophysical Research Letters, 36.

Gonzalez, A.J., 1989. Metodología y criterios de clasificación para inventario de movimientos, I Simposio suramericano de deslizamientos. Sociedad Colombiana de Geotecnia, Paipa-Colombia, pp. 677-698.

Goodman, R.E., 1989. Introduction to rock mechanics. Wiley, UK, 562 pp.

Griffith, A.A., 1921. The phenomena of rupture and flow in solids. Philosophical Transactions of the Royal Society of London, A(221): 163- 198.

Gunther, A., Carstensen, A. and Pohl, W., 2004. Automated sliding susceptibility mapping of rock slopes. Natural Hazards and Earth System Sciences, 4(1): 95-102.

Guthrie, R.H. and Evans, S.G., 2007. Work, persistence, and formative events: The geomorphic impact of landslides. Geomorphology, 88(3-4): 266-275.

Guzzetti, F., 2000. Landslide fatalities and the evaluation of landslide risk in Italy. Engineering Geology, 58(2): 89-107.

Guzzetti, F., Ardizzone, F., Cardinali, M., Rossi, M. and Valigi, D., 2009. Landslide volumes and landslide mobilization rates in Umbria, central Italy. Earth and Planetary Science Letters, 279(3-4): 222-229.

Guzzetti, F., Carrara, A., Cardinali, M. and Reichenbach, P., 1999. Landslide hazard evaluation: a review of current techniques and their application in a multi-scale study, Central Italy. Geomorphology, 31(1-4): 181-216.

Guzzetti, F., Peruccacci, S., Rossi, M. and Stark, C.P., 2007. Rainfall thresholds for the initiation of landslides in central and southern Europe. Meteorology and Atmospheric Physics, 98(3-4): 239-267.

Guzzetti, F., Peruccacci, S., Rossi, M. and Stark, C.P., 2008. The rainfall intensity-duration control of shallow landslides and debris flows: an update. Landslides, 5(1): 3-17.

Habib, A., 2008. Accuracy, Quality Assurance, and Quality Control of LiDAR Data. In: J. Shan and C.K. Toth (Editors), Topographic Laser Ranging and Scanning:

Principles and Processing. CRC Press: Taylor & Francis Group, Abingdon, Oxon, pp. 269-294.

Haefeli, R., 1948. The stability of slopes acted upon by parallel seepage, Proceedings of the International Conference on Soil Mechanics and Foundation Engineering, pp. 57-62.

Hapke, C.J., 2005. Estimation of regional material yield from coastal landslides based on historical digital terrain modelling. Earth Surface Processes and Landforms, 30(6): 679-697.

Hardy, H.R., 2003. Acoustic Emission, Microseismic Activity: Principles, techniques, and geotechnical applications. Taylor & Francis, 292 pp.

Heim, A., 1932. Bergsturz und Menschenleben. Fretz & Wasmuth Zürich.

Helmstetter, A. and Garambois, S., 2010. Seismic monitoring of Sechilienne rockslide (French Alps): Analysis of seismic signals and their correlation with rainfalls. Journal of Geophysical Research-Earth Surface, 115.

Helmstetter, A. et al., 2004. Slider block friction model for landslides: Application to Vaiont and La Clapiere landslides. Journal of Geophysical Research-Solid Earth, 109(B2).

Hertgarten, S., 2003. Landslides, sandpiles and self-organized criticality. Nat. Hazards Earth Syst. Sci., 3: 505- 514.

Hervás, J. and Bobrowsky, P., 2009. Mapping: Inventories, Susceptibility, Hazard and Risk. In: K. Sassa and P. Canuti (Editors), Landslides - Disaster Risk Reduction. Springer, Berlin, pp. 321-349.

Ho, K.K.S., 2004. Keynote paper: recent advances in geotechnology for slope stabilization and landslide mitigation—perspective from Hong Kong. In: W.A. Lacerda, M. Ehrlich, S.A.B. Fontoura and A.S.F. Sayao (Editors), Landslides, evaluation & stabilization. Proceedings of the 9th International Symposium on Landslides. Taylor & Francis, Rio de Janeiro, pp. 1507–1560.

Ho, K.K.S., Leroi, E. and Roberds, B., 2000. Quantitative risk assessment: applications,myths and future directions, GeoEng 2000 Invited Papers. . Technomic, Lancaster PA, pp. 209–312.

Hoek, E., Carranza-Torres, C. and Corkum, B., 2002. Hoek-Brown failure criterion- 2002 Edition, Proceedings of the 5th North American Rock Mechanics Symposium, Toronto, pp. 267-273.

Höfle, B. and Pfeifer, N., 2007. Correction of laser scanning intensity data: Data and model-driven approaches. ISPRS Journal of Photogrammetry and Remote Sensing, 62(6): 415-433.

Holcomb, D.J., 1993. General-theory of the Kaiser effect. International Journal of Rock Mechanics and Mining Sciences & Geomechanics Abstracts, 30(7): 929-935.

Hong, Y., Adler, R., Negri, A. and Huffman, G., 2007. Flood and landslide applications of near real-time satellite rainfall products. Natural Hazards, 43(2): 285-294.

Hong, Y. and Adler, R.F., 2007. Towards an early-warning system for global landslides triggered by rainfall and earthquake. International Journal of Remote Sensing, 28(16): 3713-3719.

Hovius, N., Stark, C.P. and Allen, P.A., 1997. Sediment flux from a mountain belt derived by landslide mapping. Geology, 25(3): 231-234.

Hudson, J.A. and Harrison, J.P., 1997. Engineering rock mechanics: An Introduction to the Principles. Pergamon, Oxford.

Hungr, O., 2009. Numerical modelling of the motion of rapid, flow-like landslides for hazard assessment. Ksce Journal of Civil Engineering, 13(4): 281-287.

Hungr, O., Corominas, J. and Eberhardt, E., 2005. Estimating landslide motion mechanism, travel distance and velocity. In: O. Hungr, R. Fell, R. Couture and E. Eberhardt (Editors), Landslide Risk Management. Taylor & Francis, London,, London, pp. 99 - 128. .

Hungr, O. and Kent, A., 1995a. Coal mine waste dump failures in BC, Canada. Landslide News, 9, : 26-28.

Hungr, O. and Kent, A., 1995b. Mined rock and overburden piles: runout characteristics of debris from dump failures in mountainous terrain stage 2: analysis, modeling and prediction, interim report Vancouver, British Colombia

Husaini, O. and Ratnasamy, M., 2001. An early warning system for active landslides. Quarterly Journal of Engineering Geology and Hydrogeology, 34: 299-305.

Hustrulid, W.A., 2000. Slope stability in surface mining. SME, 442 pp.

Hutchinson, J., 2001. Lanslide risk- to know, to foresee, to prevent. Geologica Tecnica & Ambientale, 9: 3- 24.

Inkpen, R., 2005. Science, philosophy and physical geography. Routledge, Oxon, pp.164 pp.

Innes, J.L., 1983. Lichenometric dating of debris-flow deposits in the Scottish Highlands. Earth Surface Processes and Landforms, 8(6): 579-588.

Iwamoto, M., 1990. Standard amount of rainfall for warning from debris disaster. In: A. Cancelli (Editor), Proceedings 6th International Conference and Field Workshop on Landslides ALPS 90, Milano: Ricerca Scientifica ed Educazione Permanente, 79b, pp. 77–88.

Jaboyedoff, M., Couture, R. and Locat, P., 2009. Structural analysis of Turtle Mountain (Alberta) using digital elevation model: Toward a progressive failure. Geomorphology, 103(1): 5-16.

Janbu, N., 1957. Earth Pressure and Bearing Capacity by Generalized Procedure of Slices, International Conference on Soil Mechanics, London, UK, pp. 207-212.

Kalaugher, P.G., Hodgson, R.L.P. and Grainger, P., 2000. Pre-failure strains as precursors of sliding in a coastal mudslide. Quarterly Journal of Engineering Geology and Hydrogeology, 33: 325-334.

Keefer, D.K., 1984. Landslides caused by earthquakes. Geological Society of America Bulletin, 95(4): 406-421.

Keefer, D.K., 2000. Statistical analysis of an earthquake-induced landslide distribution - the 1989 Loma Prieta, California event. Engineering Geology, 58(3-4): 231-249.

Keefer, D.K. et al., 1987. Real-time landslide warning during heavy rainfall. Science, 238(4829): 921-925.

Kennedy, B.A. and Niermeye, K.E., 1970. Slope monitoring systems used in the prediction of a major slope failure at the Chuquicamata Mine, Chile, Proceedings of the symposium on Planning Open Pit Mines. Balkema, Amsterdam, Johannesburg, South Africa, pp. 215-225.

Keqiang, H. and Sijing, W., 2006. Double-parameter threshold and its formation mechanism of the colluvial landslide: Xintan landslide, China. Environmental Geology, 49(5): 696-707.

Kilburn, C.R., 2011. Personal Communication.

Kilburn, C.R. and Voight, B., 1998. Slow rock fracture as eruption precursor at Soufriere Hills volcano, Montserrat. Geophysical Research Letters, 25(19): 3665-3668.

Kilburn, C.R.J., 2003. Multiscale fracturing as a key to forecasting volcanic eruptions. Journal of Volcanology and Geothermal Research, 125(3-4): 271-289.

Kilburn, C.R.J. and Petley, D.N., 2003. Forecasting giant, catastrophic slope collapse: lessons from Vajont, Northern Italy. Geomorphology, 54(1-2): 21-32.

Kliche, C., 1999. Rock Slope Stability. Society for Mining, Metallurgy and Explorations, Inc., 252 pp.

Korpela, I.S., 2008. Intensity of airborne discrete-return LiDAR- using it to classify forest vegetation: Mapping of understory ground lichens and tree species identification.

Korup, O., 2008. Rock type leaves topographic signature in landslide-dominated mountain ranges. Geophysical Research Letters, 35.

Krzysztofowicz, R., 2001. The case for probabilistic forecasting in hydrology. Journal of Hydrology, 249(1-4): 2-9.

Larsen, I.J., Montgomery, D.R. and Korup, O., 2010. Landslide erosion controlled by hillslope material. Nature Geoscience, 3(4): 247-251.

Larsen, M.C. and Simon, A., 1993. A rainfall intensity-duration threshold for landslides in a humid-tropical environment, Puerto Rico. Geografisker Annaler A, 75(1-2): 13-23.

Lateltin, O., 1997. Berücksichtigung der Massenbewegungsgefahren bei raumwirksamen Tätigkeiten. Swiss Federal Office for Water and Geology (FOWG). http://www.bwg.admin.ch/themen/natur/e/index.htm.

Lavrov, A., 2005. Fracture-induced physical phenomena and memory effects in rocks: A review. Strain, 41(4): 135-149.

Lawn, B., 1993. Fracture of brittle solids. University Press, Cambridge, Cambridge.

Lee, E.M. and Jones, D.K.C., 2004. Landslide Risk Assessment. Thomas Telford, UK.

Leroueil, S. et al., 1996. Geotechnical characterization of slope movements. Landslides. A a Balkema, Rotterdam, 53-74 pp.

Lichti, D.D. and Harvey, B.R., 2002. The effects of reflecting surface material properties on time-of-flight laser scanner measurements, ISPRS "Geospatial theory, processing and applications", Ottawa, Canada.

Lichti, D.D. and Jamtsho, S., 2006. Angular resolution of terrestrial laser scanners. Photogrammetric Record, 21(114): 141-160.

Lillesand, T., Kiefer, R.W. and Chipman, J., 2007. Remote Sensing and Image Interpretation. Wiley, 804 pp.

Lim, M., 2006. Coastal Cliff Evolution with Reference to Staithes, North Yorkshire, Durham, Durham.

Lim, M. et al., 2005. Combined digital photogrammetry and time-of-flight laser scanning for monitoring cliff evolution. Photogrammetric Record, 20(110): 109

Lockner, D., 1993. The role of acoustic-emission in the study of rock fracture. International Journal of Rock Mechanics and Mining Sciences & Geomechanics Abstracts, 30(7): 883-899.

Look, B., 2007. Handbook of geotechnical investigation and design tables. Routledge.

Main, I.G., 1999. Applicability of time-to-failure analysis to accelerated strain before earthquakes and volcanic eruptions. Geophysical Journal International, 139(3): F1-F6.

Main, I.G., 2000. A damage mechanics model for power-law creep and earthquake aftershock and foreshock sequences. Geophysical Journal International, 142(1): 151-161.

Main, I.G., Sammonds, P.R. and Meredith, P.G., 1993. Application of a modified Griffith Criterion to the evolution of fracta damage during compressional rock failure Geophysical Journal International, 115(2): 367-380.

Malamud, B.D., Turcotte, D.L., Guzzetti, F. and Reichenbach, P., 2004. Landslide inventories and their statistical properties. Earth Surface Processes and Landforms, 29(6): 687-711.

Malet, J.P., Maquaire, O. and Calais, E., 2002. The use of Global Positioning System techniques for the continuous monitoring of landslides: application to the Super-Sauze earthflow (Alpes-de-Haute-Provence, France). Geomorphology, 43(1-2): 33-54.

Mandrone, G., Clerici, A. and Tellini, C., 2007. Evolution of a landslide creating a temporary lake: successful prediction. Quaternary International, 171-172: 72-79.

Martel, S.J., 2004. Mechanics of landslide initiation as a shear fracture phenomenon. Marine Geology, 203(3-4): 319-339.

Martha, T.R., Kerle, N., Jetten, V., van Westen, C.J. and Kumar, K.V., 2010. Characterising spectral, spatial and morphometric properties of landslides for semi-automatic detection using object-oriented methods. Geomorphology, 116(1-2): 24-36.

Martin, D.C., 1993. Time dependent deformation of rock slopes, University of London.

Massey, C., 2010. The dynamics of reactivated landslides: Utiku and Taihape, North Island, New Zealand. Doctoral Thesis, Durham University.

Mazanti, B.B. and Sowers, G.F., 1966. Laboratory testing of rock strength. In: A.S.f.T.a. Materials (Editor), Testing techniques for rock mechanics. ASTM International, Baltimore.

McGuire, W.J. and Kilburn, C.R.J., 1997. Forecasting volcanic events: some contemporary issues. Geologische Rundschau, 86(2): 439-445.

McHugh, E. and Girard, J., 2002. Evaluating techniques for monitoring rock falls and slope stability. In: S.S. Peng, C. Mark, A. Wahab Khair and K. Heasley (Editors), Proceedings 21st International Conference on Ground Control in Mining, Morgantown, West Virginia, pp. 335-343.

Meredith, P.G., 2010. Personal Communication.

Meunier, P., Hovius, N. and Haines, J.A., 2008. Topographic site effects and the location of earthquake induced landslides. Earth and Planetary Science Letters, 275(3-4): 221-232.

Miller, P.E. et al., 2009. Intelligent integration of multisensor data for risk assessment in transport corridor environments. International Archives of Photogrammetry, Remote Sensing and Spatial Information Sciences, XXXVIII(W6): 1-6.

Mitchell, J.K., Campanella, R.G. and Singh, A., 1968. Soil creep as a rate process. J. Soil Mech. Found. Div. Am. Soc. Civil Engrs, 94(SM1, Proc. Paper 5751): 231-253.

Monserrat, O. and Crosetto, M., 2008. Deformation measurement using terrestrial laser scanning data and least squares 3D surface matching. ISPRS Journal of Photogrammetry and Remote Sensing, 63(1): 142-154.

Montgomery, D.R., 2001. Slope distributions, threshold hillslopes, and steady-state topography. American Journal of Science, 301(4-5): 432-454.

Mufundirwa, A., Fujii, Y. and Kodama, J., 2010. A new practical method for prediction of geomechanical failure-time. International Journal of Rock Mechanics and Mining Sciences, 47(7): 1079-1090.

Ng, K.Y., 2007. Mechanisms of shallow rainfall-induced landslides in residual soils in humid tropical environments, University of Durham, Durham.

Ng, K.Y. and Petley, D.N., 2009. The use of pore pressure reinflation testing in landslide management in Hong Kong. Quarterly Journal of Engineering Geology and Hydrogeology, 42: 487-498.

Noferini, L. et al., 2007. Using GB-SAR technique to monitor slow moving landslide. Engineering Geology, 95(3-4): 88-98.

Okamoto, T. et al., 2004. Displacement properties of landslide masses at the initiation of failure in quick clay deposits and the effects of. Engineering Geology, 72(3): 233-251.

Omori, F., 1894. On the aftershocks of earthquakes. Journal of College of Science, Imperial University of Tokyo, 7: 111- 200.

Panizza, M., Pasuto, A., Silvano, S. and Soldati, M., 1996. Temporal occurrence and activity of landslides in the area of Cortina d'Ampezzo (Dolomites, Italy). Geomorphology, 15(3-4): 311-326.

Parise, M. and Jibson, R.W., 2000. A seismic landslide susceptibility rating of geologic units based on analysis of characteristics of landslides triggered by the 17 January, 1994 Northridge, California earthquake. Engineering Geology, 58(3-4): 251-270.

Park, R.G., 2004. Foundation of Structural Geology. Routledge, 202 pp.

Parker, R., 2009. Controls on the distribution of landslides triggered by the 2008 Wenchuan earthquake, Sichuan Province, China, University of Durham, Durham.

Parsons, A.J., 1988. Hillslope form. Routledge, London.

Petley, D., 2008b. The global occurrence of fatal landslides 2007, Proceedings of the World Landslide Forum Satellite Conference. Japanese Landslide Society, Sendai, Japan.

Petley, D., 2009. Mass Movement Hazards. In: K. Smith and D. Petley (Editors), Environmental Hazards: Assessing risk and reducing disaster. Routledge, London, pp. 416.

Petley, D., 2010. Dave's Landslide Blog.

Petley, D. and Rosser, N.J., 2006. On the mechanics of a typhoon induced landslide, Proceedings of the 10th Taiwan Geography Conference. The Geographical Society of China, Taipei, pp. 150–162.

Petley, D.J. and Rosser, N.J., 2009. On the mechanics of a typhoon-induced landslide, The Next Generation of Research on Earthquake-induced Landslides: An International Conference in Commemoration of 10th Anniversary of the Chi-Chi Earthquake, Tapei, Taiwan.

Petley, D.N., 2004. The evolution of slope failures: mechanisms of rupture propagation. Natural Hazards and Earth System Sciences, 4(1): 147-152.

Petley, D.N. and Allison, R.J., 1997. The mechanics of deep-seated landslides. Earth Surface Processes and Landforms, 22(8): 747-758.

Petley, D.N., Bulmer, M.H. and Murphy, W., 2002. Patterns of movement in rotational and translational landslides. Geology, 30(8): 719-722.

Petley, D.N., Dunning, D.A. and Rosser, N.J., 2005. The analysis of global landslide risk through the creation of a database of worldwide landslide fatalities. In: O. Hungr, R. Fell, R. Couture and E. Eberhadt (Editors), Landslide Risk Management. A.T.Balkema, Amsterdam, pp. .367-374.

Petley, D.N. et al., 2005b. A new model for the development of movement in progressive landslides. In: O. Hungr, R. Fell, R. Couture and E. Eberhardt (Editors), Landslide Risk Management. A.T.Balkema, Amsterdam.

Petley, D.N., Higuchi, T., Petley, D.J., Bulmer, M.H. and Carey, J., 2005a. Development of progressive landslide failure in cohesive materials. Geology, 33(3): 201-204.

Petley, D.N., Mantovani, F., Bulmer, M.H. and Zannoni, A., 2005c. The use of surface monitoring data for the interpretation of landslide movement patterns. Geomorphology, 66(1-4): 133-147.

Petley, D.N., Petley, D.J. and Allison, R.J., 2008a. Temporal prediction in landslides - Understanding the Saito effect. In: Z. Chen, J.M. Zhang, Z.K. Li, F.Q. Wu and K. Ho (Editors), 10th International Symposium on Landslides and Engineered Slopes. Crc Press-Taylor & Francis Group, Xian, PEOPLES R CHINA, pp. 865-871.

Petrie, G. and Toth, C.K., 2008a. Introduction to Laser Ranging, Profiling and Scanning. In: J. Shan and C.K. Toth (Editors), Topographic Laser Ranging and Scanning: principles and processing. CRC Press, Taylor and Francis Group, Boca Raton, pp. 590.

Petrie, G. and Toth, C.K., 2008b. Terrestrial Laser Scanners. In: J. Shan and C.K. Toth (Editors), Topographic Laser Ranging and Scanning: Principles and Processing. CRC Press: Taylor & Francis Group, Abingdon, Oxon, pp. 87-127.

Pfeifer, N., Dorninger, P., Haring, A. and Fan, H., 2007. Investigating terrestrial laser scanning intensity data: quality and functional relations, 8th Conference on O3D, Zurich, Switzerland.

Picarelli, L., Oboni, F., Evans, S.G., Mostyn, G. and Fell, R., 2005a. Hazard characterisation and quantification. In: O. Hungr, R. Fell, C. Réjean and E. Eberhardt (Editors), Landslide risk management : proceedings of the International Conference on Landslide Risk Management. Balkema, Vancouver, Canada, pp. 27- 62.

Picarelli, L., Oboni, F., Evans, S.G., Mostyn, G. and Fell, R., 2005b. Hazard characterization and quantification. In: O. Hungr, R. Fell, R. Couture and E. Eberhadt (Editors), Landslide Risk Management. Taylor & Francis Group, London, pp. 27-61.

Porkess, R., 2005. Collins Internet linked- dictionary of statistics. Collins, UK.

Powrie, W., 2004. Soil Mechanics: Concepts and Applications. Spon Press, UK, pp.704

Prevost, J.H. and Hoeg, K., 1975. Soil mechanics and plasticity analysis of strain softening. Geotechnique, 25(2): 279-297.

Qin, S.Q., Jiao, J.J. and Wang, S.J., 2001. The predictable time scale of landslides. Bulletin of Engineering Geology and the Environment, 59(4): 307-312.

Read, J.R.L., 2007. Predicting the behaviour and failure of large rock slopes. Rock Mechanics: Meeting Society's Challenges and Demands, Vols 1 and 2: 1237-1243.

Reichenbach, P., Cardinali, M., De Vita, P. and Guzzetti, F., 1998. Regional hydrological thresholds for landslides and floods in the Tiber River Basin (central Italy). Environmental Geology, 35: 146-159.

Reid, G. and Stewart, D., 1986. A large scale toppling failure at Afton, Proceedings International Symposium on Geotechnical Stability in Surface Mining Calgary, Canada, pp. 215-223.

Reid, M.E., 1994. A pore-pressure diffusion-model for estimating landlside-inducing rainfall. Journal of Geology, 102(6): 709-717.

Rice, R.M., Corbett, E.S. and Bailey, R.G., 1969. Soil slips related to vegetation topography, and soil in Southern California. Water Resources Research, 5(3): 647.

Roberts, A., 1977. Geotechnology. Pergamon, Oxford.

Rose, N.D. and Hungr, O., 2007. Forecasting potential rock slope failure in open pit mines using the inverse-velocity method International Journal of Rock Mechanics and Mining Sciences, 44(2): 308- 320.

Rosser, N., Lim, M., Petley, D., Dunning, S. and Allison, R., 2007. Patterns of precursory rockfall prior to slope failure. J. Geophys. Res., 112.

Rosser, N.J., 2010. Chapter 3: Landslides and Rockfalls. In: T. Burt and R.J. Allison (Editors), Sediment Cascades: An Integrated Approach. Wiley, Oxford, pp. 55-89.

Rosser, N.J., Lim, M. and Petley, D.N., 2008. Monitoring and modelling deformation on failing slopes: Implications for understanding landslide failure. In: T.L. Society (Editor), International Conference on Management of Landslide Hazard in the Asia-Pacific Region (Satellite symposium of the First World Landlside Forum), Tokyo, Japan.

Rosser, N.J., Petley, D.N., Lim, M., Dunning, S.A. and Allison, R.J., 2005. Terrestrial laser scanning for monitoring the process of hard rock coastal cliff erosion. Quarterly Journal of Engineering Geology and Hydrogeology, 38: 363-375.

Ruina, A., 1983. Slip stability and state variable friction laws. Journal of Geophysical Research, 88((B12)): 10359-10370.

Ryan, T.M. and Call, R.D., 1992. Applications of rock mass monitoring for stability assessment of pit slope failure. In: Tillerson and Wawersik (Editors), Rock Mechanics, Proceedings of the 33rd US Symposium. Balkema, Rotterdam, Santa Fe, New Mexico, pp. 221-229.

Rybar, J., Stemberk, J. and Wagner, P., 2002. Landslides: proceedings of the First European Conference on Landslides, Prague, Czech Republic, June 24-26. Taylor & Francis, Prague.

Saito, H., Nakayama, D. and Matsuyama, H., 2010. Two Types of Rainfall Conditions Associated with Shallow Landslide Initiation in Japan as Revealed by Normalized Soil Water Index. Sola, 6: 57-60.

Saito, M., 1965. Forecasting the time of occurrence of a slope failure, Proceedings of the 6th International Conference on Soil Mechanics and Foundatin Engineering, pp. 537-541.

Saito, M., 1969. Forecasting time of slope failure by tertiary creep, Proceedings 7th International Conference on Soil Mechanics and Found Engineering, pp. 677-683.

Salciarini, D., Godt, J.W., Savage, W.Z., Baum, R.L. and Conversini, P., 2008. Modeling landslide recurrence in Seattle, Washington, USA. Engineering Geology, 102(3-4): 227-237.

Sarewitz, D., 2000. Science and environmental policy: an excess of objectivity. In: R. Frodeman (Editor), Earth Matters: The Earth Sciences, Philosophy, and the Claims of Community. Prentice-Hall, Upper Saddle RIver, NJ, pp. 79-98.

Sassa, K., 2007. Chapter 1: Progress of the International Programme on Landslides (IPL)- Objectives of the IPL and the World Landslide Forum. In: K. Sassa and P. Canuti (Editors), Landslides- Disaster Risk Reduction. Springer, Berlin, pp. 3- 14.

Schmidt, K.M. and Montgomery, D.R., 1995. Limits to Relief. Science, 270(5236): 617-620.

Schwalbe, E., Maas, H.-G., Dietrich, R. and Ewert, H., 2008. Glacier velocity determination from multi temporal terrestrial long range laser scanner point clouds, Proceedings of the XXI ISPRS Congress, Commission V, WG Beijing, China.

Selby, M.J., 2005. Hillslope Material and Processes. Oxford Press, Oxford, 451 pp.

Singh, B. and Goel, R.K., 1999. Rock Mass Classification- A Practical Apporach in Civil Engineering. Elsevier Science, Netherlands, 268 pp.

Singhroy, V., Molch, K. and Couture, R., 2005. InSAR Monitoring of the Frank Slide. In: O. Hungr, R. Fell, R.R. Couture and E. Eberhardt (Editors), Landslide Risk Management. Balkema pp. 611-614.

Siqing, Q. and Sijing, W., 2000. A homomorphic model for identifying abrupt abnormalities of landslide forerunners. Engineering Geology, 57(3): 163-168.

Skempton, A.W., 1964. Long-term stability of clay slopes Geotechnique, 14(2): 77- 101.

Skempton, A.W. and Delory, F.A., 1957. Stability of natural slopes in London clay, Proc. 4th Int. Conf. Soil Mechanics and Foundation Engineering, London, pp. 378- 381

Skempton, A.W. and Petley, D.J., 1967. The strength along structural discontinuities in stiff clays, Proceedings of the Geotechnical Conference, Oslo, Norway, pp. 29-46.

Smith, W.F. and Hashemi, J., 2006. Foundations of Materials Science and Engineering. McGraw-Hill.

Smyth, C.G. and Royle, S.A., 2000. Urban landslide hazards: incidence and causative factors in Niteroi, Rio de Janeiro State, Brazil. Applied Geography, 20(2): 95-117.

Society, A.G., 2002. Landslide risk management concepts and guidelines in Australian Geomechnaics Society Sub-committee on Landslide Risk Management (ed.). Australian Geomechanics: 51-70.

Staiger, R., 2003. Terrestrial laser scanning: technology, systems and applications, 2nd Regional Conference FIG, Marrakech, Morocco.

Starek, M., Luzum, B., Kumar, R. and Slatton, K.C., 2006. Normalizing LiDAR Intensities. Rep_2006-12-001, Geosensing Engineering and Mapping (GEM), Civil and Coastal Engineering Department, University of Florida.

Stead, D., Eberhardt, E. and Coggan, J.S., 2006. Developments in the characterization of complex rock slope deformation and failure using numerical modelling techniques. Engineering Geology, 83(1-3): 217-235.

Suwa, H., 1991. Visually observed failure of a rock slope in Japan. Landslide News, 5: 8-9.

Tagliavini, F., Mantovani, M., Marcato, G., Pasuto, A. and Silvano, S., 2007. Validation of landslide hazard assessment by means of GPS monitoring technique - a case study in the Dolomites (Eastern Alps, Italy). Natural Hazards and Earth System Sciences, 7(1): 185-193.

Terlien, M.T.J., 1998. The determination of statistical and deterministic hydrological landslide-triggering thresholds. Environmental Geology, 35(2-3): 124-130.

Terzaghi, K., 1950. Mechanism of landslides, Application of Geology to Engineering Practice (Berkeley Volume). Geological Society of America, Washington D.C., pp. 83- 123.

Teza, G., Galgaro, A., Zaltron, N. and Genevois, R., 2007. Terrestrial laser scanner to detect landslide displacement fields: a new approach. International Journal of Remote Sensing, 28(16): 3425- 3446.

Thompson, P.W., 1993. Confirmation of a failure mechanism using open pit monitoring methods. Proceedings of the Australian Conference on Geotechnical

Instrumetnation and Monitoring in Open Pit and Underground Mining, 1. Balkema, Kalgoorlie, pp. 483-489.

Thompson, P.W. and Cierlitza, S., 1993. Confirmation of a failure mechanism using open pit montiroign methods, Proceedings of the Australian Conference on Geotechnical Instrumentation and Monitoring in Open Pit and Underground Mining. Balkema, Kalgoorlie, pp. 483-489.

Travelletti, J., Oppikofer, T., Delacourt, C., Malet, J.-P. and Jaboyedoff, M., 2008. Monitoring landlside displacements during a controlled rain experiment using a long-range terrestrial laser scanning (TLS), ISPRS Beijing, China.

Tsakiri, M., Lichti, D.D. and Pfeifer, N., 2006. Terrestrial laser scanning for deformation monitoring, Proceedings of 3rd IAG/ 12th FIG Symposium, Baden, Austria, pp. 10 (unpaginated).

Ulusay, R. and Aksoy, H., 1994. Assessment of the failure mechanism of a highwall slope under spoil pile loadings at a coal mine. Engineering Geology, 38(1): 117-134.

van Westen, C.J., van Asch, T.W.J. and Soeters, R., 2006. Landslide hazard and risk zonation—why is it still so difficult? Bulletin of Engineering Geology and the Environment, 65(2): 167-184.

Varnes, D.J., 1978. Slope movement types and processes. In: R.L. Schuster and R.J. Krizek (Editors), Special Report 176: Landslides: Analysis and Control. TRB, National Research Council, Washington, D.C., pp. 11-33.

Varnes, D.J., 1983. Time-dependent deformations in creep to failure of earth materials, Proc. 7th East Asian Geotechnical Conference. South Asian Geotechnical Society, Bangkok, pp. 107- 130.

Voight, B., 1989. A relation to describe rate-dependent material failure. Science, 243(4888): 200-203.

Wainwright, J. and Mulligan, M., 2004. Modelling and Model Building. In: J. Wainwright and M. Mulligan (Editors), Environmental modelling: finding simplicity in complexity. John Wiley & Sons, pp. 7-68.

Waltham, A.C. and Dixon, N., 2000. Movement of the Mam Tor landslide, Derbyshire, UK. Quarterly Journal of Engineering Geology and Hydrogeology, 33: 105-123.

Wieczorek, G.F. and Glade, T., 2005. Climatic factors influencing occurrence of debris flows. In: M. Jakob and O. Hungr (Editors), Debris flow Hazards and Related Phenomena. Springer Berlin Heidelberg, pp. 325-362.

Wilcock, P.R. and Iverson, R.M., 2003. Prediction in geomorphology. American Geophysical Union, U.S., 256 pp.

Wilson, R.C. and Wieczorek, G.F., 1995. Rainfall thresholds for the initiation of debris flow at La Honda, California. Environmental Engineering Geosciences, 1(1): 11-27.

Wood, D.M., 1990. Soil behaviour and critical state soil mechanics. Cambridge University Press, Cambridge, 462 pp.

Wylie, D.C. and Munn, F.J., 1978. The use of movemnet monitoring to minimise production losses due to pit slope failures, Proceedings First INternational Symposium on Stability in Coal Mining, Miller Freeman, Vancouver, pp. 75-94.

Xharde, R., Long, B.F., Forbes, D.L. and Ieee, 2006. Accuracy and Limitations of Airborne LiDAR Surveys in Coastal Environments. 2006 Ieee International Geoscience and Remote Sensing Symposium, Vols 1-8, 2412-2415 pp.

Yin, K.L. and Yan, T.Z., 1988. Statistical prediction models for slope instability of metamorphosed rocks. In: C. Bonnard (Editor), Proceedings 5th International Symposium on Landslides. Balkema, Rotterdam, Lausanne, Switzerland, pp. 1269-1272.

Zavodni, Z.M. and Broadbent, C.D., 1980. Slope failure kinematics. CIM Bulletin(April): pp. 69-74.

Zschau, J. and Küppers, A.N., 2003. Early warning systems for natural disaster reduction. Springer- Nature, 834 pp.

Zvelebil, J., 1984. Time prediction of a rockfall from a sandstone rock slope, Proc. IVth International Landslide Symposium pp. 93-95.

Zvelebil, J. and Moser, M., 2001. Monitoring based time-prediction of rock falls: Three case-histories. Physics and Chemistry of the Earth Part B-Hydrology Oceans and Atmosphere, 26(2): 159-167.